

Surface Scattering Studies of Nitric Oxide off Graphene

T Greenwood

PhD 2023

Surface Scattering Studies of Nitric Oxide off Graphene

Thomas Greenwood

A thesis submitted in partial fulfilment of
the requirements of Manchester
Metropolitan University for the degree of
Doctor of Philosophy

Department of Natural Sciences
Faculty of Science and Engineering
Manchester Metropolitan University

2023

Abstract

The scattering of nitric oxide off graphene supported on gold has been investigated using a surface velocity map imaging (VMI) set-up. Nitric oxide (NO) was seeded in a helium molecular beam and directed towards the graphene surface at different velocities along the surface normal. Both the beam and the scattered NO were intersected by a laser and ionised via a (1+1) REMPI scheme at ~ 225 nm. The NO ions were accelerated towards an MCP/phosphor screen detector by the VMI optics. The NO was found to scatter off the graphene surface following one of two mechanisms, direct scatter and (non-thermal) trapping desorption. The directly scattered NO lost $\sim 80\%$ of its initial velocity to the graphene surface and the trapping desorbed NO was found to have a residence time on the order of tens to low hundreds of microseconds.

Accompanying molecular dynamics simulations were carried out using the DL_POLY Classic software package. A simulation box was selected with a 120° rhombus as a base in the x-y plane of length 17.3 \AA each and a z dimension perpendicular to the x-y plane of length 45 \AA . The graphene surface consisted of 98 carbon atoms in a 2D lattice network and was placed on a $6 \times 6 \times 6$ array of gold atoms. Periodic boundary conditions were applied along the x-y plane, but with no periodicity in the z dimension. Thousands of trajectories of NO molecules were directed onto the graphene along the surface normal, while varying impact position, but also speed, orientation, and rotational excitation of the nitric oxide. The simulations agreed qualitatively with the experiment. The directly scattered NO lost a large amount of its initial velocity and there was also the presence of a trapping desorption component.

This work addresses a gap in previous research in the area of surface dynamics, with very few studies taking advantage of surface VMI in graphene dynamics studies and its inherent ability to obtain high levels of detail in both internal and translational energy distributions.

Acknowledgements

Firstly, I would like to thank my supervisor Sven. For taking me on as an inexperienced PhD student, for his expertise and guidance but most of all for his patience, without which this research would not have been possible. I would also like to thank Dr Aidan Doyle and Dr Dale Brownson for their assistance and guidance over the years.

Thanks go to Christopher Lester for aiding in the MD computer simulations, as well as Anthony Walls for helping with my endless IT queries. Thanks to Dr Alejandro Ferrari for all his help preparing the graphene samples. I would also like to thank all the technicians for their help over the years, especially John. To Jean-Hugues Fillion and everyone at Paris for their hospitality as well as Alec Wodtke and everyone at Göttingen for a fantastic tour around the institute.

Everyone on the 7th floor for much needed respite and camaraderie. Special thanks go to Emily and Will for keeping me sane over the years (with the help of plenty of Rudy's pizza).

To my parents for their financial and moral support and always encouraging me to go further.

Finally, I would like to thank Ellie, for her kindness, understanding and for always supporting me. I can't wait for more adventures together.

Table of Contents

Abstract	3
Acknowledgements.....	4
Table of Contents	5
Table of Figures	8
Table of Tables	11
1. Introduction	12
1.1. Reaction Dynamics	12
1.2. Velocity Map Imaging.....	13
1.3. Surface Studies	16
1.4. Graphene	18
1.5. Motivation	19
2. Experimental	22
2.1. Overview of the Surface-Scattering VMI Experiment	22
2.2. Chamber	24
2.3. Laser System.....	28
2.4. Molecular Beam	29
2.5. Ion Optics.....	31
2.6. SIMION.....	32
2.7. Detector.....	33
2.7.1. MCP and Phosphor screen	33
2.7.2. Camera	34
2.8. Control and Analysis.....	35
2.8.1. Timing.....	35
2.8.2. LabView Programmes	35
3. Spectroscopy	36
3.1. Electron configuration and Term Symbols.....	37
3.2. Hund's Cases.....	38
3.3. Energy Levels	39
3.4. Selection Rules and Allowed Transitions.....	41
3.5. Resonance Enhanced Multi-Photon Ionisation.....	41
4. Molecular Dynamics Simulations.....	45
4.1. General	45
4.2. Set-up of the system.....	45

4.3.	CONFIG FILE	46
4.4.	FIELD FILE.....	49
4.5.	CONTROL FILE.....	52
5.	Nitric Oxide Scattering off Graphene using Surface-Velocity Map Imaging.....	55
5.1.	Abstract	56
5.2.	Introduction.....	57
5.3.	Experimental Methods.....	60
5.4.	Computational Methods	65
5.5.	Results and Discussion	66
5.6.	Conclusions.....	74
5.7.	Acknowledgements:.....	74
6.	Interpretation of Experimental Data through Molecular Dynamics Simulations...	75
7.	Molecular Dynamics Simulations of Nitric Oxide Scattering off Graphene.....	78
7.1.	Abstract	79
7.2.	Introduction.....	80
7.3.	Results and Discussion	82
7.4.	Conclusions.....	95
7.5.	Acknowledgements:.....	97
7.6.	Methodology	97
8.	Comparison of Internal State Distributions from Simulations with Experimental Data	103
9.	Velocity-selected Rotational State Distributions of Nitric Oxide Scattered off Graphene Revealed by Surface-Velocity Map Imaging	106
9.1.	Abstract	107
9.2.	Introduction.....	108
9.3.	Methodology	110
9.4.	Results and Discussion	112
9.5.	Conclusions.....	120
9.6.	Supporting Information.....	121
9.7.	Acknowledgements:.....	121
9.8.	Supporting Information.....	122
9.8.1.	Energy Spread of Molecular Beam.....	122
9.8.2.	Overall time-of-flight distributions	122
9.8.3.	Experimental Setup.....	124
9.8.4.	Calibration	125
9.8.5.	Nitric Oxide Energy Level Diagram.....	126

9.8.6.	Image Positions of Molecular Beam, Direct Scatter and Trapping-Desorption Component in Relation to the Thermal Background Image	127
9.8.7.	Rotational Spectra.....	129
10.	Probing the Loss of Kinetic energy of the Nitric Oxide as a Function of the Initial Kinetic Energy, and Estimation of Residence Times	130
11.	Extracting Residence Times of Nitric Oxide on Graphene through combination of Time-of-Flight and Velocity Map Imaging.....	132
11.1.	Abstract.....	133
11.2.	Introduction	134
11.3.	Experimental.....	137
11.4.	Results and Discussion.....	139
11.5.	Conclusions	146
11.6.	Acknowledgements	147
12.	Conclusions	148
13.	Future Work	151
14.	Appendices.....	154
14.1.	Photo-desorption studies with Velocity Map Imaging from interstellar ices (VMICES).....	154
14.2.	Visits.....	158
14.3.	Conferences	158
14.4.	Publications.....	158
14.5.	Funding	158
14.6.	Courses.....	159
14.7.	Copyright Statement.....	159

Table of Figures

Figure 1 - SIMION simulations of ion paths, shown in red and black, from ionisation at the left hand side of the figure, through the VMI optics and on to the MCP detector ¹⁵	15
Figure 2 - Diagram of experimental set-up with the plates cut through in the yz plane for clarity. The molecular beam travels toward the surface in the y direction between the first two plates, is intersected by the laser travelling along the x axis after ~27 cm, the NO molecules scatter off the graphene surface and are again intersected by the laser ~5 cm above the graphene surface and subsequently repelled to the detector along the z axis. The distance between the laser and the surface can be adjusted by ~1 cm, though has little influence on the images produced.	22
Figure 3 – The Vacuum chamber set-up, the molecular beam chamber at the top, main chamber directly below, followed by the time of flight region and detector to the right.....	24
Figure 4 - Diagram of the laser beam path via the YAG and dye laser, directed by a series of mirrors, through to the chamber	29
Figure 5 - Thermal rotational distributions of NO at 300 K and a rotationally colder 30 K.....	30
Figure 6 – The VMI plates held on a threaded rod covered by a ceramic shield and separated by ceramic spacers, attached to the chamber via the threaded rod inside the ceramic shield.....	32
Figure 7 - Molecular orbital diagram of NO demonstrating the overlap of the atomic orbitals of the nitrogen and oxygen atom to form the molecular orbitals; energy levels of the orbitals not drawn to scale.	38
Figure 8 - Energy levels of nitric oxide, where the splitting and relative energies of the levels are not drawn to scale for the sake of clarity, where double prime relates to the ground state and prime to the excited state. The P, Q, and R branches and parity states are defined further in the text.....	40
Figure 9 - Various ionisation schemes. In red, Single photon ionisation. In blue, Multi-photon Ionisation via two photons. In green, Resonance Enhanced Multiphoton Ionisation via one colour (1+1) REMPI.....	42
Figure 10 - Comparison of simulated spectrum of NO and an experimental REMPI spectrum of NO.....	44
Figure 11 - Diagram of set-up of the simulation cell. Starting plane of the NO molecule in the green xy plane and cut-off point for simulations in the red xy plane.	47
Figure 12 - Lennard-Jones potential between a gold and carbon atom.....	51
Figure 13 - Configuration energy of the gold slab and the graphene sheet, where a minimum energy is reached after ~3 ns. The Config energy relates to the sum of all the intra and inter molecular forces as well as any many-body interactions such as metallic forces.....	53
Figure 14 - a) Cutaway CAD drawing of our 12-plate ion optics with the molecular beam indicated; faint green arrow is the REMPI laser beam between the two plates furthest left; x- (along laser beam) and y- dimension (parallel to the molecular beam and surface normal; surface shown in gold near the bottom) chosen, as these are the dimensions which yield the velocity maps' x-y coordinates; z is along the time-of-flight direction. b) SIMION simulations of the electric fields without (red) and with (blue) the surface in place. Grounding shield omitted for clarity.....	62
Figure 15 - a) Overlay of three velocity map images of nitric oxide, NO. The downward facing molecular beam is in blue, the scattered NO in red, and the diffuse green spot in the center is thermal background NO gas, imaged to define the zero velocity coordinate (illustrated by the green cross). b) Rotationally-resolved REMPI spectra of NO in the molecular beam (blue), and scattered off graphene (red). Black arrows point to the Q ₁ (0) and R ₁ (0) lines on which most images were recorded.....	67
Figure 16 - a) Speed distributions extracted from the VM images in Figure 17 for the molecular beam in blue, and the scattered NO in red; the black data are results of molecular dynamics simulations commencing with monoenergetic NO molecules at 1600 m s ⁻¹ , indicated by the black arrow; all data (open symbols) fitted to equation 13 (lines). b) Polar angle distribution of bottom panels for the molecular beam and top panels for the scattered NO; left panels are experimental data, right panels, molecular dynamics simulations. Open circles are data points; lines are fits to a cos ⁿ θ function as shown.	70
Figure 17 - a) Velocity distribution of NO molecules (initial kinetic energy ~0.31 eV) after scattering off graphene resolved along the surface normal (y) and perpendicular to the surface (x, along the propagation direction of the laser). b) Same image, but expressed as speed and polar angle; color range from yellow (=0 intensity) to dark red. Location of graphene schematically indicated in both cases.....	72
Figure 18 - Cos ⁿ (θ) functions for Cos(θ), Cos ² (θ) and Cos ¹⁰ (θ) in part a) showing the functions in a standard x vs y plot and in part b) the same values represented in polar coordinates. Both parts of the	

figure demonstrate how the functions that the polar angle distributions were fitted to become much narrower as n increases.	77
Figure 19 - Speed distributions of NO molecules after scattering off a graphene surface, initial speeds as indicated by vertical arrows. Horizontal double-arrows indicate the loss of speed, and the blue data is an experimental speed distribution with an initial NO velocity of 1418 m/s and a width of ~ 190 m/s. All simulation data fitted to eq. 18.....	83
Figure 20 - Polar angular distributions of NO molecules after scattering off a 300 K graphene surface, initial speeds as indicated. Blue data is an experimental angular distribution with an initial NO velocity of 1418 m s ⁻¹ , and a width of ~ 190 m s ⁻¹ . All data fitted to a $\cos^n \theta$ function, with the fitting parameter n indicated.....	87
Figure 21 - Polar angles θ_{polar} as a function of the final speed of the scattered NO molecules for the five different initial speeds as indicated.....	88
Figure 22 - Four different but characteristic trajectories of NO molecules scattering off graphene. Shown is the distance between the N atom (and not the center-of-mass of NO, in order to highlight rotational effects) and the average height of the six closest C atoms in graphene (not necessarily a hexagon) as a function of time along the x axis. The 2500 m s ⁻¹ trajectory undergoes direct scattering, while the 600 m s ⁻¹ trajectory shows trapping-desorption behaviour. The two 1200 m s ⁻¹ trajectories (with the same initial slope) undergo direct scattering (yielding a rotationally excited NO) or permanent trapping (within the simulation time of 4 ps).....	90
Figure 23 - Trapping probabilities for collisions of NO molecules with graphene for the five indicated initial speeds, and separated for N-first and O-first orientation (without rotation), and NO molecules with a thermal rotational state distribution at 80 K.	91
Figure 24 - Selected rotational state distributions of NO radicals scattered off graphene. Top-two panels for N-first and O-first orientation without initial rotational excitation, bottom-two panels for initial thermal 80 K rotational distributions. Open symbols for 600, 800, and 1200 m s ⁻¹ , closed symbols for 1600 and 2500 m s ⁻¹	93
Figure 25 - Shortest distance between the N atom of NO and the average of six closest C atoms in graphene at the turning point as a function of final speed, with the linear fit only as a guide to the eye. All data for N-first orientation, but data is very similar for O-first orientation.....	95
Figure 26 - Schematic of input parameter of the molecular dynamics simulations. NO molecules are placed 12 Å above the graphene surface and given a certain velocity, and in some cases rotational excitation. They are directed along the surface normal towards a random position on the graphene, from where they scatter back before they are recorded when traversing a virtual plane 8 Å above the surface.	102
Figure 27 – The images of the various NO components along with their respective regions of interest. Blue for NO in the molecular beam at a relative time (t_{rel}) of 0 μ s, red for scattered NO ($t_{rel} + 100 \mu$ s), pink for the trapping component ($t_{rel} + 400 \mu$ s) and the green dot indicating our center spot relating to zero overall velocity in the x and y dimensions.	113
Figure 28 – Rotational spectrum of the scattered NO with the relevant lines of the O ₁₂ branch highlighted.	116
Figure 29 – a) Boltzmann plot of O ₁₂ branch of the scattered NO, b) P ₁₂ branch of the trapping desorption component., where the gradient can be used to calculate the rotational temperature, as described above.....	117
Figure 30 - Kinetic energy distribution of the incoming beam of 2% nitric oxide, NO, in He.....	122
Figure 31 - Overall time-of-flight distribution measured on the scope (in black) and distributions measured using Regions of Interest (ROI)	123
Figure 32 - Relative orientation of the laser (x, into the plane of the paper), the molecular beam (y, downwards), and the time-of-flight direction towards the multi-channel plate detector (z).	124
Figure 33 - Thermal background image of nitric oxide at 298 K with zero velocity spot indicated.....	126
Figure 34 - Raw thermal background image of nitric oxide let into the vacuum chamber through leak valve at 1×10^{-7} Torr (left), and fit of a 2-dimensional Maxwell-Boltzmann distribution to the thermal background spot (right) to determine zero velocity pixel shown in green in Figure S4.....	126
Figure 35 - Energy level diagram of nitric oxide including the probed O ₁₂ (3.5) line.....	127
Figure 36 - Composite image of the molecular beam (white bottom), directly scattered (white top) and trapping-desorption component (fuzzy white in the middle) in relation to the thermal background image in red.	128

<i>Figure 37 - Rotational spectra of scattered NO (black), thermal background NO (red), and a LIFBase simulation of 298 K (blue). The LIFBase spectrum was shifted by 0.2 nm to coincide with the experimental spectra as the laser wavelength was not calibrated.</i>	<i>129</i>
<i>Figure 38: a) Cut through experimental set-up, the molecular beam pointing vertically down along the y dimension towards the graphene surface, the beam and subsequently scattered NO molecules are intersected by the laser in the xz plane. b) Composite image of the components of NO arrival positions with their respective regions of interest. The molecular beam in blue, directly scattered NO in red and trapping desorbed NO in orange, where the green dot represents the spot of zero velocity in the x and y dimensions.</i>	<i>139</i>
<i>Figure 39: a) Time-of-flight scan of NO extracted directly from the overall detector signal, for a 2% NO mixture in He, consisting of all components. b) TOF scan of NO extracted from ROI relevant to the molecular beam for three NO mixtures. c) TOF scans of directly scattered NO. d) Delay scan of the trapping-desorbed NO for a pure helium mixture. Signal intensities for (a), (b), (c) and (d) not on the same intensity scale.</i>	<i>140</i>
<i>Figure 40: a) Velocity distributions of NO in the molecular beam extracted from VMI images for NO in the pure helium beam, 20% argon and 50% argon. b) Velocity distributions of directly scattered NO in the pure helium beam, where the scattered signal consists of a normalised composite image over a range of delay times with respect to the laser firing and molecular beam opening. c) The scattered NO velocities in the pure helium beam and 50% argon mixture over a range of delays.</i>	<i>142</i>
<i>Figure 41: a) Velocity distribution of trapping-desorbed NO in a pure helium beam, extracted from VMI images. b) Reduction in energy for directly scattered and trapping desorbed NO when compared to the incoming molecular beam, for the helium beam, 20% argon and 50% argon mixtures.</i>	<i>143</i>
<i>Figure 42 - Comparison of the time-of-flight profiles recorded within the regions-of-interest (black, red, orange) with the Monte Carlo simulated TOF profiles using the VM images (faded lines) for a) the molecular beam, b) the directly scattered nitric oxide molecules, and c) the trapping desorption component.</i>	<i>144</i>
<i>Figure 43- A cut-out view of the experimental set-up for the VMI Ices experiments, showing the cut-out holes in the optics for the incoming desorption laser and subsequent time of flight tube which attaches the plates to the reaction chamber of the Paris set-up.</i>	<i>155</i>
<i>Figure 44 - SIMION calculations of the VMICES set-up with the shields removed for clarity. Left-hand side of the image shows the molecules between the first two plates with a) no voltages applied to the VMI optics and b) voltages applied, c) demonstrating VMI conditions at the detector.</i>	<i>156</i>

Table of Tables

<i>Table 1 - Voltages for the VMI optics</i>	31
<i>Table 2 - Values of variables used for calculating rotational energy levels for any given vibrational level where all values have units of cm^{-1}.</i>	40
<i>Table 3 - Parameters for Gupta potential</i>	49
<i>Table 4 – Lennard-Jones Parameters</i> ^{49, 50}	52
<i>Table 5 - Initial and most probable final speeds (in m s^{-1}) and kinetic energies (in eV) and energy loss and ratio. The data for 600, 800, 1200, 1600 and 2500 m s^{-1} are from the simulations while the data for 1418 m s^{-1} are from experimental work.</i>	85
<i>Table 6 – Parameters used for the Gupta potential to describe interactions in gold</i> ⁴⁵	97
<i>Table 7 - Parameters for the van der Waals interactions</i> ^{49, 50}	99
<i>Table 8 – The various NO species detected in our experiment with their respective speeds at peak delay times. The beam is naturally travelling in opposite direction to the scatter and trapping-desorption components.</i>	114
<i>Table 9 - Rotational temperatures of the various NO events derived from the linear fits to the Boltzmann plots in Figure 29, errors are standard errors.</i>	118

1. Introduction

1.1. Reaction Dynamics

Reactions are a major part of chemistry, possibly the very essence of chemistry, and have been investigated for hundreds of years, with early examples such as Lavoisier's investigation of combustion in 1772.¹ The study of how fast reactions proceed, kinetics, is crucial for understanding how complex systems operate, such as the depletion of the ozone layer.^{2, 3} Reaction dynamics as a field of chemistry is concerned with how atoms and molecules interact with one another following collisions. Reaction dynamics investigates a) what kind of interaction occurs such as scattering, reaction, and adsorption and b) the energy distributions after collision both internal and translational. In terms of dynamics, one can study reaction dynamics or if collisions between atoms and molecules occur where no reactions are present, scattering dynamics. The latter is also crucial in the field of chemistry as without collisions there can be no reactions, it is hence an active area of research to study the energy distribution of atoms and molecules after collisions.^{4, 5}

When studying species at the most fundamental level, it is appropriate to consider these species in isolation, which is to say as little influence from other media as possible, hence most studies in the reaction dynamics occur in the gas phase. It is can also be helpful to perform these studies on a femtosecond timescale such that even in liquid media, the interactions with other molecules occur too slowly to have a significant impact on the results. It is this isolation of species and simplicity of interactions that meant the earlier

years of reaction dynamics were often conducted in the gas phase, though in recent years surface studies have become more prevalent.⁶ Some of the most notable research in gas phase dynamics was that conducted by the recipients of the 1986 Nobel prize in chemistry, Dudley Herschbach, Yuan T. Lee and John Polanyi.^{7, 4, 8, 9}

1.2. Velocity Map Imaging

One of the main advancements in studying reaction dynamics is the development of the velocity map imaging technique (VMI). It is useful to think of the VMI set-up as a natural extension to the mass spectrometer which has been played a key role in studying chemical species for over a century, most notably leading to a Nobel prize for Aston.¹⁰ While Aston's work mainly pushed the use of mass spectrometry as an analytical tool, there are examples of rotating mass spectrometers being deployed in crossed beam studies.^{11, 12} Where the early mass spectrometers successfully separated ions based on their mass/charge ratio, VMI set-ups replace the detector with a position sensitive imaging detector in order to record the ions in velocity space. VMI allows for the measurement of velocity distributions of particles in two dimensions all in one experiment without the need to repeat experiments while moving the mass spectrometer around to measure the full distribution.

The experimental technique of VMI was first developed by Eppink and Parker in 1997, though is mostly a further development of previous research into ion imaging by Houston and Chandler.^{13, 14} The crux of VMI is that it allows the imaging of ion products entirely based on their velocity, independent of where they were ionised. This is a huge advantage over other techniques and is why VMI as a technique is now ubiquitous in

reaction dynamics studies. VMI employs positively charged plates to guide a species of interest towards a detector once it has been ionised. The target species is ionised by a laser and repelled by a first plate and subsequently through holes in the rest of the plates and towards an MCP/phosphor screen detector. The ions hit the MCP and result in a cascade of electrons that then hit the phosphor screen causing it to fluoresce. The fluorescing screen is then recorded with a triggered camera and images are built up over thousands of laser shots to gain a full velocity distribution in two dimensions. While the earlier model developed by Chandler *et al.* made use of a wire mesh in the plates, the introduction of open lens electrodes by Eppink and Parker was a huge leap forward for ion imaging. It should be noted there is a select region where VMI conditions prevail, and this volume is more than sufficient for molecular beam studies and especially in set-ups where the beam travels along the surface normal.¹⁵

The diagram in Figure 1 features SIMION simulations taken from a previous paper from this group which shows the path of ions from the ionisation region on the left to the MCP on the right hand side after being guided by the VMI optics.¹⁵ It can be seen from the black and red particles that regardless of initial starting position, the ions with the same velocity arrive at the same spot on the MCP, e.g. particles travelling with 5 m s^{-1} upwards along the surface normal will all arrive in the same spot. Further explanation for the VMI set-up used in these experiments is given in the experimental chapter. Further SIMION simulations demonstrating the effects of the optics on the ion paths are shown in Figure 44 in the appendices.

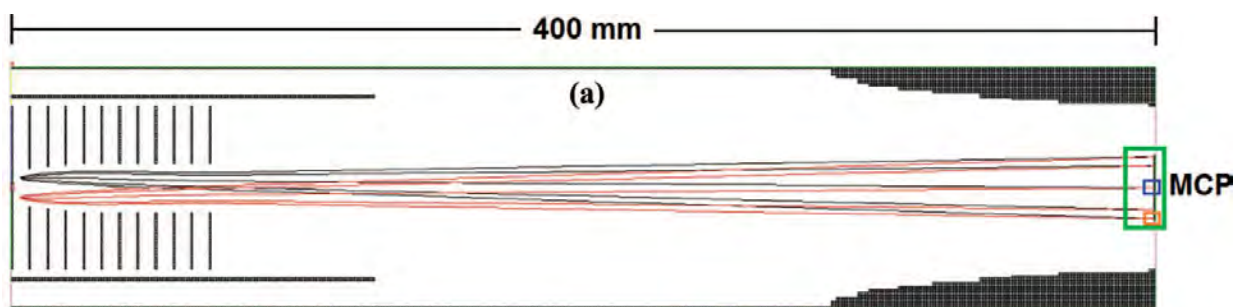


Figure 1 - SIMION simulations of ion paths, shown in red and black, from ionisation at the left hand side of the figure, through the VMI optics and on to the MCP detector¹⁵

There have been several developments in velocity map imaging studies since 1997 with improvements to resolution and the ability to study larger molecules and their fragments using time resolved multi-mass velocity map imaging.¹⁶ Advancements in the field of VMI include that by Suits *et al.*, which made use of standard video techniques along with a counting algorithm to significantly improve the resolution of the detection method, yielding sub-pixel precision.¹⁷ The laser sheet ionisation method utilised by Suzuki *et al.* made use of a cylindrical lens to focus the laser beam into a sheet to ionise a portion of an NO₂ photolysis cloud.¹⁸ By adjusting the timing of the laser sheet, they were able to reconstruct the entire ion cloud. A key advancement in ion imaging was also the slicing method developed by Kitsopoulos *et al.*¹⁹ whereby a delay was introduced between the ionisation of the target species and the introduction of the repeller being triggered. This delay allows the ion cloud to expand while a short gate opening time allows just the centre of this ion cloud to be imaged. The result being that the final image has a lot of the noise removed due to the lack of Abel transformation required.

1.3. Surface Studies

As discussed earlier, reactions are at the heart of chemistry. While earlier studies of reaction dynamics focussed on the isolated environment of gas phase reactions, reactions at surfaces are of particular interest due to their relevance in areas such as heterogenous catalysis.²⁰ The dynamics of the interactions at surfaces are one of the key factors that dictate whether reactions at surfaces occur, as such this has prompted a vast amount of research into the dynamics at surfaces.^{21, 22} Some of the most notable studies at surfaces are those by Gerhard Ertl which earned him the Nobel prize for a number of studies involving fundamental molecular processes at the gas-solid interface.²³ This included research into the Haber-Bosch process, studying N₂ adsorption onto Fe which led to the development of a complete energy scheme of the Haber-Bosch process. This perfectly demonstrates how studying reactions and dynamics at their fundamental levels can provide great insights into real world applications.²⁴

A key part of research into surface catalysis involves the use of thin oxide films, which are being utilised as a means to introduce replicability in single crystal surfaces.²⁵ The most heavily researched of these oxides being TiO₂ due to its applications in photovoltaics as a result of the pioneering research by Fujishima and Honda.²⁶ Indeed, work by White *et al.* investigated photo-desorption of oxygen from TiO₂ in one of the earlier examples of VMI surface studies.²⁷ They found evidence of two pathways, one 'fast' channel and one 'slow' channel in which the kinetic energy was linked to the temperature of the surface. Surface science research has revolutionised the field of

catalysis, though this field is broad ranging and as such is not covered extensively in this introduction.²⁸

As the VMI methodology advanced, it was expanded from studying gas phase collisions and reactions to the dynamics at surfaces. Research by Wodtke *et al.* utilised VMI to investigate Br desorbing from a KBr surface, where they developed three-dimensional surface velocity map imaging (TDS-VMI) method allowed for velocity distributions in three dimensions which revealed two hyperthermal channels of Br emission.²⁹ Further developments by the group resulted in a new instrument that can provide velocity distributions of scattering molecules as well as residence times of molecules at the surface.³⁰ Research by Greaves *et al.* investigated the issue of a dielectric surface interacting with, and potentially distorting, the electric fields in the VMI region. The study provided advancements in surface VMI studies by making use of charged scalpel blades which matched the electric field in order to maintain VMI conditions around a PTFE surface held between the ion optics rather than being held underneath.³¹

In previous work from the Köhler group, nitric oxide was found to non-thermally desorb from a gold surface following laser desorption at 355 nm.³² The NO desorbed primarily along the surface normal with a narrow distribution. These findings were revealed by 3D-VMI without the use of complex rotating mass spectrometers, which greatly reduces experimental complexity and acquisition time. This set-up was then later used to provide translational and rotational distributions of the desorbed NO which revealed the presence of two desorption pathways. The presence of these pathways depended upon the wavelength of the laser used, the non-thermal pathway described in the earlier research via electronic excitation, as well as a thermal activated mechanism when using

a shorter wavelength caused by a jump of the surface temperature.³³ The group also combined these VMI studies with DFT calculations and X-ray photoelectron spectroscopy to provide insights into NO adsorption geometry on gold.³⁴ The NO was found to adsorb 'N first' with the oxygen atom facing away from the surface along the surface normal, demonstrating that as well as investigating desorption products, VMI can be utilised for investigating alignment and orientations of adsorbates and the adsorption sites.

1.4. Graphene

Since its discovery around 20 years ago, graphene has caught the attention of surface scientists due to its unique 2D hexagonal lattice structure and promising chemical properties.³⁵ Graphene in its pristine form is a zero band gap material. This band gap can be tuned by functionalising the surface via chemical reactions which has been investigated using sum frequency generation spectroscopy by this group previously.³⁶ ³⁷ There are multiple examples of graphene now being utilised in surface dynamics studies. A key piece of research by Wodtke and co-workers scattered H atoms off graphene supported on platinum and found evidence of a bimodal distribution due to a quasi-elastic channel but also an inelastic channel caused by temporary bond formation between the H atoms and the graphene surface.³⁸ Furthermore, Minton and co-workers investigated N₂ collisions on highly orientated pyrolytic graphite, where the top layer is essentially graphene, and compared the molecular beam experiments with accompanying molecular dynamics (MD) simulations. It was found that the N₂ molecules scatter with three trajectories, single collision, multi-collision with escape and multi-collision without escape from the surface.³⁹ The extent to which the molecules became

'quasi-trapped' on the surface was strongly linked to the incidence angle, the trapping highest at an angle of $\theta_i = 70^\circ$ with respect to the surface normal, where translational energy along the surface normal is lowest. At this shallow incident angle, the molecules spend a longer amount of time travelling close to the surface compared to angles closer to the surface normal, thus more time spent interacting with attractive forces at the surface.

The interest in reactions and dynamics studies of graphene extends to theoretical research. Hase *et al.* modelled the chemical dynamics of O_2 with graphene and found that reactivity was not present in pristine or low defect graphene but was present for graphene with larger vacancies in the structure, with 4-6 C vacancies leading to dissociative chemisorption upon collision.⁴⁰ Further direct dynamics studies also found oxygen forming products on the graphene surface, with reactivity higher in defected graphene than pristine graphene and also that steering effects on O atoms already on the surface affect incoming molecules.⁴¹ Guo *et al.* also performed direct dynamics simulations investigating nitrogen molecules scattering off graphene and found that as well as direct scattering, nitridation of the graphene surface also occurred leading to desorption of various products such as CN.⁴²

1.5. Motivation

While reaction and scattering dynamics research has progressed considerably in recent years, there remains very little research investigating graphene with surface velocity map imaging, particularly not molecular scattering. There are currently very few

examples in the literature in which VMI has been used in such a way that only certain parts of the detector signal have been analysed to distinguish between various components. This thesis addresses this gap in the current literature by taking advantage of the surface velocity map imaging technique with its ability to extract internal and translational energy distributions with high resolution. Along with the addition of regions of interest for velocity selected distributions, this represents a significant advancement in the study of graphene scattering dynamics, for which there are few examples in the literature of surface studies at this level of detail. The experiments in this thesis set out to investigate the kinetic and internal energy distributions of nitric oxide scattering off graphene using a surface velocity map imaging set-up. Nitric oxide was a suitable candidate for these experiments for several reasons. Due to NO being a radical, it has the potential to react with the graphene surface, has a well documented ionisation scheme and there are numerous examples in the literature of previous scattering experiments using NO for results using graphene to be compared against. The previous literature concerning NO is discussed in Chapter 5.2, and throughout the thesis where relevant, along with further discussion around the necessity for further research on graphene in surface dynamics studies.

Chapter 5 in this thesis investigates the velocity and angular distributions of the nitric oxide scattering against the graphene surface and compares these distributions to the accompanying molecular dynamics simulations. Chapter 7 delves further into the molecular dynamics simulations by altering the incoming velocity of the nitric oxide and providing insights into the two distinct components of the nitric oxide after collision, direct scatter and trapping desorption. Chapter 9 focuses on the rotational distributions of the directly scattered and trapping desorbed NO. The chapter also introduces the use

of regions of interest to record these rotational distributions as a function of velocity. Lastly, Chapter 11 contains (currently unpublished) results concerning the use of regions of interest to extract time of flight distributions of the NO molecules as a function of velocity. These time of flight traces were compared with theoretical time of flight traces to calculate the residence times of the NO on the surface.

2. Experimental

2.1. Overview of the Surface-Scattering VMI Experiment

A molecular beam of nitric oxide (NO) is directed into a vacuum chamber via a molecular beam valve towards a sheet of graphene supported on gold. The nitric oxide then collides with the graphene surface. Both the initial molecular beam as well as the scattered beam are intersected by a laser resulting in the NO being ionised. The ionised NO is then repelled by a series of biased plates towards an MCP/Phosphor screen detector.

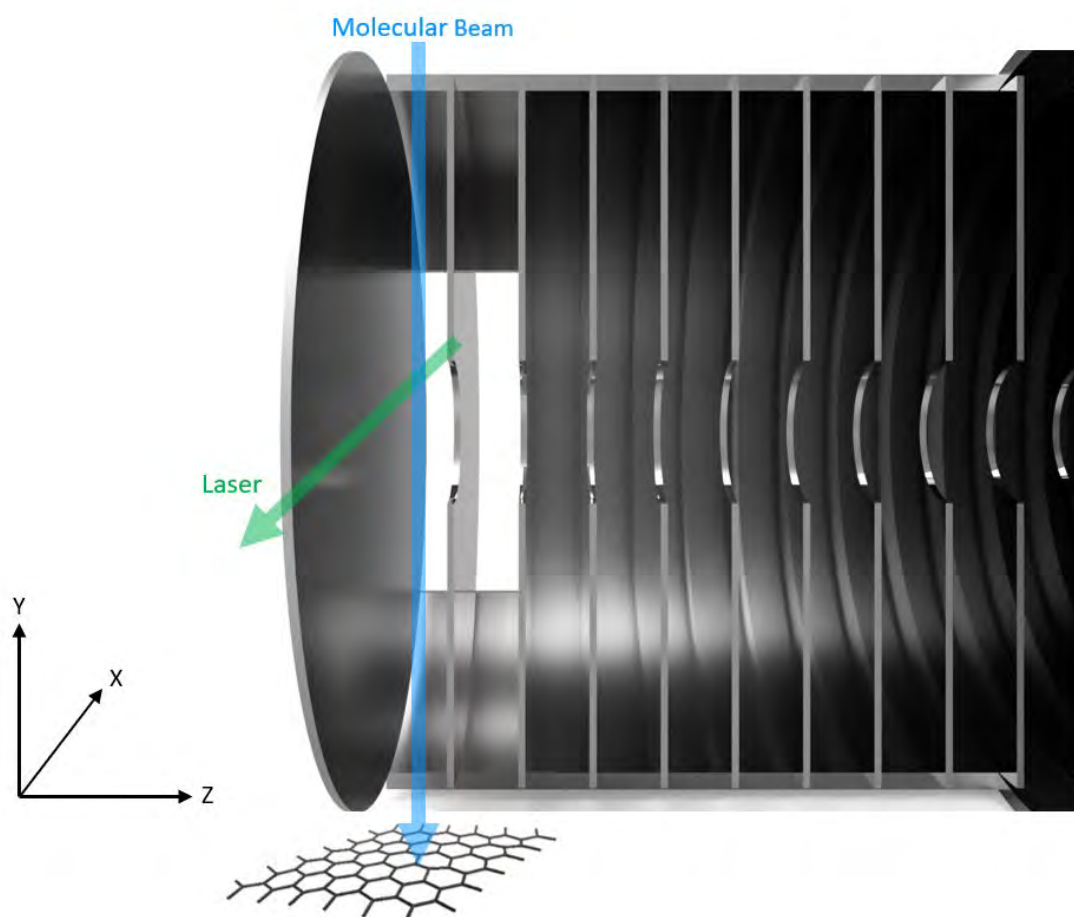


Figure 2 - Diagram of experimental set-up with the plates cut through in the yz plane for clarity. The molecular beam travels toward the surface in the y direction between the first two plates, is intersected by the laser travelling along the x axis after ~ 27 cm, the NO molecules scatter off the graphene surface and are again intersected by the laser ~ 5 cm above the graphene surface and subsequently repelled to the detector along the z axis. The distance between the laser and the surface can be adjusted by ~ 1 cm, though has little influence on the images produced.

The resulting signal is either transmitted as a purely electrical signal towards an oscilloscope yielding time of flight data, or the image on the screen is recorded via a triggered camera. The images themselves are then analysed which yields the valuable 2D velocity information achieved by this orientation of the beam and surface. While the laser, and thus the rest of the experiment, is triggered to fire at 10 Hz, a typical set of results takes around 20 minutes to complete. This is due to the fact the signal or images are averaged across tens of thousands of laser shots in order to gain a complete picture of the dynamics of NO scattering off graphene.

The components of this experiment can be separated into six parts; the vacuum chamber, the molecular beam, the laser system, the optics, the detector and finally the control and analysis portion of the experiment.

2.2. Chamber

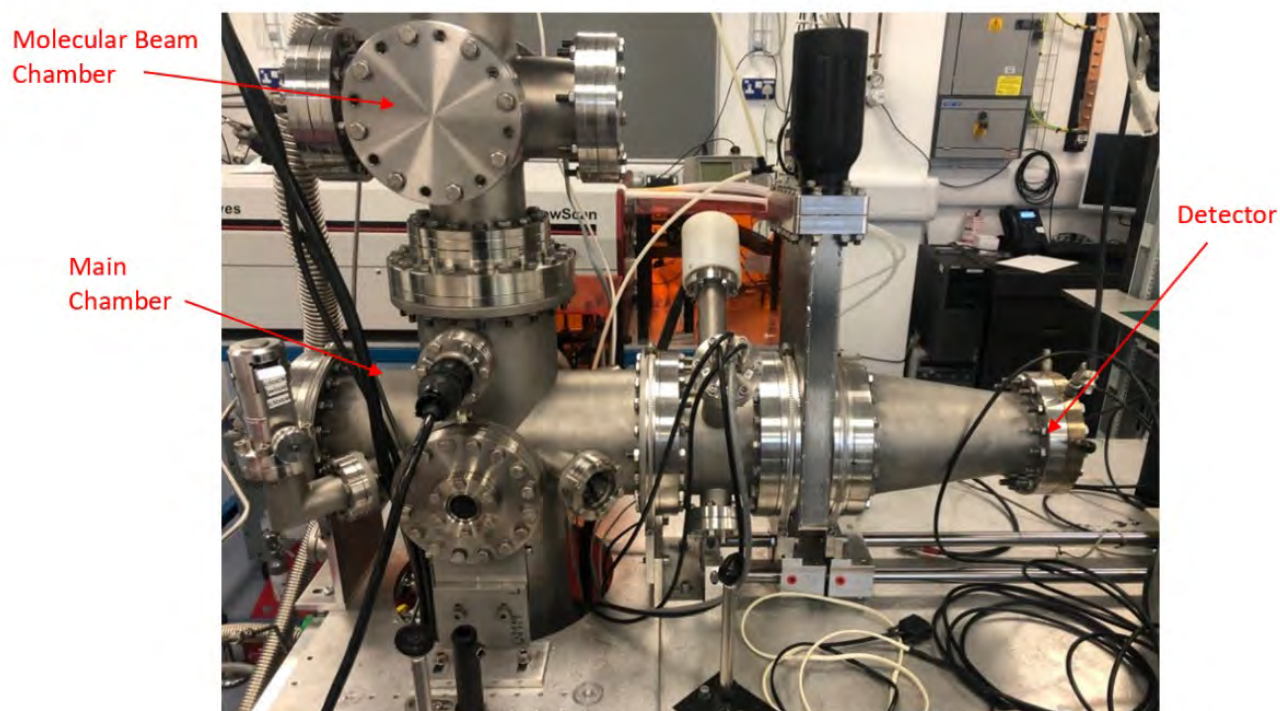


Figure 3 – The Vacuum chamber set-up, the molecular beam chamber at the top, main chamber directly below, followed by the time of flight region and detector to the right.

Figure 3 shows the vacuum chamber, it is made of 304L stainless steel and composed of two differentially pumped chambers. The first of the two sub chambers is the ‘molecular beam chamber’, this part of the set-up houses the molecular beam and the skimmer. The molecular beam chamber consists of a six-way cross, attached to a turbo molecular pump on the top flange, the main chamber on the bottom flange and the gas line for the molecular beam on the left flange with the remaining ports closed off. The second of the two sub-chambers is the ‘main chamber’ which holds the graphene surface where the scattering of NO takes place. This chamber is located below the molecular beam chamber. The two chambers are separated by a 1 cm thick plate, containing a 2 cm hole in the centre of the plate and a 1 mm skimmer to allow the molecular beam to pass through.

Also visible are a number of laser windows, with the exit port for the laser shown in the plane of the image and the one to the right of it at 45° for past and future experiments to irradiate the surface at 45°. The plates are held in the middle of the main chamber with the first two plates on either side of the centre and parallel with the laser exit window. Not visible in the figure is the manipulator which holds the graphene surface in place, this is mounted to the flange on the left-hand side of the main chamber.

To the right of the main chamber is a short 6 way cross, with the tube along the larger flanges acting as the time of flight tube, with two of the smaller flanges closed off and the remaining two being used for the electrical feedthroughs for the plates. Next in the sequence is an 8" pneumatic gate valve which is used to isolate the detector from the main chamber as the part of the chamber containing the detector must be kept under vacuum, hence a gate valve allows the chamber to be left open and worked on (such as adding the graphene surface), while the detector region is held under vacuum. After the gate valve is the 8" to 6" reducing cone, part of the TOF tube, which marks the end of the time of flight tube with the detector being mounted at the 6" flange. Altogether the chamber is ~2 m tall and ~1.5 m long.

For VMI studies, or many experiments concerned with reaction dynamics relying on the detection of ions, it is important for the experiment to be conducted under (ultra-)high vacuum conditions to ensure any molecules or ions do not undergo collisions before being detected. This is to ensure that the velocity, angular and internal energy distributions of the species in question can be probed, as any collisions after formation would alter these properties. A useful method for ensuring species will not undergo collisions and adequate internal pressure in the chamber is to calculate the mean free

path, λ , of the species being probed. The mean free path is the distance a species can travel before colliding with another molecule and must be as long as possible, though at least as long as the time of flight distance. The mean free path is given by the equation below

$$\lambda = \frac{kT}{\sqrt{2}\sigma p} \quad (1)$$

where σ is the molecule's collision cross section, in the case of N_2 this is equal to 0.43 nm^2 .⁴³ At a temperature of 298 K and operating pressure of the chamber during experiments usually equal to or below 5×10^{-8} Torr, the mean free path would be on the order of 1000 m. Achieving and maintaining this pressure requires the use of several pumps which are described in detail below.

As is often the case for ultra-high vacuum set-ups, the low pressures are achieved using turbomolecular pumps which are themselves backed by rotary pumps. The molecular beam chamber is evacuated using a refurbished Edwards STP-1000C turbo pump and the main chamber is evacuated by its own Edwards STP-1003 turbo pump.

The turbo pumps are essential for reaching the low pressures required for VMI experiments but require a pressure of lower than 10^{-2} Torr to operate. The turbo pump blades operate at 35,000 rpm and while in operation are levitated using magnets in order to eliminate friction and avoid the use of lubricants. These turbo pumps are capable of reaching pressures as low as 10^{-10} Torr.

As previously stated, the turbo pumps are only in operation once the pressure in the chambers is suitably low, this is achieved by two Edwards E2M28 rotary pumps, one for each turbo pump. Contamination of the pumps with particles of oil from the seals on

the pumps is prevented through the use of an oil mist filter. The evacuated gas from the chamber is then removed with the use of an independent extraction system to ensure no toxic gases such as nitric oxide is pumped into the laboratory itself. The turbo pumps themselves have KJ Lesker pneumatic angle valves at their outlets, these angle valves can be closed to isolate the turbo pumps from the rotary pumps which is necessary when opening and closing the chamber between experiments or for quick maintenance on the rotary pumps.

It is important to note there are a further two rotary pumps, one for evacuating the gas manifold and the other for evacuating the differentially pumped rotational manipulator which holds the surface in place.

The pressure inside the chamber and the lines is monitored via several pressure gauges permanently mounted on the pumps and chamber. The rotary pump pressures are continuously monitored via a mix of SRS-PG105 and Edwards APGX-M-NW16/ALI Pirani gauges which are vital for checking the pressure in the gas manifold as well as ensuring the fore line for the turbopumps is at an adequately low pressure.

The pressure in the main chamber is monitored intermittently via an SRS-NW-F-UHV ion gauge which provides accurate values for the pressure inside the main chamber to as low as 10^{-11} Torr but cannot run continuously as it only operates at pressures below 10^{-3} Torr and the resulting photons and electrons from the tungsten wire interfere with the experiments. The pressure in the molecular beam chamber is monitored by an Edwards AIM-X-DN40CF gauge.

2.3. Laser System

The VMI experiments conducted in this thesis made use of a 'one colour' 1+1 resonance enhanced multi-photon ionisation (REMPI) scheme, where only one wavelength was used for the excitation and ionisation of the NO. In order to achieve the wavelength of ~ 225 nm necessary, the laser system makes use of a dye laser powered by an Yttrium Aluminium Garnet (YAG) laser as shown in detail in Figure 4. The YAG laser is a Continuum Surelite II-10 Nd:YAG laser, the frequency of the YAG laser makes use of a doubling crystal to achieve 532 nm and then tripling crystal to reach the 355 nm which pumps the dye laser. The dye laser in the set-up is a Radiant Dyes Narrowscan laser which uses Coumarin 450 and a BBO crystal to achieve wavelengths of ~ 225 nm. The laser system produced laser pulses at 10 Hz with a typical energy of 0.8 mJ at ~ 225 nm.

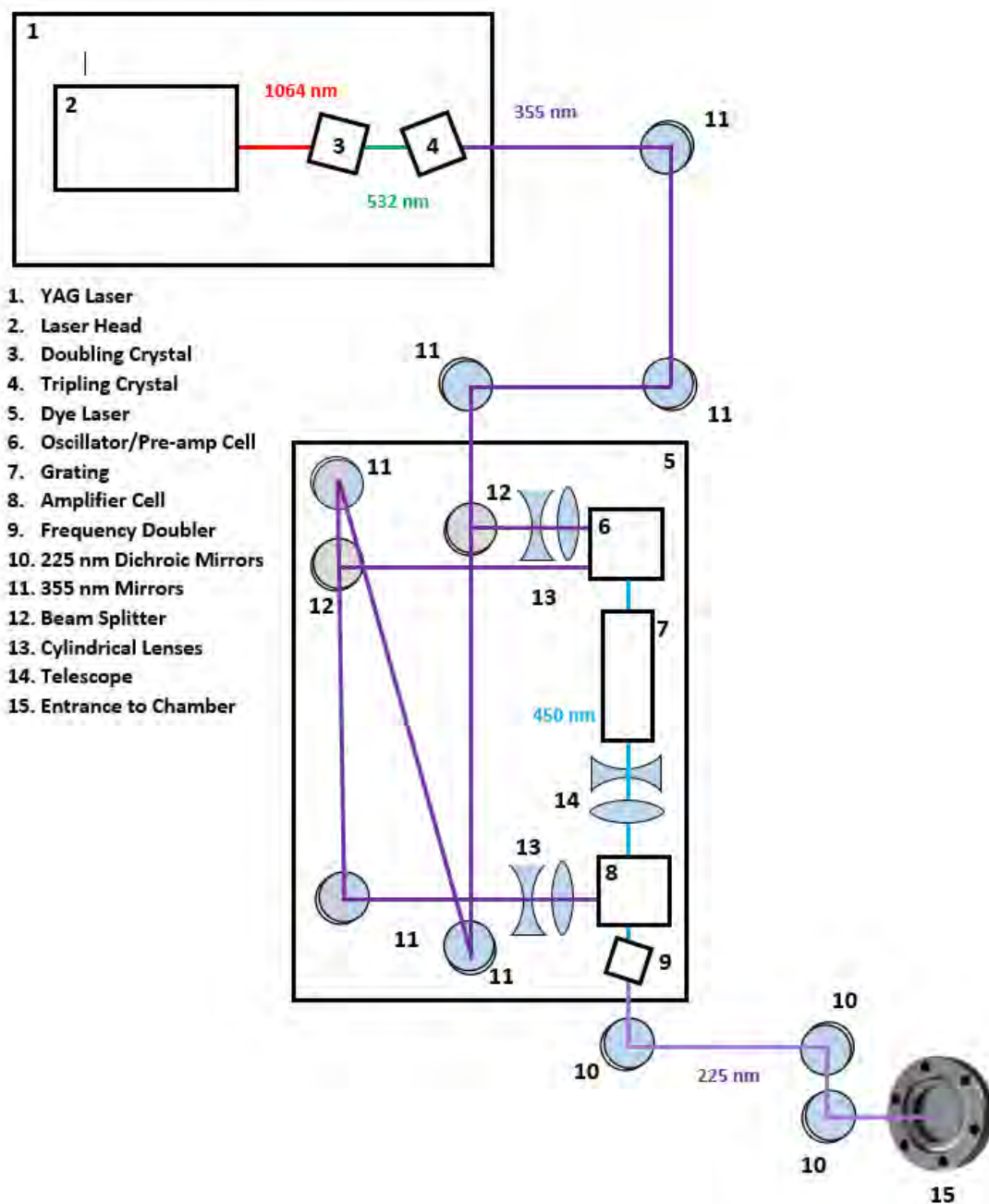


Figure 4 - Diagram of the laser beam path via the YAG and dye laser, directed by a series of mirrors, through to the chamber

2.4. Molecular Beam

In surface scattering studies, it is necessary for the scattered molecule, in this case NO, to occupy as few quantum states as possible in order to correctly identify any resulting changes in the energy distribution to be a result of the scattering process. Therefore, the ideal situation is for narrow angular, speed and internal energy distributions. In a

room temperature sample of NO, the molecules may be in the ground state in both vibrational and electronic states, yet there will still be a broad rotational state distribution and the molecules' translational energy distribution can be described by a Maxwell-Boltzmann distribution. Hence, most reaction dynamics studies make use of a molecular beam in which the rotational temperature is rather cold thereby ensuring the internal energy is well defined and the velocity distribution of the beam is also narrow even at the high translational energies. Typically, experiments in this thesis made use of a skimmed (General Valve series 9 nozzle via a Beam Dynamics, 0.5 mm orifice) molecular beam 2-5% mixture of NO seeded in a He carrier gas. Figure 5 shows the

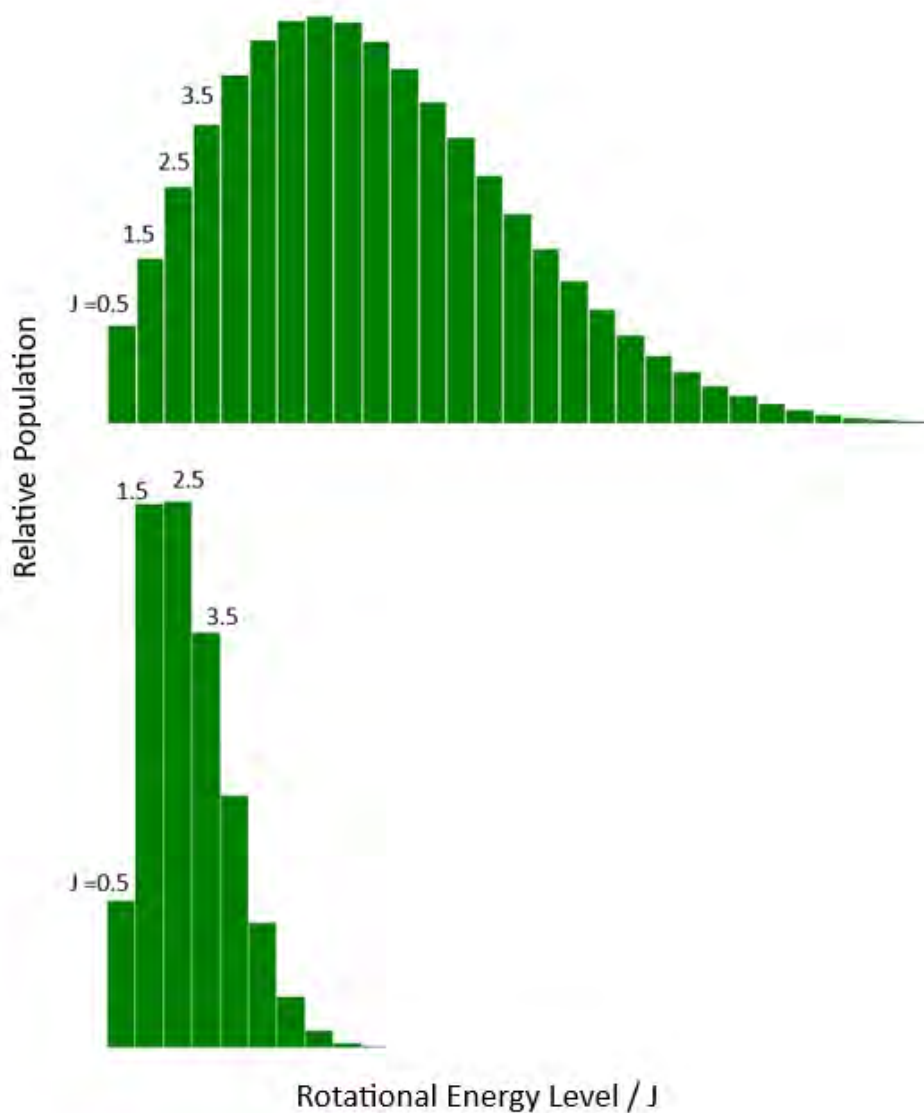


Figure 5 - Thermal rotational distributions of NO at 300 K and a rotationally colder 30 K.

difference in rotational distributions in thermal samples at 300 K in the upper portion of the figure and in a much cooler sample temperature of 30 K in the lower portion. It should be noted the temperatures of the samples shown were chosen for illustrative purposes and do not represent the experimental data from this thesis.

2.5. Ion Optics

The optics that guide the NO ions to the detector consist of 12 electrodes biased between 0 and ~1000 V detailed in Table 1. While in traditional VMI studies the set-up typically contains 3 electrodes, but the experiment here makes use of 12 electrodes as it allows for a softer extraction of the ionised species and a larger volume in which VMI conditions prevail.

The plates are biased by four Applied Kilovolts HP Series precision high voltage 5 kV modules (HP005PPP025) via insulated copper wire. The first four plates are controlled by one supply, plates 5 and 6 require their own supply each, followed by plates seven to eleven on the remaining supply, with the 12th plate at 0 V. After the voltage has been set for the first plate on each power supply, the remaining plates are biased using resistive bridges from the initial voltage within a given range. While voltages are initially calculated using a combination of SIMION, detailed in the next section of this chapter, followed by experimental adjustment, the voltages used in this thesis were taken from prior experiments using this experimental set-up for which they had been optimised.

Table 1 - Voltages for the VMI optics

<i>Plate</i>	<i>1</i>	<i>2</i>	<i>3</i>	<i>4</i>	<i>5</i>	<i>6</i>	<i>7</i>	<i>8</i>	<i>9</i>	<i>10</i>	<i>11</i>	<i>12</i>
Voltage / V	982	945	890	835	741	671	576	483	371	275	129	0

The plates themselves are shown in Figure 6, they are 10.5 cm in diameter and with holes in the centre, beginning with a diameter of 20 mm for the first 3 plates, then increasing to 30 mm from plate 4 onwards. The plates are 1 mm thick and separated by 9.5 mm ceramic spacers and mounted onto ceramic tubing in order to keep the plates insulated from one another. Ceramic tubing is used to prevent the plates from coming into contact with the metal rods which hold up the plates and mount them to a hollow cylinder which itself is mounted onto the chamber. The plates are surrounded by a metal shield to minimise stray fields.

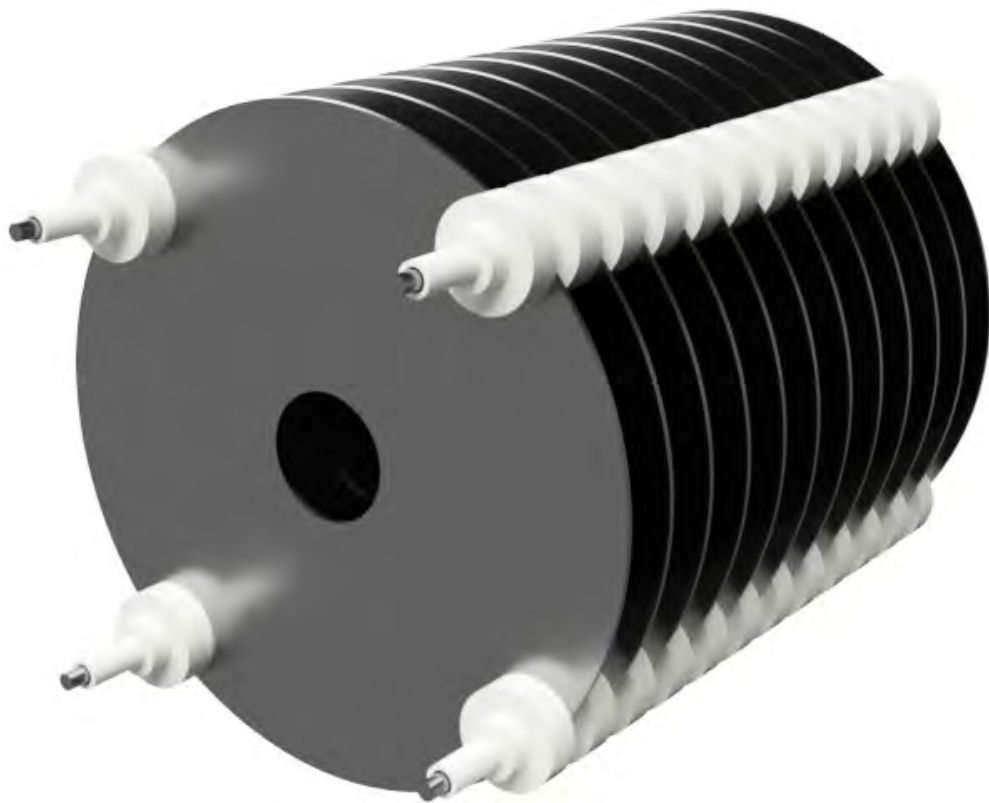


Figure 6 – The VMI plates held on a threaded rod covered by a ceramic shield and separated by ceramic spacers, attached to the chamber via the threaded rod inside the ceramic shield.

2.6. SIMION

An estimate of the voltages on the plates required in the experiment were calculated using the software programme SIMION. A 3D CAD drawing of the plates, detector,

surface, and surface holder were imported into SIMION and each metal part assigned a voltage. User-defined particles, in this case NO, were inserted into the simulation and assigned a representative kinetic energy while flying at 45° increments to cover 180° (the hemisphere above the surface), as demonstrated (though for a separate experimental set-up) in Figure 44. In recreating the chamber, plates and detector in the software and fine tuning the voltages, the path of the ions can be visualised, initially hitting the detector not under true VMI conditions but by tuning the voltages, eventually the ions of a given velocity all arrive at the same point on the detector. The simulations result in a set of voltages that can be taken as a starting point for fine tuning voltages in the physical set up, removing the need for lots of manual trial and error. The software informed not only which voltages yielded VMI conditions but also aided in visualising to what extent the graphene surface holder influences the electric field, as shown by Figure 14 in Chapter 5.3 of this thesis or Figure 1 in the published paper.

2.7. Detector

The detector set-up used in these experiments makes use of a microchannel plate (MCP) detector followed by a phosphor screen where the images are recorded by a triggered camera and connected to a computer via a frame-grabber card.

2.7.1. MCP and Phosphor screen

The MCP used for the experiments is a Photonis 40 mm model which makes use of a dual chevron design containing two plates. Each MCP plate contains an array of pores acting as electron multiplier tubes which have a 10 µm diameter. The MCP is coupled to a P43 phosphor screen which in this case emits a yellow-green light upon being

bombarded with electrons with a decay time of ~ 1 ms, as per the manual. The MCP can be pulsed using a DEI PVX-4140 pulser, where the MCP is kept a lower voltage the majority of the time and is pulsed to a higher voltage when NO particles are expected to hit the detector.

2.7.2. Camera

Perhaps the most notable difference in the detection portion of our experiment compared to previous VMI experiments, including those in our own group, is the use of a camera with a complementary metal oxide semiconductor (CMOS) sensor as opposed to the traditionally used charge-coupled device (CCD) sensor due to changes in the sensor industry.

The fluorescence of the NO ions hitting the phosphor screen were captured using a NET C-IC4133BU-U3V camera that was triggered at the same frequency as the experiment and with the shutter only exposed for up to 500 μ s in order to reduce noise in the images i.e. the camera was only recording while the detector was actively fluorescing.

The resulting image was then transferred to the computer via a USB-3.0 connection to a National Instruments PCIe-8242 frame grabber card, the data from these images this was then manipulated and composited using custom-written LabView software which is described in further detail later.

2.8. Control and Analysis

2.8.1. Timing

In order for the experiments to function correctly, each component in the set-up is required to be activated at the appropriate time in relation to each other, namely, the laser, the molecular beam pulser, the MCP pulser and the camera, all of which are triggered at 10 Hz to match the frequency of the laser. This timing of the equipment is achieved with the use of a Stanford Research Systems DG-645 digital delay generator and custom written software in the LabView software programme.

2.8.2. LabView Programmes

Several LabView scripts (Virtual Instruments/VI's) were utilised for the recording and analysis of the VMI data, several of which were written specifically for these experiments to make use of the regions of interest.

Delay Scan with ROI

The Delay Scan with region of interest (ROI) VI allows for time of flight profiles of several components of NO (or any species of interest) to be recorded simultaneously. Historically, the profile is the sum of all the signal intensity at the detector being fed to an oscilloscope. In using a camera/phosphor screen and regions of interest these profiles can be plotted for different components simultaneously as a function of velocity. This VI first requires the user to have recorded VMI images of the component of interest, such as the downward travelling molecular beam, and note the dimensions of the region around the component in pixels. In the case of this VI, the regions are squares/rectangles and any number of regions of interest can be created. A time of flight scan is then

conducted where the signal at the detector is measured as a function of the delay between the molecular beam opening and the laser firing, thus giving a time of flight profile.

Wavelength Scan with ROI

The Wavelength Scan with ROI VI similarly makes use of the phosphor screen/camera to record rotational spectra of separate components of a species simultaneously, such as that of a molecular beam and direct scatter. The user inputs regions of interest and the signal in those regions is recorded as a function of wavelength providing rotational spectra of components independently.

Imaging Vi with thresholding

The imaging with thresholding VI allows for the VMI images to be extracted from the phosphor screen to be combined to build a composite image as the signal from one image alone is not sufficient to build an entire velocity distribution. The thresholding portion of the VI allows the accumulation of thousands of images without gradual background noise build-up by ignoring any pixels below a certain intensity.

3. Spectroscopy

All the information concerning the internal energy of the products in these experiments was derived using laser spectroscopy and the images recorded on the VMI detector. Indeed, due to the multi photon ionisation schemes of the nitric oxide molecules, spectroscopy was crucial in every experiment, and it is hence essential to include information about the spectroscopy of NO. The information presented in this chapter

was compiled with the help of Atkins and de Paula's *Atkins' Physical Chemistry* and Herzberg's *Molecular Spectra and Molecular Structure - Spectra of Diatomic Molecules*.^{43, 44}

3.1. Electron configuration and Term Symbols

Nitrogen has an electron configuration of $1s^2 2s^2 2p^3$, and for oxygen it is $1s^2 2s^2 2p^4$. The atoms form nitric oxide via the overlap of the 2p orbitals from the nitrogen atom and the 2p orbitals of the oxygen atom resulting in $2s\sigma$, $2s\sigma^*$, $2p\sigma$, $2p\pi$, $2p\pi^*$ and $2p\sigma^*$ molecular orbitals, as shown in Figure 7. In the ground state of NO, the molecular orbitals are filled with the eleven available electrons resulting in the following electron configuration $(\sigma_{2s})^2 (\sigma_{2s}^*)^2 (\sigma_{2p})^2 (\pi_{2p})^4 (\pi_{2p}^*)^1$ with the unpaired electron in the antibonding orbital yielding a bond order of 2.5. When an electron is promoted to the first excited state, this configuration changes to $(\sigma_{2s})^2 (\sigma_{2s}^*)^2 (\sigma_{2p})^2 (\pi_{2p})^3 (\pi_{2p}^*)^2$. In the ground state, the π_{2p}^* orbital contains an unpaired electron yielding a multiplicity of 2 as shown by equation 2 below, where M is the multiplicity and S is the sum of the spins of the unpaired electrons. This unpaired electron residing in the π orbital gives rise to ${}^2\Pi_{1/2}$ and ${}^2\Pi_{3/2}$ states in the electronic ground state.

$$M = 2S + 1 \quad (2)$$

Molecular Orbitals

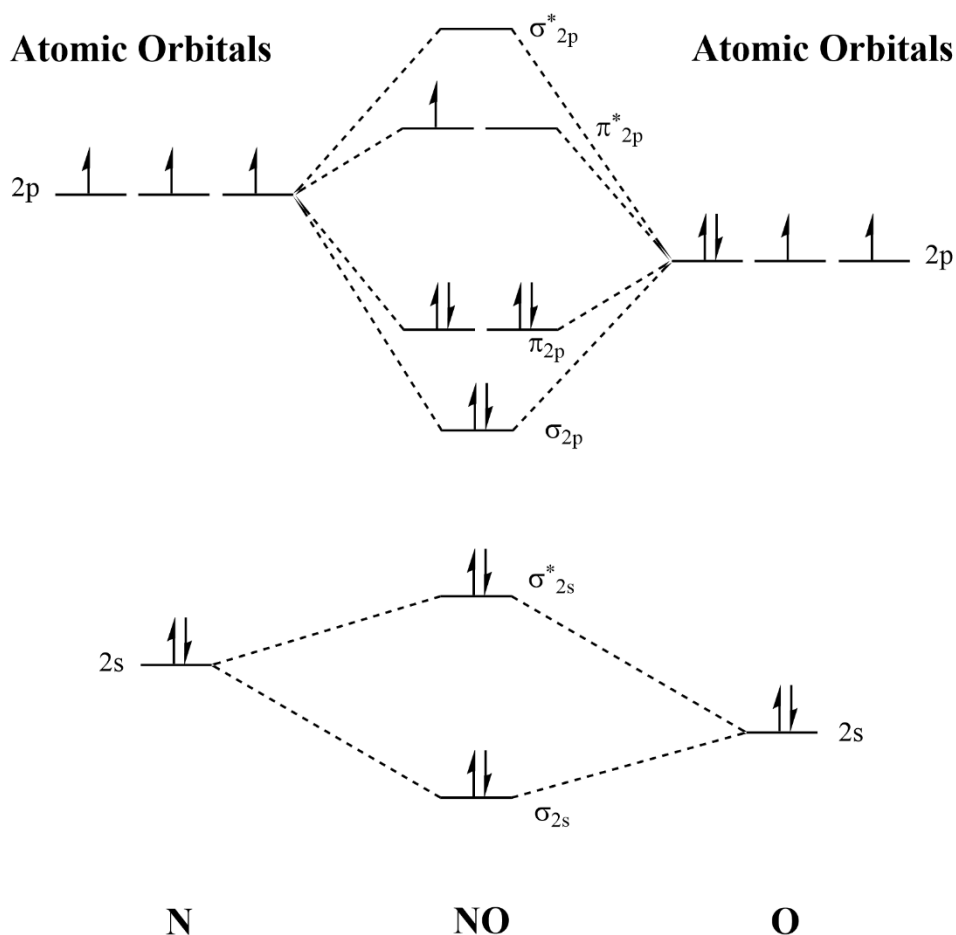


Figure 7 - Molecular orbital diagram of NO demonstrating the overlap of the atomic orbitals of the nitrogen and oxygen atom to form the molecular orbitals; energy levels of the orbitals not drawn to scale.

3.2. Hund's Cases

Nitric Oxide is described by the first and second of the five Hund's cases (a and b), as such, only those are described here.

Hund's case (a) describes a non-rotating molecule or molecules for low levels of J , where the electronic angular momentum, L , is coupled to the internuclear axis. The electronic spin angular momentum, S , is also coupled to the inter-nuclear axis, giving projections about the internuclear axis Λ and Σ , respectively. Λ and Σ couple to form the electronic angular momentum Ω which can take values of $\frac{1}{2}$ and $\frac{3}{2}$. The molecule's rotational

angular momentum R is coupled to Ω such that the total angular momentum J can be described as $J = R + \Omega$.

Hund's case (b) describes a molecule where spin-orbit coupling is weak, this spin-orbit coupling gives rise to the $\pi_{\frac{1}{2}}$ and $\pi_{\frac{3}{2}}$ in the ground state as well as the splitting in the excited state. The electronic orbital angular momentum Λ first couples to R to give N which describes the molecule's total angular momentum with the exception of spin. S then couples to N rather than Λ to give J from the following values

$$J = N + S, N + S - 1, \dots, |N - S|.$$

3.3. Energy Levels

The internal energy of the nitric oxide molecule can be described by combining the energy of the vibrational (ν) and rotational (J) quantum numbers which are shown by equation 3 below, where T_e is the electronic energy, ω_e is the vibrational wavenumber and has associated anharmonicity constants x_e and y_e .

$$E(\nu, J) = T_e + (\nu + \frac{1}{2})\omega_e - (\nu + \frac{1}{2})^2 x_e \omega_e + (\nu + \frac{1}{2})^3 y_e \omega_e + B_\nu J(J + 1) \quad (3)$$

where the value of the rotational constant for a B_ν changes as a function of the vibrational energy level according to equation 4

$$B_\nu = B_e + a_e (\nu + \frac{1}{2}) \quad (4)$$

where the values of the equilibrium rotational constant B_e and the anharmonicity constant a_e may change depending upon on the level of electronic excitation. The values of these variables for NO are given below.

Table 2 - Values of variables used for calculating rotational energy levels for any given vibrational level where all values have units of cm^{-1} .⁴⁴

Variable / State	$X^2\Pi_{1/2}$	$X^2\Pi_{3/2}$	A
T_e / cm^{-1}	0	121.1	43965.7
$\omega_e / \text{cm}^{-1}$	1904.03	1903.68	2371.3
$x_e\omega_e / \text{cm}^{-1}$	13.97	13.97	14.48
$y_e\omega_e / \text{cm}^{-1}$	-0.0012	-0.0012	-0.28
B_e / cm^{-1}	1.7046	1.7046	1.9952
a_e / cm^{-1}	0.0178	0.0178	0.0164

As calculated using the equations above, the rotational energy levels of nitric oxide are shown in Figure 8, though it should be noted the energy gaps between levels are exaggerated for clarity and not to scale.

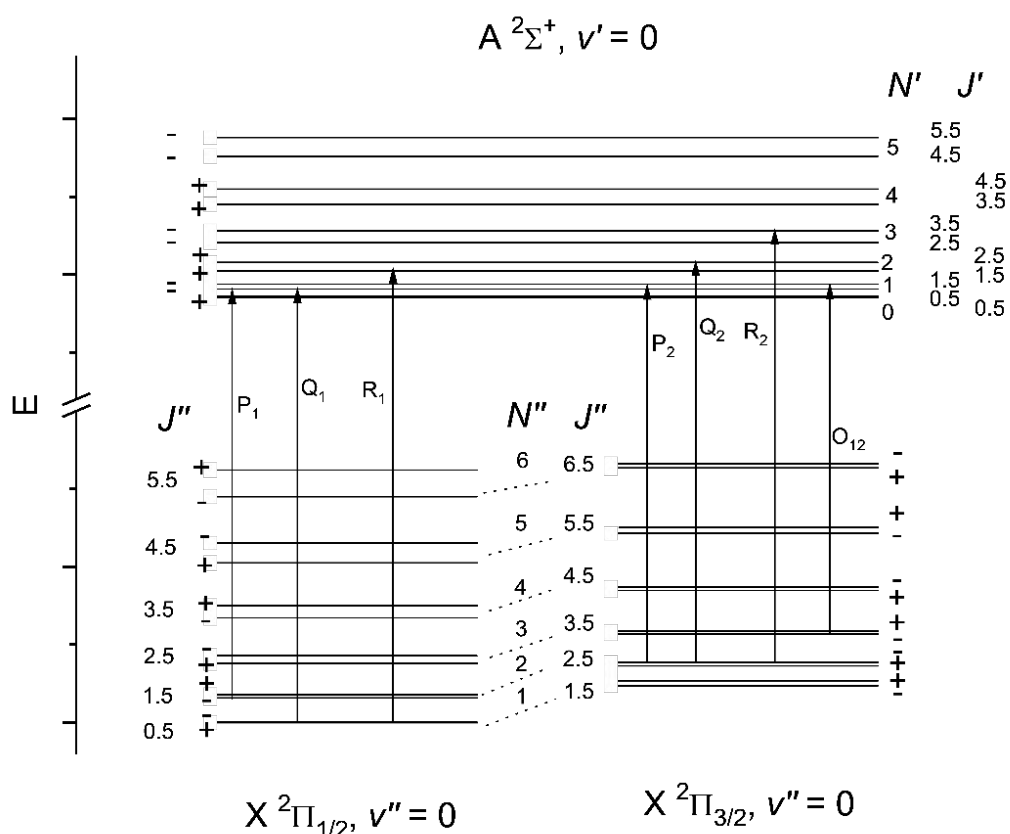


Figure 8 - Energy levels of nitric oxide, where the splitting and relative energies of the levels are not drawn to scale for the sake of clarity, where double prime relates to the ground state and prime to the excited state. The P, Q, and R branches and parity states are defined further in the text.

3.4. Selection Rules and Allowed Transitions

Firstly, only molecules with a permanent dipole produce the transitions being recorded in these experiments, in addition to this, transitions may only take place where

$$\Delta J = 0, \pm 1 \quad (5)$$

with the exception of $J = 0$ in the X state to $J = 0$ in the A state which is forbidden.

This selection rule describes why the P Q and R branches ($\Delta J = -1, 0$ and $+1$ respectively) are significantly stronger than the O and S ($\Delta J = -2$ and $+2$ respectively) branch. It is also the case that

$$\Delta S = 0 \quad (6)$$

$$\Delta \Lambda = 0, \pm 1 \quad (7)$$

$$+ \leftrightarrow -, + \leftrightarrow +, - \leftrightarrow - \quad (8)$$

Equation 6 states that the multiplicity must not change for a given transition. Equation 7 describes how the orbital angular momentum, Λ , can only change by a maximum of ± 1 hence the $A^2\Sigma^+ - X^2\Pi_1$ transitions shown in this thesis are allowed. Equation 8 relates to the parity selection rule where the transitions must occur between states of different parity (symmetry with respect to a centre of inversion).

3.5. Resonance Enhanced Multi-Photon Ionisation

While ionisation of molecules is possible with the use of a single photon, this method of ionisation is prohibitive due to the low wavelength required. While a singular deep UV photon can have sufficient energy to ionise NO, this process would not be selective and other species such as water could be ionised and provide interferences in signal. Therefore, it is necessary to use as selective a process as possible. If the wavelength and density of photons is sufficient, it is possible for two or more photons to interact with the target atom or molecule in a multi-photon process and cause ionisation. In using a

multiphoton process, a tabletop laser can be employed, and multiple photons with a longer wavelength can be used. By using a resonant scheme for ionisation, the selectivity and sensitivity of the ionisation method are greatly improved. Hence, resonance enhanced multiphoton ionisation, REMPI, is frequently employed for reaction dynamics studies.

The REMPI technique makes use of an excited intermediate state which the atom or molecule is first excited to, with the use of one or more photons, followed by another photon which excites the atom or molecule further to above the ionisation limit. Figure 9 shows the different schemes that can be employed for ionisation.

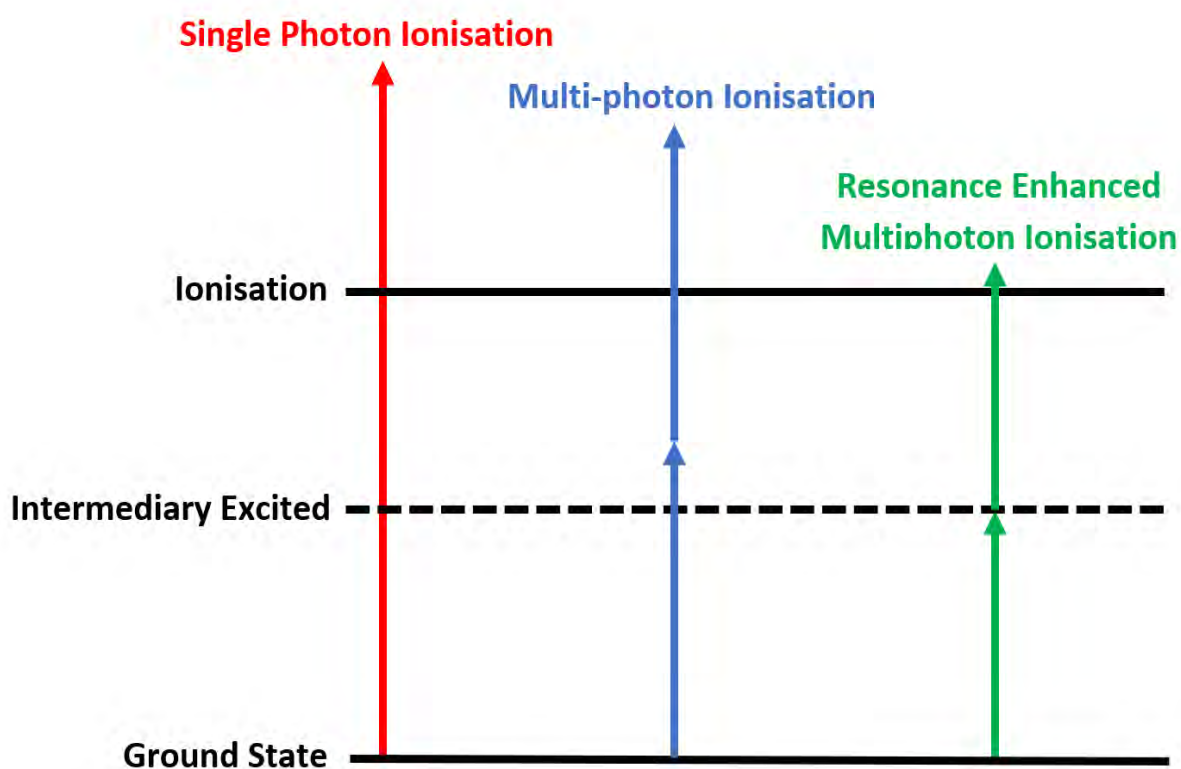


Figure 9 - Various ionisation schemes. In red, Single photon ionisation. In blue, Multi-photon Ionisation via two photons. In green, Resonance Enhanced Multiphoton Ionisation via one colour (1+1) REMPI.

The REMPI technique employed can be described in various ways depending on the wavelength, colloquially described as colour, of the photons and the number of photons employed in each step of the process. For example, one photon to promote the species to the intermediate state and one photon of the same wavelength for ionisation would yield a (1+1) REMPI scheme. If the second photon is of a different wavelength, this would yield a (1+1') REMPI scheme. While many schemes are available and commonly used, such as 2+1, 3+1 etc., the experiments described here make use of a 1+1 REMPI scheme via the $A^2\Sigma^+$ state due to it being a strong transition and the wavelengths required being easily achieved.

The dye laser system employed in these experiments has a resolution high enough ($\sim 0.08 \text{ cm}^{-1}$) such that most rotational lines in a particular branch are easily resolved, as can be shown in Figure 10, which compares a simulated thermal sample of nitric oxide from the LIFBASE software and a rotationally resolved REMPI spectrum of thermal background NO.

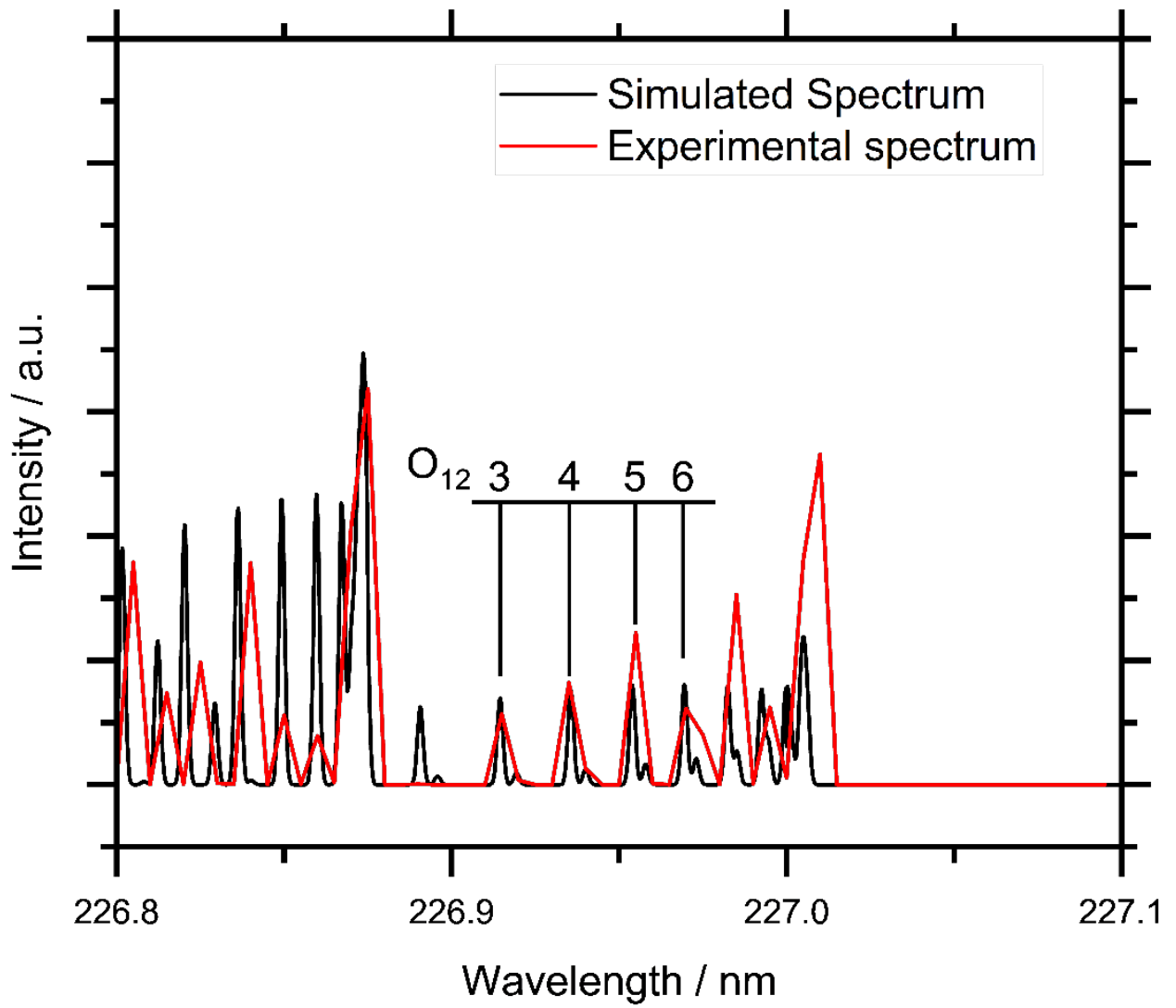


Figure 10 - Comparison of simulated spectrum of NO and an experimental REMPI spectrum of NO

4. Molecular Dynamics Simulations

Molecular dynamics simulations were performed to gain insights into both the experimental results and to investigate the scattering process on the graphene surface on a molecular level.

4.1. General

When undertaking molecular level computer simulations, it is important to consider the level of complexity of the simulations themselves, known as the 'level of theory'. These range from the least computationally demanding studies in molecular dynamics simulations all the way to highly complex *ab initio* calculations. *Ab initio* calculations are a quantum mechanical approach and explicitly consider electrons. Molecular dynamics do not consider electrons and interactions are governed by attractive and repulsive forces such as van der Waals forces. In molecular dynamics, bonds are treated as harmonic potentials and therefore these simulations cannot model reactions as bonds cannot be broken. It is the lack of including the interaction of electrons in the simulations (which is computationally very expensive), however, that make molecular dynamics simulations useful for simulating large chemical systems such as surfaces and scattering of molecules without being prohibitively expensive in terms of computing power. Further details on the basic principles, advantages/disadvantages and foundational work of molecular dynamics simulations are given in Chapter 7.2.

4.2. Set-up of the system

The molecular dynamic simulations were ran using the software package DL_POLY Classic. While there are other DL_POLY packages available, such as DL_POLY 4, the

classic programme is more suitable for lower computer processor counts and systems of less than 30,000 atoms.

The simulations consisted of a graphene surface resting on a gold substrate to simulate the surface in the physical experiments. Nitric oxide was modelled colliding with graphene in 3 different orientations for 2000 runs each; nitrogen facing down, oxygen facing down with no rotational energy assigned to the molecule or with the molecule rotating to simulate the various other orientations of the nitric oxide as it collides with the surface. Each orientation was simulated at 5 different velocities: 600 m s^{-1} , 800 m s^{-1} , 1200 m s^{-1} , 1600 m s^{-1} , 2500 m s^{-1} resulting in 30,000 runs in total.

The set-up of the system is essentially explained by 3 input files, the CONFIG, the CONTROL, and the FIELD file, which are explained in further detail below. These files describe everything from the atoms in the system and their orientations, the forces between these atoms and the boundaries of the system itself, as well as the instructions for the software on how to run the simulations.

4.3. CONFIG FILE

The CONFIG file deals with the layout and the shape of the system, the boundaries, and the atoms themselves. Due to the shape of a gold surface with a staggered formation of the atoms, a parallelogram was used as the geometry for the system. The system itself had dimensions of 17.3 \AA in the x and y planes and 45 \AA in height. As shown in Figure 11.

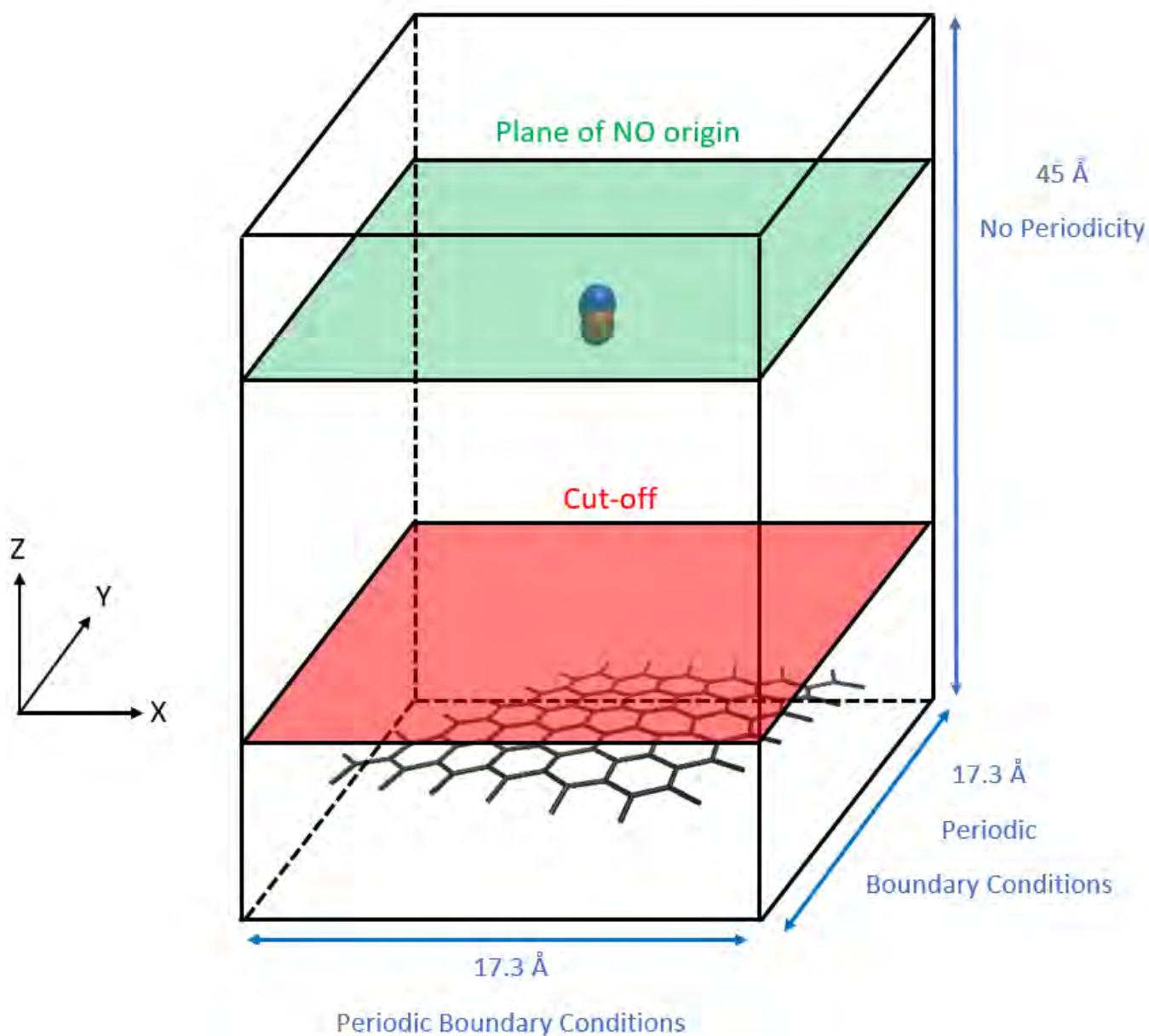


Figure 11 - Diagram of set-up of the simulation cell. Starting plane of the NO molecule in the green xy plane and cut-off point for simulations in the red xy plane.

The graphene surface consisted of a 2D hexagonal lattice of 98 carbon atoms which sat approximately 3 Å above the gold substrate after the equilibration, which itself was composed of a 6x6x6 array of gold atoms. The nitric oxide molecule was held in place approximately 12 Å above the graphene surface in one of the three orientations as described earlier, with the position in the x-y plane varying slightly to ensure the NO molecule was interacting with the graphene sheet across both the atoms themselves and the gaps between the atoms.

Monte-Carlo simulations were used to assign rotational energy to one third of the NO molecules for each velocity. This was done to ensure that some simulations didn't have NO molecules simply facing nitrogen or oxygen down, as well as to investigate the effect of initial rotational energy on scattering dynamics. Across the 2000 runs for each velocity containing the rotating NO molecules, rotational energy was randomly assigned to the molecules, gradually building up a thermal 80 K rotational energy distribution, similar to a molecular beam, this gives a rotational energy distribution similar to that given in the lower part of Figure 5. It should be noted that this rotational energy was given to the molecules in addition to the translational energy already assigned.

To simulate a much larger surface while keeping computational cost at a minimum, 2D periodic boundary conditions were used in the x and y planes, meaning that if an atom were to leave via one of the 4 walls of the system it would enter from the opposite wall. This means that in effect the surface atoms e.g., on the left side of the system are interacting with those on the right of the system and as such the surface is in effect infinitely large, while the cut-off distances for forces is large enough that an atom cannot interact with itself. These conditions and dimensions were chosen in order to accurately model the interactions of the gold and graphene surfaces while limiting computational cost, with considerations such as the plane of NO origin being high enough to avoid interacting with the surface at the point of origin, while being a short enough distance that the simulations did not last too long and increase computational costs.

4.4. FIELD FILE

The FIELD file contains all the information relating to how the atoms described in the CONFIG file interact with each other. This input file also provided the instruction for the bottom row of gold atoms, the row furthest from the graphene surface, to be ‘frozen’ in space. This ‘frozen’ command was to ensure a completely flat gold surface and prevent the gold atoms forming a sphere due to the attractive forces, while also reducing computational cost during the equilibration of the graphene surface and gold substrate.

The interactions of the gold atoms were described by a Gupta potential with parameters shown in Table 3.

Table 3 - Parameters for Gupta potential⁴⁵

λ	μ	$\alpha_{\infty}[eV]$	ζ	n_0	δ	$\beta_{\infty}[eV]$
12.728	3.173	0.1730	6.5149	-1.234	1.593	2.7565
γ	Δ	η	$R_{\infty}[\text{\AA}]$	ρ_0	ν	ξ
0.628	-2.041	1.952	2.927	0.144	6.247	3.330

The bonds between the atoms in the graphene sheet were treated with a Morse potential given in the equation below, which is more realistic to a fixed bond length as it reconstructs the compressions and stretches between atoms. The parameters used were proposed by Kalosakas and co-workers where the carbon-carbon internuclear distance in a sheet of graphene is 1.42 Å and where the well depth $D = 5.7$ eV and $\alpha = 1.96 \text{ \AA}^{-1}$, where α is a constant related to the force constant.⁴⁶ The nitric oxide bond

was also described by a Morse potential with parameters $D_e = 6.61736$ eV, $\alpha = 2.636 \text{ \AA}^{-1}$ and $r_e = 1.151 \text{ \AA}$.⁴⁷

$$V_s(r) = D[e^{-\alpha(r-r_0)} - 1]^2 \quad (9)$$

The angles θ , and dihedrals ω , of the graphene sheet were described by quartic and cosine functions, respectively, and are described by equations 10 and 11.

$$V_b(\theta) = \frac{k}{2} \left(\theta - \frac{2\pi}{3} \right)^2 - \frac{k'}{3} \left(\theta - \frac{2\pi}{3} \right)^3 \quad (10)$$

$$V_t(\omega) = \frac{1}{2} V_2 [1 - \cos(2\omega)] \quad (11)$$

where $k = 7.0$ eV rad⁻² and $k' = 4.0$ eV rad⁻³, and $V_2 = 0.23$ eV.⁴⁸

Non-bonding interactions between the atoms were described by Lennard-Jones 12-6 potentials of the form

$$U(r) = 4\varepsilon \left[\left(\frac{\sigma}{r} \right)^{12} - \left(\frac{\sigma}{r} \right)^6 \right] \quad (12)$$

where ε is the depth of the potential well, r is the internuclear distance and σ is the distance at which the particle-particle potential energy is zero.

The Lennard-Jones 12-6 potential was only applied to C-C interactions of carbon atoms at least four C-C bonds apart, i.e. not yet described by Morse bond potentials or angular or dihedral potentials.

The parameters set out by Helgee and Isacson were used for the gold and graphene interactions, as shown in Figure 12 and the remaining parameters, described by the universal force field developed by Skiff and co-workers, shown in Table 4.^{49, 50}

As well as describing the interactions between gold and graphene, the Lennard-Jones potential also described the interactions between the NO and the graphene surface and gold substrate, as when the NO is interacting with the graphene it is also likely to be interacting with the gold substrate. The parameters for NO are also given in Table 4, where the values are given for both the nitrogen and the oxygen atom of the molecule interacting with carbon or gold, in order to account for the molecule interacting with the surface in a number of orientations, such as the nitrogen atom approaching the surface first. The values in Table 4 were calculated using the values for individual atoms and the relevant equations presented with the forcefield developed by Skiff and co-workers, where the formulas and further details can be found in the relevant publication.⁵⁰

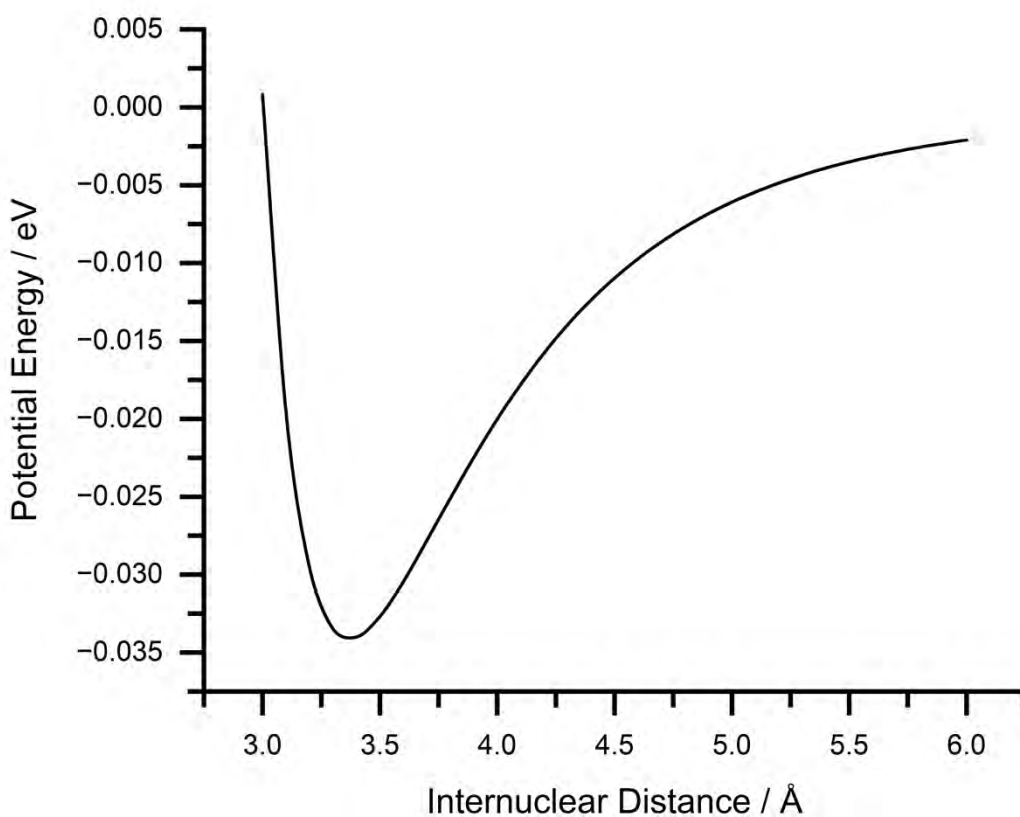


Figure 12 - Lennard-Jones potential between a gold and carbon atom.

Respective values are provided in Table 4.

Table 4 – Lennard-Jones Parameters ^{49, 50}

<i>Interaction</i>	<i>ϵ [eV]</i>	<i>σ [Å]</i>
C-C	0.004553	3.431
C-O	0.003442	3.2745
C-N	0.003691	3.346
N-Au	0.00225	3.0972
C-Au	0.0341	3.003
O-Au	0.002098	3.0259

As the forces cut-off point is at 7 Å, the nitric oxide molecules were registered once they crossed a plane 8 Å above the graphene as there will no longer be any interactions between the NO molecule and the surface. Properties such as the positions and velocity components of both the N and O atoms in all three dimensions separately were recorded. Molecular speeds were extracted from centre-of-mass shifts per unit time and binned in 20 m s⁻¹ wide intervals.

4.5. CONTROL FILE

The CONTROL file contains most of the information for how the software handles running the simulations. It describes the thermostat for the simulations, temperature of the simulations, in this case 300 K, as well as the cut off point for interactions between atoms which in the simulations was set to 7 Å as after this point the interactions are minimal. The CONTROL file also determines the length of the simulations, which are ran in steps, where each step is one picosecond. The simulations ran for 4000 steps equating

to 4 ps each, except for the 600 m s⁻¹ molecules which were ran for 8 ps. The lengths of simulations are a trade-off between computational time and allowing enough time for the NO to interact with the surface either by trapping or scattering. The slower molecules at 600 m s⁻¹ required a longer simulation time due to the slower incoming velocity as well as the increased likelihood of trapping. This is also the file which dictates how often the system prints the results, these are especially useful to monitor where simulations may break down or to view the results in software such as Visual Molecular Dynamics (VMD).⁵¹

The gold and graphene had equilibrated in an NVT ensemble at 300 K by a Nosé-Hoover thermostat and the energy of the system had reached a stable minimum as shown in Figure 13 after ~3 ns. The 'NVT' refers to parameters, where number of particles (N), volume (V) and temperature (T) are all kept constant during the simulation. The simulations were all ran after this equilibration which had the benefit of reducing the

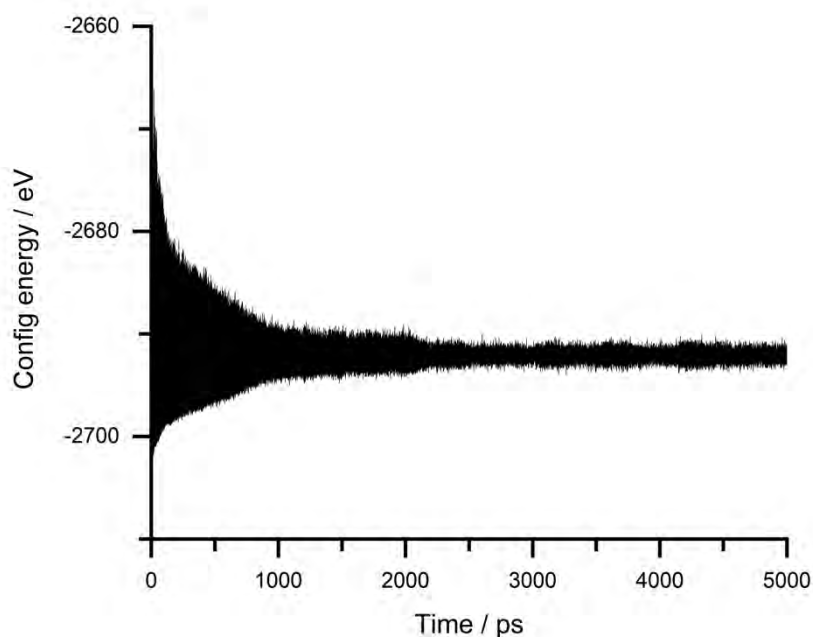


Figure 13 - Configuration energy of the gold slab and the graphene sheet, where a minimum energy is reached after ~3 ns. The Config energy relates to the sum of all the intra and inter molecular forces as well as any many-body interactions such as metallic forces.

overall job time as it ensured an equilibrated surface as well as the atoms having exactly the same positions prior to each run.

While further discussions are provided in later chapters, in summary, molecular dynamics simulations are ideal for simulating large systems, such as surfaces, and can be used to create molecular movies over large timescales (on the order of nanoseconds) to visualise the interactions between molecules. The simulations outlined here aided discussions around experimental velocity distributions in Chapter 5. The simulations also provided deep insights in Chapter 7, into the effect of incoming velocity on the amount of energy lost to the surface, as well as the presence of a trapping desorption component, which was then discussed experimentally in Chapters 9 and 11.

5. Nitric Oxide Scattering off Graphene using Surface-Velocity Map Imaging

Thomas Greenwood, Sven P. K. Koehler*

Department of Natural Sciences, Manchester Metropolitan University, M1 5GD, UK

*Corresponding author.

Email: s.koehler@mmu.ac.uk

Manchester Metropolitan University

Department of Natural Sciences

Manchester

M1 5GD

United Kingdom

T. Greenwood, S. P. K. Koehler, *J. Phys. Chem. C*, 2021, **125**, 17853

5.1. Abstract

We investigated the scattering of nitric oxide, NO, off graphene supported on gold. This is of fundamental importance to chemistry as collisions are the necessary first step to chemical reactions on graphene, and nitric oxide molecules are inherently radicals, with the potential to bond to graphene. We directed a molecular beam of NO in helium onto graphene and detected the directly scattered molecules using surface-velocity map imaging. In contrast to previous scattering studies off graphite which detected only a modest reduction of the translational energy of the NO, we observe a loss of ~80% of the molecules' kinetic energy. Our classical molecular dynamics simulations still predict a loss of ~60% of the translational energy in the scattering process. This energy appears to partly go into the NO rotations, but mostly into collective motion of the carbon atoms in the graphene sheet. At 0° incidence angle, we also observe a very narrow angular scattering distribution. Both findings may be unique to pristine graphene on gold as 1) the two-dimensional (2D) honeycomb structure is perfectly flat, and 2) the graphene is only loosely held to the gold at a distance of 3.4 Å, thus it can absorb much of the projectiles' kinetic energy.

Keywords: graphene, scattering, velocity map imaging, surface scattering, REMPI, nitric oxide

5.2. Introduction

Chemical reactions are at the very heart of chemistry,⁵² and collisions between reactants are a necessary first steps towards any chemical reaction.⁵³ Collisions between gas-phase species, both nonreactive and reactive processes, have hence long been studied in the field of reaction dynamics in order to understand the re-distribution of energy.⁵⁴ Equally, the investigation of the detailed scattering dynamics of gas-phase species off surfaces has a long tradition,⁵⁵ not least because of its enormous importance for heterogeneous catalysis.²⁵ Reactive and nonreactive scattering,^{56,57} adsorption and (photo-)desorption⁵⁸ studies have all been performed on various types of solid surfaces incl. metal single crystals, metal oxides, and stepped and corrugated surfaces, to name a few. Graphite surfaces have also heavily featured in surface scattering experiments,⁵⁹ and more recently graphene, a 2-dimensional (2D) hexagonal arrangement of sp²-hybridized C-atoms.⁶⁰

Graphene research has increased exponentially since the discovery of its remarkable electronic, physical, and chemical properties almost 20 years ago.³⁵ Some of these properties such as the band gap (pristine graphene is a zero band gap material) can be tuned by functionalization through chemical reactions on graphene, and we have in our group modified chemical vapour deposition (CVD) graphene with functional groups such a phenyl groups or hydrogen atoms, and investigated these graphene derivatives using sum-frequency generation spectroscopy.^{36, 37}

Studies of the detailed scattering dynamics of actual collisions on graphene that potentially lead to the formation of such functionalised graphene derivatives have recently emerged. It is important in this context to remember that graphene is a surface

held together by a two-dimensional (2D) network of covalent bonds, and collisions between (reactive) species and graphene could potentially lead to truly covalent bond formation.

Minton and co-workers measured the kinetic energy and angular distribution of N₂ scattered off highly oriented pyrolytic graphite (HOPG) in sophisticated molecular beam experiments coupled with classical molecular dynamics (MD) simulations. They found that the N₂ 1) scatters off after a single collision, or is 2) temporarily or 3) permanently trapped at the surface.³⁹ Hase and co-workers modelled the collisional dynamics of N₂ with graphite at collision energies of 26 kJ mol⁻¹ and 60 kJ mol⁻¹ and found that for all incidence angles, single collision scattering is the dominant process; at the lower collision energy (similar to what is used in our work here) close to normal incidence angles, roughly 50% of the initial translational energy is channelled away, primarily to the graphene surface vibrational modes.⁶¹ This was taken one step further by Nieman *et al.* and Jaye *et al.* in their primarily modelling studies of the reaction of N(⁴S) and O(³P) atoms with graphene, though at vastly higher collision energies relevant to the re-entry of spacecrafts into Earth's atmosphere.^{42, 41} Both the high collision energy as well as the fact that a reactive atomic species is scattered off graphene cause not only non-reactive scattering to be observed, but also reactions with the graphene itself (functionalization), and the formation of ablation products such as CN radicals in the gas-phase. Juaristi and co-workers modelled the scattering of O₂ off HPOG by *ab initio* molecular dynamics at lower collision energies of ~20 kJ mol⁻¹, focusing on the effects of the initial alignment of the impinging O₂ molecule.⁶²

Many early state-resolved studies were concerned with the collision dynamics of NO with graphite.⁶³ Specular scattering occurs when the molecules scatter back with the

same angle as the incidence angle, though in the opposite direction, it was noted that specular scattering dominates at higher temperatures. Whereas isotropic scattering, where the diffusely scattered molecules are not scattered along the specular angle but distributed around the surface normal, due to trapping desorption, is dominant at lower temperatures.²¹ However, later studies by Walther and co-workers found no diffusely scattered molecules at surface temperatures below 70 K, with only the inelastic scattering channel remaining.⁶⁴ When angular distributions were investigated – typically at incidence angles varying from 45° to 60° – the direct channel displayed a narrow distribution but still with a width of 10° or more.⁶⁵ Even at fairly steep incidence angles of 30°, Frenkel *et al.* still observed a diffuse isotropic trapping component, and a width of the angular distribution of the specular component of ~20°.⁶⁶

As far as reactions on graphene go, hydrogenation is probably the simplest modification to graphene,^{37,67} and the reactivity has been modelled by Lischka and co-workers,⁶⁸ and also investigated both in rather elegant dynamics experiments as well as modelled by Wodtke and co-workers.^{38,69} A short pulse of H atoms was scattered off graphene under UHV conditions, and the angular and kinetic energy distribution extracted by detecting the hydrogen using an H-atom Rydberg tagging scheme. Most strikingly, evidence for temporary bond formation between the H atoms and graphene was found.

Velocity Map Imaging (VMI) is one of the most successful recent techniques to probe reaction dynamics;^{13, 14} VMI is typically applied to gas-phase dynamics, but more recently expanded to surface processes,^{29, 27, 70, 31} and we have ourselves applied it to the laser-desorption of NO from gold single crystals.^{32, 33} Surface-VMI not only delivers the velocity (i.e. speed and angular) distribution of scattering products after surface collision, but due to the resonance enhanced multiphoton ionization (REMPI) scheme

frequently employed, can also establish the vibrational and rotational state distribution of the scattered products. We hence chose to perform surface-VMI collision experiments by scattering nitric oxide off graphene, because 1) NO is intrinsically a radical and can hence potentially react with the graphene substrate, and 2) because NO as a diatomic molecule allows us to also investigate the internal energy distribution after scattering off graphene.

5.3. Experimental Methods

Our surface-VMI apparatus has been described previously,^{15, 34} but a number of key features and changes warrant a more detailed description. The spectrometer consists of two vacuum chambers, the first housing the molecular beam (firing vertically downwards in the lab frame), and the second chamber houses the graphene surface on a gold substrate, together with the 12 VMI optics plates and the multi-channel plate detector/phosphor screen assembly. The chambers are each evacuated using 1000 L s^{-1} turbomolecular pumps which in turn are backed by their own rotary pumps to achieve a base pressure in the main chamber below 5×10^{-9} Torr. The molecular beam consists of a 2-4% NO mixture seeded in He which is supersonically expanded through a pulsed valve (500 mm diameter orifice, 300 μs opening time) to a velocity of $\sim 1500 \text{ m s}^{-1}$. The NO molecules travel ~ 27 cm downwards into the space between the first two VMI plates where they are intersected by the laser beam, crossing horizontally through the center of the chamber between those first two plates. The NO molecules travel a further ~ 5 cm and scatter off the graphene surface, recoiling to cross the laser beam a second time in the center of the VMI optics. The three axes of 1) probe laser along x , 2) counter-propagating molecular beam (from top)/surface normal (with the surface near the bottom of the VMI optics in the lab frame), y , and 3) the time-of-flight (TOF) axis of the

VMI apparatus, z , are mutually perpendicular as shown in Figure 14 a). We have chosen this xyz axes labelling as the x and y axis in the lab frame are now the same as the x and y dimension of the resulting 2D VM images. We highlight that this positioning of the surface within the VMI optics is a departure from our previous work in which the surface normal was aligned along the main axis of the TOF spectrometer, and which delivered velocity distribution in all three dimensions in space independently. However, due to the much longer timescales of a molecular beam pulse compared to a laser pulse, we are losing this timing option in the current scattering experiments, and hence have to extract the speed along the surface normal from the y coordinate of the VM images instead. The remaining x dimension of the images delivers – after appropriate transformation – the polar angle distribution. For scattering experiments from a flat surface as described here, it is reasonable to assume a homogeneous azimuthal distribution around the surface normal, and hence only the velocity component along the surface normal and one velocity component parallel to the surface need to be measured. The grounded surface is positioned ~ 5 cm below the laser beam axis close to a grounded shield surrounding the ion optics, and as such, does not disturb the VMI field in the ionization region noticeably, see Figure 14 b). Previous research on the scattering off liquid surfaces by Greaves and co-workers employing a similar geometry to image the scattering plane used an elegant arrangement involving charged razor blades in order to ensure that the field lines between the ion plates are not distorted.³¹ We note, however, that the distance between the ionization region and the surface in those experiments is much shorter (i.e. the surface is placed in-between the first two ion plates), but thanks to the ease with which NO can be laser-ionized here, we can afford to locate the surface much further away from the laser beam and in fact close to the ground shield surrounding the ion optics, such that the field lines in the central region

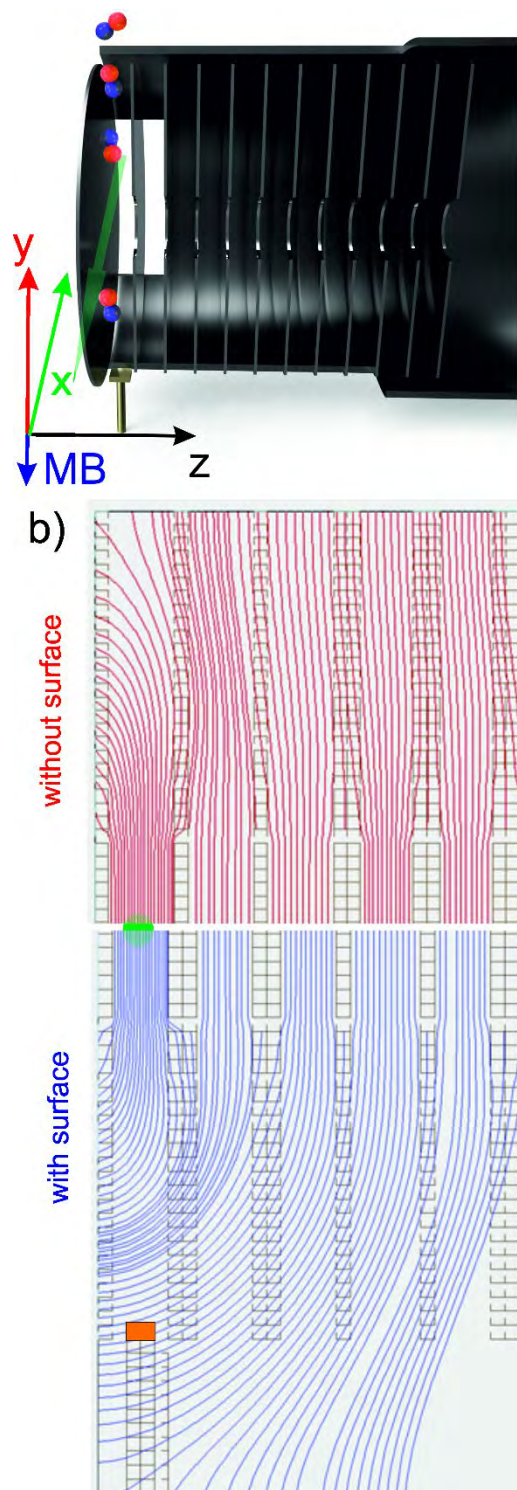


Figure 14 - a) Cutaway CAD drawing of our 12-plate ion optics with the molecular beam indicated; faint green arrow is the REMPI laser beam between the two plates furthest left; x- (along laser beam) and y-dimension (parallel to the molecular beam and surface normal; surface shown in gold near the bottom) chosen, as these are the dimensions which yield the velocity maps' x-y coordinates; z is along the time-of-flight direction. b) SIMION simulations of the electric fields without (red) and with (blue) the surface in place. Grounding shield omitted for clarity.

of the VMI spectrometer are not distorted. Wodtke and co-workers use a shorter flight distance in a similar setup and crucially a fs laser to nonresonantly ionize desorbed molecules, and can conveniently switch between spatial and velocity map imaging,³⁰

while on the other hand, the ease of (1 + 1) REMPI detection in our setup negates the need for a focusing lens, and we do not need to scan the probe laser across the ionization region. The longer flight path from the surface to the ionization laser potentially limits the width of the angular distribution that can be recorded, but since the detection laser is not focused (and hence all ionized NO molecules with a clear trajectory to the detector are recorded, up to 12.5 mm either side of the center of the VMI optics), we appear to record a much narrower polar angle distribution of the scattered NO molecules than theoretically possible, i.e. we are not biasing against NO molecules at larger polar angles. We note that the exact distance between the surface and the laser is not required as we extract the velocity from the VM images, and not from time-of-flight times to the laser.

The surface is resting (i.e. no spring clips used that would cover part of the surface) on a surface holder mounted on a manipulator, and the sample itself consists of a silicon wafer onto which a thin layer of chromium and then gold has been evaporated, covering the whole wafer, before graphene – CVD-grown on copper – was transferred onto the gold. The correct vertical alignment of the surface normal was checked by shining a He/Ne laser pointer along the central y axis of the chamber (in-line with the molecular beam) and ensuring that the back-reflection from the wafer travels along the same path as the incoming beam, guaranteeing that the surface normal is aligned with the molecular beam.

Nitric oxide molecules are ionized ~ 5 cm above the surface using a (1+1) REMPI scheme via the $A \leftarrow X$ transition. The third harmonic of a Continuum Surelite II-10 Nd:YAG laser was used to pump a Radiant Dyes NarrowScan laser using Coumarin 450 dye, and the

dye laser output was then frequency-doubled using a BBO crystal to achieve ~ 226 nm laser pulses at 10 Hz with a pulse energy of ~ 0.8 mJ.

The ionized NO particles are then accelerated over a potential difference of 1000 V towards a multi-channel plate (MCP) detector coupled to a phosphor screen. The MCP is pulsed at 10 Hz to reduce background noise caused by ions other than NO^+ . We do not 'DC-slice' the ion cloud by pulsing the MCP to only capture a very narrow time window of our scattered NO molecules, as can often be the case in VMI studies containing an ion cloud, where one wishes to obtain the centre portion of the cloud. This is due to the fact that the long flight path from the scattering region to the ionization region causes our images to be optically sliced, any NO molecules travelling forward or backward (along the z axis) fly out of the path of the laser and are therefore not detected, essentially imaging one scattering plane (the x-y plane). The phosphor screen captures the ions' positions and image acquisition is performed by a 10 Hz synchronized camera (NET C-IC4133BU-U3V) connected to a personal computer via a National Instruments PCIe-8242 frame grabber.

Since we are not operating a molecular beam directed along the spectrometer's time-of-flight axis, we have to establish the central spot (equating to zero velocity along the x and y dimension and hence essential for image analysis) on the detector by different means: instead we back-fill the chamber with pure nitric oxide at a background pressure of 2×10^{-7} Torr;⁷¹ ionizing this thermal gas ensemble yields a 2-dimensional Maxwell-Boltzmann distribution on the detector with a peak along x and y at 0 m s^{-1} each, thus establishing the center of our images. Calibration of the VMI setup was performed by NO_2 dissociation at ~ 226 nm as previously described.^{34, 72}

5.4. Computational Methods

All molecular dynamics simulations here were performed within the DL_POLY Classic suite using a combination of force fields.⁷³ A simulation box was selected with a parallelogram as a base (in the x - y plane) and periodic boundary conditions along the two dimensions of that base (parallel to the interfaces present here), but with no periodicity in the z direction which is along the surface normal. The substrate was formed of a $6 \times 6 \times 6$ array of gold atoms whose interactions were described by a Gupta potential.⁴⁵ Ninety-eight carbon atoms were positioned in a hexagonal 2D network in the x - y plane on top of the gold substrate. The bonds in the graphene sheet were described by a harmonic potential (rather than fixed bond lengths) to accurately reflect any compressions and stretches in the bonds as the NO collides with the graphene surface. A Morse bond potential described the C-C bonds with parameters proposed by Kalosakas *et al.*,⁴⁶ using the accepted carbon-carbon internuclear distance in graphene of 1.42 \AA , with $D = 5.7 \text{ eV}$ and $\alpha = 1.96 \text{ \AA}^{-1}$. Angles and dihedrals were described by quartic and cosine functions, respectively.⁴⁶ This system was relaxed by running simulations in an NVT ensemble regulated to 300 K by a Nosé-Hoover thermostat for 4 ns with a relaxation constant of 1 ps . A single nitric oxide molecule was then placed in a randomly selected position in the x - y plane, but $\sim 18 \text{ \AA}$ above the graphene surface. The nitric oxide bond was described by a Morse potential with parameters $D_e = 6.61736 \text{ eV}$, $\alpha = 2.636 \text{ \AA}^{-1}$ and $r_e = 1.151 \text{ \AA}$.⁴⁷ To complete the force field, non-bonding interactions were described by Lennard-Jones 12-6 potentials, with parameters either provided by the force fields above, or taken from the universal force field set out by Skiff and co-workers,⁵⁰ with the exception of the gold and graphene interaction being developed by Helgee and Isacson.⁴⁹ Lorentz-Berthelot combining rules were applied for

interactions between unlike atoms. Interatomic forces were truncated after 7 Å. It should be noted that more sophisticated neural network potential energy surfaces have recently been calculated even for surface scattering processes related to the one presented here;^{74, 75, 76} however, not all of these studies take the metal substrate into account, and the literature force fields mentioned above while not verified for the NO-graphene interaction are likely to be sufficient to at least qualitatively reproduce the trends observed experimentally.

The NO was directed at the graphene either N- or O-head first with 1600 m s⁻¹ along the surface normal, and 2000 trajectories were run and analyzed for each orientation. After collision with the graphene, the NO was detected once traversing a virtual plane 8 Å above the graphene, where there is no longer any interaction between the graphene and the NO. Properties such as the velocity components of both the N and O atoms in all three dimensions were recorded separately. Molecular speeds and polar angles were calculated from center-of-mass shifts and binned in 20 m s⁻¹ and 5° wide intervals, respectively.

5.5. Results and Discussion

Figure 15 a) shows an overlay of three ion images all of which were recorded on the Q₁(0) line of the A ← X transition of NO as per Figure 15 b), but control experiments on the R₁(0) line yield the same results. The signal due to the molecular beam travelling towards the surface is shown in blue, while the scattered signal is shown in red. The scattered signal was recorded at a time delay (between the molecular beam and the probe laser) which was increased by 100 μs compared to the molecular beam images; this is to account for the round-trip time from the laser to the surface and back (~10 cm),

such that we probe 'the same' directly scattered NO molecules whose velocity distribution in the molecular beam we established before collision with the graphene. This is to say that the same portion of the distribution of the beam was probed in the scatter, the molecules that are ionised in the beam are guided towards the detector and do not reach the surface.

Finally, the more diffuse spot in the middle in green is from the ionization of thermal background NO ($p_{bg} = 5 \times 10^{-7}$ Torr), and this image is fitted to a two-dimensional

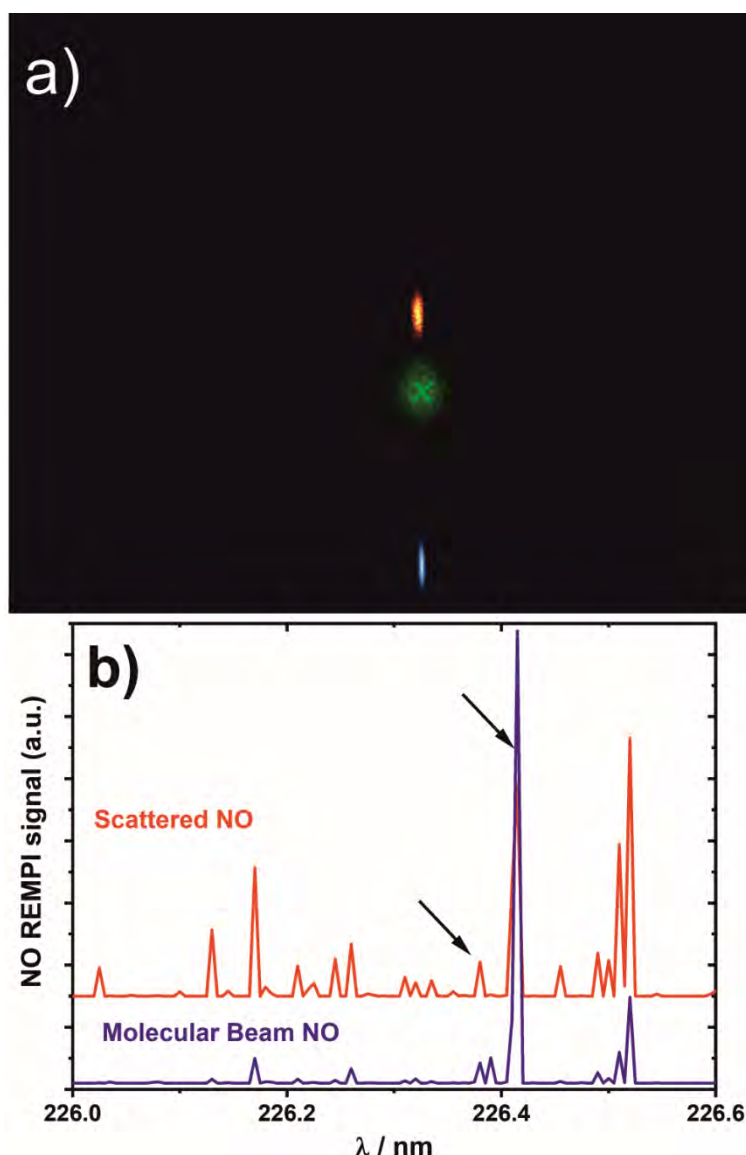


Figure 15 - a) Overlay of three velocity map images of nitric oxide, NO. The downward facing molecular beam is in blue, the scattered NO in red, and the diffuse green spot in the center is thermal background NO gas, imaged to define the zero velocity coordinate (illustrated by the green cross). b) Rotationally-resolved REMPI spectra of NO in the molecular beam (blue), and scattered off graphene (red). Black arrows point to the $Q_1(0)$ and $R_1(0)$ lines on which most images were recorded.

Maxwell-Boltzmann velocity distribution. In absence of a molecular beam aligned along the main VMI axis, the center spot of this distribution, highlighted in the image as a green cross, corresponds to our zero velocity coordinate.

The speed distributions shown in Figure 16 a) are established relative to this zero velocity coordinate (which does not vary by more than one pixel or 5.1 m s^{-1} from day to day) and after application of the appropriate density-to-flux conversion by multiplication with speed.²² The initial molecular beam (blue) and the scattered molecules (red) are naturally in opposite directions. All distributions are fitted to equation 13 as we are measuring a 2D distribution

$$F(c)dc = A c^2 \exp \frac{-(c - c_0)^2}{\alpha^2} dc \quad (13)$$

where A is a scaling factor, α is related to the width of the distribution, c_0 is the stream velocity and c is the incident velocity.⁷⁷ While the NO in the molecular beam has an average kinetic energy $\langle E_{\text{kin}} \rangle$ of 0.31 eV (30 kJ mol^{-1}), the scattered NO has lost around 80% of its kinetic energy, as determined by full width at half maximum, down to 0.06 eV; this is a much greater loss of kinetic energy than observed in the direct channel of the NO scattering off graphite.⁶⁶ In the simplest form of the Baule model and assuming collision with one surface C atom only, the NO would not scatter off the surface at all due to the much larger mass of NO compared to a single C atom in graphene.^{78, 79} Instead, the Baule model predicts that the mass equivalent of just over six C atoms together would account for the observed energy loss of the projectile, which is not unrealistic, given the tight covalent network of the 2D lattice, though the fact that the number of C atoms is close to one hexagon in graphene is likely coincidental. The translational energy distribution is – as expected – also broader than the initial molecular beam. Despite this dramatic energy loss, the scattered NO cannot be

described as thermal. We have attempted to fit the scattered data to the equation describing a Maxwell-Boltzmann distribution for desorption from a surface,⁸⁰ but obtained a worse fit which did not reproduce the experimental data as well. This indicates that the dominant scattering channel in our case of 0° incidence angle is a direct scattering mechanism, but associated with a significant loss of energy which most likely goes into the collective motion of the carbon atoms in graphene. Efficient transfer of energy to the substrate's phonon modes has also been observed, e.g., for NO scattering of Ag(111).⁸¹ We observe a diffuse and very weak spot at slower NO velocities that could be due to a trapping-desorption mechanism, but this channel is far less pronounced compared to the directly scattered NO. While the spectra shown in Figure 15 b) demonstrate that some energy is channelled into rotational degrees of freedom, this only accounts for a small fraction of the lost energy. Much of the earlier work on collisions of NO with graphite had focused on the rotational distribution of the inelastically scattered NO, and found evidence for rotational cooling.^{82, 83} For the vibrationally elastic scattering of NO($v = 3$) off Au(111), NO loses around half its initial kinetic energy for incidence energies close to those employed here; interestingly, the final kinetic energy of the NO decreases with increasing rotational state, an effect we have not been able to probe yet.⁸⁴ While a complete analysis of the rotational state population is reserved for a later publication, with the focus here on the velocity distributions, we have not been successful in detecting NO($v = 1$) in the scattered beam; this is in contrast to, e.g., nitric oxide scattering off metal single crystal surfaces such as Au(111) at similar incidence energies, during which fractions of a percent of NO($v = 1$) were detected at surface temperatures close to the room temperature graphene employed here.⁸⁵

The results of our classical molecular dynamics simulations in which NO molecules were approaching the graphene surface with a velocity of 1600 m s^{-1} along the surface normal (black vertical arrow in Figure 16 a) and collided with the graphene in a random position were fitted to the 3D variant of equation 13 (replacing the c^2 with a c^3), see black data in Figure 16 a).

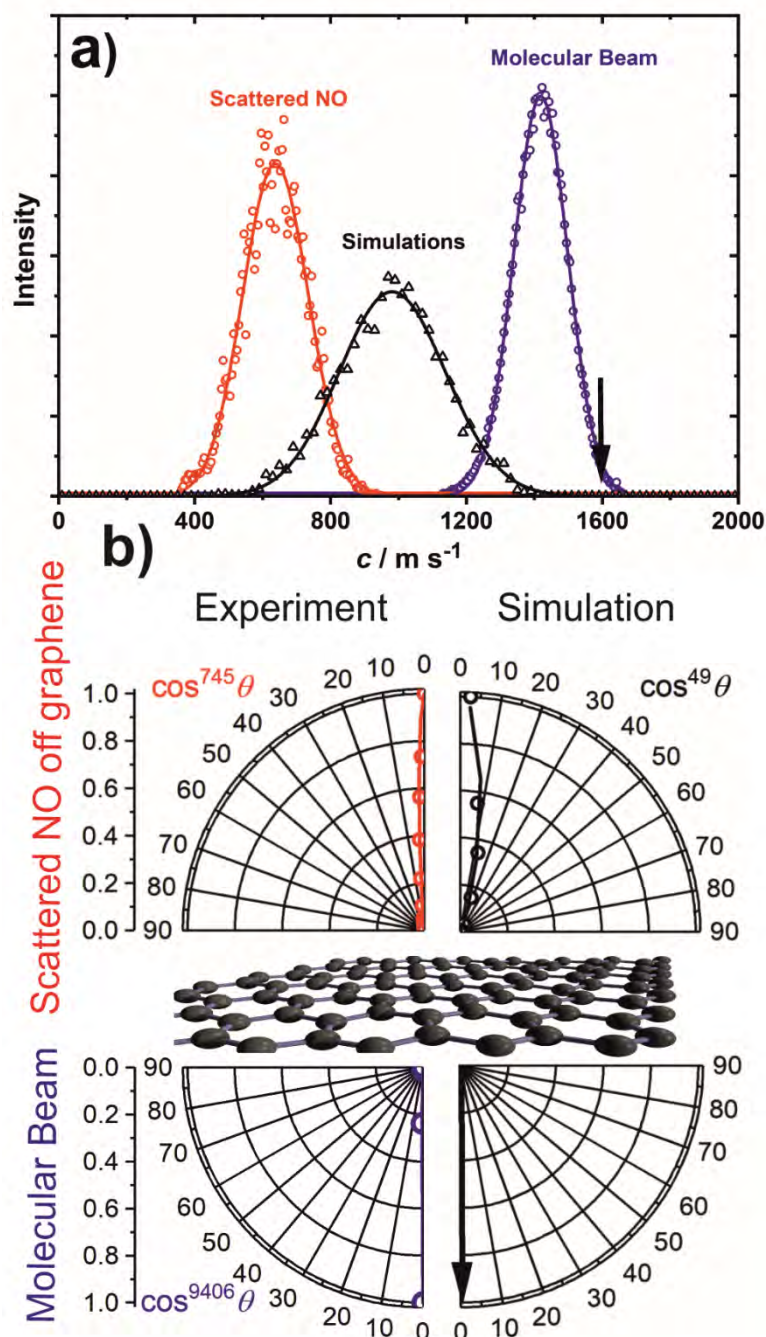


Figure 16 - a) Speed distributions extracted from the VM images in Figure 17 for the molecular beam in blue, and the scattered NO in red; the black data are results of molecular dynamics simulations commencing with monoenergetic NO molecules at 1600 m s^{-1} , indicated by the black arrow; all data (open symbols) fitted to equation 13 (lines). b) Polar angle distribution of bottom panels for the molecular beam and top panels for the scattered NO; left panels are experimental data, right panels, molecular dynamics simulations. Open circles are data points; lines are fits to a $\cos^n \theta$ function as shown.

There is some qualitative agreement in that the scattered NO molecules lose more than 60% of their mean kinetic energy (from 0.4 to 0.15 eV), but this energy loss is less pronounced compared to the experiments. This discrepancy is likely due to the limitations of the employed force field and could be improved using density functional theory (DFT)-based force fields, but the overall trend observed is reproduced qualitatively.^{74, 75, 76} Future scattering experiments with aligned NO molecular beams could serve as a benchmark for improving the force fields. We obtain better agreement for the polar angle distribution shown in Figure 16 b). The downward facing molecular beam is naturally very narrow with barely any discernible transversal velocity contribution, and from purely geometric considerations based on the distance between our skimmer and the laser interaction region, the divergence is $<1^\circ$. The MD simulations account for that by aligning all NO trajectories along the surface normal (black arrow in the right bottom panel in Figure 16 b). The scattered NO molecules – while displaying a wider angular distribution than the molecular beam – still show a surprisingly narrow angular distribution. When fitted to a $\cos^n \theta$ distribution, we obtain a value of 745 for n . A thermal desorption process would yield $n = 1$, indicating that despite the significant loss in kinetic energy, a trapping-desorption mechanism does not seem to play a significant role here. The simulated polar angle distribution follows a \cos^{49} distribution, i.e. a little wider than the experimentally measured distribution, but still very narrow, and much narrower than the angular distributions measured for NO scattered off graphite,^{65,66} albeit these were measured at non-zero incidence angles. This demonstrates that both in the experiment and the simulations, a direct scattering mechanism closely along the surface normal is by far the dominant process. We note that the narrow scattering distribution is not an artefact of the geometry of our VMI instrument. Since the ionization laser for NO (1+1) REMPI spectroscopy does not need

to be focused, we can detect all NO molecules that scatter within a polar angle of 14° , and the majority of the ionized molecules would follow true VMI conditions due to us using soft extraction conditions with 12 plates.³⁴ Any slow moving NO molecules can be detected by altering the delay between the laser firing and the molecular beam opening. However, it is due to the narrow angular distribution in the experiment, see Figure 17,

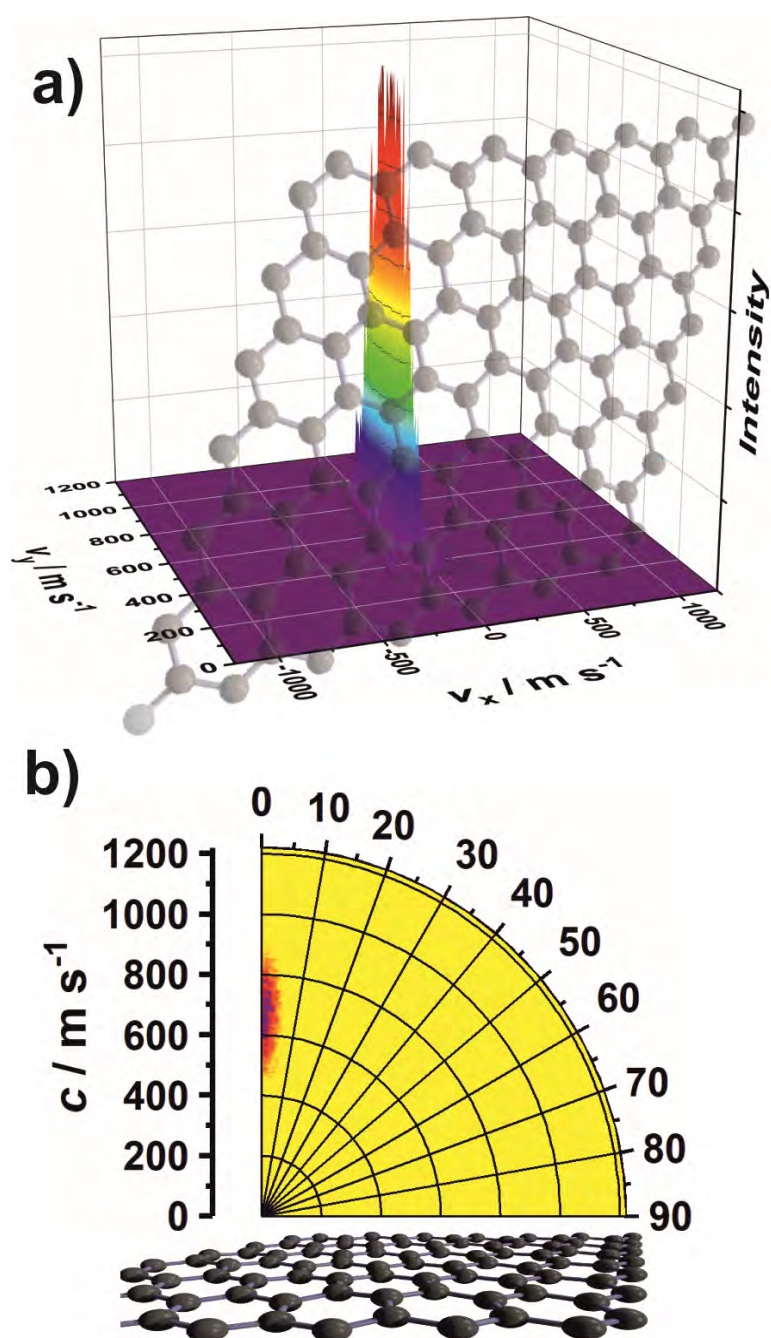


Figure 17 - a) Velocity distribution of NO molecules (initial kinetic energy ~ 0.31 eV) after scattering off graphene resolved along the surface normal (y) and perpendicular to the surface (x , along the propagation direction of the laser). b) Same image, but expressed as speed and polar angle; color range from yellow (=0 intensity) to dark red. Location of graphene schematically indicated in both cases.

that we can assume to detect all scattered NO molecules under true VMI conditions. If the recorded signal intensity towards the edges of a component in the images dropped off suddenly then it would raise concerns that some of the NO molecules that scatter are not accounted for and don't reach the detector. However, combined with our signal gradually decaying and as well as the narrow angular distribution, both experimental and simulated, it is a safe assumption that all the scattered products are recorded i.e. there is no indication of another component that is missed in these studies.

The MD simulations naturally cannot model reactions between the NO and the graphene, but the results can nevertheless provide information about the trapping-desorption probability. We have directed 4000 trajectories onto graphene and have observed a trapping mechanism for only ~2% of the trajectories. 'Trapping' in this case is for the entire length of each simulation run (4 ps), but does not account for 'double- or multi-bounce' trajectories in which the NO bounces off in a first collision, though does not escape the well and returns to the graphene surface for a further bounce, before finally escaping. This 2% trapping probability provides further evidence that trapping-desorption is not a dominant process for normal incidence NO scattering off graphene at kinetic energies of ~0.31 eV.

We can also rule out addition reactions of the NO onto graphene. After exposing the pristine graphene samples to our NO/He molecular beam over a period between two weeks and two months, we performed Raman spectroscopy and X-ray photoelectron spectroscopy (XPS) of the samples before and after exposure. For both techniques, this analysis was done *ex-situ*, i.e. the sample removed from the VMI chamber and transferred to the XPS and Raman instrument in ambient air. Neither did the Raman data indicate the formation of defects (absence of a D peak before and after NO

bombardment), nor did the XPS data indicate the addition of N or O species; some oxygen species were present before and after NO exposure, but their relative surface coverage did not change.

5.6. Conclusions

In summary, scattering of ~ 0.31 eV NO molecules off room-temperature graphene at 0° incidence angle takes away a significant amount of kinetic energy from the projectile in a predominantly direct-inelastic process; some of the energy goes into rotation, however, most energy goes into collective motions of the 2D honeycomb lattice of the graphene. This energy loss might be unique to graphene on gold with a fairly large separation of 3.4 \AA , with the graphene acting as a 'worn-out trampoline'. Despite this large energy loss, the angular distribution remains remarkably narrow, possibly a testament to the flatness of the graphene. However, we expect to learn more about collisional energy transfer processes and the possible observation of a trapping-desorption mechanism on graphene in future experiments by varying incidence angles and surface temperature.

5.7. Acknowledgements:

We thank the Royal Society for funding (IEC\R2\181028), and Prof Nick Lockyer and Dr Mark Dickinson at The University of Manchester for the loan of a frequency-tripling unit. We also thank Christopher Lester for help with the Molecular Dynamics simulations, Dr Alejandro Ferrari for help with the preparation of the graphene samples, and Dilruba Tazmin and Harsimran Singh-Bhaker for assistance during data acquisition.

6. Interpretation of Experimental Data through Molecular Dynamics Simulations

From the results in Chapter 5, it is clear a significant amount of translational energy is lost to the surface, it is not possible from the VMI (Velocity Map Imaging) images alone to infer where the available energy is channelled to and whether the molecules at the surface scatter directly or remain at the surface for any given amount of time.

One way of probing deeper is to model the system using molecular dynamics simulations, a type of computer simulations which are particularly useful for modelling larger groups of atoms while keeping computational expense at a minimum. Where computationally expensive *ab-initio* calculations consider electrons to calculate energies, molecular dynamics simulations describe atoms and molecules using classical potentials and forcefields and so cannot deal in discrete quanta of energy or adequately simulate reactions. One of the main benefits of modelling a system using molecular dynamics compared to *ab initio* simulations, is that it allows one to create a form of 3D movie of the interaction/reaction that is being investigated across a much longer period of time, in this case up to the order of nanoseconds. This allows one to 'see' what is occurring in actual experiments step by step without the significant computational resources required for *ab initio* simulations. One can immediately imagine how this presents an opportunity to view the nature of molecular interactions of nitric oxide and the graphene surface as well as how this may impact both species after collision, such as surface phonons or de-excitation of the NO. It is important for experimental studies

to be underpinned by theoretical modelling in order to fully understand the results in question and the conditions that gave rise to them.

Another benefit to using computer simulations to model experiments is that it allows for one to rapidly alter different variables in the system without the need to carry out these experiments in the lab reducing the requirement for expensive materials and lab time.

Chapter 5 in this thesis provides a comparison between the velocities and polar angle distribution of the scattered NO in the experimental and theoretical studies, demonstrating slight discrepancies but qualitative agreement in the large reduction in incoming velocity (80% and 60% for experiment and theory respectively) and also a narrow scattering angle ($\cos^n \theta$ where n is 745 and 49 for experiment and theory, respectively; these seem far apart but are both very narrow distributions). An example of how these angular distributions change as n increases is shown in Figure 18, it is clear from the figure that even as n reaches 10, the distribution is much narrower than a thermal desorption distribution at $n = 1$. It is clear how the distributions shown in Figure 16 are extremely narrow distributions when compared to the lower values of n shown in Figure 18. However, as discussed above, a more thorough investigation of this experiment via molecular dynamics would be beneficial to both understand the current experimental results and give insights into future experiments.

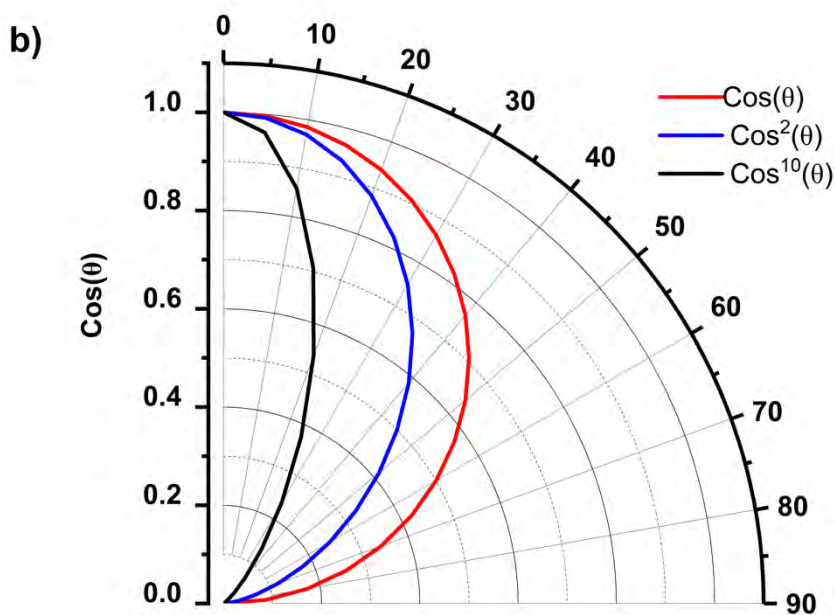
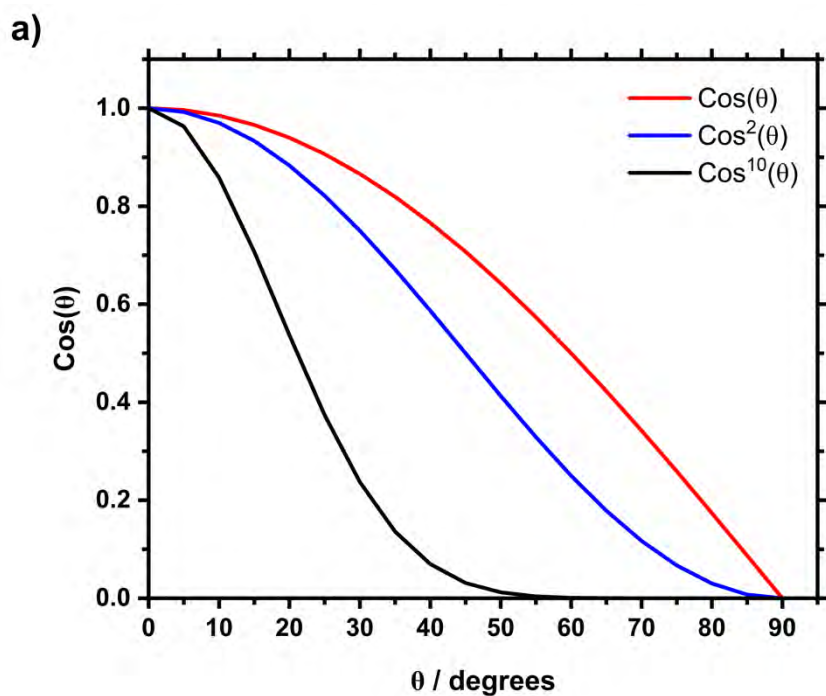


Figure 18 - $\text{Cos}^n(\theta)$ functions for $\text{Cos}(\theta)$, $\text{Cos}^2(\theta)$ and $\text{Cos}^{10}(\theta)$ in part a) showing the functions in a standard x vs y plot and in part b) the same values represented in polar coordinates. Both parts of the figure demonstrate how the functions that the polar angle distributions were fitted to become much narrower as n increases.

Chapter 7 delves deeper into the molecular dynamics simulations and investigates how the initial energy of the incoming NO can affect the energy of the scattered NO, most notably in how lower initial velocities increase the likelihood of NO becoming trapped at the graphene surface, a pathway which was also briefly alluded to in the predominantly experimental Chapter 5.

7. Molecular Dynamics Simulations of Nitric Oxide Scattering off Graphene

Thomas Greenwood,^{a,*} Prof. Dr. Sven P. K. Koehler^{a,b}

a) Department of Natural Sciences, Manchester Metropolitan University, M1 5GD, UK

b) Fakultät II, Hochschule Hannover, Ricklinger Stadtweg 120, 30459 Hannover, Germany

URL: <http://www.koehler.wp.hs-hannover.de>

*Corresponding author.

Email: thomas.greenwood@stu.mmu.ac.uk

Manchester Metropolitan University

Department of Natural Sciences

Manchester

M1 5GD

United Kingdom

T. Greenwood, S. P. K. Koehler, *Chem. Phys. Chem.*, 2022, **23**,

e202200216

7.1. Abstract

We performed classical molecular dynamics simulations to model the scattering process of nitric oxide, NO, off graphene supported on gold. This is motivated by our desire to probe the energy transfer in collisions with graphene. Since many of these collision systems comprising of graphene and small molecules have been shown to scatter non-reactively, classical molecular dynamics appear to describe such systems sufficiently. We directed thousands of trajectories of NO molecules onto graphene along the surface normal, while varying impact position, but also speed, orientation, and rotational excitation of the nitric oxide, and compare the results with experimental data. While experiment and theory do not match quantitatively, we observe agreement that the relative amount of kinetic energy lost during the collision increases with increasing initial kinetic energy of the NO. Furthermore, while at higher collision energies, all NO molecules lose some energy, and the vast majority of NO is scattered back, in contrast at low impact energies, the fraction of those nitric oxide molecules that are trapped at the surface increases, and some NO molecules even gain some kinetic energy during the collision process. The collision energy seems to preferentially go into the collective motion of the carbon atoms in the graphene sheet.

Keywords: graphene, scattering, molecular dynamics, surface scattering, nitric oxide

7.2. Introduction

Molecular dynamics (MD) simulations are a useful way to model both static molecular structures,^{86,87} but also non-reactive (chemical) processes such as adsorption and desorption phenomena.^{88,80} Classical MD simulations are based on force fields and do not explicitly include contributions from electrons,⁸⁹ and as such in their simplest form cannot model chemical reactions.^{90,91} They also lack the precision of *ab initio* methods,⁹² and naturally cannot model quantum effects. However, due to the reduced computational cost compared to quantum methods, MD simulations allow processes over much longer timescales to be modelled, and hence can help to catch a glimpse of such processes in a fashion not too dissimilar to a molecular movie.

We have recently investigated experimentally the scattering of nitric oxide, NO, off graphene.⁹³ This was in part motivated by the fact that NO is a diatomic radical, hence potentially reactive with graphene, but NO also allows rotational distributions to be observed, unlike monoatomic radicals. However, the by far largest contribution of scattered NO is due to *direct inelastic* scattering, and this is a process that can conveniently be modelled using MD simulations, allowing us to create snapshots of the actual scattering process. We have hence performed MD simulations of NO directed with various speeds at normal incidence angle at graphene supported by 6 layers of gold. This allows us to derive speed and angular distribution of the scattered NO for comparison with experimental results. The experiment also delivers rotational energy distributions of NO, and we also derived these classically in the simulations presented here. Furthermore, the MD simulations allow us to extract properties that are currently not accessible in our experiments such as the range of heights of the NO above the graphene at the turning point, i.e. when it is closest to the graphene surface, and the

effect of varying conditions such as the initial velocity, which will guide us in future experiments.

The scattering of hydrogen off graphene has already been investigated both experimentally and theoretically.^{68, 38, 69} The scattering of atoms other than hydrogen (N(⁴S) and O(³P), respectively) with graphene has also been modelled by Nieman *et al.* and Jaye *et al.*;^{42, 41} quantum-methods guaranteed that chemical reactions with the graphene (insertion) and ablation reactions could be observed.

Both classical mechanics as well as *ab initio* molecular dynamics simulations were also employed in modelling the collisions of homo-diatomic molecules (N₂ and O₂) with highly oriented pyrolytic graphite (HOPG),^{39, 61, 62} in which direct scattering has been found to be the dominant process, but some evidence for trapping-desorption was observed, too. The fact that MD simulations allow for larger entities (many more atoms) to be modelled allowed Hase and co-workers to observe that most of the initial kinetic energy is channelled into the surface motions of the graphene substrate.^{39, 61, 62}

Collisions of NO with graphite were also experimentally and theoretically investigated from the 1980s onwards. Nyman *et al.* modelled the scattering process classically and in a statistical fashion;^{94, 65} they observed 'rotational cooling' (at surface temperatures of 300 K or higher) and even rotational rainbows. Many more studies investigated the NO-graphite system experimentally by measuring in particular speed and angular distributions as well as rotational state distributions.^{59, 63} Specular scattering is almost always observed, especially at higher temperatures, and an isotropic component, presumably due to a trapping desorption mechanism, becomes dominant at lower temperatures,^{21, 64} even at fairly steep incidence angles.⁶⁶

We here set out to perform simulations of the scattering of NO radicals off graphene supported on gold using classical MD methods, i.e. without considering quantum effects. We replicate the conditions in our own experiment, with the aim in particular to establish translational energy and rotational state distributions.

7.3. Results and Discussion

Figure 19 shows the speed distributions of NO molecules after collision with a graphene layer supported on gold for initial NO velocities of 600, 800, 1200, 1600 and 2500 m s⁻¹ (0.06, 0.10, 0.22, 0.40 and 0.97 eV) from dark-red to orange; the initial velocities are indicated by short vertical arrows at the top, while the horizontal arrows illustrate the difference of speed between the initial speed and the most probable final speed. We only plotted in Figure 19 the case of no rotational excitation, N-atom oriented towards the surface, with a surface temperature equilibrated at 300 K. All data (data points as open circles) are fitted to the 3D flux distribution in equation 14

$$F(c)dc = A c^3 \exp \frac{-(c - c_0)^2}{\alpha^2} dc \quad (14)$$

where A is a scaling factor and α is related to the width of the distribution.⁷⁷ The blue curve is a fit to an experimental speed distribution with an initial NO velocity of 1418 m s⁻¹ and a full width at half maximum of ~190 m s⁻¹. A few observations can be made straight away: 1) The faster the incoming NO molecule, the more kinetic energy is transferred (most likely to the graphene surface motions); 2) while for the fastest speeds, all NO molecules are scattered with speeds that are *slower* than the incoming NO, for the slower incoming projectiles, a significant portion actually gains some kinetic energy in the scattering process; 3) while the experimental data is qualitatively similar,

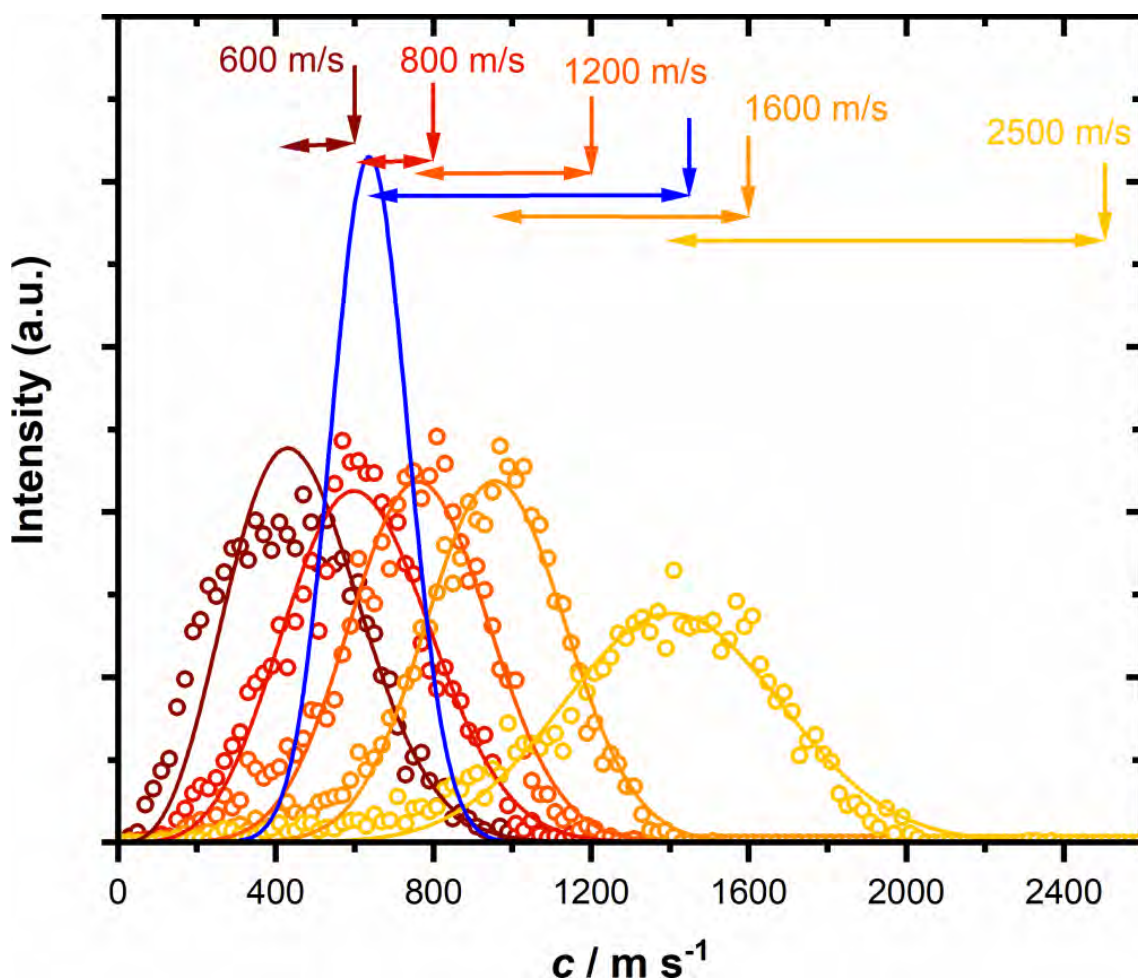


Figure 19 - Speed distributions of NO molecules after scattering off a graphene surface, initial speeds as indicated by vertical arrows. Horizontal double-arrows indicate the loss of speed, and the blue data is an experimental speed distribution with an initial NO velocity of 1418 m/s and a width of ~ 190 m/s. All simulation data fitted to eq. 18.

it appears as if more kinetic energy is lost during the scattering process in the experiment than predicted in the MD simulations, and interestingly that the speed distribution is *narrower* in the experiment than in the simulations, despite the initial width of the speeds distribution in the experiment being *significantly wider* than in the simulations (where no spread is assumed). This wider speed distribution of the scattered NO molecules in the simulations, however, might be a direct result of the classical rather than quantum nature of the simulations. Naturally, vibrational energy is quantised, but in our simulations, energy exchange of fractions of vibrational quanta are allowed, thus an incoming NO molecule might lose or gain small amounts of energy from e.g. vibrations in the substrate that would not be allowed had a rigorous quantum-

mechanical treatment be applied. This possibly leads to the wider velocity distribution in the simulations, but quantum corrections of the classical simulations could solve this issue.⁹⁵ The loss of a significant amount of energy for the higher incoming velocities contrasts with previous simulations of scattering on graphene,⁶⁹ but this loss is expected due to the different masses of the incoming projectiles, and furthermore it is not straightforward to compare those two experiments due to the different incidence angles. The NO in our simulations is travelling along the surface normal, resulting in more energy being transferred into the surface, whereas the scattering simulations were performed at angles that are removed from the surface normal and as such show less energy transfer as kinetic energy in the surface plane tends to be conserved.^{39, 61} Scattering simulations of atomic nitrogen with pristine graphene at kinetic energies of 14.9 kcal/mol (0.646 eV) found an energy loss ratio of roughly 0.6,⁴² this could again be due to the scattering angle of the nitrogen, or in this case due to a monoatomic particles (N atoms) being scattered rather than a diatomic NO. Nevertheless, the results show that even at this relatively high initial kinetic energy, there is little evidence for reactions such as insertion reactions into pristine graphene.

Research by Hase *et al.* demonstrates how at similar velocities to this study, the vast majority of the initial energy is transferred into surface vibrations and kinetic energy of the scattered N₂, again showing that the higher the incident angle (with respect to the surface normal), the less energy is transferred to the surface due to the velocity component along the surface being conserved.⁶¹

The initial and final speeds and kinetic energies (and energy loss and ratio) for the present molecular dynamics simulations are shown in Table 5.

Table 5 - Initial and most probable final speeds (in m s^{-1}) and kinetic energies (in eV) and energy loss and ratio. The data for 600, 800, 1200, 1600 and 2500 m s^{-1} are from the simulations while the data for 1418 m s^{-1} are from experimental work.

$c_i / \text{m s}^{-1}$	$c_{f,max} [\text{m s}^{-1}]$	$E_i [\text{eV}]$	$E_{f,max} [\text{eV}]$	$\Delta E [\text{eV}]$	E_f / E_i
600	440	0.06	0.03	0.03	0.5
800	606	0.10	0.06	0.04	0.6
1200	755	0.22	0.09	0.13	0.4
1418 ± 95	621 ± 115	0.31 ± 0.08	0.06 ± 0.04	0.25 ± 0.09	0.2 ± 0.1
1600	949	0.40	0.14	0.26	0.3
2500	1384	0.97	0.30	0.67	0.3

Impact angles in all simulations and the experiment are along the surface normal, and if the Baule model in its simplest form was applied, the NO would not scatter off the surface at all as it is heavier than a single C atom. Instead, it appears that in order of increasing speed of the incoming molecules, the NO interacts with a pseudo-atom with a mass of 15, 20, 12, 11, 10 C atoms (for $c_i = 600, 800, 1200, 1600, 2500 \text{ m s}^{-1}$), and with a pseudo-atom with a mass of ~ 7 C atoms if the experimental results are used. This means firstly that fewer atoms in the carbon lattice ‘work together’ or are involved in the scattering process the faster the incoming projectiles are flying (at least for velocities of 800 m s^{-1} or greater), and secondly that the ‘real’ 2D graphene network seems more rigid than described in the MD simulations, leading to the lowest ‘effective mass’ of a surface atom in the experiments. The reason for the only qualitative rather than

quantitative agreement is most likely due to the fact that while the graphene and gold potentials in literature are well-established, the universal force fields used for the interactions between the incoming NO and the graphene and gold were developed for a large range of chemical systems and are hence necessarily a compromise. Ab initio calculations would have likely yielded better potentials and thus a more quantitative agreement with experiment.

Just as the simulations underestimate how much kinetic energy is lost in the collision process, they seem to overestimate the polar angle distribution, see Figure 20. The angular distributions become narrower with increasing initial NO speed as expected, but this increase is not overly pronounced. When fitting the angular distributions to a $\cos^n \theta$ function (where a fitting factor of $n = 1$ would indicate a thermal desorption process), the fitting parameter n only increases from 40 to 51 as the initial NO speed increases. All those parameters are a lot smaller than $n = 745$ for the experimental data, which remarkably shows the narrowest angular distribution by far, though $\cos^n \theta$ functions with $n > 40$ are already fairly narrow, and the much larger fitting parameter n for the experimental work perhaps overstates that the width of the distribution only changes from a rather narrow $\pm 10^\circ$ (simulations) to approximately $\pm 3^\circ$ (experiment). Both simulation data and experimental data include rotational excitation of the incoming NO, but differences in the experimental and simulated rotational temperature could lead to (slightly) different angular distributions. However, it seems that the graphene surface appears even 'flatter' towards incoming NO molecules than the simulations can reproduce. The narrow scattering distributions at higher incoming velocities match similar studies of H atom scattering off graphene at similar kinetic energies (1 eV) with scattering distributions close to the specular angle.⁶⁹ Studying the scattering of N₂ off

graphite at a range of incidence angles, Hase and co-workers found that scattering preferentially occurs close to the specular angle (but at slightly larger angles relative to the surface normal) and with fairly narrow angular distributions,⁶¹ matching well the narrow scattering in the experiments here.

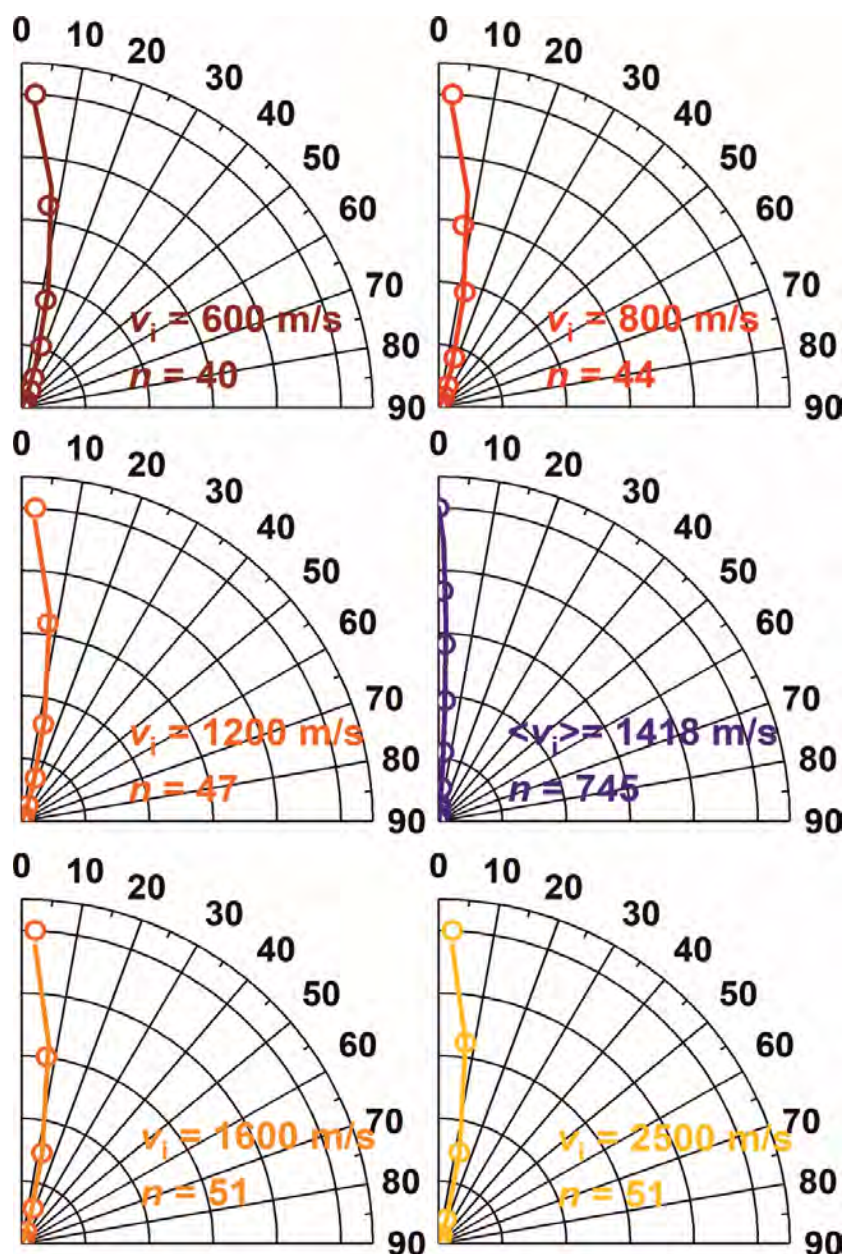


Figure 20 - Polar angular distributions of NO molecules after scattering off a 300 K graphene surface, initial speeds as indicated. Blue data is an experimental angular distribution with an initial NO velocity of 1418 m s^{-1} , and a width of $\sim 190 \text{ m s}^{-1}$. All data fitted to a $\cos^n\theta$ function, with the fitting parameter n indicated.

The wider polar angle distributions at lower incoming kinetic energies can also be observed in Figure 21, which shows the correlation between the polar angle and the final speed of the scattered NO molecules (but – ignoring the y-axis – also shows the

speed distribution and its shift towards speeds higher than the incoming speed which has already been better illustrated in Figure 19). The downward trend (or slope) for all incoming speeds shows that scattering along the surface normal retains the most kinetic energy, while more energy is lost to rotations or the graphene lattice vibrations when the NO scatters away from the surface normal.

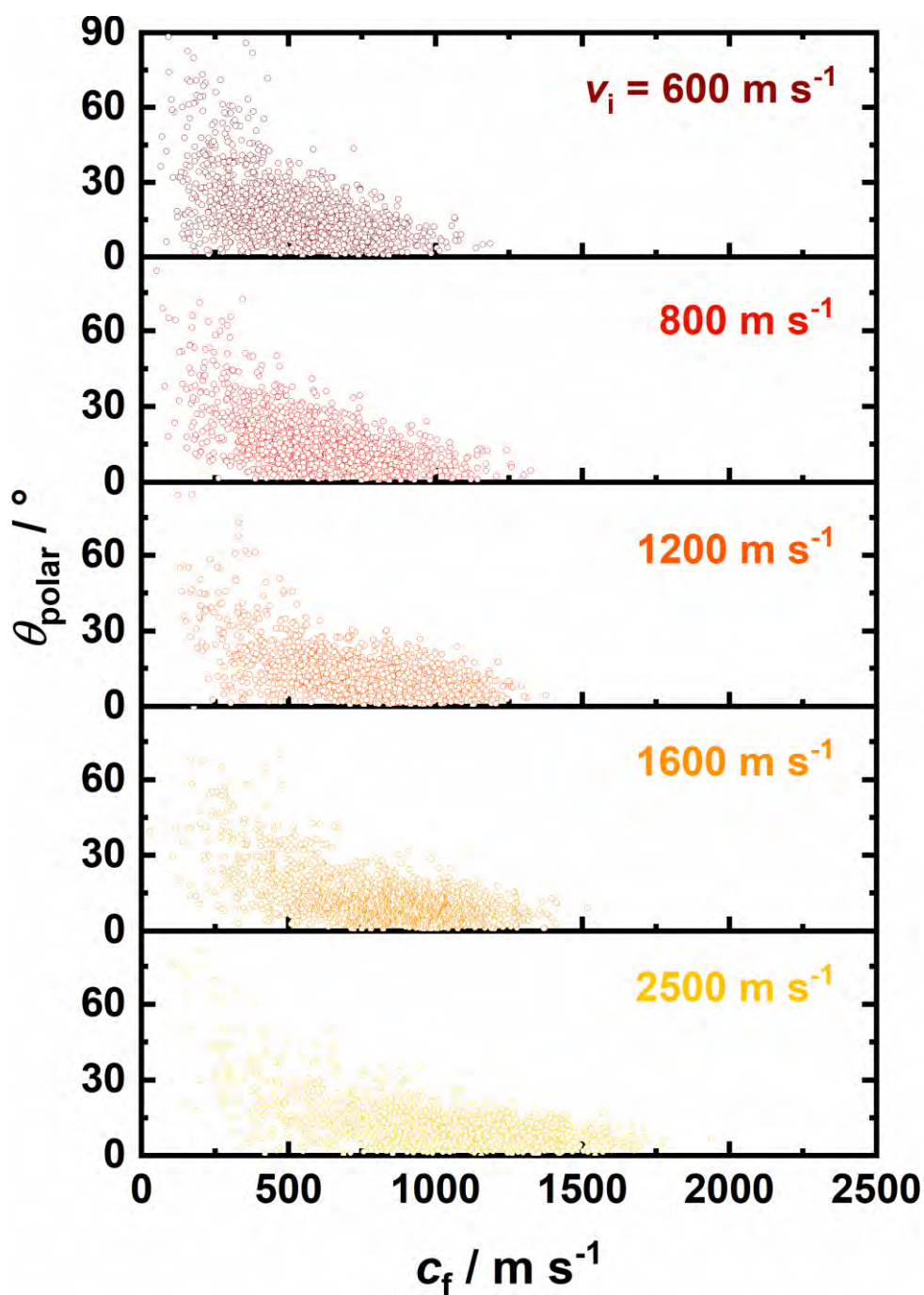


Figure 21 - Polar angles θ_{polar} as a function of the final speed of the scattered NO molecules for the five different initial speeds as indicated.

There are several distinct scattering mechanisms when the NO interacts with the graphene surface which largely depend on the incoming velocity, with some examples being shown in Figure 22. Previous studies have demonstrated that NO scatters off (a number of different) surfaces via two different mechanisms, namely an inelastic component which dominates at high incidence energies, and a trapping-desorption mechanism which dominates at low incidence energies and glancing angles.^{63, 64, 66} A typical result of the NO scattering with higher initial velocities is a single 'bounce' off the graphene surface with very little rotation of the NO molecule itself, resulting in the almost straight yellow line in Figure 22 for an initial velocity of 2500 m s⁻¹. At lower initial velocities, a higher likelihood of trapping on the graphene surface can be observed, either 1) trapping for a short time, during which the NO bounces several times on the surface before being released into the vacuum as is the case for the 600 m s⁻¹ initial velocity trajectory, or 2) the NO can be trapped for the entire simulation duration (4 ps) as shown for the second 1200 m s⁻¹ trajectory. Previous work also displayed these three scattering pathways although using longer simulation times of 10 ps and 25 ps.^{39, 61, 62} Evidence from experimental work suggests that the majority of those molecules which are 'trapped' at the end of a simulation run do eventually leave the surface (at adsorption energies a fraction of the thermal energy, residence times are likely to be short) and do *not* thermalize at the surface.³⁹ Theoretical work involving O₂ scattering

off graphite demonstrated that around 60% of the molecules scattered with just a single bounce and a further 20% underwent multiple bounces.⁶²

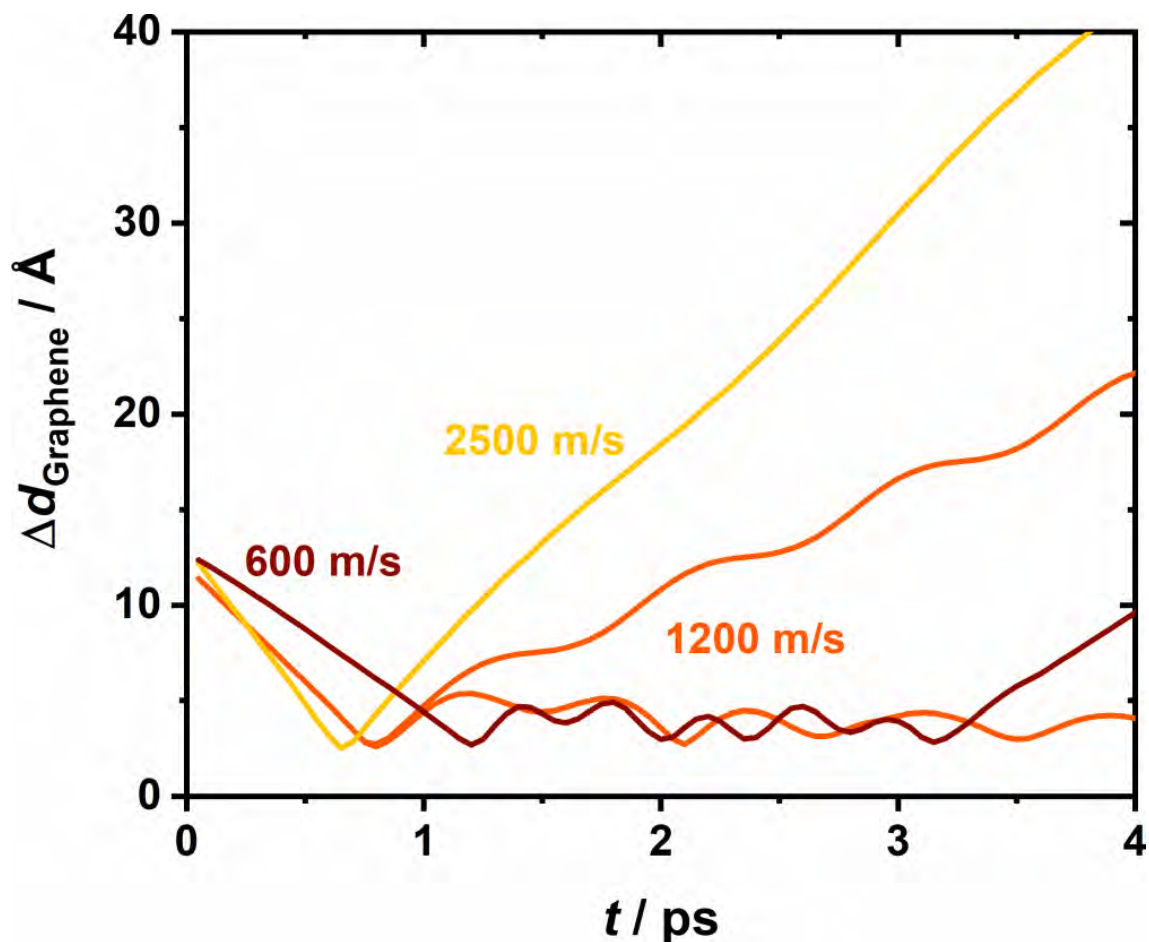


Figure 22 - Four different but characteristic trajectories of NO molecules scattering off graphene. Shown is the distance between the N atom (and *not* the center-of-mass of NO, in order to highlight rotational effects) and the average height of the six closest C atoms in graphene (not necessarily a hexagon) as a function of time along the x axis. The 2500 m s^{-1} trajectory undergoes direct scattering, while the 600 m s^{-1} trajectory shows trapping-desorption behaviour. The two 1200 m s^{-1} trajectories (with the same initial slope) undergo direct scattering (yielding a rotationally excited NO) or permanent trapping (within the simulation time of 4 ps).

Permanent trapping of NO at the surface is more likely to occur at lower initial velocities where there is less chance of the NO having sufficient energy to overcome the attractive van der Waals (vdW) forces after rebound, as shown in Figure 23. As is expected, the higher the initial velocity, the lower the chance of trapping. Interestingly, we also observe that for the five highest initial velocities, the rotationally excited molecules seem to have higher trapping probabilities (despite the initial kinetic energy of the NO

molecules with and without rotational excitation being the same). A possible reason for this is that the rotating molecules are more likely to approach the graphene surface in a 'side-on' configuration, which would lead to a greater likelihood for the vdW forces to 'take a hold' of the NO. Another reason for this increased trapping could be that the rotating molecules are likely to scatter under a wider polar angle and hence spend more time close to the surface compared to NO molecules that scatter closer to the surface normal, again increasing the likelihood of vdW interactions between the graphene surface and the NO to trap the nitric oxide. Previous work has shown that trapping increases in likelihood as the incidence angle increases,³⁹ this suggests the increased

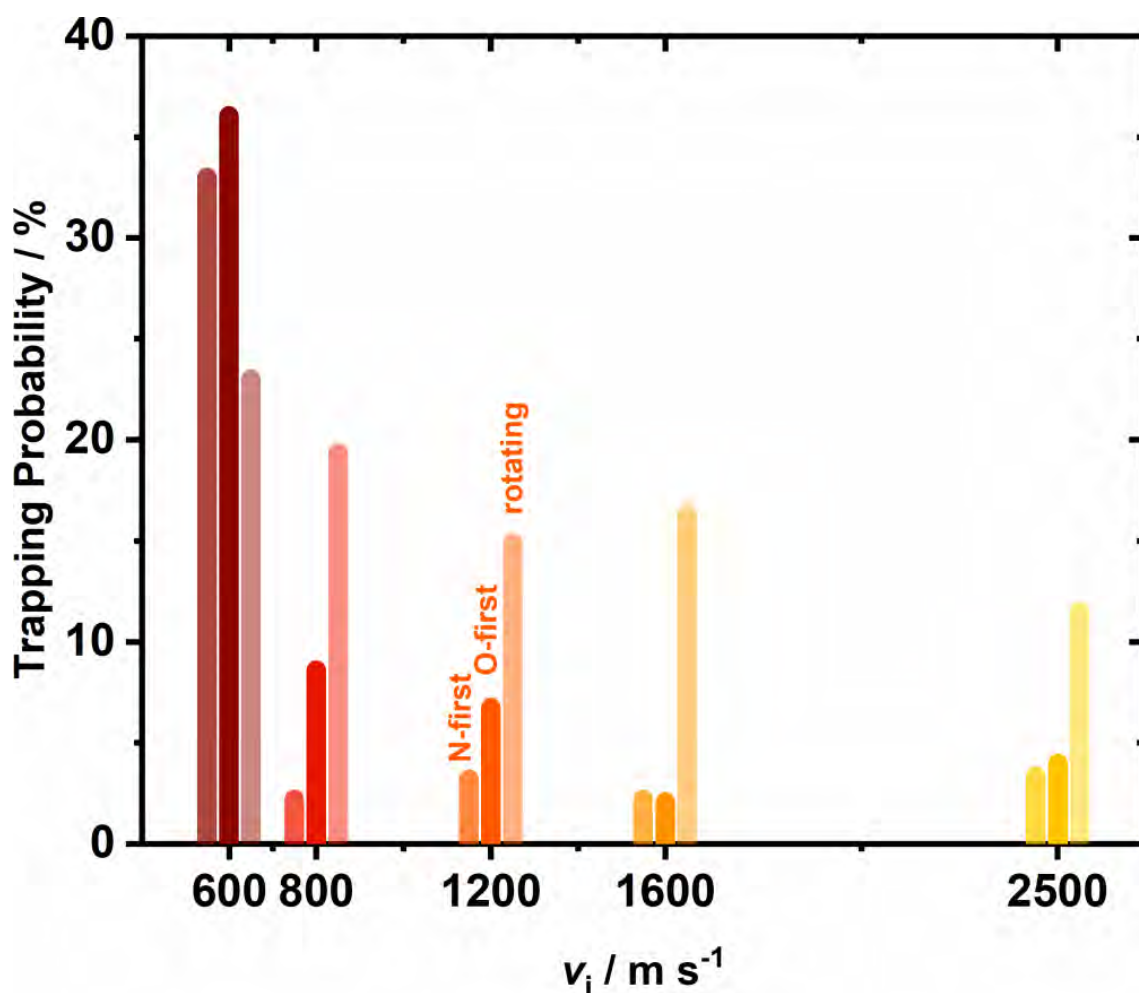


Figure 23 - Trapping probabilities for collisions of NO molecules with graphene for the five indicated initial speeds, and separated for N-first and O-first orientation (without rotation), and NO molecules with a thermal rotational state distribution at 80 K.

trapping at lower velocities and in case of rotating molecules are indeed due to the vdW interactions as these effects would be felt more strongly at larger incidence angles. Research at even longer timescales (25 ps) also shows trapping probabilities increasing at lower velocities and higher incidence angles.⁶¹

The final rotational state distributions after scattering off the graphene surface shown in Figure 24 reveal two findings. Firstly, the faster initial velocities result in higher rotational energy levels being populated, i.e. translational motion is coupled to rotational motion. Secondly, the initially rotationally excited molecules also have a higher rotational energy after collisions. Research by Hase and co-workers suggest that energy transfer is slightly dependent on incident velocity with a slightly higher proportion of energy going into rotations at lower velocities. If we focus on the 1600 m s⁻¹ and 2500 m s⁻¹ trajectories for the rotating NO molecules, there appears to be evidence for rotational rainbows, where the population in rotational states rises and falls for specific rotational energy levels rather than gradually decaying. Most interestingly in the case for the 2500 m s⁻¹ which looks to display a 'double rainbow' whereby the population rises and falls before rising and falling again as a function of rotational energy levels. Rotational rainbows from NO scattering have been observed experimentally in both the gas phase⁹⁶ and from solid surfaces.⁹⁷ Theoretical studies have shown the presence of rotational rainbows off graphite, though only at high surface temperatures.^{94, 65} Seminal studies on the scattering of NO off Ag(111) have also found evidence for rotational rainbows.^{98, 55} Later studies involving NO on Ag(111) concluded that the orientation of the incoming molecule has an effect on the prominence of rotational rainbows, perhaps explaining why the rainbows are better

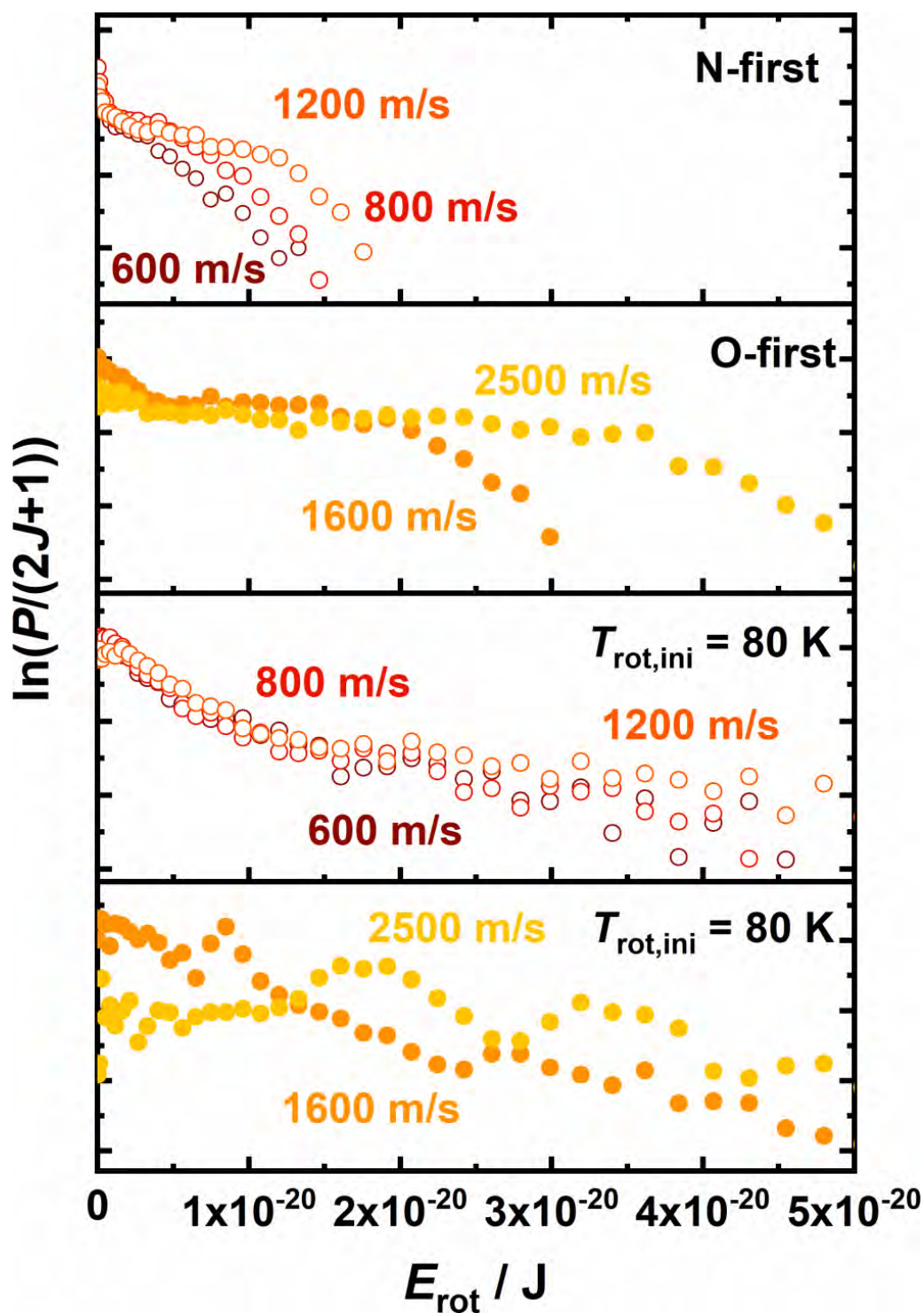


Figure 24 - Selected rotational state distributions of NO radicals scattered off graphene. Top-two panels for N-first and O-first orientation without initial rotational excitation, bottom-two panels for initial thermal 80 K rotational distributions. Open symbols for 600, 800, and 1200 m s^{-1} , closed symbols for 1600 and 2500 m s^{-1} .

seen in the simulations with rotating NO.⁹⁹ Studies of NO off graphite found that the NO is fully rotationally accommodated at surface temperatures below 170 K and scatters off with a rotational distribution that can be described by the surface temperature.

Above 250 K, however, the NO is only partially accommodated and its rotational distribution can often not be described by a single temperature.^{21, 64} It was also found that in the case of NO off Ag(111) at low rotational levels ($J < 20$), a Boltzmann-like distribution can be observed, followed by higher populations again at higher J levels similar to our results shown in Figure 24, thus making it impossible to assign one single rotational temperature to the scattered NO molecules.

Figure 25 shows the height of the N atom in NO above the average of the six closest C atoms at the turning point of the NO (i.e. at the closest approach) as a function of the *final* velocity of that NO molecule. A clear inverse correlation can be seen between the shortest distance and the final velocity. Despite the graphene surface not being perfectly flat with shallow peaks and troughs due to surface phonons (leading to slight variations in the shortest distance), it can be assumed that this inverse correlation is due to those NO radicals which happen to get closer to the graphene surface experiencing a greater repulsive force, resulting in a faster scattering velocity.

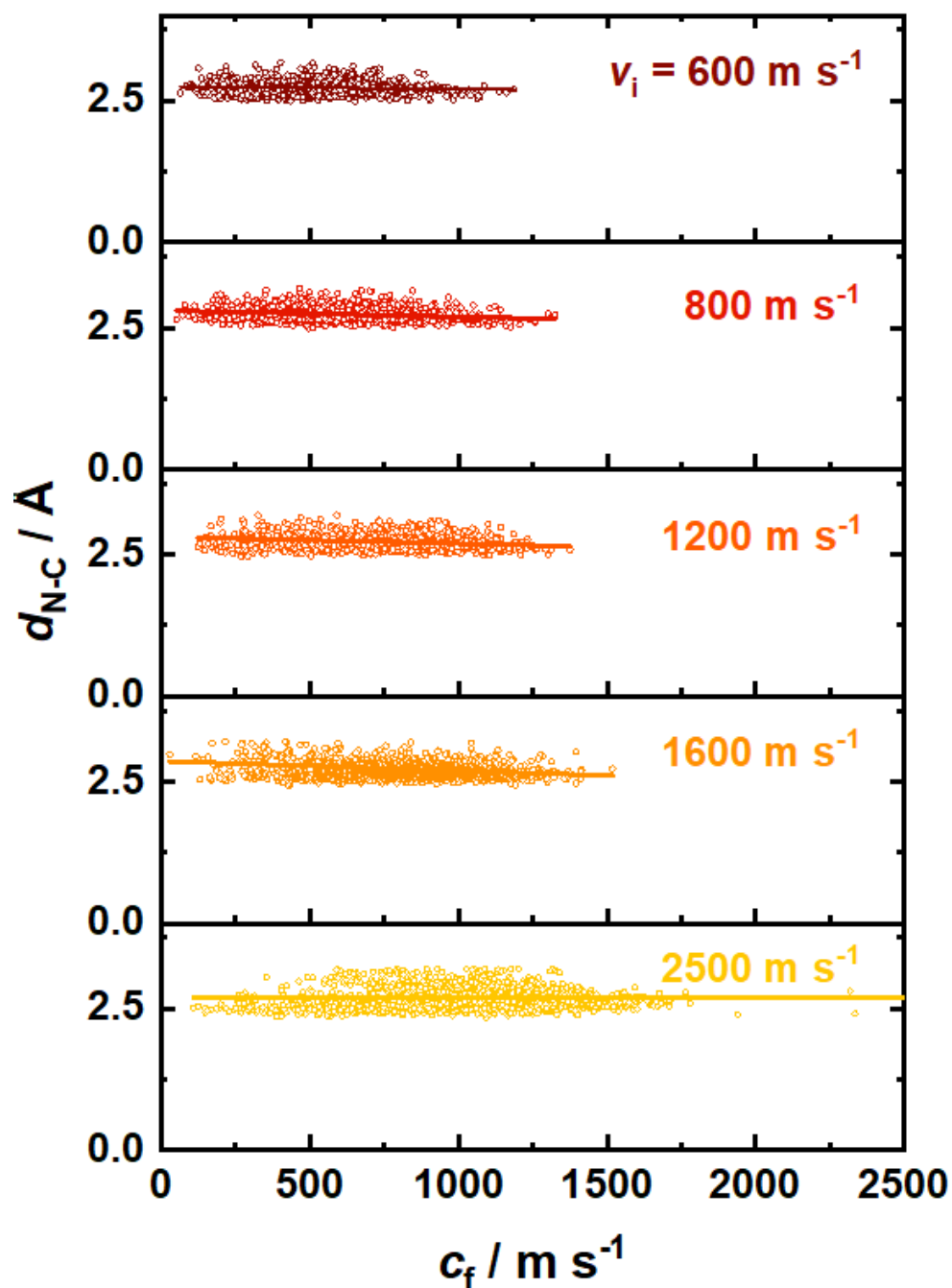


Figure 25 - Shortest distance between the N atom of NO and the average of six closest C atoms in graphene at the turning point as a function of final speed, with the linear fit only as a guide to the eye. All data for N-first orientation, but data is very similar for O-first orientation.

7.4. Conclusions

In summary, NO scattering off graphene using MD simulations qualitatively agrees with the previous experiments in that a lot of energy is lost to the graphene surface. The

molecular dynamics simulations also show however, that the more energy the NO has initially, the higher the energy lost as a ratio of the total initial energy, i.e. a larger fraction of energy is lost to the graphene, which the previous experimental studies could not investigate owing to the single incoming velocity. Separate modes can be seen once the NO collides with the graphene in both direct scattering which is dominant at higher incoming velocities, and trapping/multiple bounces dominating at lower incidence velocities. In terms of trapping probabilities, the likelihood of trapping greatly increased at lower incidence velocities but also for the rotating NO at each initial velocity, with the exception of 600 m s^{-1} . Narrow polar angle distributions were observed, with these distributions becoming narrower as the initial velocity of the NO increased; those narrow angular distributions confirmed that we did not miss in our experimental work, in which we are not able to detect the whole 2π hemisphere above the surface, any contributions to the overall distribution. We detected a range of turning points for each of the five monoenergetic initial velocities, and these turning points correlate with the final velocity such that the closer the approach, the faster the final velocity. Two features stand out in the rotational distributions, namely 1) the translational energy of the NO is converted to rotational energy as seen by the fact that the higher the initial velocity, the higher the rotational energy levels populated, and 2) some evidence at higher incidence velocities for rotational rainbows. These simulations trigger us to perform further laboratory experiments at different initial velocities, which will also allow us to extract residence times at the surface.

7.5. Acknowledgements:

We thank the Royal Society for funding (IEC\R2\181028), Christopher Lester for help with the Molecular Dynamics simulations, and Emmanuel Nwokedi and Dafydd Marshman for performing some of the simulation runs.

7.6. Methodology

The molecular dynamics simulations described here were performed within the DL_POLY Classic suite using a combination of force fields.⁷³ A simulations box was selected with a 120° rhombus as a base in the x-y plane of length 17.3 Å each and a z dimension perpendicular to the x-y plane of length 45 Å. Periodic boundary conditions were applied along the x-y plane, but with no periodicity in the z dimension. The metal substrate was formed of a 6×6×6 array of gold atoms (with only the bottom layer being frozen in position, i.e. those Au atoms furthest away from the surface) whose interactions were described by a Gupta potential with parameters shown in Table 6.⁴⁵

Table 6 – Parameters used for the Gupta potential to describe interactions in gold⁴⁵

λ	μ	$\alpha_{\infty}[\text{eV}]$	ζ	n_0	δ	$\theta_{\infty}[\text{eV}]$
12.728	3.173	0.1730	6.5149	-1.234	1.593	2.7565
γ	Δ	η	$R_{\infty}[\text{Å}]$	ρ_0	ν	ξ
0.628	-2.041	1.952	2.927	0.144	6.247	3.330

98 carbon atoms were positioned in a hexagonal 2D network in the x - y plane on top of the gold substrate. The bonds in the graphene sheet were described by a harmonic potential (rather than fixed bond lengths) to accurately reflect any compressions and stretches in the bonds as the NO collides with the graphene surface. A Morse bond potential as per equation 15 described the C-C bonds

$$V_s(r) = D[e^{-\alpha(r-r_0)} - 1]^2 \quad (15)$$

with parameters proposed by Kalosakas and co-workers,⁴⁶ using the accepted carbon-carbon internuclear distance in graphene of 1.42 Å, with $D = 5.7$ eV and $\alpha = 1.96$ Å⁻¹. This force field was selected as it has been derived from first principles, accurately describes the interactions in graphene and is suitable for atomistic simulations. Angles and dihedrals were described by quartic and cosine functions, respectively, of the form (equations 16 and 17):

$$V_b(\theta) = \frac{k}{2} \left(\theta - \frac{2\pi}{3} \right)^2 - \frac{k'}{3} \left(\theta - \frac{2\pi}{3} \right)^3 \quad (16)$$

$$V_t(\omega) = \frac{1}{2} V_2 [1 - \cos(2\omega)] \quad (17)$$

where $k = 7.0$ eV rad⁻² and $k' = 4.0$ eV rad⁻³, and $V_2 = 0.23$ eV.⁴⁸

Non-bonding interactions were described by Lennard-Jones 12-6 potentials of the form

$$U(r) = 4\epsilon \left[\left(\frac{\sigma}{r} \right)^{12} - \left(\frac{\sigma}{r} \right)^6 \right] \quad (18)$$

with all parameters given by the universal force field set out by W. M. Skiff and co-workers,⁵⁰ with the exception of the gold and graphene interaction being developed by E. E. Helgee and A. Isacson.⁴⁹ Respective values are provided in Table 7. We stress here that we have *not* benchmarked these potentials against ab initio calculations which

would have likely yielded a much better potential,⁶¹ and this possible discrepancy is one of the contributing factors for the only qualitative agreements between the simulations and experiments. Lorentz-Berthelot combining rules were applied for interactions between unlike atoms. The Lennard-Jones 12-6 potential was only applied to C-C interactions of carbon atoms at least four C-C bonds apart, i.e. not yet described by Morse bond potentials or angular or dihedral potentials.

Table 7 - Parameters for the van der Waals interactions^{49, 50}

<i>Interaction</i>	ϵ [eV]	σ [Å]
<i>C-C</i>	0.004553	3.431
<i>C-O</i>	0.003442	3.2745
<i>C-N</i>	0.003691	3.346
<i>N-Au</i>	0.00225	3.0972
<i>C-Au</i>	0.0341	3.003
<i>O-Au</i>	0.002098	3.0259

The gold and graphene were relaxed and equilibrated by running simulations in an NVT ensemble regulated to 300 K by a Nosé-Hoover thermostat for 4 ns with a relaxation constant of 1 ps prior to the addition of a nitric oxide molecule. The equilibrated distance between the graphene and the top-layer of Au atoms is around 3 Å.

A single NO molecule was then positioned above the graphene surface, and its bond potential was also defined by a Morse potential with parameters $D_e = 6.61736$ eV, $\beta = 2.636$ Å⁻¹ and $r_e = 1.151$ Å.⁴⁷ Placing such a single NO molecule in a randomly selected position in the x - y plane ~ 12 Å above the graphene is sufficient as interatomic forces were truncated after 7 Å. Both the N and O atom were then given a velocity of 600, 800, 1200, 1600, or 2500 m s⁻¹ along the z axis towards the graphene (same geometry as in our experiments), i.e. no vibrational excitation was given to the NO molecule, just as no NO($v=1$) is expected in the cold molecular beam in our experiments. While these velocities do not match our experimental velocity exactly, they cover a range of velocities achievable in molecular beam experiments, and match our experimental kinetic energy to <0.1 eV.

Three cases in terms of orientation and rotational excitation of the nitric oxide were investigated: 1) no rotational excitation, NO aligned along the surface normal with the N-oriented towards the surface (Figure 19); 2) same as 1), but with O facing the surface; 3) with a rotational distribution representative of a thermal 80 K sample (roughly equivalent to a molecular beam) *in addition to* the translational energy, and a random orientation in space. 2000 trajectories were run for each orientation/rotational excitation case, with the NO originating from a different position within the x - y plane for every run in each of those cases, giving 6000 trajectories in total for each of the five velocities, making a total of 30,000 trajectories.

The molecular dynamics simulations were run with a timestep of 1 fs for 4 ps (8 ps for 600 m s⁻¹ simulations, all starting after the 4 ns equilibration of the graphene and gold). After the NO has interacted with the graphene, it was registered once traversing a virtual plane 8 Å above the graphene, where there is no longer any interaction between the

graphene and the NO. Properties such as the positions and velocity components of both the N and O atoms in all three dimensions separately were recorded. Molecular speeds were extracted from center-of-mass shifts per unit time and binned in 20 m s^{-1} wide intervals. The simulation parameters are schematically shown in Figure 26.

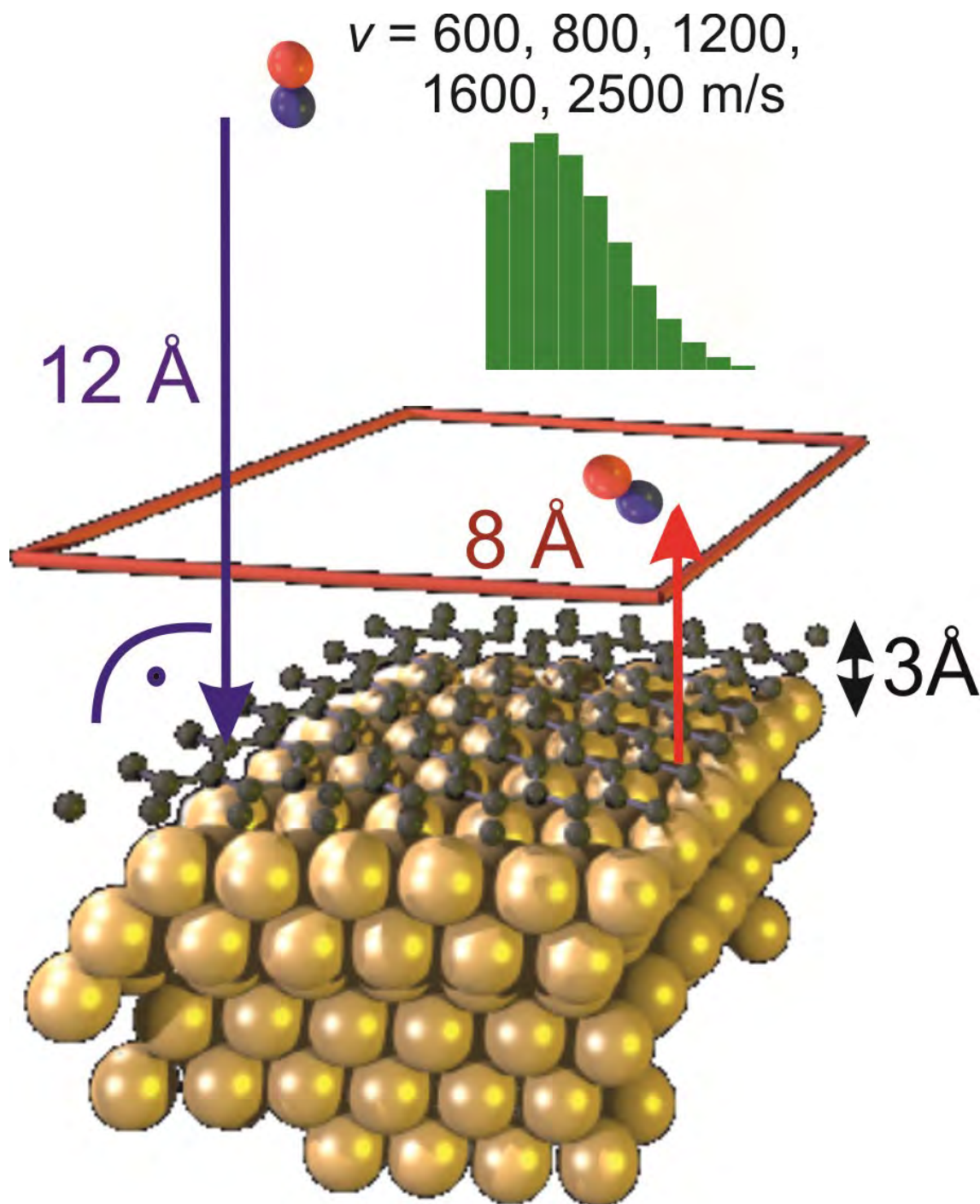


Figure 26 - Schematic of input parameter of the molecular dynamics simulations. NO molecules are placed 12 \AA above the graphene surface and given a certain velocity, and in some cases rotational excitation. They are directed along the surface normal towards a random position on the graphene, from where they scatter back before they are recorded when traversing a virtual plane 8 \AA above the surface.

8. Comparison of Internal State

Distributions from Simulations with Experimental Data

Chapter 7 in this thesis provides increased detail on the molecular dynamics simulations, demonstrating that as the incoming translational energy of the NO is decreased, the relative energy lost to the surface decreases and the probability of trapping desorption significantly increases. The results also investigated how incoming velocity may affect polar angle distributions and how the outgoing velocity of the NO is likely to be linked to the turning point of the NO molecule in an inverse relationship, i.e., the closer the molecule is to the graphene surface at the turning point, the higher its upward velocity distribution.

Once one gains an understanding into how translational energy of a species changes upon collision, the natural question one asks is how this translational energy is transferred? As has been discussed, some of this translational energy of the NO will have been transferred to the graphene surface as phonons, however, it is also important to consider the internal energy of the molecule and how this may change after collision. With the molecular beam of NO being rotationally (and vibrationally) cold, there is opportunity for the translational energy to transfer into rotational energy or potentially vibrationally excite the NO, though there were no molecules in higher vibrational states detected in these experiments. A final key component in the molecular dynamics results was how rotational energy distributions change as a function of incoming velocity where

higher incoming velocities led to higher rotational energy levels being populated as well as the potential presence of rotational rainbows.

It is also important to consider how well the molecular dynamics simulations model the experimental system, especially in terms of internal energy, with the molecular dynamics simulations not considering energy in quantised terms, therefore rotations of molecules are dealt with on a continuous scale rather than in discrete quanta and so a careful comparison between experimental data and results from simulations can reveal limitations of a purely classical approach. On the other hand, the molecular dynamics simulations allowed the simulated incoming NO to approach the graphene surface with no rotational energy whatsoever, to investigate how much rotational energy is gained upon impact with the graphene surface.

Chapter 5 in this thesis focuses on the velocity and angular distributions of nitric oxide scattering off the graphene surface along with a short comparison to the MD simulations. The molecular dynamics simulations were discussed in greater detail in Chapter 7 of this thesis with greater insights into the rotational distributions of directly scattered NO but almost more importantly demonstrating a trapping desorption pathway for NO colliding with a graphene surface and how NO can leave the surface with one of two very distinct velocity and rotational distributions. It is only logical therefore to investigate rotational distributions further, yet also focus on how prevalent the trapping desorption pathway seen in the molecular dynamics simulations is in the physical experiments. Chapter 9 focuses on the rotational distributions of both the directly scattered component and the trapping desorption component and explores how these are measured independently as a function of their arrival position on the detector (region of interest) and hence their kinetic energy. The ability to record

rotational distributions as a function of kinetic energy and what mechanism was followed is a major advantage of VMI compared with other detection methods, where the entire signal intensity is recorded by the MCP and integrated.

9. Velocity-selected Rotational State Distributions of Nitric Oxide Scattered off Graphene Revealed by Surface- Velocity Map Imaging

Thomas Greenwood,*¹ Huda AlSalem,² Sven P. K. Koehler^{1,3}

¹ Department of Natural Sciences, Manchester Metropolitan University, M1 5GD, UK

² Department of Chemistry, College of Science, Princess Nourah bint Abdulrahman University, P.O. Box 84428, Riyadh 11671, Saudi Arabia

³ Hochschule Hannover, Institut für Verfahrenstechnik, Energietechnik und Klimaschutz, Ricklinger Stadtweg 120, 30459 Hannover, Germany.

*Corresponding author.

Email: sven.koehler@hs-hannover.de

Hochschule Hannover

Institut für Verfahrenstechnik, Energietechnik und Klimaschutz

Ricklinger Stadtweg 120

30459 Hannover

Germany

T. Greenwood, H. AlSalem, S. Koehler, *J. Phys. Chem. A*, 2023, **127**, 1124–1129

9.1. Abstract

We report velocity-dependent internal energy distributions of nitric oxide molecules, NO, scattered off graphene supported on gold to further explore the dynamics of the collision process between NO radicals and graphene. These experiments were performed by directing a molecular beam of NO onto graphene in a surface-velocity map imaging setup, which allowed us to record internal energy distributions of the NO radicals as a function of their velocity. We do not observe bond formation, but 1) major contributions from direct inelastic scattering, and 2) a smaller trapping-desorption component where some physisorbed NO molecules have residence times on the order of microseconds. This is in agreement with our classical molecular dynamics simulations which also observe a small proportion of two- and multi-bounce collisions events, but likewise a small proportion of NO radicals trapped at the surface for the entire length of the molecular dynamics simulations (a few picoseconds). Despite a collision energy of 0.31 eV, which would be sufficient to populate NO($v=1$), we do not detect vibrationally excited nitric oxide.

Keywords: graphene, scattering, state-selective, rotational distributions, surface scattering, REMPI, nitric oxide

9.2. Introduction

Internal state distributions of radicals after reactions, where reactions include both chemical reactions and pure collision processes, allow us a glimpse of the detailed dynamics of such processes.^{54,100} This is because knowing the degrees of freedom into which some of the available energy is channelled enables us to learn about the flow of energy during the entire reaction, and to draw conclusions from that information with regards to the actual dynamics of the process.¹⁰¹ Most famously, the Polanyi rules – broadly speaking – allow us to determine the position of the transition state of a chemical reaction along the reaction coordinate based on the vibrational state distribution of the products.¹⁰² Equally, the rotational state distributions can yield information about e.g. the geometry of a transition state,^{103,104} and phenomena such as *rainbow scattering* can provide insight into oscillatory behaviour during reactions.^{105, 63}

One of the collision processes that has garnered much attention in the past few years is between atoms or molecules and graphene, i.e. the scattering off a graphene surface. The modification of graphene by chemical reactions on its surface to form covalent bonds is technologically important as such functionalizations can introduce a tuneable band gap (pristine graphene is a zero band gap material),^{36, 37} and scattering studies of graphene can reveal the fundamentals of the collision process and the potential bond-formation process on the graphene surface. While much of the experimental and computational work focussed on translational energy and angular distributions of the scattered particles (the only possible degree of freedom for *atomic* collisions),^{39,42,41,68, 59, 38} Juaristi and co-workers, Rutigliano and Pirani,^{62, 106} and Hase and co-workers⁶¹ also explored the rotational state distribution of O₂ and N₂ scattered off **graphite**. Hase and co-workers found that only a small fraction of the available energy is channelled into

rotations, but none into vibrations. Our group has previously investigated the translational energy distribution of NO after scattering off graphene supported on gold, and detected a significant loss of ~80% of the molecules' kinetic energy and a surprisingly narrow angular distribution.⁹³ In addition to this, we can also learn from state-resolved scattering studies off graphite.^{63, 21} Walther and co-workers found that cold surfaces could lead to a cooling of the rotational temperature of the NO radicals in a rotationally hot molecular beam after collision with the graphite,⁸² however, a cold molecular beam of NO tends to result in a hotter rotational temperature for those NO radicals that are quasi-specularly scattered, and an even hotter rotational distribution close to the surface temperature for the diffusely scattered NO molecules, i.e. the trapping-desorption component.⁸³ Higher surface temperatures lead to hotter rotational temperatures of the specularly scattered NO.⁶⁶ The same group found that at cryogenic graphite temperatures, the rotational temperature of the scattered NO is almost constant, and concluded that the formation of a short-lived collision complex which unimolecularly decomposes is responsible for this almost constant rotational distribution.⁶⁴ Nyman *et al.* also found a rotational temperature of the NO after collision with graphite colder than the surface temperature (rotational cooling) in their modelling studies, and even rotational rainbows at higher surface temperatures.⁶⁵

We hence set out to record rotational state distributions of nitric oxide radicals after collisions with graphene in our surface-velocity map imaging (VMI) setup.^{13, 32} VMI - typically applied to gas-phase dynamics - has recently been applied more and more to study surface dynamics,^{27,29,70,31,33} allowing one to derive speed and angular distributions of the scattered products. A resonance-enhance multi-photon ionization (REMPI) scheme is frequently applied in VMI studies, guaranteeing state-selectivity. The

beauty of combining VMI with REMPI in these surface scattering studies here is due to the fact that while REMPI spectra traditionally integrate over the entire ion yield, we can now define regions of interest (ROI) in the VM images (which record the velocity information) and only sum over the ion yield in those ROIs, corresponding in our case to NO radicals flying with a certain speed in a certain direction.¹⁰⁷ Since we measured the velocity distributions of NO after scattering off graphene already,⁹³ we now investigate the rotational state distributions of the various components that make up the scattered cloud (i.e. inelastically scattered and trapping-desorbed NO) in *the same* experiment to derive information about the collision dynamics of NO radicals with graphene.

9.3. Methodology

Our surface-VMI apparatus has been described previously, but specifics to the measurement of velocity-selected rotational state distributions are briefly described here.⁹³ The skimmed (Beam Dynamics, 0.5 mm) molecular beam of ~2% NO in He (a General Valve Series 9 valve is used; the FWHM of the kinetic energy distribution is ~0.08 eV, see Figure 30) is expanded into the main chamber housing the graphene surface (at room temperature) at a base pressure of 5×10^{-9} Torr, increasing to 3×10^{-8} Torr when the beam is on. The NO molecules fly towards the graphene along the surface normal, and are intersected by the REMPI laser at right angle in the center of the VMI chamber twice, both on the way towards the surface as well as after the scattering event. Nitric oxide molecules are ionized in a (1+1) REMPI scheme (via the $A^2\Sigma$ state) using the frequency-doubled output of a Radiant Dyes NarrowScan laser running on Coumarin 450, yielding pulse energies of ~0.8 mJ at around 227 nm with a resolution of around 0.08 cm^{-1} . The doubled dye laser output is unfocussed due to the ease with

which NO can be ionized. The ionized NO particles are then accelerated towards the position-sensitive detector (in a direction normal to the plane spanned by the molecular beam and the laser, see Figure 32) where the images are recorded by a NET GmbH CMOS camera. The time at which the laser fires in relation to the opening of the molecular beam is adjusted via an SRS DG645 delay generator, this adjustment of the timing is necessary to select for events in the scattering process which are separated in time such as 1) the molecular beam on the way down to the surface or 2) once it has scattered which is usually 100-300 μs later. Due to the opening time of the molecular beam ($\sim 300 \mu\text{s}$), the signal on the detector can be a combination of molecular beam and scattered molecules, but crucially, NO molecules in the molecular beam (which are flying 'downwards' in the lab frame) appear in the lower half of the velocity-mapped image, i.e. below our zero velocity pixel, while scattered NO molecules with an upward velocity component in our laboratory frame appear in the upper half of the detector. We can thus not only differentiate the various components of the beam and the scattering event by varying the delay time between the molecular beam and the REMPI laser, but in a much better way by observing certain ROIs on the detector. We hence extract rotational distributions of scattered NO molecules for 1) a fast and narrow spot presumably due to direct inelastic scattering and 2) a much weaker component likely due to trapping-desorption which appears as a broad and slower diffuse cloud in the images, and we thus integrate over the ion signals on the imaging detector for the various components separately by concentrating on the ROI relevant to each component.

The accompanying classical molecular dynamics simulations have been described previously.¹⁰⁸ The gold substrate was formed of a $6 \times 6 \times 6$ array of gold atoms, and 98 carbon atoms were positioned in a hexagonal 2D network in the x-y plane on top of the gold substrate. Periodic boundary conditions were applied along the x-y plane, but with

no periodicity in the z dimension. We stress that these are purely classical calculations which do not account for the quantum behaviour of molecular motions.

9.4. Results and Discussion

Before delving into the rotational spectra, we first briefly discuss the various NO species we investigated. As discussed in the Methodology section, the various rotational spectra were collected by integrating the ion signal only over certain ROI on the detector, these regions are shown in Figure 27, which itself is a composite image consisting of individual images recorded at different delay times between the molecular beam and the REMPI laser, purely for the benefit of highlighting the different components.

One can observe the signal from the molecular beam itself (within the blue rectangle in Figure 27), the directly scattered component (red), and a slow (but crucially upward in the lab frame, pink) component. This slower component, which we assign to a trapping-desorbing mechanism, is much weaker than the scattered component, and we in fact failed to observe it in our previous work.⁹³ While it appears as if some components may overlap in the images, most notably the signal for the direct inelastic scattering and the slower trapping component, varying the delay time between the molecular beam and the REMPI laser allows us to separate the integrated signals. Relative to the molecular beam itself, which was recorded at its peak in the time-of-flight profile, the directly scattered NO signal was recorded 100 μs after the molecular beam in order to image the 'same' NO molecules that were imaged in the beam initially, and the trapping-desorption component was recorded a further 300 μs after the directly scattered NO.

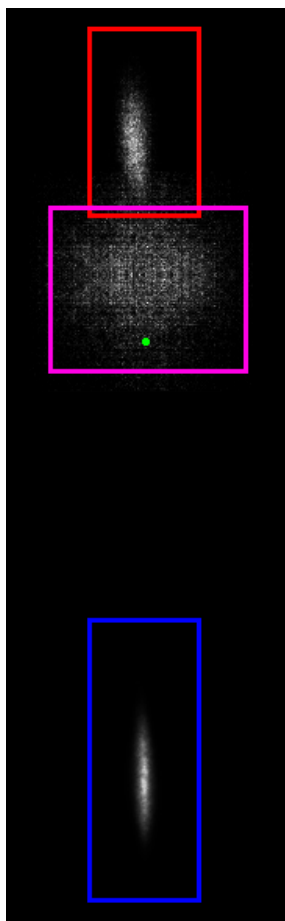


Figure 27 – The images of the various NO components along with their respective regions of interest. Blue for NO in the molecular beam at a relative time (t_{rel}) of 0 μ s, red for scattered NO ($t_{rel} + 100 \mu$ s), pink for the trapping component ($t_{rel} + 400 \mu$ s) and the green dot indicating our center spot relating to zero overall velocity in the x and y dimensions.

The trapping-desorption component is rather wide such that not all ions detected follow true VMI conditions, and due to the long image acquisition time, noise and background ions are appearing.

Table 8 shows the average velocities of those events; not shown in the table is the thermal gas-phase background NO (see section 4 of the SI), which has been discussed previously,⁹³ but briefly: Nitric oxide gas was admitted into the chamber through a leak valve at a temperature of 298 K. Imaging those thermal background molecules yields a 2-dimensional Maxwell-Boltzmann distribution on the detector whose center is taken to be the zero-velocity center of our actual images, i.e. the green dot in Figure 27. A composite image of all components including the thermal background spot is shown in Figure 36 in the SI, highlighting the difference in position between the thermal

background image and the trapping-desorption components. The three components (molecular beam, direct scatter, trapping desorption) were velocity-analysed separately and with respect to the center spot of zero velocity using a conversion factor of $5.1 \text{ m s}^{-1} / \text{pixel}$, fitted to equation 19

$$F(c)dc = A c^3 \exp \frac{-(c - c_0)^2}{\alpha^2} dc \quad (19)$$

where A is a scaling factor and α is related to the width of the distribution,⁷⁷ and errors are standard errors.

The average translational energy of the Maxwell-Boltzmann distribution of particles originating from a flat surface is $2kT$ (equivalent to $\sim 575 \text{ m s}^{-1}$ for nitric oxide desorbing from a 298 K surface), thus the directly scattered component is despite the large energy loss noticeable faster, while the trapping-desorption component is slower.

Table 8 – The various NO species detected in our experiment with their respective speeds at peak delay times. The beam is naturally travelling in opposite direction to the scatter and trapping-desorption components.

<i>Event</i>	<i>Beam</i>	<i>Scatter</i>	<i>Trapping-Desorption</i>
$v / \text{m s}^{-1}$	1428 ± 114	638 ± 108	184 ± 161

Rotationally-resolved REMPI spectra were recorded by scanning the laser over the desired wavelength range (at the appropriate delay time) while using the MCP detector in imaging mode, and by integrating the ion signal in each of the three ROIs separately for each wavelength. The resulting spectra are then converted to rotational state populations using a relative calibration scheme by means of comparison with a thermal

background spectrum in LIFBase as a reference.¹⁰⁹ Only the O₁₂ and P₁₂ branches were recorded to avoid overlapping lines, as in particular the first 20 transitions of the O₁₂ branch do not overlap with any other lines. A raw REMPI spectrum of scattered NO is shown in Figure 28, and a composite of a scattered, thermal background and LIFBase simulation spectra are shown in Figure 37 in the SI.

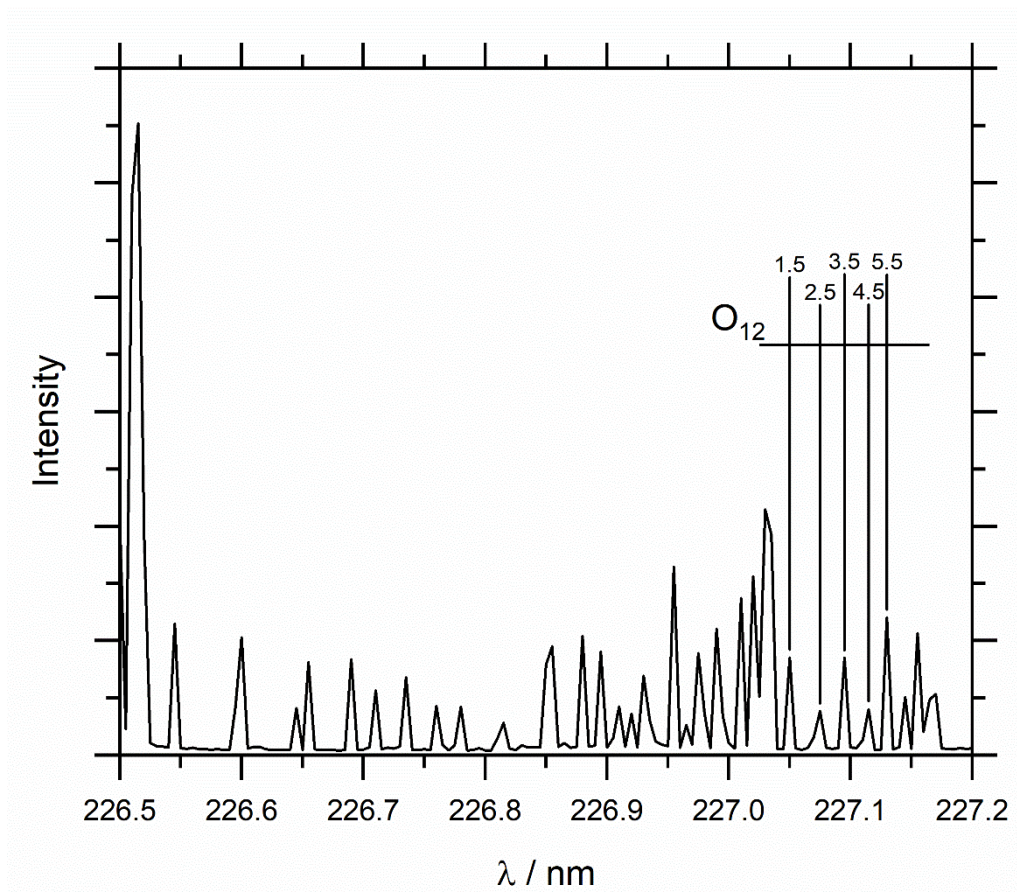


Figure 28 – Rotational spectrum of the scattered NO with the relevant lines of the O₁₂ branch highlighted.

Once the populations of the rotational energy levels were assigned, Boltzmann plots were created for each branch. An example plot from the O₁₂ branch of the scattered NO and the P₁₂ branch of the trapping desorption component are shown in Figure 29. Equation 20 shows how the population of rotational levels can be related to the rotational temperature,

$$P = (2J + 1) \exp\left(\frac{-E_{rot}}{K_b T}\right) \quad (20)$$

by rearranging this equation, one can plot $\ln\left(\frac{P}{2J+1}\right)$ against E_{Rot} to give a line with a gradient of $-1/K_b T$ and thus calculate the rotational temperature of a given component.

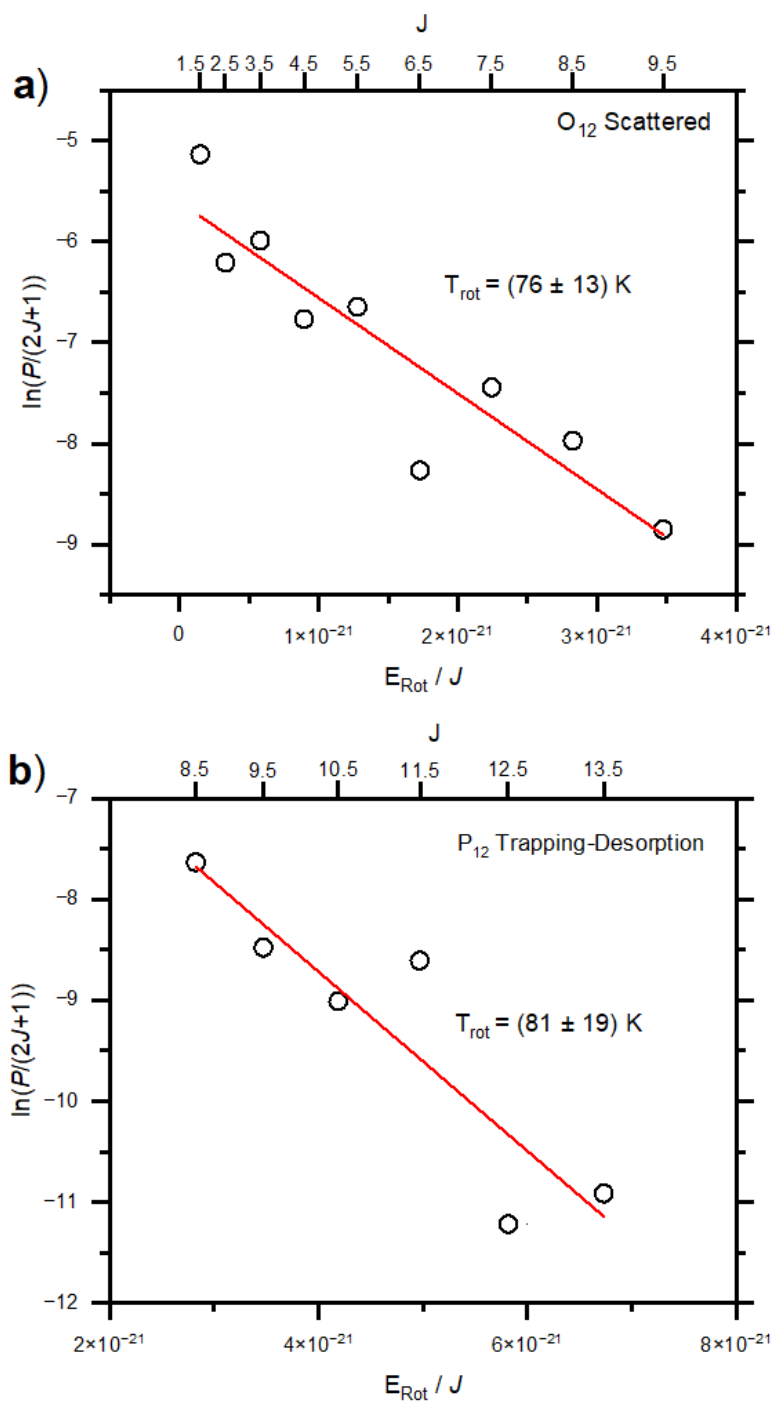


Figure 29 – a) Boltzmann plot of O₁₂ branch of the scattered NO, b) P₁₂ branch of the trapping desorption component, where the gradient can be used to calculate the rotational temperature, as described above.

Rotational temperatures for each component were derived from the gradients of these Boltzmann plots. While there is no reason for either rotational distribution here to follow a Boltzmann distribution, the assignment of a single rotational temperature eases

comparison between the components. The temperatures of the various NO components are shown in Table 9.

Table 9 - Rotational temperatures of the various NO events derived from the linear fits to the Boltzmann plots in Figure 29, errors are standard errors.

<i>Event</i>	<i>Beam</i>	<i>Scatter</i>	<i>Trapping- Desorption</i>
$T_{\text{rot}} / \text{K}$	64 ± 11	76 ± 11	81 ± 19

As is clear from the velocities derived from the images and now the rotational temperatures, there are two channels from the scattering of NO, the directly scattered component and a trapping-desorption component. While the errors of the rotational temperatures overlap between components, the results still clearly show a trend that the rotational temperature increases from the NO in the molecular beam to the directly scattered NO and then to the trapping desorption component. The directly scattered component is likely only undergoing a single collision with the surface and expectedly does not gain much rotational energy. However, even the trapping-desorption component – despite losing a significant amount of translational energy – does not gain much more rotational energy as compared to the directly scattered component. It appears as if the NO molecules transfer much of their translational energy to the graphene substrate in just a few collisions, but it is possible that only those with a cold(er) rotational temperature are scattered back, while those that are (partly) thermalizing may become trapped, leading to the relatively cold rotational state distribution of the trapping-desorption component. Our previous MD simulations for NO

scattering off graphene can shed some light onto that,¹⁰⁸ though they do not compare quantitatively, and do *not* reproduce the two well-separated scattered components observed here (directly scattered and trapping-desorption). In the simulations, the majority of NO scatters off graphene directly, undergoing only a single collision, but there is a small fraction of NO molecules that interact with the surface for only a couple of picoseconds before desorbing again (though these do not show up as a separate component in our time-of-flight profiles), presumably undergoing too few collisions to rotationally thermalize.

Directly scattered and diffuse spots for scattered NO have also been recorded after interactions with graphite.⁸³ A slower diffuse component was observed which was likely to be due to temporary, i.e. non-equilibrium trapping, similar to our experimental results.

This behaviour of incomplete thermalization of NO has also been identified before in the scattering off graphite,^{66, 110} where NO only accommodates to the surface temperature up to 170 K, above which the surface temperature and the rotational temperature deviate. However, a direct comparison to our experiments is not entirely justified due to the different properties of graphene vs. graphite, of course, but mainly due to the different incidence angles.

A further notable difference, however, is that the rotational temperature of both components in our study here on graphene are rotationally cooler than previous studies of scattering of NO off graphite at around room temperature, and our values align better with those rotational temperatures measured at graphite temperatures of around 80 K as reported by Häger et al.⁶⁴ In the case of NO scattered off graphite at 80 K, the resulting rotational temperatures were 88 and 90 K for the directly scattered and trapped NO,

respectively, similar to our results, though our experiments were performed at a surface temperature of 298 K; however, incidence angles are not the same in these two studies. It is worth highlighting, though, the fact that in the studies by Häger et al. as well as in our studies here, the rotational temperatures of the two components do not differ much.

While experimental studies of NO scattering off e.g. silver have led to rotational rainbows,⁵⁵ and we have found evidence for those in our MD simulations, no rotational rainbows were observed in this experimental study here nor in other experimental studies of NO on graphite.⁶⁵

9.5. Conclusions

A molecular beam of nitric oxide molecules was scattered off graphene supported on gold, and the velocities and internal energy distributions of the scattered NO molecules were probed using a surface-velocity map imaging set-up. No bond formation was observed at the graphene surface, and despite sufficient collision energies of 0.31 eV, no vibrationally excited NO molecules were observed. Two components of scattered NO were observed, namely 1) a directly scattered component and 2) a trapping desorption component which had lost a significant proportion of its initial translational energy. This compares at least qualitatively with our previous MD simulations in which most NO molecules collide with the graphene surface only once, but a small fraction undergoes multiple collisions, though in our MD work, this latter component could not be separated clearly from the direct component based on time-of-flight profiles.

Both the direct and the trapping desorption component gain some rotational energy but are remarkably similar in their rotational temperatures, with the trapping desorption

component only marginally hotter, but far away from having reached thermal equilibrium with the surface.

This fairly unusual behaviour appears typical for graphene with its perfectly flat structure, but since we were limited to incidence angles along the surface normal and room temperature surfaces in these studies, we intend to perform further studies to shed light onto this behaviour in graphene scattering.

9.6. Supporting Information

The Supporting Information is available free of charge and provides further details on: Experimental Setup, Raw data, Molecular Beam characterisation, Calibration of VMI Setup and Beam positions, and the Spectroscopy of Nitric Oxide.

9.7. Acknowledgements:

We thank the Royal Society for funding (IEC\R2\181028), and Princess Nourah bint Abdulrahman University Researchers Supporting Project number (PNURSP2022R185), Princess Nourah bint Abdulrahman University, Riyadh, Saudi Arabia. We also thank Prof Nick Lockyer and Prof Mark Dickinson at The University of Manchester for the loan of a frequency-tripling unit.

9.8. Supporting Information

9.8.1. Energy Spread of Molecular Beam

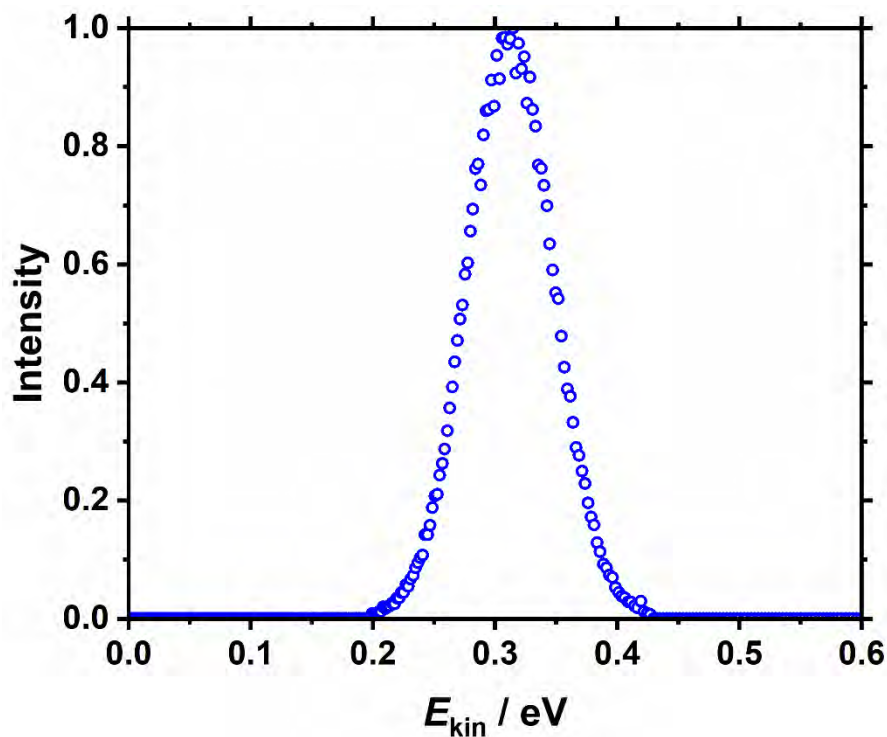


Figure 30 - Kinetic energy distribution of the incoming beam of 2% nitric oxide, NO, in He.

9.8.2. Overall time-of-flight distributions

The time-of-flight distributions recorded as a signal on the oscilloscope integrating over all regions of the detector (in black), and the same distributions but recorded for different regions of interest showing the molecular beam (red), the directly scattered component (blue), and the trapping-desorption component (green).

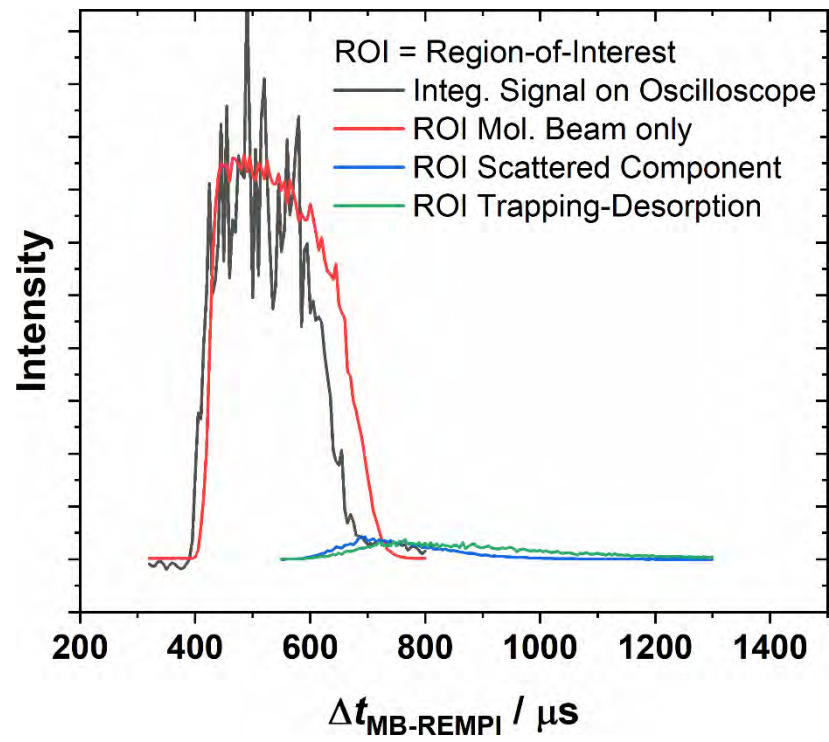


Figure 31 - Overall time-of-flight distribution measured on the scope (in black) and distributions measured using Regions of Interest (ROI)

At a repetition rate of 10 Hz and hence a duty cycle of 100 ms or 100,000 μs , one can see that the scattered signal all but disappears around 1300 μs after the molecular beam fires, and contributions to our signal from background NO is negligible.

9.8.3. Experimental Setup

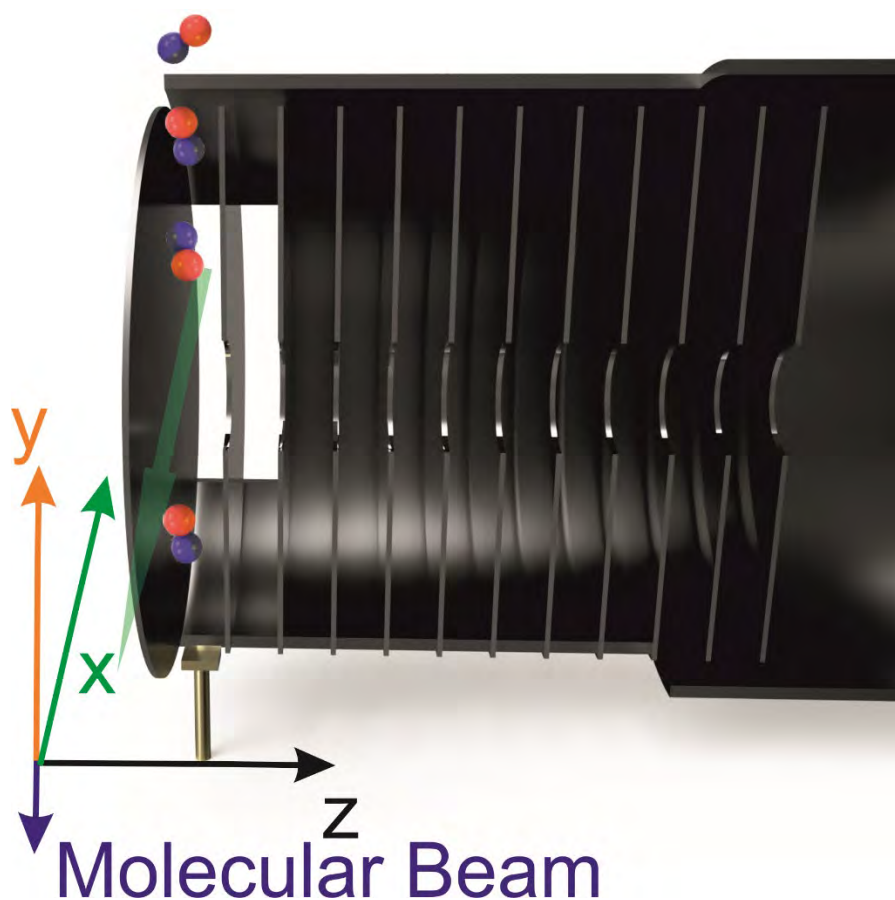


Figure 32 - Relative orientation of the laser (x , into the plane of the paper), the molecular beam (y , downwards), and the time-of-flight direction towards the multi-channel plate detector (z).

The molecular beam is created using a General Valve Series 9 valve with an opening time of around $300 \mu\text{s}$. The expansion passes through a skimmer (Beam Dynamics, 0.5 mm) placed 30 mm away from the valve. The graphene surface is mounted 320 mm away from the valve such that a beam of ca. 5.5 mm diameter is impinging on the graphene surface.

The sample holder is a simple stainless-steel cylinder of 5 mm diameter on which the graphene sample rests. The sample consists of a $10 \times 10 \text{ mm}^2$ quartz wafer covered with a thin layer of evaporated gold on to which the graphene adheres (after having been transferred using PMMA). The dimensions of the graphene are barely smaller than the

wafer itself, hence the 5.5 mm diameter molecular beam impinges mostly on graphene indeed.

The ~227 nm laser beam is unfocused and around 7 mm in diameter, though can be cut down using an iris. Due to the equal ionisation efficiency along the laser path (unfocused beam), we can ionise any NO molecule within the laser beam, but only those within 10 mm either side of the center axis will be able to be accelerated to the detector, allowing a detection angle of 23°.

We have previously shown that VMI conditions prevail in our spectrometer up to 6-7 mm either side of the centre axis,¹⁵ i.e. we have a small proportion of NO molecules here that are not focused truly under VMI conditions, but only the small fraction further away from the surface normal.

9.8.4. Calibration

Figure 33 shows an image of thermal nitric oxide at 298 K let into the chamber through a leak valve at 1×10^{-7} Torr. The same image is shown in 3D as Figure 34, left image. A fit of this thermal background image to a 2-dimensional Maxwell-Boltzmann distribution is shown on the right of Figure 34, and allows us to determine the zero velocity pixel on our detector shown as a green dot in Figure 33.

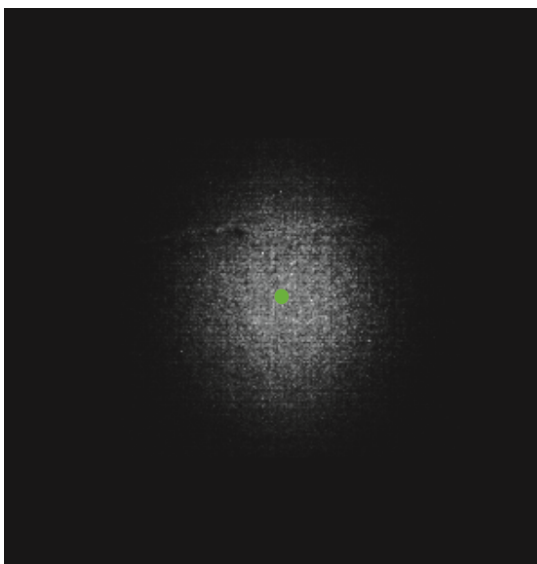


Figure 33 - Thermal background image of nitric oxide at 298 K with zero velocity spot indicated.

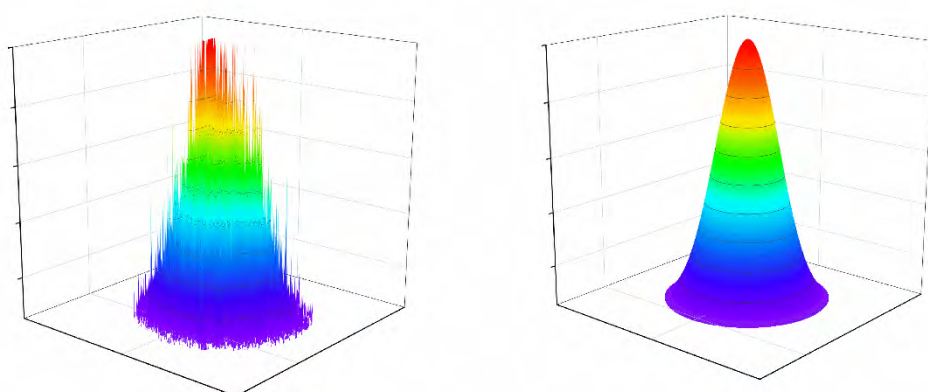


Figure 34 - Raw thermal background image of nitric oxide let into the vacuum chamber through leak valve at 1×10^{-7} Torr (left), and fit of a 2-dimensional Maxwell-Boltzmann distribution to the thermal background spot (right) to determine zero velocity pixel shown in green in Figure S4.

9.8.5. Nitric Oxide Energy Level Diagram

Figure 35 shows an energy level diagram of nitric oxide for the vibrational ground states of the electronic ground states $X^2\Pi_{1/2}$ and $X^2\Pi_{3/2}$, and the first excited $A^2\Sigma^+$ state, including one of the probed lines, namely the $O_{12}(3.5)$ transition, where $\Delta J = -2$ and the transition originates in $J'' = 3.5$, from the upper of the two ground states ($X^2\Pi_{3/2}$) to the lower of the $J' = 1.5$ states, i.e. $N' = 1$, not $N' = 2$.

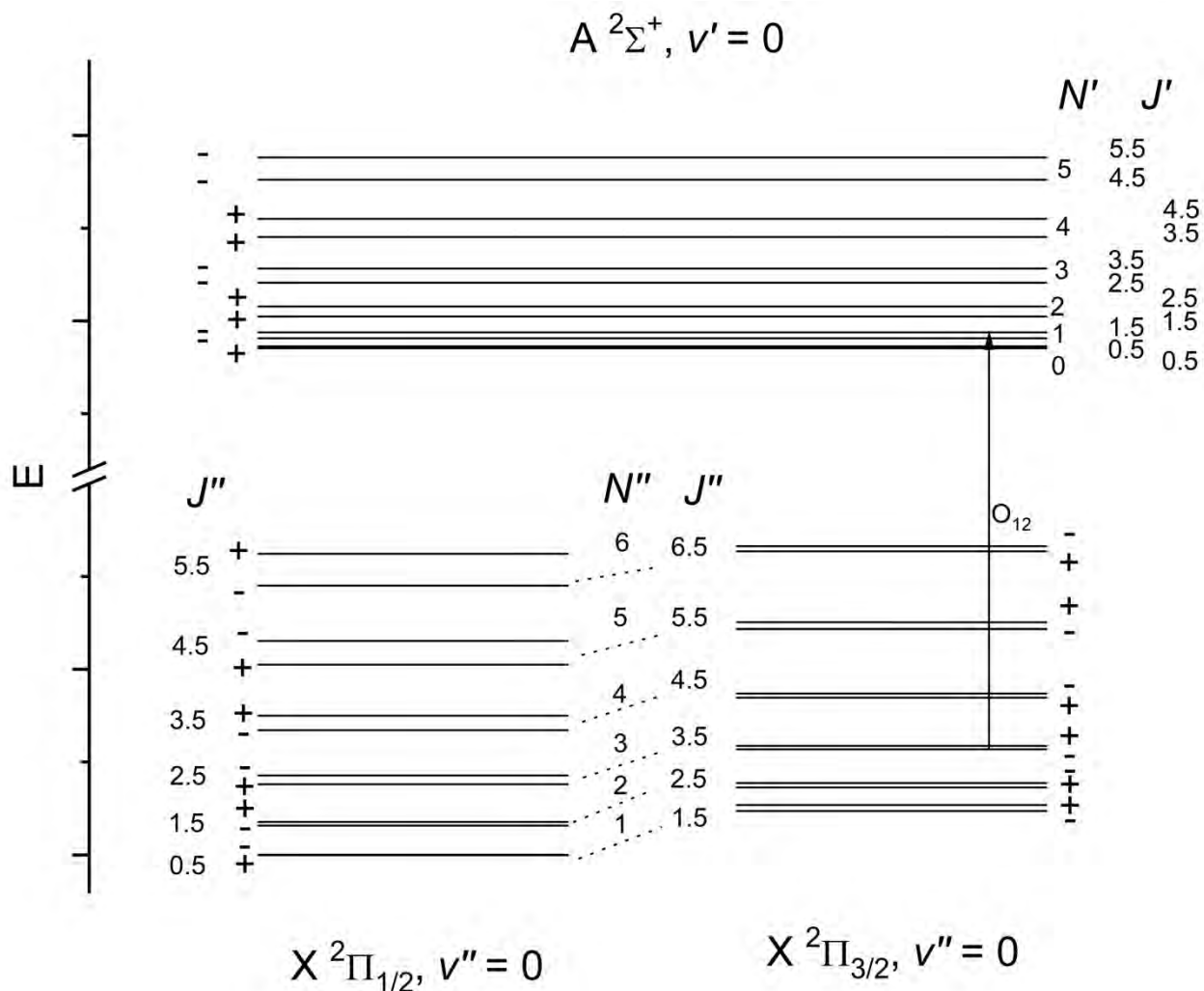


Figure 35 - Energy level diagram of nitric oxide including the probed O₁₂(3.5) line.

9.8.6. Image Positions of Molecular Beam, Direct Scatter and Trapping-Desorption Component in Relation to the Thermal Background Image

Figure 36 shows a composite image showing the positions of the molecular beam, directly scattered image and trapping-desorption component in relation to the thermal background image (in red). We note that the images were recorded at different delay times between the molecular beam and the REMPI laser (or even under different conditions in the case of the red background image), such that we can differentiate the

components both by their timing (through some components overlap) as well as by their position on the detector. While the camera might move in the horizontal plane slightly, its vertical alignment is far more robust, and the trapping-desorption spot can always be seen to have an overall upward velocity component. Furthermore, the trapping-desorption spot decreases in intensity as a function of time.

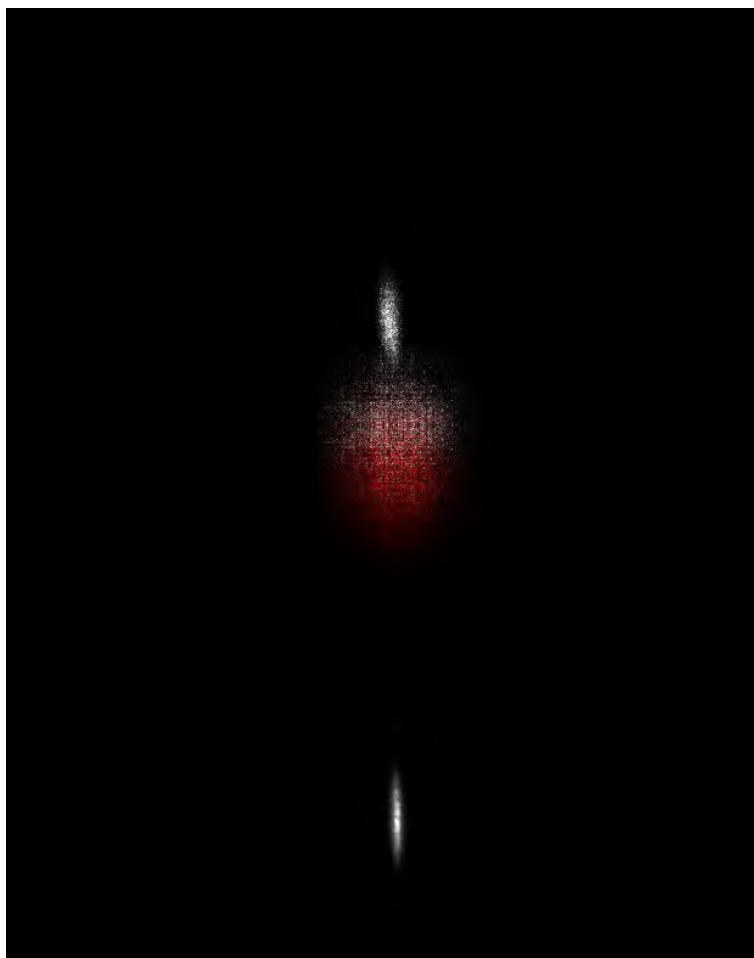


Figure 36 - Composite image of the molecular beam (white bottom), directly scattered (white top) and trapping-desorption component (fuzzy white in the middle) in relation to the thermal background image in red.

9.8.7. Rotational Spectra

Figure 37 shows a rotational spectrum of the scattered NO (at the fundamental of the laser, not the doubled), a rotational spectrum of the thermal background NO, and a LIFBase simulation of 298 K thermal NO, demonstrating the cold rotational temperature of the scattered component. The latter two are not identical due to e.g. saturation effects, where the detector becomes saturated with signal and therefore does not produce a linear response.¹¹¹

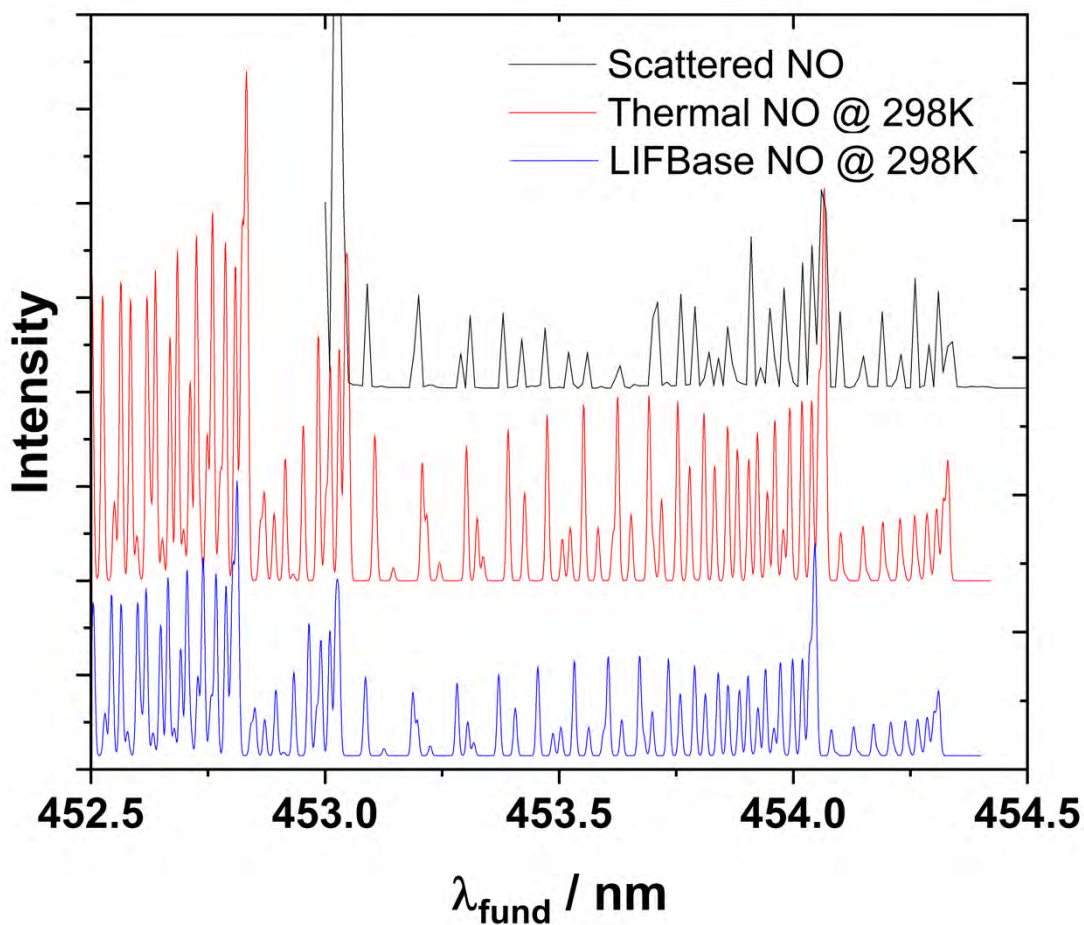


Figure 37 - Rotational spectra of scattered NO (black), thermal background NO (red), and a LIFBase simulation of 298 K (blue). The LIFBase spectrum was shifted by 0.2 nm to coincide with the experimental spectra as the laser wavelength was not calibrated.

10. Probing the Loss of Kinetic energy of the Nitric Oxide as a Function of the Initial Kinetic Energy, and Estimation of Residence Times

The molecular dynamics simulations discussed earlier in this thesis have demonstrated how the incoming velocity of the NO can affect both the velocity and rotational distributions of the scattered NO, while the velocity of the NO in the molecular beam of the experiments has remained constant. While the experiments so far involve a molecular beam with a carrier gas of just helium (i.e. constant velocity), the initial translational energy of the beam is now varied by altering the composition of gases in the molecular beam. Chapter 11 investigates how adding argon into the molecular beam seed gas, thus reducing the incoming velocity, affects the velocity distribution of the directly scattered NO.

While collisions resulting in directly scattered components provide insights into both a surface and the species under investigation, it is of great interest whether species remain on the surface for a significant amount of time. The investigations discussed thus far demonstrate that there are two pathways for the NO scattering off the graphene, directly scattered and trapping desorption. Utilising the newly developed regions of interest from Chapter 9, the time of flight profiles of the beam and two upwards components were recorded as a function of their velocity. Velocity distributions were also recorded for the three components of NO. A theoretical time of flight trace was

simulated using a Monte-Carlo approach, these simulated TOF traces were compared with those recorded with the detector in the experiments. The difference between the two TOF traces being due to the residence time of NO on the graphene surface. The residence times extracted in these experiments was found to be on the order of the tens to low hundreds of microseconds.

11. Extracting Residence Times of Nitric Oxide on Graphene through combination of Time-of-Flight and Velocity Map Imaging

Thomas Greenwood,^{*a} Sven P. K. Koehler^b

Department of Natural Sciences, Manchester Metropolitan University, Manchester M1
5GD, UK

Institut für Verfahrenstechnik, Energietechnik und Klimaschutz, Hochschule Hannover,
30459 Hannover, Germany.

11.1. Abstract

In this work, energy transfer between nitric oxide radicals and graphene was measured as a function of incidence energy, and residence times of the trapped NO molecules were extracted. This was done by combining Time-of-Flight methods with Surface-Velocity Map Imaging and by forward-simulation of the expected arrival profiles. Combining these two techniques makes it possible to derive residence times even though the employed molecular beams have opening times that would otherwise prevent such measurements if only one of these experimental techniques was used in isolation. We find that significant energy transfer to the graphene occurs, increasing with increasing incidence energy, and that trapped NO may reside on the graphene for tens of microseconds at room temperature.

11.2. Introduction

Scattering events of atoms or molecules on surfaces can broadly be divided into two mechanisms, namely 1) a direct scattering mechanism in which the incoming projectile scatters off the surface elastically or – more frequently - inelastically, and 2) a trapping-desorption mechanism in which the incoming atom or molecule may reside at the surface for some time (the residence time) before desorbing from the surface.¹¹² The molecule may even thermalise at the surface before desorbing, or may become permanently trapped.⁶³

The residence times of the incoming projectiles at a surface have been measured using various techniques, but have probably been more successfully calculated over the past decades, as the measurement of residence times on the order of microseconds or less using (commercial) molecular beams with pulse lengths of tens or hundreds of microseconds poses a variety of challenges.⁶

We have over the last few years applied the technique of surface-velocity map imaging (S-VMI) to the photodesorption^{32, 33, 34} and scattering off surfaces,^{93, 113} and in the latter case realised that the velocity of the incoming and outgoing projectiles can be measured using both, the time-of-flight (TOF) as well as the VMI technique. TOF methods measure the time to travers a known flight path and calculate the speed using $c = s/t$, but if collisions with a surface are involved during that flight, and the molecule is trapped at the surface, the flight time t also includes contributions from the residence time, hence potentially distorting the obtained results towards slower velocities. Since VMI yields the velocity of incoming and scattered molecules directly, the simultaneous measurement of TOF data and VM images can help to extract residence times.

The chemical system to which this S-VMI/TOF combination has been applied is the scattering of nitric oxide, NO, off graphene supported on gold. NO was chosen as a radical which can potentially react with the graphene through its unpaired electron. It is, of course, also straightforwardly detected using resonance enhance multi-photon ionisation (REMPI) spectroscopy,¹¹⁴ and we have previously studied the speed and angular distribution of NO scattered off graphene on gold,^{93, 113} and performed molecular dynamics simulations on the system.¹⁰⁸

Graphene, a 2-dimensional hexagonal arrangement of sp^2 -hybridised carbon atoms, has gained much attention over the past 20 or so years since the discovery of its unusual physical and chemical properties.⁶⁰ Amongst these is e.g. the tunability of its band gap (pristine graphene is actually a zero band gap material) by functionalisation through chemical reactions.^{115, 116} We have in the past modified graphene attaching phenyl groups or hydrogen atom;^{36, 37} the latter also has the potential as a light-weight solid hydrogen storage medium.¹¹⁷ A first step towards understanding such chemical reactions on graphene are scattering studies which can reveal the fundamentals of the collision process and the potential bond-formation process on graphene.

There are only a handful of groups who have studied the scattering dynamics of projectiles off graphene, graphite or HOPG, e.g. through modelling by Hase and co-workers (N₂ with graphite, detecting mainly single scattering events with much of the energy lost to the graphite lattice), by Nieman *et al.* and Jayee *et al.* for N(⁴S) and O(³P) atoms off graphene (at high collision energies relevant to the re-entry of spacecrafts), by Juaristi and co-workers (O₂ scattered off HPOG), and experimentally by Minton and co-workers (N₂ off HOPG).^{61,42,41,62,39} More recently, Jackson and Beck combined

quantum-mechanical calculations with elegant state-to-state scattering experiments of CH₄ on Nickel surfaces, and Ni surfaces passivated by graphene.¹¹⁸

It may be important to note here that graphene, a single layer of carbon atoms held together by covalent bonds, is only loosely bound to the substrate (typically a metal such as e.g. copper, gold, or iridium) with distances between 3 Å and 4 Å, and hence has potential to undergo reactive collisions with the incoming projectile, though graphite and HOPG can also be thought of as a single layer of graphene held to graphite with similar interlayer distances, and could therefore be equally susceptible to chemical reactions.

The work by Wodtke and co-workers serves as a benchmark for atomic scattering off graphene.³⁸ Short H-atom pulses were directed onto graphene, and a combination of experimental and theoretical analysis revealed temporary bond formation between the H atoms and graphene.

The large body of state-resolved NO scattering studies off graphite from the 1980s broadly found that 1) isotropic scattering dominates at lower surface temperatures caused by trapping desorption, whereas 2) specular scattering dominates at higher temperatures.^{21, 66, 83, 110, 65} At our 0° incidence angle experiments at room temperature, we find narrow angular distributions, significant energy loss,⁹³ and a weak trapping desorption mechanism, and since these scattering dynamics are established, though interestingly not always in agreement with the earlier graphite studies (the much narrower angular distributions from graphene is highlighted here), this paper describes the effect of incidence energy on energy transfer and the estimation of residence times through the combination of TOF and S-VMI measurements.

11.3. Experimental

The experimental set-up has been described previously,^{93, 113} but is briefly summarised here, with the most important aspects highlighted, see also Figure 38. Molecular beams with three different velocities were prepared in these experiment by expanding 1) a 2% mixture of NO in He, 2) a mixture of 4% NO, 20% Ar and 76% He, and 3) 4% NO with 50% Ar and 46% He, to investigate the influence of incident energy on energy loss to the graphene lattice. The respective molecular beam is expanded through a General Valve nozzle and skimmed via a Beam Dynamics 0.5 mm skimmer before entering the differentially-pumped surface chamber (base pressure of 5×10^{-9} Torr) housing the graphene sample supported on gold. The graphene sample was CVD grown on copper and transferred onto gold prior to insertion into the vacuum chamber. The NO molecules fly along the surface normal (the y dimension in Figure 38 a, downwards in the lab frame) towards the graphene surface where they are scattered back up along the y axis, while being intersected, both on approach of the surface as well as after being scattered, by an unfocused laser beam (~ 225 nm at ~ 0.8 mJ per pulse) perpendicular to the surface normal (along x in Figure 38 a) and 5.5 cm above the graphene using a Radiant Dyes NarrowScan laser.

The NO is ionised in a 1+1 REMPI scheme and the cations subsequently accelerated by the VMI optics towards an MCP/Phosphor screen detector. The signal on the MCP is either recorded as the overall signal, or alternatively the fluorescence on the phosphor screen is imaged by a triggered Net GmbH CMOS camera. The experiment as a whole is triggered at 10 Hz using an SRS DG645 delay generator. This allows for the timing to be altered between the beam opening and the laser, which can coarsely help to distinguish e.g. the initial molecular beam from the scattered beam. However, at typical molecular

beam opening times of $\sim 300 \mu\text{s}$ and round-trip times of the molecular beam from the laser intersection to the graphene surface and the scattered beam back to the laser ($\sim 11 \text{ cm}$) of tens of microseconds, these pure time-of-flight time measurements are error-prone, and the surface-VMI technique plays to its strength: Being able to distinguish the molecular beam (blue in Figure 38) from the directly scattered NO molecules (red) from the trapping-desorption (TD) component (orange) in the composite image of Figure 38 b), one can – by defining regions-of-interest (ROI) for the various components as shown – record time-of-flight profiles for each component separately.

11.4. Results and Discussion

As briefly discussed in the experimental section, three separate components could be distinguished in the composite VM images as shown in Figure 38 b, namely the molecular beam itself (blue rectangle), the directly scattered NO (red) and trapping-desorbed NO in orange.

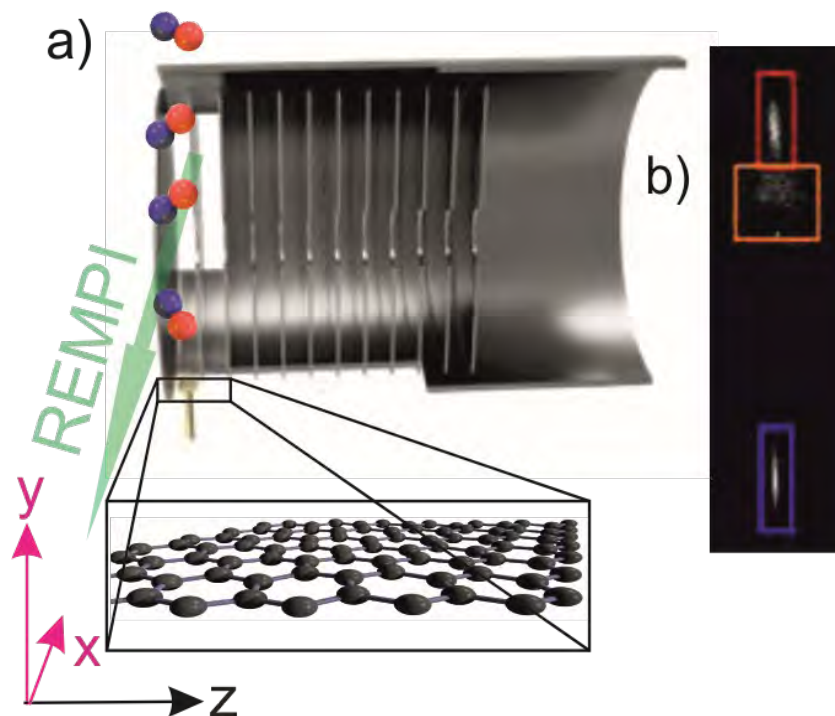


Figure 38: a) Cut through experimental set-up, the molecular beam pointing vertically down along the y dimension towards the graphene surface, the beam and subsequently scattered NO molecules are intersected by the laser in the xz plane. b) Composite image of the components of NO arrival positions with their respective regions of interest. The molecular beam in blue, directly scattered NO in red and trapping desorbed NO in orange, where the green dot represents the spot of zero velocity in the x and y dimensions.

The coloured rectangles show the regions-of-interest (ROI) for each component. The signals integrated over each ROI (i.e. for the three components separately) as a function of delay time between the opening of the molecular beam and the REMPI laser are shown in Figure 39 b)-d) and are significantly more intense for the incoming molecular beam (Figure 39 b) than for the directly scattered component (c) which is again much more intense than that of the trapping desorbed NO (d).

Figure 39 a shows the signal integrated over the entire detector region, which is not only unable to distinguish between the different components, but it can be seen that the signals due to scattering and trapping are so weak that they barely show up above the noise in the tail of the total signal.

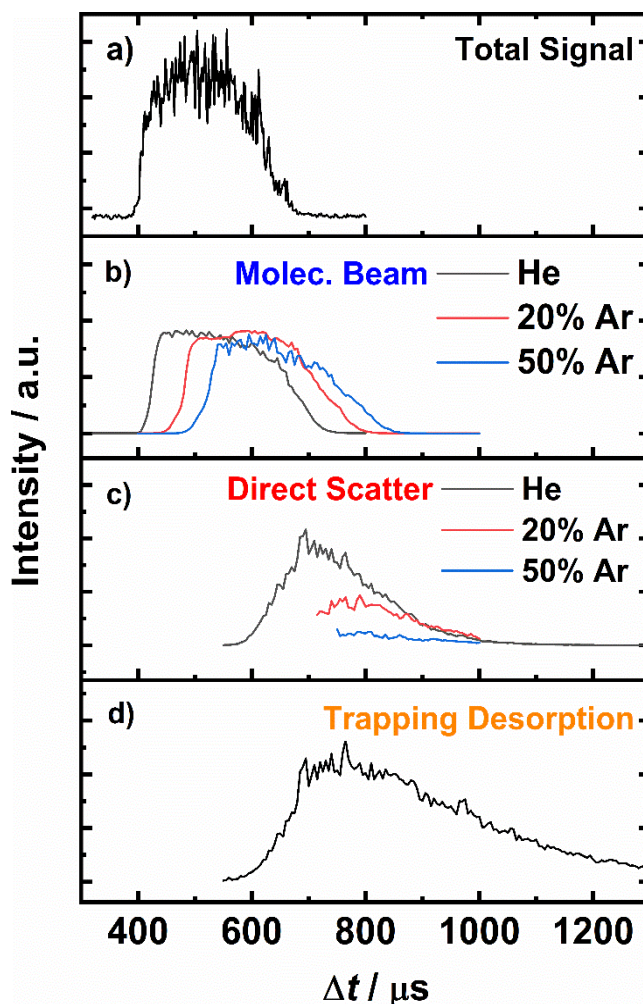


Figure 39: a) Time-of-flight scan of NO extracted directly from the overall detector signal, for a 2% NO mixture in He, consisting of all components. b) TOF scan of NO extracted from ROI relevant to the molecular beam for three NO mixtures. c) TOF scans of directly scattered NO. d) Delay scan of the trapping-desorbed NO for a pure helium mixture. Signal intensities for (a), (b), (c) and (d) not on the same intensity scale.

It can be seen that the onset of the total signal in Figure 39 a) coincides with the onset of the molecular beam signal (b) as expected, and that the scatter (c) and TD component (d) rise 200-300 μs later than the molecular beam due to the round-trip time to the graphene surface and back to the laser detection region. It should be noted that

the rising edge for the two argon mixtures in Figure 39 c has been removed as for the slower beams, the ROIs are closer together, and the much more intense direct scatter quickly saturates, 'spilling' over into the ROI of the trapping desorption component. It should also be noted that the trapping desorption trace, shown in Figure 39 d, was only recorded for the pure helium mixture.

The slower molecular beam velocity of the Ar-heavy mixtures can be observed in Figure 39 b, and this extends to the directly scattered NO molecules, Figure 39 c; the signal of the TD component for the Ar-heavy mixtures was too weak to be detected, Figure 39 d, and the proximity of the trapping desorption signal to the directly scattered NO impedes a meaningful separation.

It is worth noting that the trapping desorption signal is recorded only in a small region of interest above the centre of the VMI zero-velocity spot of the detector and appears on similar timescales to the directly scattered signal (i.e. is not due to background NO), but the TD signal declines over a much longer timescale compared to the directly scattered signal.

While the TOF distributions contains some information about the speed of the incoming and scattered NO molecules, the velocities can of course be directly established from the VM images such as those shown in Figure 38 b.

By recoding images of e.g., the molecular beam at different delay times (to capture all contributions to the molecular beam, as the velocity distribution is different at different delay times while the molecular nozzle is open) and weighing them appropriately according to their intensity at a given delay time, speed distributions such as the ones in Figure 40 a for the three different beams can be derived.

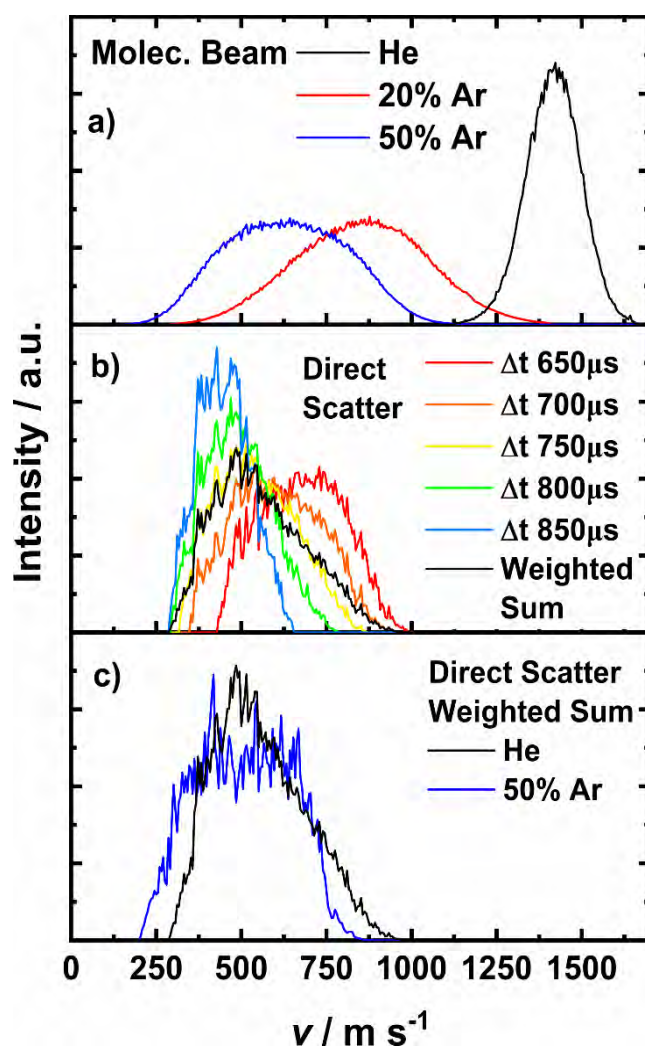


Figure 40: a) Velocity distributions of NO in the molecular beam extracted from VMI images for NO in the pure helium beam, 20% argon and 50% argon. b) Velocity distributions of directly scattered NO in the pure helium beam, where the scattered signal consists of a normalised composite image over a range of delay times with respect to the laser firing and molecular beam opening. c) The scattered NO velocities in the pure helium beam and 50% argon mixture over a range of delays.

Figure 40 b shows the contributions of the directly scattered NO molecules at different delay times and the weighted sum of these components. The chosen delay times become apparent when comparing with the TOF trace in Figure 39 c.

The weighted sum in black is again shown in Figure 40 c in comparison with the same (normalised) result for the slowest (50% Ar) beam. While there is some memory of the velocity of the incoming molecular beam, much of the kinetic energy is lost in the collision process even for the directly scattered component, and this energy loss is clearly much more pronounced the faster the molecular beam. The signal of the trapping

desorption component is shown for the pure He mixture in Figure 41 a, but was too weak to be recorded for the two Ar-rich mixtures.

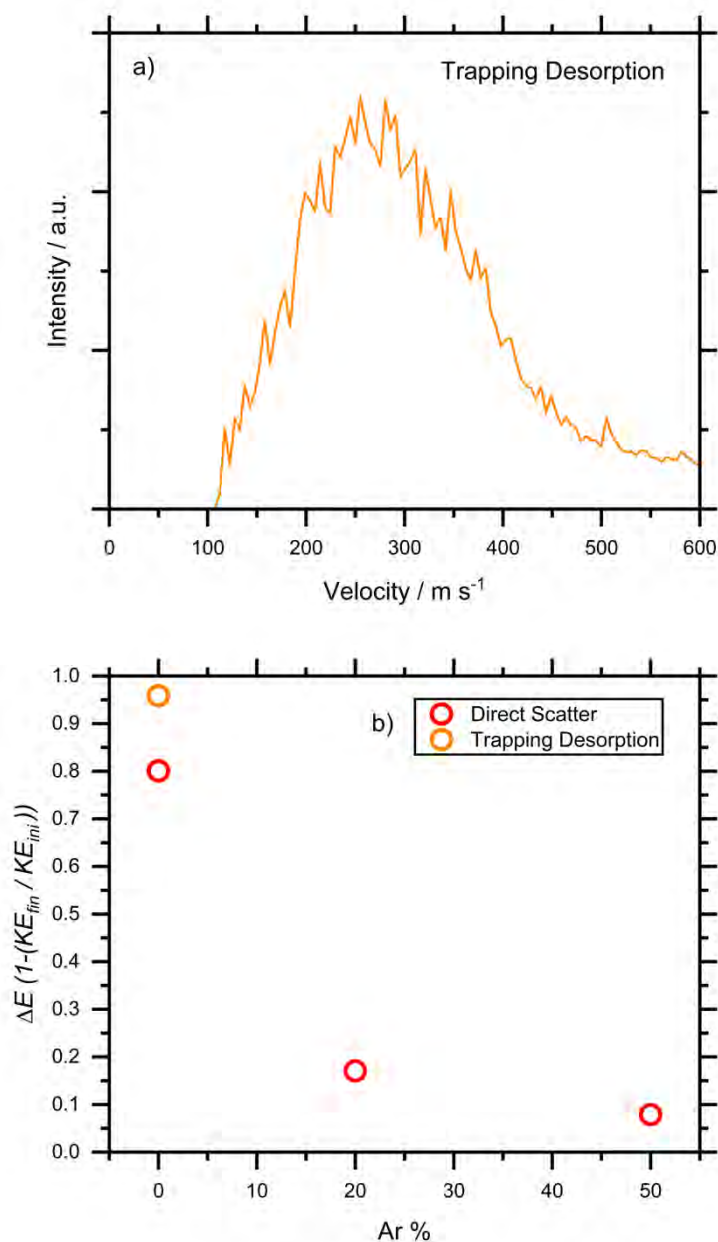


Figure 41: a) Velocity distribution of trapping-desorbed NO in a pure helium beam, extracted from VMI images. b) Reduction in energy for directly scattered and trapping desorbed NO when compared to the incoming molecular beam, for the helium beam, 20% argon and 50% argon mixtures.

The previously described trend that more kinetic energy is lost in the scattering process the higher the initial kinetic energy of the molecular beam is illustrated in Figure 41 b. It is feasible to assume that a high-velocity projectile impinging on the graphene is

deforming the graphene lattice to a greater degree, and our previous molecular dynamics simulations indeed show ripples in the graphene after scattering. The energy transfer characteristics hence shift from strongly inelastic for high impact energies to almost elastic at low collision energies. However, even for the fastest beam, the energy in the directly scattered component is still higher than that in the trapping desorption component.

As previously mentioned, the simultaneous measurement of TOF profiles and VM images allows us to estimate residence times of the NO molecules on the graphene by forward convolution of the velocity profiles, see Figure 42.

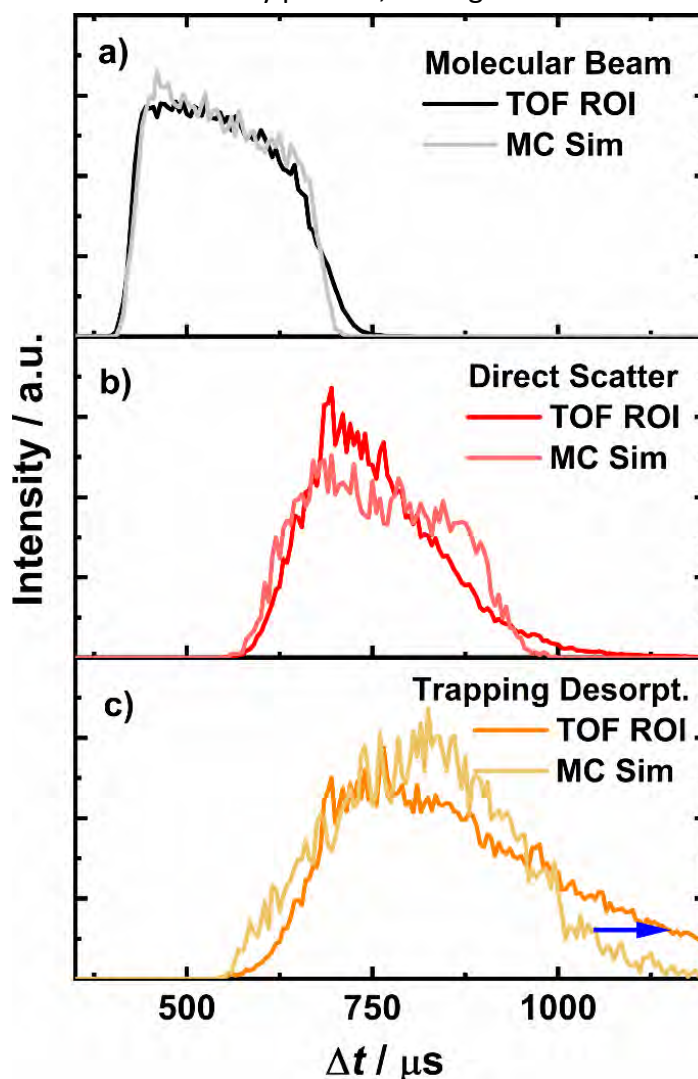


Figure 42 - Comparison of the time-of-flight profiles recorded within the regions-of-interest (black, red, orange) with the Monte Carlo simulated TOF profiles using the VM images (faded lines) for a) the molecular beam, b) the directly scattered nitric oxide molecules, and c) the trapping desorption component.

This was done by simulating in a Monte Carlo fashion the TOF profile of the initial molecular beam crossing the laser beam on its downward path; knowing 1) the velocity distribution of the molecular beam from the VM images with high precision (see Figure 39 b), 2) the distance between the molecular beam and the laser beam, 3) the opening time of the molecular beam, and 4) estimating that the backing pressure in the nozzle linearly reduces during the opening of the molecular beam nozzle, we simulated the TOF profile purely from the VMI data, see Figure 42 a). Knowing both the velocity of the directly scattered component and the trapping desorption component, we could similarly simulate the TOF profiles of the returning NO molecules and compare to the TOF profiles recorded for the ROI of each, see Figure 42 b) and c). While the simulated and measured TOF profiles overlap well for the direct scattering component (if anything, the simulated TOF profiles extend to slightly longer delay times, see Figure 42 b), the comparison of the measured and simulated (from the VM image of the TD ROI) trapping desorption TOF profiles differ. At longer delay times, the experimental TOF profile decays tens or hundreds of microseconds later than the simulated TOF profile, see the blue arrow in Figure 42 c). This is likely due to the residence times during which some NO molecules are trapped at the surface, and which is not accounted for in the simulations based on the VM images. The differences between the simulated and the measured TOF profiles are hence attributed to these residence times. Since trapping can range from a few collisions with the surface to tens or hundreds of collisions with the surface, the residence times naturally span a wide range, but can with some confidence be estimated to be in the range of tens or (low) hundreds of microseconds at room temperature and at the conditions in these experiments.

11.5. Conclusions

A molecular beam of nitric oxide in helium was scattered off a graphene surface supported on gold, where the ratio of helium and argon in the beam were varied yielding three distinct mixtures and thus, incoming velocities. The nitric oxide was ionised and the two observed components, namely 1) directly scattered NO and 2) trapping desorbed NO were probed using the surface-velocity map imaging set-up, where velocity and time of flight distributions for the two components were recorded for each beam mixture.

In the case of the directly scattered NO, as the proportion of argon in the beam increased and the incoming velocity of the nitric oxide decreased, the proportion of energy lost to the surface decreased. The proportion of energy lost during the scattering process was 0.8, 0.17 and 0.07 for the pure helium, 20% argon and 50% argon respectively. In the case of the pure helium mixture, the trapping desorbed NO was shown to have lost almost all (0.96) of its initial energy while for the Ar rich mixtures, the signal for the trapping desorption component was too weak for analysis.

In the case of the pure helium mixture, time of flight profiles of all three components of nitric oxide (including the molecular beam) were recorded using the appropriate regions of interest and compared against Monte-Carlo simulated distributions resulting from the velocity distributions taken from the VM images. It is clear from these comparisons that the trapping desorbed nitric oxide resides on the graphene surface on the order of the tens to low hundreds of microseconds.

While the NO molecules lose increasing amounts of their kinetic energy to the graphene surface as the incoming velocity increases, it is interesting to note that the energy lost

to the surface as a proportion of the incoming velocity actually decreases with slower molecular beams, i.e. faster beams lose more of their energy to the surface not just in total but proportionally, too. It has also been demonstrated that time of flight traces and velocity distributions taken from velocity map images can be used to estimate residence times, even in this case where the molecular beam has quite a wide time of flight distribution. This estimation of residence times on the order of 100 μ s provides experimental supporting evidence for the trapping pathways described in our previously described MD simulations. Though due to the vastly different timescales (the simulations only lasted 4-8 ps), quantitative comparisons cannot be drawn.

It is clear from these results that further studies are required to investigate these residence times. Further experiments employing a wider range of molecular beam velocities with shorter opening times and different surface temperatures are planned.

11.6. Acknowledgements

We thank the Royal Society for funding through grant IEC\R2\181028. We also thank Prof Nick Lockyer and Prof Mark Dickinson at The University of Manchester for the loan of a frequency-tripling unit for the YAG laser.

12. Conclusions

When nitric oxide molecules collide with graphene at a velocity of $\sim 1400 \text{ ms}^{-1}$, they are scattered off the graphene surface and display an extremely narrow angular distribution with a $\sim 80\%$ loss in kinetic energy, some of which is transferred into rotational energy while the vast majority is transferred to the graphene surface itself. The accompanying MD simulations also demonstrated the narrow angular distribution and dramatic loss in kinetic energy to the surface though both to a lesser extent.

The MD simulations also revealed the presence of both a directly scattered pathway for the NO molecules but also a trapping-desorption pathway. The simulations also revealed that as the incoming velocity of the NO is increased, a greater proportion of the kinetic energy is transferred to the surface and higher rotational energy levels are populated along with the potential presence of rotational rainbows.

Rotational distributions of the molecular beam, directly scattered NO and the trapping-desorption components of the NO were recorded independently as a function of their velocity, with the rotational temperatures of the upwards components (direct and TD) being remarkably similar and both still rotationally cool with respect to the surface temperature, i.e. there was little thermalisation at the surface even in the trapping-desorption component.

The molecular beam composition was modified to consist of increasing amounts of argon which in turn reduced the incoming velocity of the NO. In agreement with the previous MD studies, as the incoming velocity decreased, so too did the proportion of energy lost to the surface, though in the argon-containing mixtures, the signals were too weak for analysis of the trapping-desorption components. For the mixture comprising of

only helium and NO, time of flight distributions were recorded for the three components (MB, direct, TD) as a function of their velocity. Residence times of nitric oxide at the surface were extracted via comparing the recorded time of flight distributions with Monte-Carlo simulated traces from the velocity distributions. These residence times were found to be up to the order of the tens to low hundreds of microseconds.

To conclude, the findings in this thesis represent significant advancements in the study of surface dynamics studies, in this case on graphene, an area lacking in the literature despite the material's widespread investigation in other fields. The studies in this thesis utilised the surface velocity map imaging technique, in combination with molecular dynamics simulations, to study the internal and external energy distributions of scattered NO molecules and provide insights in the interactions that occur on graphene when molecules collide with the surface.

The use of regions of interest to enable one to investigate several components simultaneously in order to collect velocity dependent rotational distributions has also been absent in the surface dynamics literature. The use of regions of interest here represents advancements in the VMI method as a whole and will therefore be of interest for any future studies that could involve multiple components that require simultaneous analysis, such as crossed beam and surface desorption experiments, not only surface scattering studies. One example of future uses of regions of interest would be experiments that involve reactions on surfaces, where one could detect directly scattered molecules but also secondary species that have formed and desorbed from the surface and probe these components independently. These results also demonstrate how VMI images can be used in combination with time of flight profiles to

investigate residence times at surfaces despite the long opening times of our molecular beam which would usually inhibit such measurements.

Overall, the work in this thesis provides insights into the scattering dynamics of nitric oxide off graphene using the surface velocity map imaging technique. Perhaps most important are the implications for the VMI technique going forward. The results in this thesis demonstrate how velocity dependent energy distributions and residence times can be extracted and calculated, which will be of interest to the wider field outside of the NO/graphene system studied here, though suggestions for further studies on this particular system are given in Chapter 13.

13. Future Work

In the immediate term, increased signal strengths would allow for the detection of the trapping desorption and direct scatter components for the argon containing molecular beam mixtures, as well as more robust time of flight and velocity distributions, allowing one to provide in depth residence times calculations as has been done for the helium mixtures. It would also allow one to record rotational distributions for these components in the Ar mixtures which the current signals do not allow for, allowing for greater comparisons between mixtures such as whether more energy is transferred into rotational energy levels for the slower incoming velocities.

One route to increased signal is to situate the graphene surface closer to the laser, while at its current position there is no substantial effect on the VMI region, the field may be affected with the surface in between the plates themselves. While there is the possibility of reducing the plate sizes by for example a factor of 4 giving a 2.5 cm diameter, this in turn reduces the area where true VMI conditions prevail which could result in NO either being ionised under non-VMI conditions or even not travelling through the cut-outs in the plates and not hitting the detector at all. Therefore possible improvement to this experiment is to reduce the surface-laser distance while adopting a method much like that employed by other research groups that make use of charged blades either side of the surface to reduce impact on the VMI region.³¹

A further development for this research would be to study the effects of functionalised graphene on the scattering process. This thesis has shown how the flat surface of pristine graphene leads to massive reduction in translational energy of the NO but also

very narrow scattering angles. There is a likelihood that as graphene is functionalised such as with the addition of aryl groups, the surface's ability to absorb the translational energy will be increased due to the additional degrees of freedom. This functionalisation may also increase the possibility of trapping (within the side chains) or indeed even reactions at the graphene surface.

In the same way that altering the surface of the graphene may influence the interactions between the nitric oxide and the graphene, it is also the case that altering the metal substrate may have a similar effect. One could substitute the gold substrate with another metal which binds more strongly to the graphene such as nickel, this again may increase the rigidity of the graphene surface, limiting the dispersion of the nitric oxide's incoming velocity.¹¹⁹

In the experiments outlined in this thesis, NO could only be detected in the $v = 0$ state. Research from other groups has demonstrated excitation of NO to $v = 1$ by heating the surface between 373 K and 873 K.¹²⁰ A possible avenue of further investigation would be to alter the surface temperature in the set-up to a range of temperatures up to ~900 K. There is then a high possibility of detecting NO in higher vibrational levels and also the possibility of probing whether NO with varying incident velocities exhibits non-adiabatic behaviour as shown by Meyer et al.¹²⁰ This would allow for one to compare how other distributions change as a function of surface temperature such as how much energy is transferred to the surface, i.e. is there still the dramatic loss in kinetic energy previously reported. One could also investigate how much of this energy is transferred into rotational/vibrational excitation but most importantly how is the trapping/desorption pathway affected.

This adjustment to surface temperature could also be coupled with altering the incident angle of the NO. The NO in these experiments collided with the graphene along the surface normal, changing this incidence angle is likely to affect the velocity and angular distributions and most likely, the trapping desorption probabilities. As the incidence angle is altered to be further from the surface normal, the velocity component along the surface normal will be reduced as the velocity component perpendicular to the surface normal increase. As the molecules collide with the surface at more of a 'glancing' angle, it is likely that the graphene is less compressed by the collision, which will lead to a) different energy distributions in the NO after collisions and b) differences in the scattering pathways for the NO, potentially an increase in trapping desorption prevalence.

The molecular dynamics simulations provided insights into the pathways of the NO colliding with the surface, allowing one to view the motion as a form of movie at a relatively low computational cost. The next stage of computer simulations would involve DFT or ab initio calculations to both better reproduce the distributions of energy in the system and also adequately model reactions or chemisorption on the graphene surface.

Graphene and derivatives of graphene have recently been utilised in the creation of NO sensors for health monitoring.^{121, 122} A further development to this research would be to monitor whether NO does indeed bond to the graphene surface, specifically under what temperatures, angles and velocity of the incoming beam, i.e. does NO only bind to the surface under or above certain velocities. Raman and XPS methods were used in this thesis to investigate whether any NO is left on the surface after the experiments i.e. a permanent bond, though no NO was found remaining on the graphene. Previous research has utilised in-situ Sum-Frequency Generation in UHV conditions to monitor

bond formations on surfaces, there is an opportunity to use SFG to monitor shorter term or indeed permanent potential bond formations on graphene by combining the VMI and SFG methods.^{123, 124}

14. Appendices

14.1. Photo-desorption studies with Velocity Map

Imaging from interstellar ices (VMICES)

During the PhD there was an opportunity for collaboration with the LERMA laboratory at Sorbonne University, Paris. The group headed by Professor Jean-Hugues Fillion are in the early stages of designing an experiment investigating the desorption of neutral particles from ice analogues replicating interstellar ice grains via a new Velocity Map Imaging set-up. The following set-up, shown in Figure 43, was designed as part of the collaboration between the two research groups. The set-up is similar to the one used in the experiments for this thesis, with a few necessary changes due to the nature of the experiment.

The ice surface is held in the plane of the first plate with the desorbing laser hitting the surface at an angle of 45°. The region surrounding the surface needs to be kept at ground, meaning the VMI optics needed to gradually increase in charge, now negative, rather than gradually decreasing in charge. The optics are held in the centre of a large reaction chamber by being attached to a long steel cylinder forming a time of flight tube which is then itself attached to a 6" flange at the exit of the reaction chamber, on the other side of which is placed the newly purchased detector and camera set-up to mimic the detection portion of our experimental set-up described in this thesis.

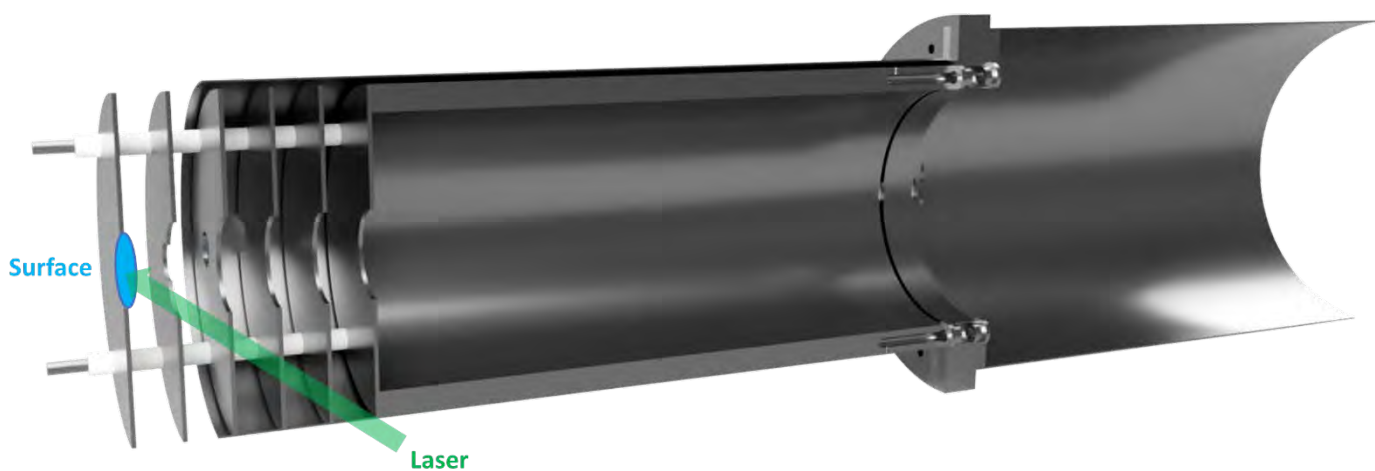


Figure 43- A cut-out view of the experimental set-up for the VMI Ices experiments, showing the cut-out holes in the optics for the incoming desorption laser and subsequent time of flight tube which attaches the plates to the reaction chamber of the Paris set-up.

The nature of this unique set-up has two effects; 1) there is less of a consideration of the surface itself impacting the VMI conditions and so the surface can sit flush with the first plate, 2) while also meaning an effort has to be made to ensure the plates and time of flight region remain charged while avoiding passing this charge to the entire chamber.

In order for VMI conditions to remain undisturbed, a 'field free region' is required between the last plate at -2000 V and the detector at -2000 V. This was achieved by

placing a charge on the metal time of flight tube before the flange, and charged shields after the flange, both of which were isolated from the rest of the set-up with the use of ceramic spacers.

Initially, SIMION simulations of the proposed set-up were carried out to determine what voltages of not just the plates but the entire set-up, such as that of the cylinder and metal shields, would be required for VMI conditions to be achieved in these unique circumstances. A simplified version of these SIMION simulations, where shields for the plates are removed for clarity, is shown in Figure 44.

The particles originate at 3 distinct locations each 1 mm apart, shown in red, green and blue, with 5 particles at each origin point. The particles at each point are then given one

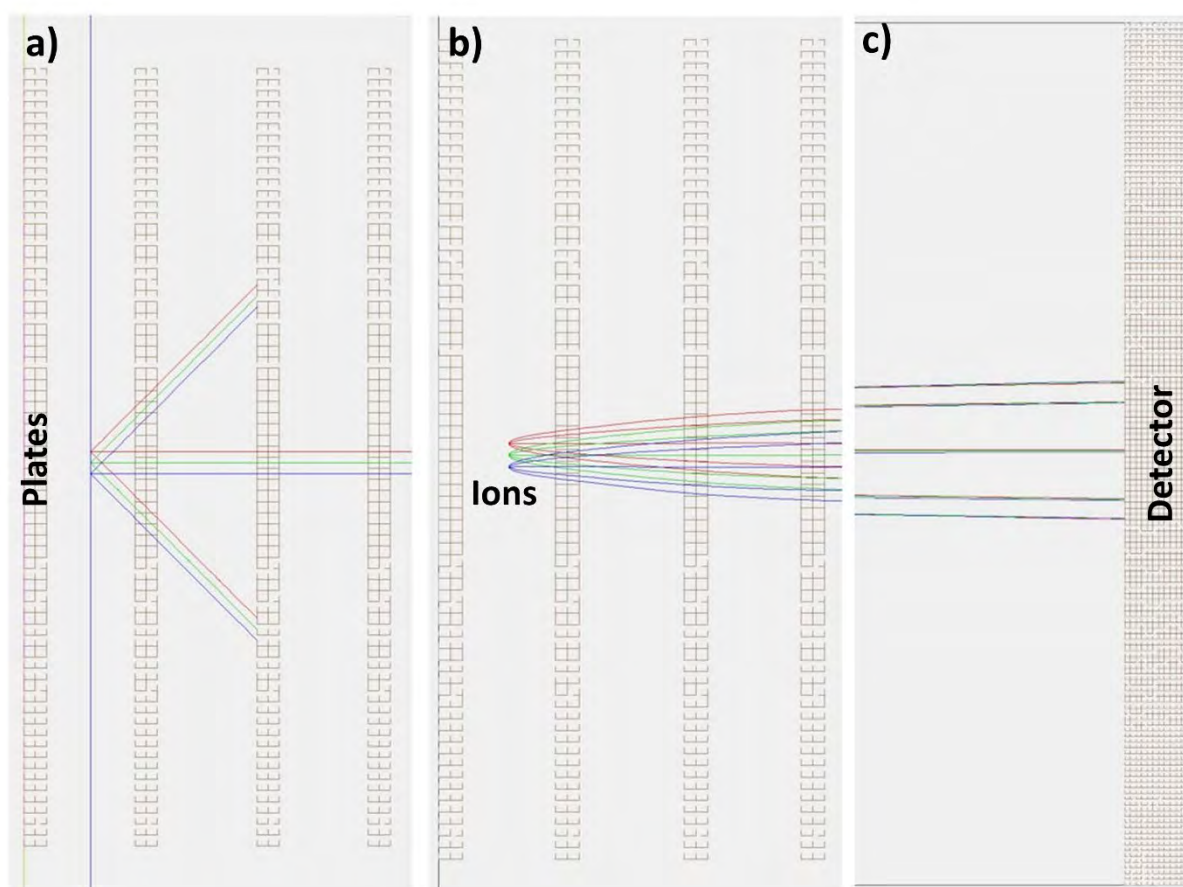


Figure 44 - SIMION calculations of the VMICES set-up with the shields removed for clarity. Left-hand side of the image shows the molecules between the first two plates with a) no voltages applied to the VMI optics and b) voltages applied, c) demonstrating VMI conditions at the detector.

of 5 velocities either travelling upwards, downwards or at 45° in between the horizontal and vertical axes. When the voltages are not applied, the ion trajectories result in the paths shown in the left of Figure 44 and in the centre when the voltages are applied. The figure also illustrates how particles with the same velocity end up on the same spot on the detector regardless of their initial position. 3D CAD designs were then constructed in Autodesk Fusion in order for the bespoke parts to be manufactured.

14.2. Visits

- Sorbonne University, Paris, June 2022.
- Hochschule Hannover, Hannover, June 2022.
- Max Planck Institute, University of Göttingen, Göttingen, June 2022.

14.3. Conferences

- ANUMOCP 2019 – Attended
- SDG 2021 – Attended
- Faraday Joint Interest Group Conference 2021 - Attended
- ISMB2021 - Poster
- SDG 2022 - Talk
- ANUMOCP 2022 - Talk

14.4. Publications

- T. Greenwood, S. P. K. Koehler, *J. Phys. Chem. C*, 2021, **125**, 17853
- T. Greenwood, S. P. K. Koehler, *Chem. Phys. Chem.*, 2022, **23**, e202200216
- T. Greenwood, H. AlSalem, S. Koehler, *J. Phys. Chem. A*, 2023, **127**, 1124–1129

14.5. Funding

Travel grant for the research visit to Germany was received via the Turing Scheme.

14.6. Courses

- Product design with Autodesk Fusion 360
- Python coding
- Javascript
- Labview

14.7. Copyright Statement

Reprinted (adapted) with permission from T. Greenwood, S. P. K. Koehler, *J. Phys. Chem.*

C, 2021, **125**, 17853. Copyright 2021 American Chemical Society.

-
- ¹ H. Guerlac, *Lavoisier-The Crucial Year: The Background and Origin of His First Experiments on Combustion in 1772*, Cornell University Press, New York, 2019.
- ² M. J. Rosker, M. Dantus, A. H. Zewail, *Science*, 1988, **241**, 1200-1202.
- ³ P. Crutzen, *Angew. Chem. Int. Ed. Engl.*, 1996, **35**, 1758-1777.
- ⁴ J. Polanyi, *Science*, 1987, **236**, 680-690.
- ⁵ M. Ashfold, N. Nahler, A. Orr-Ewing, O. Vieuxmaire, R. Toomes, T. Kitsopoulos, I. Garcia, D. Chestakov, S. Wu and D. Parker, *Phys. Chem. Chem. Phys.*, 2006, **8**, 26-53.
- ⁶ D. J. Auerbach, J. C. Tully, A. M. Wodtke, *Nat. Sci.*, 2021, **1**, e10005.
- ⁷ J. Van Houten, *J. Chem. Educ.*, 2002, **79**, 926-933.
- ⁸ D. Herschbach, *Angew. Chemie Int. Engl. Ed.*, 1987, **26**, 1221-1243.
- ⁹ Y. T. Lee, *Science*, 1987, **236**, 793-798.
- ¹⁰ F. W. Aston, *Philos. Mag.*, 1919, **38**, 707.
- ¹¹ M. Alagia, N. Balucani, P. Casavecchia, D. Stranges, G. Volpi, *J. Chem. Soc., Faraday Trans.*, 1995, **91**, 575-596.
- ¹² Y.T. Lee, J. McDonald, P. Le Breton, D. Herschbach, *Rev. Sci. Instrum.*, 1969, **40**, 1402.
- ¹³ A. Eppink, D. Parker, *Rev. Sci. Instrum.*, 1997, **68**, 3477-3484.
- ¹⁴ D. W. Chandler, P. L. Houston, *J. Chem. Phys.*, 1987, **87**, 1445.
- ¹⁵ M. Reid, S. Koehler, *Rev. Sci. Instrum.*, 2013, **84**, 044101.
- ¹⁶ C. Vallance, *Chem. Commun.*, 2019, **55**, 6336-6352.
- ¹⁷ W. Li, S. Chambreau, S. Lahankar, A. Suits, *Rev. Sci. Instrum.*, 2005, **76**, 063106.
- ¹⁸ K. Tonokura, T. Suzuki, *Chem. Phys. Lett.*, 1994, **224**, 1-6.
- ¹⁹ C. Gebhardt, T. Rakitzis, P. Samartzis, V. Ladopoulos, T. Kitsopoulos, *Rev. Sci. Instrum.*, 2001, **72**, 3848-3853.
- ²⁰ G. Somorjai, *Surf. Sci.*, 1979, **89**, 496-524.
- ²¹ M. C. Lin, G. Ernt, *Ann. Rev. Phys. Chem.*, 1986, **37**, 587-615.
- ²² I. Rahinov, R. Cooper, C. Yuan, X. Yang, D. Auerbach, A. Wodtke, *J. Chem. Phys.*, 2008, **129**, 214708.
- ²³ http://nobelprize.org/nobel_prizes/chemistry/laureates/2007.
- ²⁴ M. Bowker, *ACS Nano*, 2007, **1**, 253-257.
- ²⁵ H. J. Freund, *J. Am. Chem. Soc.* 2016, **138**, 8985-8996.
- ²⁶ A. Fujishima, K. Honda, *Nature*, 1972, **238**, 37-38.
- ²⁷ D. Sporleder, D. Wilson, M. White, *J. Phys. Chem. C*, 2009, **113**, 13180-13191.
- ²⁸ G. Somorjai, *Science*, 1985, **227**, 902-908.
- ²⁹ S. Koehler, Y. Ji, D. Auerbach, A. Wodtke, *Phys. Chem. Chem. Phys.*, 2009, **11**, 7540-7544.
- ³⁰ D. Harding, J. Neugeboren, H. Hahn, D. Auerbach, T. Kitsopoulos, A. Wodtke, *J. Chem. Phys.*, 2017, **147**, 013939.
- ³¹ D. Hadden, T. Messider, J. Leng, S. Greaves, *Rev. Sci. Instrum.*, 2016, **87**, 106104.
- ³² S. Abujarada, H. AlSalem, U. Chohan, G. Draper, S. Koehler, *J. Chem. Phys.*, 2016, **145**, 184201.
- ³³ S. Abujarada, C. Flathmann, S. Koehler, *J. Phys. Chem. C*, 2017, **121**, 19922-19929.
- ³⁴ S. Abujarada, A. Walton, A. Thomas, U. Chohan, S. Koehler, *Phys. Chem. Chem. Phys.*, 2019, **21**, 10939-10946.
- ³⁵ A. Geim, *Science*, 2009, **324**, 1530-1534.
- ³⁶ H. S. AlSalem, C. Holroyd, M. Danial Iswan, A. B. Horn, M. A. Denecke, S. P. K. Koehler, *Phys. Chem. Chem. Phys.*, 2018, **20**, 8962.
- ³⁷ H. S. AlSalem, X. Just-Baringo, I. Larrosa, U. Monteverde, X. Jiang, Y. Feng, S. P. K. Koehler, *J. Phys. Chem. C*, 2019, **123**, 25883.
- ³⁸ H. Jiang, M. Kammler, F. Ding, Y. Dorenkamp, F. Man, A. Wodtke, T. Miller, A. Kandratsenka, O. Bünermann, *Science*, 2019, **364**, 379-382.
- ³⁹ N. Mehta, V. Murray, C. Xu, D. Levin, T. Minton, *J. Phys. Chem. C*, 2018, **122**, 9859-9874.
- ⁴⁰ S. Hariharan, M. Majumder, R. Edel, T. Grabnic, S. Sibener, W. Hase, *J. Phys. Chem. C*, 2018, **122**, 29368-29379.
- ⁴¹ B. Jayee, R. Nieman, T. Minton, W. Hase, H. Guo, *J. Phys. Chem. C*, 2021, **125**, 9795-9808.
- ⁴² R. Nieman, R. Spezia, B. Jayee, T. Minton, W. Hase, H. Guo, *J. Chem. Phys.*, 2020, **153**, 184702.
- ⁴³ P. Atkins, J. de Paula, *Atkins' Physical Chemistry 10th Edition*, Oxford University Press, Oxford, 2014.
- ⁴⁴ G. Herzberg, *Molecular Spectra and Molecular Structure, Volume I. Spectra of Diatomic Molecules*, Krieger Publishing Company, Malabar, 1989.
- ⁴⁵ J. T. Titantah, M. Karttunen, *Eur. Phys. J. B*, 2013, **86**, 1.

-
- ⁴⁶ G. Kalosakas, N. N. Lathiotakis, C. Galiotis, K. Papagelis, *J. Appl. Phys.*, 2013, **113**, 134307.
- ⁴⁷ S. Mishra, M. Meuwly, *Biophys. J.*, 2009, **96**, 2105.
- ⁴⁸ Z. G. Fthenakis, G. Kalosakas, G. D. Chatzidakis, C. Galiotis, K. Papagelis, N. N. Lathiotakis, *Phys. Chem. Chem. Phys.*, 2017, **19**, 30925.
- ⁴⁹ E. E. Helgee, A. Isacsson, *AIP Adv.*, 2016, **6**, 015210.
- ⁵⁰ A. K. Rappe, C. J. Casewit, K. S. Colwell, W. A. Goddard, W. M. Skiff, *J. Am. Chem. Soc.*, 1992, **114**, 10024.
- ⁵¹ W. Humphrey, A. Dalke, K. Schulte, *J. Mol. Graph.*, 1996, **14**, 33-38.
- ⁵² J. T. Hynes, *Annu. Rev. Phys. Chem.*, 2015, **66**, 1.
- ⁵³ J. N. Murrell, S. D. Bosanac, *Chem. Soc. Rev.*, 1992, **21**, 17.
- ⁵⁴ J. J. Valentini, *Annu. Rev. Phys. Chem.*, 2001, **52**, 15.
- ⁵⁵ A. W. Kley, A. C. Luntz, D. J. Auerbach, *Phys. Rev. Lett.*, 1981, **47**, 1169.
- ⁵⁶ M. J. Gordon, X. Qin, A. Kutana, K. P. Giapis, *J. Am. Chem. Soc.*, 2009, **131**, 1927.
- ⁵⁷ A. Tamtögl, A. Ruckhofer, D. Campi, W. Allison, W. E. Ernst, *Phys. Chem. Chem. Phys.*, 2021, **23**, 7637.
- ⁵⁸ R. R. Cavanagh, D. S. King, *Phys. Rev. Lett.*, 1981, **47**, 1829.
- ⁵⁹ J. Oh, T. Kondo, K. Arakawa, Y. Saito, W. W. Hayes, J. R. Manson, J. Nakamura, *J. Phys. Chem. A*, 2011, **115**, 7089.
- ⁶⁰ K. S. Novoselov, V. I. Fal'ko, L. Colombo, P. R. Gellert, M. G. Schwab, K. Kim, *Nature*, 2012, **490**, 192.
- ⁶¹ M. Majumder, H. N. Bhandari, S. Pratihar, W. L. Hase, *J. Phys. Chem. C*, 2018, **122**, 612.
- ⁶² A. R. Santamaría, M. Alducin, R. D. Muiño, J. I. Juaristi, *J. Phys. Chem. C*, 2019, **123**, 31094.
- ⁶³ J. A. Barker, D. J. Auerbach, *Surf. Sci. Rep.*, 1985, **4**, 1.
- ⁶⁴ J. Häger, M. Fink, H. Walther, *Surf. Sci.*, 2004, **550**, 35.
- ⁶⁵ G. Nyman, L. Holmlid, J. B. C. Pettersson, *J. Chem. Phys.*, 1990, **93**, 845.
- ⁶⁶ F. Frenkel, J. Häger, W. Krieger, H. Walther, G. Ertl, J. Segner, W. Vielhaber, *Chem. Phys. Lett.*, 1982, **90**, 225.
- ⁶⁷ H. Kim, T. Balgar, E. Hasselbrink, *Chem. Phys. Lett.*, 2011, **508**, 1.
- ⁶⁸ R. Nieman, A. J. A. Aquino, H. Lischka, *J. Phys. Chem. A*, 2021, **125**, 1152.
- ⁶⁹ H. Jiang, X. Tao, M. Kammler, F. Ding, A. M. Wodtke, A. Kandratsenka, T. F. Miller, III, O. Bünermann, *J. Phys. Chem. Lett.*, 2021, **12**, 1991.
- ⁷⁰ J. R. Roscioli, D. J. Bell, D. J. Nelson, D. J. Nesbitt, *Phys. Chem. Chem. Phys.*, 2012, **14**, 4070.
- ⁷¹ Y. Ji, S. P. K. Koehler, D. J. Auerbach, A. M. Wodtke, *J. Vac. Sci. Technol. A*, 2010, **28**, 807.
- ⁷² I. Wilkinson, M. P. de Miranda, B. J. Whitaker, *J. Chem. Phys.*, 2009, **131**, 054308.
- ⁷³ I. T. Todorov, W. Smith, K. Trachenko, M. T. Dove, *J. Mater. Chem.*, 2006, **16**, 1911.
- ⁷⁴ R. Yin, Y. Zhang, B. Jiang, *J. Phys. Chem. Lett.*, 2019, **10**, 5969.
- ⁷⁵ S. Wille, H. Jiang, O. Bünermann, A. Wodtke, J. Behler, A. Kandratsenka, *Phys. Chem. Chem. Phys.*, 2020, **22**, 26113.
- ⁷⁶ A. Santamaría, M. Ramos, M. Alducin, H. Busnengo, R. Muiño, J. Juaristi, *J. Phys. Chem. A*, 2021, **125**, 2588.
- ⁷⁷ C. T. Rettner, E. K. Schweizer, C. B. Mullins, *J. Chem. Phys.*, 1989, **90**, 3800.
- ⁷⁸ B. Baule, *Ann. Phys.*, 1914, **349**, 145.
- ⁷⁹ M. Bonfanti, R. Martinazzo, *Int. J. Quantum Chem.*, 2016, **116**, 1575.
- ⁸⁰ E.-H. Patel, M. A. Williams, S. P. K. Koehler, *J. Phys. Chem. B*, 2017, **121**, 233.
- ⁸¹ J. Kimman, C. Rettner, D. Auerbach, J. Barker, J. Tully, *Phys. Rev. Lett.*, 1986, **57**, 2053.
- ⁸² J. Häger, C. Roth, M. Fink, H. Walther, *Chem. Phys. Lett.*, 1992, **189**, 420.
- ⁸³ J. Häger, Y. R. Shen, H. Walther, *Phys. Rev. A*, 1985, **31**, 1962.
- ⁸⁴ K. Golibrzuch, P. Shirhatti, I. Rahinov, D. Auerbach, A. Wodtke, C. Bartels, *Phys. Chem. Chem. Phys.*, 2014, **16**, 7602.
- ⁸⁵ R. Cooper, C. Bartels, A. Kandratsenka, I. Rahinov, N. Shenvi, K. Golibrzuch, Z. Li, D. Auerbach, J. Tully, A. Wodtke, *Angew. Chem., Int. Ed.*, 2012, **51**, 4954.
- ⁸⁶ P. R. Arantes, A. Saha, G. Palermo, *ACS Cent. Sci.*, 2020, **6**, 1654.
- ⁸⁷ D. J. Tildesley M.P. Allen, *Computer Simulation of Liquids*, Clarendon Press, Oxford, 1987.
- ⁸⁸ C. Verma, H. Lgaz, D. K. Verma, E. E. Ebenso, I. Bahadur, M. A. Quraishi, *J. Mol. Liq.*, 2018, **260**, 99.
- ⁸⁹ J. N. Murrell, S. D. Bosana, *Chem. Soc. Rev.*, 1992, **21**, 17.
- ⁹⁰ A. Monari, J.-L. Rivail, X. Assfeld, *Acc. Chem. Res.*, 2013, **46**, 596.
- ⁹¹ T. V. Albu, J. C. Corchado, D. G. Truhlar, *J. Phys. Chem. A*, 2001, **105**, 8465.
- ⁹² T. D. Kühne, *Wiley Interdiscip. Rev. Comput. Mol. Sci.*, 2014, **4**, 391.

-
- ⁹³ T. Greenwood, S. P. K. Koehler, *J. Phys. Chem. C*, 2021, **125**, 17853.
- ⁹⁴ J. B. C. Pettersson, G. Nyman, L. Holmlid, *J. Chem. Phys.*, 1988, **89**, 6963.
- ⁹⁵ A. Rodríguez-Fernández, L. Bonnet, C. Crespos, P. Larrégaray, R. Díez Muiño, *J. Phys. Chem. Lett.*, 2019, **10**, 7629.
- ⁹⁶ X. D. Wang, P. A. Robertson, F. J. J. Cascarini, M. S. Quinn, J. W. McManus, A. J. Orr-Ewing, *J. Phys. Chem. A*, 2019, **123**, 7758.
- ⁹⁷ A. E. Wiskerke, C. A. Taatjes, A. W. Kleyn, R. J. W. E. Lahaye, S. Stolte, D. K. Bronnikov, B.E. Hayden, *Faraday Discuss.*, 1993, **96**, 297.
- ⁹⁸ A.W. Kleyn, A.C. Luntz, D. J. Auerbach, *Surf. Sci.*, 1982, **117**, 33.
- ⁹⁹ A. W. Kleyn, *Surf. Rev. Lett.*, 1994, **1**, 157.
- ¹⁰⁰ J. C. Whitehead, *Rep. Prog. Phys.*, 1996, **59**, 993-1040.
- ¹⁰¹ K. Liu, *Annu. Rev. Phys. Chem.*, 2001, **52**, 139-164.
- ¹⁰² J. C. Polanyi, *Acc. Chem. Res.*, 1972, **5**, 161-168.
- ¹⁰³ P. Andresen, A. C. Luntz, *J. Chem. Phys.*, 1980, **72**, 5842-5850.
- ¹⁰⁴ F. Ausfelder, K. G. McKendrick, *Prog. Reaction Kinet. Mech.*, 2000, **25**, 299-370.
- ¹⁰⁵ C. Xiahou, J. N. L. Connor, *Phys. Chem. Chem. Phys.*, 2021, **23**, 13349-13369.
- ¹⁰⁶ M. Rutigliano, F. Pirani, *J. Phys. Chem. C*, 2019, **123**, 11752-11762.
- ¹⁰⁷ A. G. Suits, C. K. Bishwakarma, L. Song, G. C. Groenenboom, A. van der Avoird, D. H. Parker, *J. Phys. Chem. A*, 2015, **119**, 5925-5931.
- ¹⁰⁸ T. Greenwood, S. P. K. Koehler, *Chem. Phys. Chem.*, 2022, **23**, e202200216.
- ¹⁰⁹ J. Luque, D.R. Crosley, "LIFBASE: Database and Spectral Simulation Program (Version 1.5)", SRI International Report MP 99-009 (1999).
- ¹¹⁰ J. Häger, H. Walther, *J. Vac. Sci. Technol. B*, 1985, **3**, 1490-1497.
- ¹¹¹ Sven P. K. Köhler, Mhairi Allan, Hailey Kelso, David A. Henderson, Kenneth G. McKendrick, *J. Chem. Phys.*, 2005, **122**, 024712-0247129.
- ¹¹² M. P. D'Evelyn, R. J. Madix, *Surf. Sci. Rep.*, 1984, **3**, 413.
- ¹¹³ T. Greenwood, H. S. AlSalem, S. P. K. Koehler, *J. Phys. Chem.*, 2023, **127**, 1124.
- ¹¹⁴ M. Hippler, J. Pfab, *Chem. Phys. Lett.*, 1995, **243**, 500.
- ¹¹⁵ C. Xu, P. A. Brown, J. Lu, K. L. Shuford, *Phys. Chem. C*, 2015, **119**, 17271.
- ¹¹⁶ J. M. Englert, C. Dotzer, G. Yang, M. Schmid, C. Papp, J. M. Gottfried, H.-P. Steinrück, E. Spiecker, F. Hauke, A. Hirsch, *Nat. Chem.*, 2011, **3**, 279.
- ¹¹⁷ V. Jain, B. Kandasubramanian, *J. Mater. Sci.*, 2020, **55**, 1865.
- ¹¹⁸ J. Werdecker, B.-J. Chen, M. E. Van Reijzen, A. Farjamnia, B. Jackson, R. D. Beck, *Phys. Rev. Res.*, 2020, **2**, 043251.
- ¹¹⁹ J. Wintterlin, M.-L. Bocquet, *Surf.Sci.*, 2009, **603**, 1841-1852.
- ¹²⁰ S. Meyer, PhD Thesis, University of Göttingen, 2022.
- ¹²¹ N. Wenninger, U. Bračić, A. Kollau, K. Pungjunun, G. Leitinger, K. Kalcher, A. Ortner, *Sens. Actuators B: Chem.*, 2021, **346**, 130532.
- ¹²² L. Yang, G. Zheng, Y. Cao, C. Meng, Y. Li, H. Ji, X. Chen, G. Niu, J. Yan, Y. Xue, H. Cheng, *Microsyst. Nanoeng.*, 2022, **8**, 78.
- ¹²³ G. Rupprechter, T. Dellwig, H. Unterhalt and H.-J. Freund, *Top. Catal.*, 2001, **15**, 19-26.
- ¹²⁴ X. Li, V. Pramhaas, C. Rameshan, P. Blaha, G. Rupprechter, *J. Phys. Chem. C.*, 2020, **124**, 18102-18111.


Nitric Oxide Scattering off Graphene Using Surface-Velocity Map Imaging

Thomas Greenwood and Sven P. K. Koehler*

 Cite This: *J. Phys. Chem. C* 2021, 125, 17853–17860

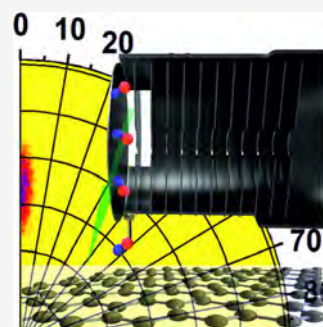
 Read Online

ACCESS |

 Metrics & More

 Article Recommendations

ABSTRACT: We investigated the scattering of nitric oxide, NO, off graphene supported on gold. This is of fundamental importance to chemistry as collisions are the necessary first step to chemical reactions on graphene, and nitric oxide molecules are inherently radicals, with the potential to bond to graphene. We directed a molecular beam of NO in helium onto graphene and detected the directly scattered molecules using surface-velocity map imaging. In contrast to previous scattering studies off graphite, which detected only a modest reduction of the translational energy of the NO, we observe a loss of $\sim 80\%$ of the molecules' kinetic energy. Our classical molecular dynamics simulations still predict a loss of $\sim 60\%$ of the translational energy in the scattering process. This energy appears to partly go into the NO rotations but mostly into collective motion of the carbon atoms in the graphene sheet. At 0° incidence angle, we also observe a very narrow angular scattering distribution. Both findings may be unique to pristine graphene on gold as (1) the two-dimensional (2D) honeycomb structure is perfectly flat and (2) the graphene is only loosely held to the gold at a distance of 3.4 \AA , thus it can absorb much of the projectiles' kinetic energy.



1. INTRODUCTION

Chemical reactions are at the very heart of chemistry,¹ and collisions between reactants are a necessary first step toward any chemical reaction.² Collisions between gas-phase species, both nonreactive and reactive processes, have hence long been studied in the field of reaction dynamics to understand the redistribution of energy.³ Equally, the investigation of the detailed scattering dynamics of gas-phase species off surfaces has a long tradition,⁴ not least because of its enormous importance for heterogeneous catalysis.⁵ Reactive and non-reactive scattering,^{6,7} adsorption and (photo-)desorption⁸ studies have all been performed on various types of solid surfaces, including metal single crystals, metal oxides, and stepped and corrugated surfaces, to name a few. Graphite surfaces have also heavily featured in surface scattering experiments,⁹ and more recently graphene, a two-dimensional (2D) hexagonal arrangement of sp^2 -hybridized C atoms.¹⁰

Graphene research has increased exponentially since the discovery of its remarkable electronic, physical, and chemical properties almost 20 years ago.¹¹ Some of these properties such as the band gap (pristine graphene is a zero band gap material) can be tuned by functionalization through chemical reactions on graphene, and we have in our group modified chemical vapor deposition (CVD) graphene with functional groups such as phenyl groups or hydrogen atoms and investigated these graphene derivatives using sum-frequency generation spectroscopy.^{12,13}

Studies of the detailed scattering dynamics of actual collisions on graphene that potentially lead to the formation of such functionalized graphene derivatives have recently

emerged. It is important in this context to remember that graphene is a surface held together by a two-dimensional (2D) network of covalent bonds, and collisions between (reactive) species and graphene could potentially lead to a truly covalent bond formation.

Minton and co-workers measured the kinetic energy and angular distribution of N_2 scattered off highly oriented pyrolytic graphite (HOPG) in sophisticated molecular beam experiments coupled with classical molecular dynamics (MD) simulations. They found that the N_2 (1) scatters off after a single collision or is (2) temporarily or (3) permanently trapped at the surface.¹⁴ Hase and co-workers modeled the collisional dynamics of N_2 with graphite at collision energies of 26 and 60 kJ mol^{-1} and found that for all incidence angles, single collision scattering is the dominant process; at the lower collision energy (similar to what is used in our work here) close to normal incidence angles, roughly 50% of the initial translational energy is channeled away, primarily to the graphene surface vibrational modes.¹⁵ This was taken one step further by Nieman et al. and Jayee et al. in their primarily modeling studies of the reaction of $N(^4S)$ and $O(^3P)$ atoms with graphene, though at vastly higher collision energies

Received: June 7, 2021
Revised: July 22, 2021
Published: August 4, 2021



relevant to the reentry of spacecrafts into Earth's atmosphere.^{16,17} Both the high collision energy as well as the fact that a reactive atomic species is scattered off graphene cause not only nonreactive scattering to be observed but also reactions with the graphene itself (functionalization), and the formation of ablation products such as CN radicals in the gas-phase. Juaristi and co-workers modeled the scattering of O₂ off HPOG by ab initio molecular dynamics at lower collision energies of ~ 20 kJ mol⁻¹, focusing on the effects of the initial alignment of the impinging O₂ molecule.¹⁸

Many early state-resolved studies were concerned with the collision dynamics of NO with graphite.¹⁹ It seems as if specular scattering dominates at higher temperatures, whereas an isotropic scattering due to trapping/desorption is dominant at lower temperatures.²⁰ However, later studies by Walther and co-workers found no diffusely scattered molecules at surface temperatures below 70 K, with only the inelastic scattering channel remaining.²¹ When angular distributions were investigated—typically at incidence angles varying from 45 to 60°—the direct channel displayed a narrow distribution but still with a width of 10° or more.²² Even at fairly steep incidence angles of 30°, Frenkel et al. still observed a diffuse isotropic trapping component and a width of the angular distribution of the specular component of $\sim 20^\circ$.²³

As far as reactions on graphene go, hydrogenation is probably the simplest modification to graphene,^{13,24} and the reactivity has been modeled by Lischka and co-workers,²⁵ and also investigated both in rather elegant dynamics experiments as well as modeled by Wodtke and co-workers.^{26,27} A short pulse of H atoms was scattered off graphene under UHV conditions, and the angular and kinetic energy distribution was extracted by detecting the hydrogen using an H-atom Rydberg tagging scheme. Most strikingly, evidence for temporary bond formation between the H atoms and graphene was found.

Velocity map imaging (VMI) is one of the most successful recent techniques to probe reaction dynamics;^{28,29} VMI is typically applied to gas-phase dynamics, but more recently expanded to surface processes,^{30–34} and we have ourselves applied it to the laser-desorption of NO from gold single crystals.^{35,36} Surface-VMI not only delivers the velocity (i.e., speed and angular) distribution of scattering products after surface collision but due to the resonance-enhanced multiphoton ionization (REMPI) scheme frequently employed, can also establish the vibrational and rotational state distribution of the scattered products. We hence chose to perform surface-VMI collision experiments by scattering nitric oxide off graphene because (1) NO is intrinsically a radical and can hence potentially react with the graphene substrate, and (2) because NO as a diatomic molecule allows us to also investigate the internal energy distribution after scattering off graphene.

2. EXPERIMENTAL METHODS

Our surface-VMI apparatus has been described previously,^{37,38} but a number of key features and changes warrant a more detailed description. The spectrometer consists of two vacuum chambers, the first housing the molecular beam (firing vertically downward in the lab frame), and the second chamber houses the graphene surface on a gold substrate, together with the 12 VMI optics plates and the multichannel plate (MCP) detector/phosphor screen assembly. The chambers are each evacuated using 1000 L s⁻¹ turbomolecular pumps, which in turn are backed by their own rotary pumps to achieve a base

pressure in the main chamber below 5×10^{-9} Torr. The molecular beam consists of a 2–4% NO mixture seeded in He which is supersonically expanded through a pulsed valve (500 μ m diameter orifice, 300 μ s opening time) to a velocity of ~ 1500 m s⁻¹. The NO molecules travel ~ 27 cm downward into the space between the first two VMI plates, where they are intersected by the laser beam, crossing horizontally through the center of the chamber between those first two plates. The NO molecules travel a further ~ 5 cm and scatter off the graphene surface, recoiling to cross the laser beam a second time in the center of the VMI optics. The three axes of (1) probe laser along *x*, (2) counter-propagating molecular beam (from top)/ surface normal (with the surface near the bottom of the VMI optics in the lab frame), *y*, and (3) the time-of-flight (TOF) axis of the VMI apparatus, *z*, are mutually perpendicular as shown in Figure 1a. We have chosen this *xyz* axes labeling, as the *x* and *y*-axis in the lab frame are now the same as the *x* and *y* dimension of the resulting 2D VM images. We highlight that this positioning of the surface within the VMI optics is a departure from our previous work in which the surface normal was aligned along the main axis of the TOF spectrometer and which delivered velocity distribution in all three dimensions in space independently. However, due to the much longer timescales of a molecular beam pulse compared to a laser pulse, we are losing this timing option in the current scattering experiments and hence have to extract the speed along the surface normal from the *y* coordinate of the VM images instead. The remaining *x* dimension of the images delivers—after appropriate transformation—the polar angle distribution. For scattering experiments from a flat surface as described here, it is reasonable to assume a homogeneous azimuthal distribution around the surface normal, and hence only the velocity component along the surface normal and one velocity component parallel to the surface need to be measured.

The grounded surface is positioned ~ 5 cm below the laser beam axis close to a grounded shield surrounding the ion optics, and as such, does not disturb the VMI field in the ionization region noticeably, see Figure 1b. Previous research on the scattering off liquid surfaces by Greaves and co-workers employing a similar geometry to image the scattering plane used an elegant arrangement involving charged razor blades to ensure that the field lines between the ion plates are not distorted.³³ We note, however, that the distance between the ionization region and the surface in those experiments is much shorter (i.e., the surface is placed in-between the first two ion plates), but thanks to the ease with which NO can be laser-ionized here, we can afford to locate the surface much further away from the laser beam and in fact close to the ground shield surrounding the ion optics, such that the field lines in the central region of the VMI spectrometer are not distorted. Wodtke and co-workers use a shorter flight distance in a similar setup and crucially a fs laser to nonresonantly ionize desorbed molecules, and can conveniently switch between spatial and velocity map imaging,³⁴ while on the other hand, the ease of (1 + 1) REMPI detection in our setup negates the need for a focusing lens, and we do not need to scan the probe laser across the ionization region. The longer flight path from the surface to the ionization laser potentially limits the width of the angular distribution that can be recorded, but since the detection laser is not focused (and hence all ionized NO molecules with a clear trajectory to the detector are recorded, up to 12.5 mm either side of the center of the VMI optics), we appear to record a much narrower polar angle distribution of

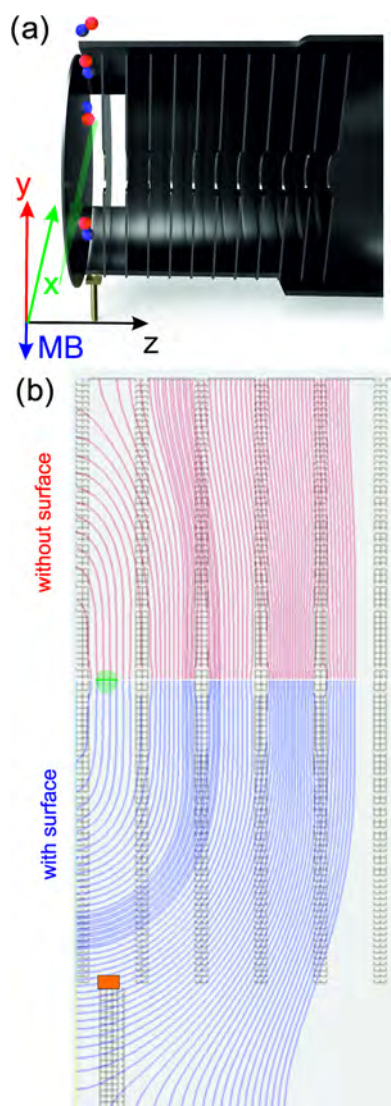


Figure 1. (a) Cutaway CAD drawing of our 12-plate ion optics with the molecular beam indicated; the faint green arrow is the REMPI laser beam between the two plates furthest left; x - (along laser beam) and y -dimension (parallel to the molecular beam and surface normal; surface shown in gold near the bottom) chosen, as these are the dimensions which yield the velocity maps' x - y coordinates; z is along the time-of-flight direction. (b) SIMION simulations of the electric fields without (red) and with (blue) the surface in place. Grounding shield omitted for clarity.

the scattered NO molecules than theoretically possible, i.e., we are not biasing against NO molecules at larger polar angles. We note that the exact distance between the surface and the laser is not required as we extract the velocity from the VM images, and not from time-of-flight times to the laser.

The surface is resting (i.e., no spring clips are used that would cover part of the surface) on a surface holder mounted on a manipulator, and the sample itself consists of a silicon wafer onto which a thin layer of chromium and then gold has been evaporated, covering the whole wafer, before graphene—CVD-grown on copper—was transferred onto the gold. The correct vertical alignment of the surface normal was checked by shining a He/Ne laser pointer along the central y -axis of the chamber (in-line with the molecular beam), and ensuring that the back-reflection from the wafer travels along the same path

as the incoming beam, guaranteeing that the surface normal is aligned with the molecular beam.

Nitric oxide molecules are ionized ~ 5 cm above the surface using a $(1 + 1)$ REMPI scheme via the $A \leftarrow X$ transition. The third harmonic of a Continuum Surelite II-10 Nd:YAG laser was used to pump a Radiant Dyes NarrowScan laser using Coumarin 450 dye, and the dye laser output was then frequency-doubled using a BBO crystal to achieve ~ 226 nm laser pulses at 10 Hz with a pulse energy of ~ 0.8 mJ.

The ionized NO particles are then accelerated over a potential difference of 1000 V toward a multichannel plate (MCP) detector coupled to a phosphor screen. The MCP is pulsed at 10 Hz to reduce background noise caused by ions other than NO^+ . We do not “DC-slice” the ion cloud, as the long flight path from the scattering region to the ionization region causes our images to be optically sliced, essentially imaging one scattering plane (the x - y plane). The phosphor screen captures the ions' positions, and image acquisition is performed by a 10 Hz synchronized camera (NET C-IC4133BU-U3V) connected to a personal computer via a National Instruments PCIe-8242 frame grabber.

Since we are not operating a molecular beam directed along the spectrometer's time-of-flight axis, we have to establish the central spot (equating to zero velocity along the x and y dimension and hence essential for image analysis) on the detector by different means: instead, we backfill the chamber with pure nitric oxide at a background pressure of 2×10^{-7} Torr;³⁹ ionizing this thermal gas ensemble yields a two-dimensional Maxwell–Boltzmann distribution on the detector with a peak along x and y at 0 m s^{-1} each, thus establishing the center of our images. Calibration of the VMI setup was performed by NO_2 dissociation at ~ 226 nm, as previously described.^{38,40}

3. COMPUTATIONAL METHODS

All molecular dynamics simulations here were performed within the DL_POLY Classic suite using a combination of force fields.⁴¹ A simulation box was selected with a parallelogram as a base (in the x - y plane) and periodic boundary conditions along the two dimensions of that base (parallel to the interfaces present here), but with no periodicity in the z -direction, which is along the surface normal. The substrate was formed of a $6 \times 6 \times 6$ array of gold atoms whose interactions were described by a Gupta potential.⁴² Ninety-eight carbon atoms were positioned in a hexagonal 2D network in the x - y plane on top of the gold substrate. The bonds in the graphene sheet were described by a harmonic potential (rather than fixed bond lengths) to accurately reflect any compressions and stretches in the bonds as the NO collides with the graphene surface. A Morse bond potential described the C–C bonds with parameters proposed by Kalosakas et al.,⁴³ using the accepted carbon–carbon internuclear distance in graphene of 1.42 \AA , with $D = 5.7 \text{ eV}$ and $\alpha = 1.96 \text{ \AA}^{-1}$. Angles and dihedrals were described by quartic and cosine functions, respectively.⁴³ This system was relaxed by running simulations in an NVT ensemble regulated to 300 K by a Nosé–Hoover thermostat for 4 ns with a relaxation constant of 1 ps. A single nitric oxide molecule was then placed in a randomly selected position in the x - y plane, but $\sim 18 \text{ \AA}$ above the graphene surface. The nitric oxide bond was described by a Morse potential with parameters $D_e = 6.61736 \text{ eV}$, $\alpha = 2.636 \text{ \AA}^{-1}$ and $r_e = 1.151 \text{ \AA}$.⁴⁴ To complete the force field, nonbonding interactions were described by Lennard-Jones 12-6 potentials,

with parameters either provided by the force fields above or taken from the universal force field set out by Skiff and co-workers,⁴⁵ with the exception of the gold and graphene interaction being developed by Helgee and Isacson.⁴⁶ Lorentz–Berthelot combining rules were applied for interactions between unlike atoms. Interatomic forces were truncated after 7 Å. It should be noted that more sophisticated neural network potential energy surfaces have recently been calculated even for surface scattering processes related to the one presented here;^{47–49} however, not all of these studies take the metal substrate into account, and the literature force fields mentioned above—while not verified for the NO–graphene interaction—are likely to be sufficient to at least qualitatively reproduce the trends observed experimentally.

The NO was directed at the graphene either N- or O-head first with 1600 m s⁻¹ along the surface normal, and 2000 trajectories were run and analyzed for each orientation. After collision with the graphene, the NO was detected once traversing a virtual plane 8 Å above the graphene, where there is no longer any interaction between the graphene and the NO. Properties such as the velocity components of both the N and O atoms in all three dimensions were recorded separately. Molecular speeds and polar angles were calculated from center-of-mass shifts and binned in 20 m s⁻¹ and 5° wide intervals, respectively.

4. RESULTS AND DISCUSSION

Figure 2a shows an overlay of three ion images, all of which were recorded on the Q₁(0) line of the A ← X transition of NO as per Figure 2b, but control experiments on the R₁(0) line yield the same results. The signal due to the molecular beam traveling toward the surface is shown in blue, while the scattered signal is shown in red. The scattered signal was recorded at a time delay (between the molecular beam and the probe laser) which was increased by 100 μs compared to the molecular beam images; this is to account for the round-trip time from the laser to the surface and back (~10 cm), such that we probe “the same” directly scattered NO molecules, whose velocity distribution in the molecular beam we established before collision with the graphene.

Finally, the more diffuse spot in the middle in green is from the ionization of thermal background NO ($p_{\text{bg}} = 5 \times 10^{-7}$ Torr), and this image is fitted to a two-dimensional Maxwell–Boltzmann velocity distribution. In the absence of a molecular beam aligned along the main VMI axis, the center spot of this distribution, highlighted in the image as a green cross, corresponds to our zero velocity coordinate.

The speed distributions shown in Figure 3a are established relative to this zero velocity coordinate (which does not vary by more than one pixel or 5.1 m s⁻¹ from day to day) and after application of the appropriate density-to-flux conversion by multiplication with speed.⁵⁰ The initial molecular beam (blue) and the scattered molecules (red) are naturally in opposite directions. All distributions are fitted to eq 1 as we are measuring a 2D distribution

$$F(c)dc = Ac^2 \exp \frac{-(c - c_0)^2}{\alpha^2} dc \quad (1)$$

where A is a scaling factor and α is related to the width of the distribution.⁵¹ While the NO in the molecular beam has average kinetic energy $\langle E_{\text{kin}} \rangle$ of 0.31 eV (30 kJ mol⁻¹), the scattered NO has lost around 80% of its kinetic energy, down

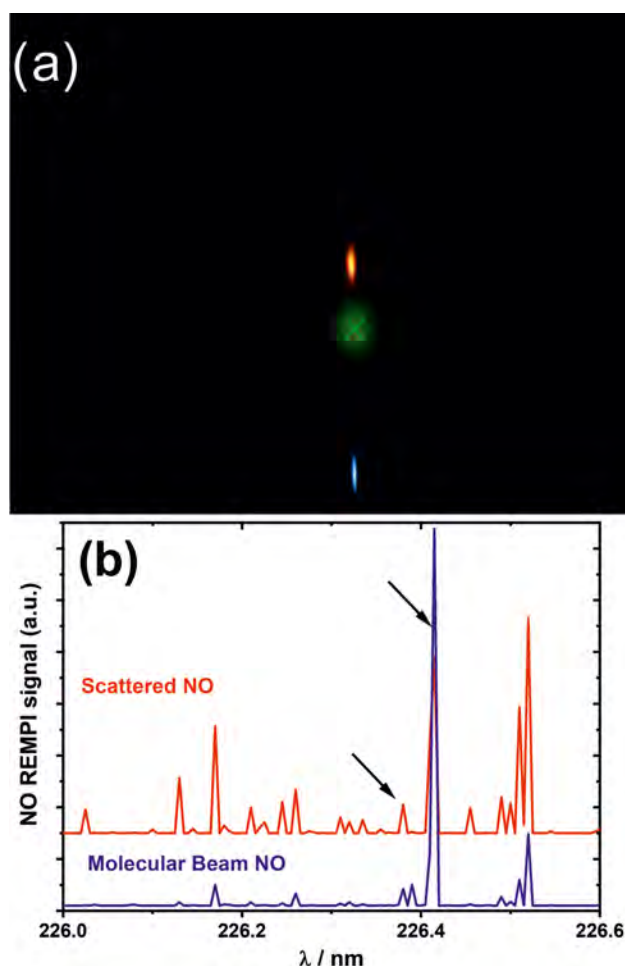


Figure 2. (a) Overlay of three velocity map images of nitric oxide, NO. The downward-facing molecular beam is in blue, the scattered NO in red, and the diffuse green spot in the center is thermal background NO gas, imaged to define the zero velocity coordinate (illustrated by the green cross). (b) Rotationally-resolved REMPI spectra of NO in the molecular beam (blue), and scattered off graphene (red). Black arrows point to the Q₁(0) and R₁(0) lines on which most images were recorded.

to 0.06 eV; this is a much greater loss of kinetic energy than observed in the direct channel of the NO scattering off graphite.²³ In the simplest form of the Baule model and assuming collision with one surface C atom only, the NO would not scatter off the surface at all due to the much larger mass of NO compared to a single C atom in graphene.^{52,53} Instead, the Baule model predicts that the mass equivalent of just over six C atoms together would account for the observed energy loss of the projectile, which is not unrealistic, given the tight covalent network of the 2D lattice, though the fact that the number of C atoms is close to one hexagon in graphene is likely coincidental. The translational energy distribution is—as expected—also broader than the initial molecular beam. Despite this dramatic energy loss, the scattered NO cannot be described as thermal. We have attempted to fit the scattered data to the equation describing a Maxwell–Boltzmann distribution for desorption from a surface⁵⁴ but obtained a worse fit, which did not reproduce the experimental data as well. This indicates that the dominant scattering channel in our case of 0° incidence angle is a direct scattering mechanism but associated with a significant loss of energy, which most likely

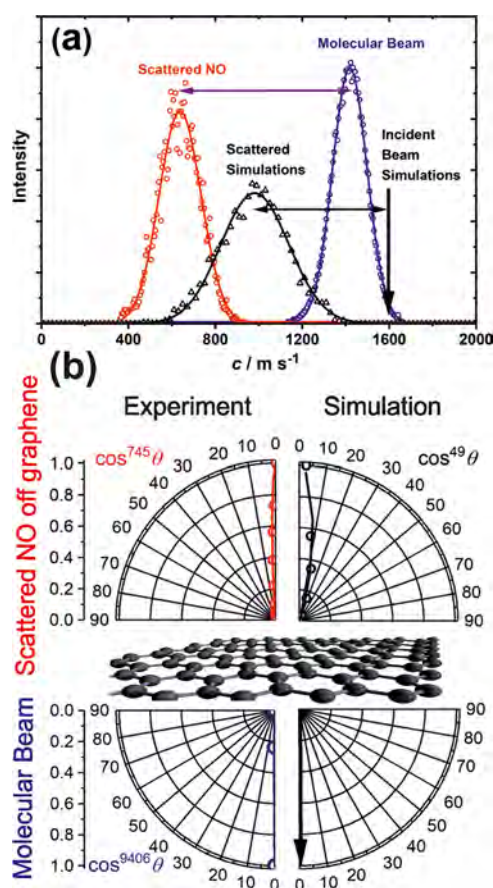


Figure 3. (a) Speed distributions extracted from the VM images in Figure 2 for the molecular beam in blue and the scattered NO in red; the black data are results of molecular dynamics simulations commencing with monoenergetic NO molecules at 1600 m s^{-1} , indicated by the black arrow; all data (open symbols) fitted to eq 1 (lines). (b) Polar angle distribution of bottom panels for the molecular beam and top panels for the scattered NO; left panels are experimental data, right panels, molecular dynamics simulations. Open circles are data points; lines are fits to a $\cos^n \theta$ function as shown.

goes into the collective motion of the carbon atoms in graphene. Efficient transfer of energy to the substrate's phonon modes has also been observed, e.g., for NO scattering of Ag(111).⁵⁵ We observe a diffuse and very weak spot at slower NO velocities that could be due to a trapping-desorption mechanism, but this channel is far less pronounced compared to the directly scattered NO. While the spectra shown in Figure 2b demonstrate that some energy is channeled into rotational degrees of freedom, this only accounts for a small fraction of the lost energy. Much of the earlier work on collisions of NO with graphite had focused on the rotational distribution of the inelastically scattered NO,^{56,57} and found evidence for rotational cooling. For the vibrationally elastic scattering of NO($\nu = 3$) off Au(111), NO loses around half its initial kinetic energy for incidence energies close to those employed here; interestingly, the final kinetic energy of the NO decreases with increasing rotational state,⁵⁸ an effect we have not been able to probe yet. While a complete analysis of the rotational state population is reserved for a later publication, with the focus here on the velocity distributions, we have not been successful in detecting NO($\nu = 1$) in the scattered beam; this is in contrast to, e.g., nitric oxide scattering off metal single

crystal surfaces such as Au(111) at similar incidence energies,⁵⁹ during which fractions of a percent of NO($\nu = 1$) were detected at surface temperatures close to the room-temperature graphene employed here.

The results of our classical molecular dynamics simulations in which NO molecules were approaching the graphene surface with a velocity of 1600 m s^{-1} along the surface normal (black vertical arrow in Figure 3a) and collided with the graphene in a random position were fitted to the 3D variant of eq 1 (replacing the c^2 with a c^3), see black data in Figure 3a). There is some qualitative agreement in that the scattered NO molecules lose more than 60% of their mean kinetic energy (from 0.4 to 0.15 eV), but this energy loss is less pronounced compared to the experiments. This discrepancy is likely due to the limitations of the employed force field and could be improved using density functional theory (DFT)-based force fields,^{47–49} but the overall trend observed is reproduced qualitatively. Future scattering experiments with aligned NO molecular beams could serve as a benchmark for improving the force fields. We obtain better agreement for the polar angle distribution shown in Figure 3b. The downward-facing molecular beam is naturally very narrow with barely any discernible transversal velocity contribution, and from purely geometric considerations based on the distance between our skimmer and the laser interaction region, the divergence is $<1^\circ$. The MD simulations account for that by aligning all NO trajectories along the surface normal (black arrow in the right bottom panel in Figure 3b). The scattered NO molecules—while displaying a wider angular distribution than the molecular beam—still show a surprisingly narrow angular distribution. When fitted to a $\cos^n \theta$ distribution, we obtain a value of 745 for n . A thermal desorption process would yield $n = 1$, indicating that despite the significant loss in kinetic energy, a trapping-desorption mechanism does not seem to play a significant role here. The simulated polar angle distribution follows a \cos^{49} distribution, i.e., a little wider than the experimentally measured distribution, but still very narrow and much narrower than the angular distributions measured for NO scattered off graphite,^{22,23} albeit these were measured at non-zero incidence angles. This demonstrates that both in the experiment and the simulations, a direct scattering mechanism closely along the surface normal is by far the dominant process. We note that the narrow scattering distribution is not an artifact of the geometry of our VMI instrument. Since the ionization laser for NO (1 + 1) REMPI spectroscopy does not need to be focused, we can detect all NO molecules that scatter within a polar angle of 14° , and the majority of the ionized molecules would follow true VMI conditions due to us using soft extraction conditions with 12 plates.³⁷ However, it is due to the narrow angular distribution in the experiment, see Figure 4, that we can detect all scattered NO molecules under true VMI conditions.

The MD simulations naturally cannot model reactions between the NO and the graphene, but the results can nevertheless provide information about the trapping-desorption probability. We have directed 4000 trajectories onto graphene and have observed a trapping mechanism for only $\sim 2\%$ of the trajectories. “Trapping” in this case is for the entire length of each simulation run (4 ps), but does not account for “double- or multi-bounce” trajectories in which the NO bounces off in a first collision, though it does not escape the well and returns to the graphene surface for a further bounce, before finally escaping. This 2% trapping probability provides

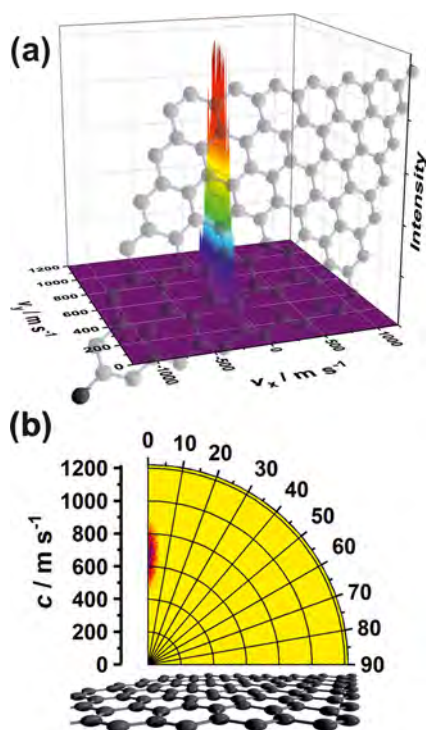


Figure 4. (a) Velocity distribution of NO molecules (initial kinetic energy ~ 0.31 eV) after scattering off graphene resolved along the surface normal (y) and perpendicular to the surface (x , along the propagation direction of the laser). (b) Same image, but expressed as speed and polar angle; color range from yellow ($=0$ intensity) to dark red. Location of graphene schematically indicated in both cases.

further evidence that trapping-desorption is not a dominant process for normal incidence NO scattering off graphene at kinetic energies of ~ 0.31 eV.

We can also rule out addition reactions of the NO onto graphene. After exposing the pristine graphene samples to our NO/He molecular beam over a period between two weeks and two months, we performed Raman spectroscopy and X-ray photoelectron spectroscopy (XPS) of the samples before and after exposure. For both techniques, this analysis was done *ex situ*, i.e., the sample was removed from the VMI chamber and transferred to the XPS and Raman instrument in ambient air. Neither did the Raman data indicate the formation of defects (absence of a D peak before and after NO bombardment), nor did the XPS data indicate the addition of N or O species; some oxygen species were present before and after NO exposure, but their relative surface coverage did not change.

5. CONCLUSIONS

In summary, scattering of ~ 0.31 eV NO molecules off room-temperature graphene at 0° incidence angle takes away a significant amount of kinetic energy from the projectile in a predominantly direct-inelastic process; some of the energy goes into rotation; however, most energy goes into collective motions of the 2D honeycomb lattice of the graphene. This energy loss might be unique to graphene on gold with a fairly large separation of 3.4 \AA , with the graphene acting as a “worn-out trampoline.” Despite this large energy loss, the angular distribution remains remarkably narrow, possibly a testament to the flatness of the graphene. However, we expect to learn more about collisional energy transfer processes and the possible observation of a trapping-desorption mechanism on

graphene in future experiments by varying incidence angles and surface temperature.

AUTHOR INFORMATION

Corresponding Author

Sven P. K. Koehler – Department of Natural Sciences, Manchester Metropolitan University, Manchester M1 5GD, U.K.; orcid.org/0000-0002-6303-6524; Email: s.koehler@mmu.ac.uk

Author

Thomas Greenwood – Department of Natural Sciences, Manchester Metropolitan University, Manchester M1 5GD, U.K.

Complete contact information is available at:

<https://pubs.acs.org/10.1021/acs.jpcc.1c05014>

Notes

The authors declare no competing financial interest.

ACKNOWLEDGMENTS

The authors thank the Royal Society for funding (IEC \R2\181028), and Prof Nick Lockyer and Prof Mark Dickinson at the University of Manchester for the loan of a frequency-tripling unit. The authors also thank Christopher Lester for help with the Molecular Dynamics simulations, Dr. Alejandro Ferrari for help with the preparation of the graphene samples, and Dilruba Tazmin and Harsimran Singh-Bhaker for assistance during data acquisition. The authors would also like to thank the reviewers for their insightful comments.

REFERENCES

- (1) Hynes, J. T. Molecules in Motion: Chemical Reaction and Allied Dynamics in Solution and Elsewhere. *Annu. Rev. Phys. Chem.* **2015**, *66*, 1.
- (2) Murrell, J. N.; Bosanac, S. D. The theory of atomic and molecular collisions. *Chem. Soc. Rev.* **1992**, *21*, 17.
- (3) Valentini, J. J. State-to-state chemical reaction dynamics in polyatomic systems: case studies. *Annu. Rev. Phys. Chem.* **2001**, *52*, 15.
- (4) Kleyn, A. W.; Luntz, A. C.; Auerbach, D. J. Rotational Energy Transfer in Direct Inelastic Surface Scattering: NO on Ag(111). *Phys. Rev. Lett.* **1981**, *47*, 1169.
- (5) Freund, H.-J. The Surface Science of Catalysis and More, Using Ultrathin Oxide Films as Templates: A Perspective. *J. Am. Chem. Soc.* **2016**, *138*, 8985.
- (6) Gordon, M. J.; Qin, X.; Kutana, A.; Giapis, K. P. Gas-Surface Chemical Reactions at High Collision Energies? *J. Am. Chem. Soc.* **2009**, *131*, 1927.
- (7) Tamtögl, A.; Ruckhofer, A.; Campi, D.; Allison, W.; Ernst, W. E. Atom-surface van der Waals potentials of topological insulators and semimetals from scattering measurements. *Phys. Chem. Chem. Phys.* **2021**, *23*, 7637.
- (8) Cavanagh, R. R.; King, D. S. Rotational- and Spin-State Distributions: NO Thermally Desorbed from Ru(001). *Phys. Rev. Lett.* **1981**, *47*, 1829.
- (9) Oh, J.; Kondo, T.; Arakawa, K.; Saito, Y.; Hayes, W. W.; Manson, J. R.; Nakamura, J. Angular intensity distribution of a molecular oxygen beam scattered from a graphite surface. *J. Phys. Chem. A* **2011**, *115*, 7089.
- (10) Novoselov, K. S.; Fal'ko, V. I.; Colombo, L.; Gellert, P. R.; Schwab, M. G.; Kim, K. A roadmap for graphene. *Nature* **2012**, *490*, 192.
- (11) Geim, A. K. Graphene: Status and Prospects. *Science* **2009**, *324*, 1530.
- (12) AlSalem, H. S.; Holroyd, C.; Danial Iswan, M.; Horn, A. B.; Denecke, M. A.; Koehler, S. P. K. Characterisation, coverage, and

orientation of functionalised graphene using sum-frequency generation spectroscopy. *Phys. Chem. Chem. Phys.* **2018**, *20*, 8962.

(13) AlSalem, H. S.; Just-Baringo, X.; Larrosa, I.; Monteverde, U.; Jiang, X.; Feng, Y.; Koehler, S. P. K. Evidence for Site-Specific Reversible Hydrogen Adsorption on Graphene by Sum-Frequency Generation Spectroscopy and Density Functional Theory. *J. Phys. Chem. C* **2019**, *123*, 25883.

(14) Mehta, N. A.; Murray, V. J.; Xu, C.; Levin, D. A.; Minton, T. K. Nonreactive Scattering of N₂ from Layered Graphene Using Molecular Beam Experiments and Molecular Dynamics. *J. Phys. Chem. C* **2018**, *122*, 9859.

(15) Majumder, M.; Bhandari, H. N.; Pratihari, S.; Hase, W. L. Chemical Dynamics Simulation of Low Energy N₂ Collisions with Graphite. *J. Phys. Chem. C* **2018**, *122*, 612.

(16) Nieman, R.; Spezia, R.; Jayee, B.; Minton, T. K.; Hase, W. L.; Guo, H. Exploring reactivity and product formation in N(4S) collisions with pristine and defected graphene with direct dynamics simulations. *J. Chem. Phys.* **2020**, *153*, No. 184702.

(17) Jayee, B.; Nieman, R.; Minton, T. K.; Hase, W. L.; Guo, H. Direct Dynamics Simulations of Hyperthermal O(³P) Collisions with Pristine, Defected, Oxygenated, and Nitridated Graphene Surfaces. *J. Phys. Chem. C* **2021**, *125*, 9795.

(18) Rivero Santamaría, A. R.; Alducin, M.; Muiño, R. D.; Juaristi, J. I. Ab Initio Molecular Dynamics Study of Alignment-Resolved O₂ Scattering from Highly Oriented Pyrolytic Graphite. *J. Phys. Chem. C* **2019**, *123*, 31094.

(19) Barker, J. A.; Auerbach, D. J. Gas-surface interactions and dynamics; Thermal energy atomic and molecular beam studies. *Surf. Sci. Rep.* **1984**, *4*, 1.

(20) Lin, M. C.; Ertl, G. Laser Probing of Molecules Desorbing and Scattering from Solid Surfaces. *Ann. Rev. Phys. Chem.* **1986**, *37*, 587.

(21) Häger, J.; Fink, M.; Walther, H. Scattering of NO from a graphite surface at cryogenic temperatures. *Surf. Sci.* **2004**, *550*, 35.

(22) Nyman, G.; Holmlid, L.; Pettersson, J. B. C. Surface scattering of NO from graphite: A statistical description of energy distributions. *J. Chem. Phys.* **1990**, *93*, 845.

(23) Frenkel, F.; Häger, J.; Krieger, W.; Walther, H.; Ertl, G.; Segner, J.; Vielhaber, W. Rotational state populations and angular distributions on surface scattered molecules: NO on graphite. *Chem. Phys. Lett.* **1982**, *90*, 225.

(24) Kim, H.; Balgar, T.; Hasselbrink, E. The stretching vibration of hydrogen adsorbed on epitaxial graphene studied by sum-frequency generation spectroscopy. *Chem. Phys. Lett.* **2011**, *508*, 1.

(25) Nieman, R.; Aquino, A. J. A.; Lischka, H. Exploration of Graphene Defect Reactivity toward a Hydrogen Radical Utilizing a Preactivated Circumcoronene Model. *J. Phys. Chem. A* **2021**, *125*, 1152.

(26) Jiang, H. Y.; Kammler, M.; Ding, F. Z.; Dorenkamp, Y.; Manby, F. R.; Wodtke, A. M.; Miller, T. F.; Kandratsenka, A.; Bünermann, O. Imaging covalent bond formation by H atom scattering from graphene. *Science* **2019**, *364*, 379.

(27) Jiang, H.; Tao, X.; Kammler, M.; Ding, F.; Wodtke, A. M.; Kandratsenka, A.; Miller, T. F., III; Bünermann, O. Small Nuclear Quantum Effects in Scattering of H and D from Graphene. *J. Phys. Chem. Lett.* **2021**, *12*, 1991.

(28) Chandler, D.; Houston, P. Two-dimensional imaging of state-selected photodissociation products detected by multiphoton ionization. *J. Chem. Phys.* **1987**, *87*, 1445.

(29) Eppink, A. T. J. B.; Parker, D. H. Velocity map imaging of ions and electrons using electrostatic lenses: Application in photoelectron and photofragment ion imaging of molecular oxygen. *Rev. Sci. Instrum.* **1997**, *68*, 3477.

(30) Koehler, S. P. K.; Ji, Y.; Auerbach, D. J.; Wodtke, A. M. Three-dimensional velocity map imaging of KBr surface photochemistry. *Phys. Chem. Chem. Phys.* **2009**, *11*, 7540.

(31) Sporleder, D.; Wilson, D. P.; White, M. G. Final State Distributions of O₂ Photodesorbed from TiO₂(110). *J. Phys. Chem. C* **2009**, *113*, 13180.

(32) Roscioli, J. R.; Bell, D. J.; Nelson, D. J.; Nesbitt, D. J. State-resolved velocity map imaging of surface-scattered molecular flux. *Phys. Chem. Chem. Phys.* **2012**, *14*, 4070.

(33) Hadden, D. J.; Messider, T. M.; Leng, J. G.; Greaves, S. J. Velocity map imaging the scattering plane of gas surface collisions. *Rev. Sci. Instrum.* **2016**, *87*, No. 106104.

(34) Harding, D. J.; Neugeboren, J.; Hahn, H.; Auerbach, D. J.; Kitsopoulos, T. N.; Wodtke, A. M. Ion and velocity map imaging for surface dynamics and kinetics. *J. Chem. Phys.* **2017**, *147*, No. 013939.

(35) Abujarada, S.; AlSalem, H.; Chohan, U. K.; Draper, G. L.; Koehler, S. P. K. Photodesorption of NO from Au(100) using 3D surface-velocity map imaging. *J. Chem. Phys.* **2016**, *145*, No. 184201.

(36) Abujarada, S.; Flathmann, C.; Koehler, S. P. K. Translational and Rotational Energy Distributions of NO Photodesorbed from Au(100). *J. Phys. Chem. C* **2017**, *121*, 19922.

(37) Abujarada, S.; Walton, A.; Thomas, A.; Chohan, U. K.; Koehler, S. P. K. Adsorption site, orientation and alignment of NO adsorbed on Au(100) using 3D-velocity map imaging, X-ray photoelectron spectroscopy and density functional theory. *Phys. Chem. Chem. Phys.* **2019**, *21*, 10939.

(38) Reid, M.; Koehler, S. P. K. Validation of velocity map imaging conditions over larger areas. *Rev. Sci. Instrum.* **2013**, *84*, No. 044101.

(39) Ji, Y.; Koehler, S. P. K.; Auerbach, D. J.; Wodtke, A. M. Surface three-dimensional velocity map imaging: A new technique for the study of photodesorption dynamics. *J. Vac. Sci. Technol. A* **2010**, *28*, 807.

(40) Wilkinson, I.; de Miranda, M. P.; Whitaker, B. J. Photodissociation of NO₂ in the (2) ²B₂ state: The O(¹D₂) dissociation channel. *J. Chem. Phys.* **2009**, *131*, No. 054308.

(41) Todorov, I. T.; Smith, W.; Trachenko, K.; Dove, M. T. DL_POLY_3: new dimensions in molecular dynamics simulations via massive parallelism. *J. Mater. Chem.* **2006**, *16*, 1911.

(42) Titantah, J. T.; Karttunen, M. Multiphase density functional theory parameterization of the interatomic potential for silver and gold. *Eur. Phys. J. B* **2013**, *86*, No. 288.

(43) Kalosakas, G.; Lathiotakis, N. N.; Galiotis, C.; Papagelis, K. In-plane force fields and elastic properties of graphene. *J. Appl. Phys.* **2013**, *113*, No. 134307.

(44) Mishra, S.; Meuwly, M. Nitric Oxide Dynamics in Truncated Hemoglobin: Docking Sites, Migration Pathways, and Vibrational Spectroscopy from Molecular Dynamics Simulations. *Biophys. J.* **2009**, *96*, 2105.

(45) Rappe, A. K.; Casewit, C. J.; Colwell, K. S.; Goddard, W. A.; Skiff, W. M. UFF, a full periodic table force field for molecular mechanics and molecular dynamics simulations. *J. Am. Chem. Soc.* **1992**, *114*, 10024.

(46) Helgee, E. E.; Isacson, A. Adsorption of metal atoms at a buckled graphene grain boundary using model potentials. *AIP Adv.* **2016**, *6*, No. 015210.

(47) Yin, R.; Zhang, Y.; Jiang, B. Strong Vibrational Relaxation of NO Scattered from Au(111): Importance of the Adiabatic Potential Energy Surface. *J. Phys. Chem. Lett.* **2019**, *10*, 5969.

(48) Wille, S.; Jiang, H.; Bünermann, O.; Wodtke, A. M.; Behler, J.; Kandratsenka, A. An experimentally validated neural-network potential energy surface for H-atom on free-standing graphene in full dimensionality. *Phys. Chem. Chem. Phys.* **2020**, *22*, 26113.

(49) Rivero Santamaría, A. R.; Ramos, M.; Alducin, M.; Busnengo, H. F.; Muiño, R. D.; Juaristi, J. I. High-Dimensional Atomistic Neural Network Potential to Study the Alignment-Resolved O₂ Scattering from Highly Oriented Pyrolytic Graphite. *J. Phys. Chem. A* **2021**, *125*, 2588.

(50) Rahinov, I.; Cooper, R.; Yuan, C.; Yang, X.; Auerbach, D. J.; Wodtke, A. M. Efficient vibrational and translational excitations of a solid metal surface: State-to-state time-of-flight measurements of HCl ($\nu = 2, J = 1$) scattering from Au(111). *J. Chem. Phys.* **2008**, *129*, No. 214708.

(51) Rettner, C. T.; Schweizer, E. K.; Mullins, C. B. Desorption and trapping of argon at a 2H-W(100) surface and a test of the

applicability of detailed balance to a nonequilibrium system. *J. Chem. Phys.* **1989**, *90*, 3800.

(52) Baule, B. Theoretische behandlung der erscheinungen in verdünnten gasen. *Ann. Phys.* **1914**, *349*, 145.

(53) Bonfanti, M.; Martinazzo, R. Classical and quantum dynamics at surfaces: Basic concepts from simple models. *Int. J. Quantum Chem.* **2016**, *116*, 1575.

(54) Patel, E.-H.; Williams, M. A.; Koehler, S. P. K. Kinetic energy and angular distributions of He and Ar atoms evaporating from liquid dodecane. *J. Phys. Chem. B* **2017**, *121*, 233.

(55) Kimman, J.; Rettner, C. T.; Auerbach, D. J.; Barker, J. A.; Tully, J. C. Correlation between Kinetic-Energy Transfer to Rotation and to Phonons in Gas-Surface Collisions of NO with Ag(111). *Phys. Rev. Lett.* **1986**, *57*, 2053.

(56) Häger, J.; Roth, C.; Fink, M.; Walther, H. Scattering of rotationally excited NO molecules from a graphite surface. *Chem. Phys. Lett.* **1992**, *189*, 420.

(57) Häger, J.; Shen, Y. R.; Walther, H. State-selective velocity and angular distributions of NO molecules scattered from a graphite surface. *Phys. Rev. A* **1985**, *31*, 1962.

(58) Golibrzuch, K.; Shirhatti, P. R.; Rahinov, I.; Auerbach, D. J.; Wodtke, A. M.; Bartels, C. Incidence Energy Dependent State-to-State Time-of-Flight Measurements of NO($v = 3$) Collisions with Au(111): the Fate of Incidence Vibrational and Translational Energy. *Phys. Chem. Chem. Phys.* **2014**, *16*, 7602.

(59) Cooper, R.; Bartels, C.; Kandratsenka, A.; Rahinov, I.; Shenvi, N.; Golibrzuch, K.; Li, Z.; Auerbach, D. J.; Tully, J. C.; Wodtke, A. M. Multiquantum Vibrational Excitation of NO Scattered from Au(111): Quantitative Comparison of Benchmark Data to Ab Initio Theories of Nonadiabatic Molecule–Surface Interactions. *Angew. Chem., Int. Ed.* **2012**, *51*, 4954.

Molecular Dynamics Simulations of Nitric Oxide Scattering Off Graphene

Thomas Greenwood^{*[a]} and Sven P. K. Koehler^[a, b]

We performed classical molecular dynamics simulations to model the scattering process of nitric oxide, NO, off graphene supported on gold. This is motivated by our desire to probe the energy transfer in collisions with graphene. Since many of these collision systems comprising of graphene and small molecules have been shown to scatter non-reactively, classical molecular dynamics appear to describe such systems sufficiently. We directed thousands of trajectories of NO molecules onto graphene along the surface normal, while varying impact position, but also speed, orientation, and rotational excitation of the nitric oxide, and compare the results with experimental

data. While experiment and theory do not match quantitatively, we observe agreement that the relative amount of kinetic energy lost during the collision increases with increasing initial kinetic energy of the NO. Furthermore, while at higher collision energies, all NO molecules lose some energy, and the vast majority of NO is scattered back, in contrast at low impact energies, the fraction of those nitric oxide molecules that are trapped at the surface increases, and some NO molecules even gain some kinetic energy during the collision process. The collision energy seems to preferentially go into the collective motion of the carbon atoms in the graphene sheet.

Introduction

Molecular dynamics (MD) simulations are a useful way to model both static molecular structures,^[1,2] but also non-reactive (chemical) processes such as adsorption and desorption phenomena.^[3,4] Classical MD simulations are based on force fields and do not explicitly include contributions from electrons,^[5] and as such in their simplest form cannot model chemical reactions.^[6,7] They also lack the precision of *ab initio* methods,^[8] and naturally cannot model quantum effects. However, due to the reduced computational cost compared to quantum methods, MD simulations allow processes over much longer timescales to be modelled, and hence can help to catch a glimpse of such processes in a fashion not too dissimilar to a molecular movie.

We have recently investigated experimentally the scattering of nitric oxide, NO, off graphene.^[9] This was in part motivated by the fact that NO is a diatomic radical, hence potentially reactive with graphene, but NO also allows rotational distributions to be observed, unlike monoatomic radicals. However, the by far largest contribution of scattered NO is due to *direct inelastic* scattering, and this is a process that can conveniently

be modelled using MD simulations, allowing us to create snapshots of the actual scattering process. We have hence performed MD simulations of NO directed with various speeds at normal incidence angle at graphene supported by 6 layers of gold. This allows us to derive speed and angular distribution of the scattered NO for comparison with experimental results. The experiment also delivers rotational energy distributions of NO, and we also derived these classically in the simulations presented here. Furthermore, the MD simulations allow us to extract properties that are currently not accessible in our experiments such as the range of heights of the NO above the graphene at the turning point, i.e. when it is closest to the graphene surface, and the effect of varying conditions such as the initial velocity, which will guide us in future experiments.

The scattering of hydrogen off graphene has already been investigated both experimentally and theoretically.^[10–12] The scattering of atoms other than hydrogen (N(⁴S) and O(³P), respectively) with graphene has also been modelled by Nieman *et al.* and Jaye *et al.*,^[13,14] quantum-methods guaranteed that chemical reactions with the graphene (insertion) and ablation reactions could be observed.

Both classical mechanics as well as *ab initio* molecular dynamics simulations were also employed in modelling the collisions of homo-diatom molecules (N₂ and O₂) with highly oriented pyrolytic graphite (HOPG),^[15–17] in which direct scattering has been found to be the dominant process, but some evidence for trapping-desorption was observed, too. The fact that MD simulations allow for larger entities (many more atoms) to be modelled allowed Hase and co-workers to observe that most of the initial kinetic energy is channelled into the surface motions of the graphene substrate.^[15–17]

Collisions of NO with graphite were also experimentally and theoretically investigated from the 1980s onwards. Nyman *et al.* modelled the scattering process classically and in a statistical fashion;^[18,19] they observed ‘rotational cooling’ (at surface

[a] T. Greenwood, Prof. Dr. S. P. K. Koehler
Department of Natural Sciences
Manchester Metropolitan University
M1 5GD, Manchester, UK
E-mail: thomas.greenwood@stu.mmu.ac.uk

[b] Prof. Dr. S. P. K. Koehler
Fakultät II, Hochschule Hannover
Ricklinger Stadtweg 120, 30459 Hannover, Germany
Homepage: <http://www.koehler.wp.hs-hannover.de>

© 2022 The Authors. ChemPhysChem published by Wiley-VCH GmbH.
This is an open access article under the terms of the Creative Commons Attribution Non-Commercial NoDerivs License, which permits use and distribution in any medium, provided the original work is properly cited, the use is non-commercial and no modifications or adaptations are made.

temperatures of 300 K or higher) and even rotational rainbows. Many more studies investigated the NO-graphite system experimentally by measuring in particular speed and angular distributions as well as rotational state distributions.^[20,21] Specular scattering is almost always observed, especially at higher temperatures, and an isotropic component, presumably due to a trapping-desorption mechanism, becomes dominant at lower temperatures,^[22,23] even at fairly steep incidence angles.^[24]

We here set out to perform simulations of the scattering of NO radicals off graphene supported on gold using classical MD methods, i.e. without considering quantum effects. We replicate the conditions in our own experiment, with the aim in particular to establish translational energy and rotational state distributions.

Results and Discussion

Figure 1 shows the speed distributions of NO molecules after collision with a graphene layer supported on gold for initial NO velocities of 600, 800, 1200, 1600 and 2500 ms^{-1} (0.06, 0.10, 0.22, 0.40 and 0.97 eV) from dark-red to orange; the initial velocities are indicated by short vertical arrows at the top, while the horizontal arrows illustrate the difference of speed between the initial speed and the most probable final speed. We only plotted in Figure 1 the case of no rotational excitation, N-atom oriented towards the surface, with a surface temperature equilibrated at 300 K. All data (data points as open circles) are fitted to the 3D flux distribution in equation 1

$$F(c)dc = A c^3 \exp \frac{-(c - c_0)^2}{\alpha^2} dc \quad (1)$$

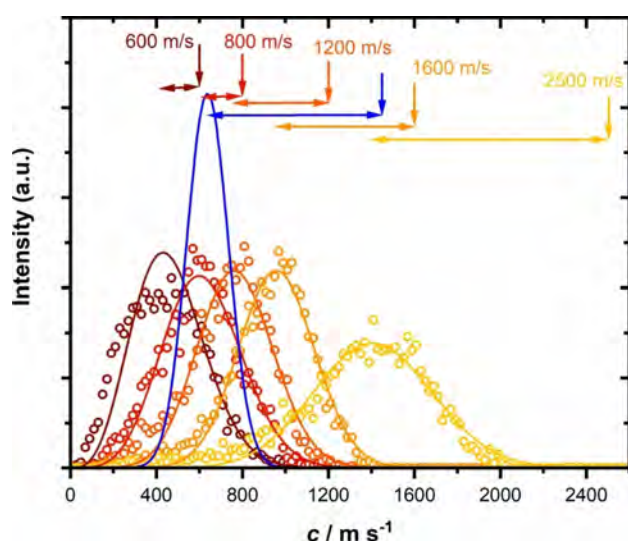


Figure 1. Speed distributions of NO molecules after scattering off a graphene surface, initial speeds as indicated by vertical arrows. Horizontal double-arrows indicate the loss of speed, and the blue data is an experimental speed distribution with an initial NO velocity of 1418 m/s and a width of $\sim 190 \text{ m/s}$. All simulation data fitted to eq. 5.

where A is a scaling factor and α is related to the width of the distribution.^[25] The blue curve is a fit to an experimental speed distribution with an initial NO velocity of 1418 m/s and a full width at half maximum of $\sim 190 \text{ m/s}$. A few observations can be made straight away: 1) The faster the incoming NO molecule, the more kinetic energy is transferred (most likely to the graphene surface motions); 2) while for the fastest speeds, all NO molecules are scattered with speeds that are slower than the incoming NO, for the slower incoming projectiles, a significant portion actually gains some kinetic energy in the scattering process; 3) while the experimental data is qualitatively similar, it appears as if more kinetic energy is lost during the scattering process in the experiment than predicted in the MD simulations, and interestingly that the speed distribution is narrower in the experiment than in the simulations, despite the initial width of the speeds distribution in the experiment being significantly wider than in the simulations (where no spread is assumed). This wider speed distribution of the scattered NO molecules in the simulations, however, might be a direct result of the classical rather than quantum nature of the simulations. Naturally, vibrational energy is quantised, but in our simulations, energy exchange of fractions of vibrational quanta are allowed, thus an incoming NO molecule might lose or gain small amounts of energy from e.g. vibrations in the substrate that would not be allowed had a rigorous quantum-mechanical treatment be applied. This possibly leads to the wider velocity distribution in the simulations, but quantum corrections of the classical simulations could solve this issue.^[26] The loss of a significant amount of energy for the higher incoming velocities contrasts with previous simulations of scattering on graphene,^[12] but this loss is expected due to the different masses of the incoming projectiles, and furthermore it is not straightforward to compare those two experiments due to the different incidence angles. The NO in our simulations is travelling along the surface normal, resulting in more energy being transferred into the surface, whereas the scattering simulations were performed at angles that are removed from the surface normal and as such show less energy transfer as kinetic energy in the surface plane tends to be conserved.^[15,16] Scattering simulations of atomic nitrogen with pristine graphene at kinetic energies of 14.9 kcal/mol (0.646 eV) found an energy loss ratio of roughly 0.6,^[13] this could again be due to the scattering angle of the nitrogen, or in this case due to a monoatomic particles (N atoms) being scattered rather than a diatomic NO. Nevertheless, the results show that even at this relatively high initial kinetic energy, there is little evidence for reactions such as insertion reactions into pristine graphene.

Research by Hase *et al.* demonstrates how at similar velocities to this study, the vast majority of the initial energy is transferred into surface vibrations and kinetic energy of the scattered N_2 , again showing that the higher the incident angle (with respect to the surface normal), the less energy is transferred to the surface due to the velocity component along the surface being conserved.^[16]

The initial and final speeds and kinetic energies (and energy loss and ratio) for the present molecular dynamics simulations are shown in Table 1:

$c_i/\text{m s}^{-1}$	$c_{f,\text{max}} [\text{m s}^{-1}]$	$E_i [\text{eV}]$	$E_{f,\text{max}} [\text{eV}]$	$\Delta E [\text{eV}]$	E_f/E_i
600	440	0.06	0.03	0.03	0.5
800	606	0.10	0.06	0.04	0.6
1200	755	0.22	0.09	0.13	0.4
1418 ± 95	621 ± 115	0.31 ± 0.08	0.06 ± 0.04	0.25 ± 0.09	0.2 ± 0.1
1600	949	0.40	0.14	0.26	0.3
2500	1384	0.97	0.30	0.67	0.3

Impact angles in all simulations and the experiment are along the surface normal, and if the Baule model in its simplest form was applied, the NO would not scatter off the surface at all as it is heavier than a single C atom. Instead, it appears that in order of increasing speed of the incoming molecules, the NO interacts with a pseudo-atom with a mass of 15, 20, 12, 11, 10 C atoms (for $c_i = 600, 800, 1200, 1600, 2500 \text{ m s}^{-1}$), and with a pseudo-atom with a mass of ~ 7 C atoms if the experimental results are used. This means firstly that fewer atoms in the carbon lattice 'work together' or are involved in the scattering process the faster the incoming projectiles are flying (at least for velocities of 800 m s^{-1} or greater), and secondly that the 'real' 2D graphene network seems more rigid than described in the MD simulations, leading to the lowest 'effective mass' of a surface atom in the experiments. The reason for the only qualitative rather than quantitative agreement is most likely due to the fact that while the graphene and gold potentials in literature are well-established, the universal force fields used for the interactions between the incoming NO and the graphene and gold were developed for a large range of chemical systems and are hence necessarily a compromise. Ab initio calculations would have likely yielded better potentials and thus a more quantitative agreement with experiment.

Just as the simulations underestimate how much kinetic energy is lost in the collision process, they seem to overestimate the polar angle distribution, see Figure 2. The angular distributions become narrower with increasing initial NO speed as expected, but this increase is not overly pronounced. When fitting the angular distributions to a $\cos^n\theta$ function (where a fitting factor of $n=1$ would indicate a thermal desorption process), the fitting parameter n only increases from 40 to 51 as the initial NO speed increases. All those parameters are a lot smaller than $n=745$ for the experimental data, which remarkably shows the narrowest angular distribution by far, though $\cos^n\theta$ functions with $n > 40$ are already fairly narrow, and the much larger fitting parameter n for the experimental work perhaps overstates that the width of the distribution only changes from a rather narrow $\pm 10^\circ$ (simulations) to approximately $\pm 3^\circ$ (experiment). Both simulation data and experimental data include rotational excitation of the incoming NO, but differences in the exact rotational temperature could lead to (slightly) different angular distributions. However, it seems that the graphene surface appears even 'flatter' towards incoming NO molecules than the simulations can reproduce. The narrow scattering distributions at higher incoming velocities match similar studies of H atom scattering off graphene at similar

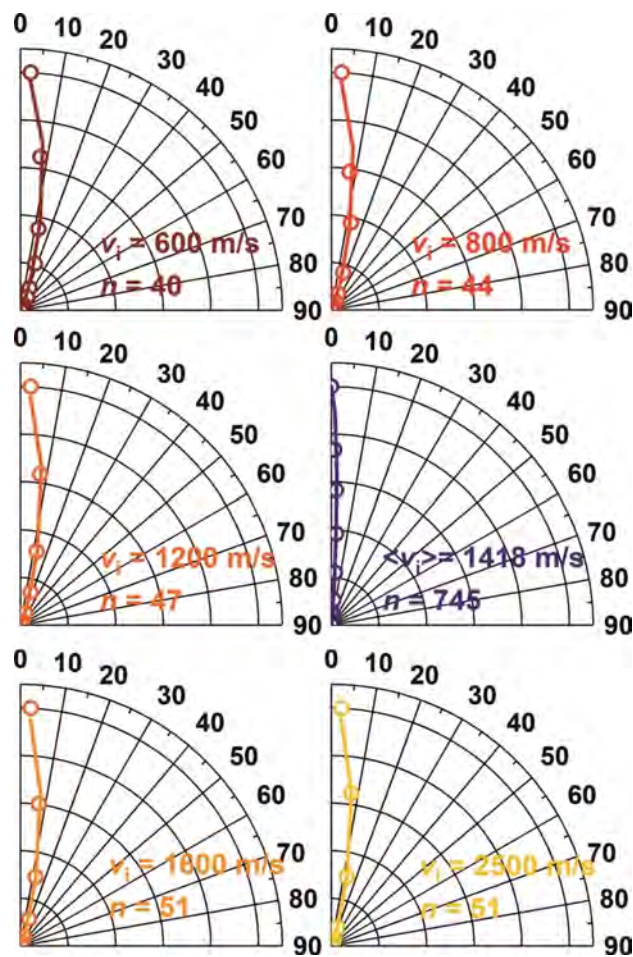


Figure 2. Polar angular distributions of NO molecules after scattering off a 300 K graphene surface, initial speeds as indicated. Blue data is an experimental angular distribution with an initial NO velocity of 1418 m s^{-1} , and a width of $\sim 190 \text{ m s}^{-1}$. All data fitted to a $\cos^n\theta$ function, with the fitting parameter n indicated.

kinetic energies (1 eV) with scattering distributions close to the specular angle.^[12] Studying the scattering of N_2 off graphite at a range of incidence angles, Hase and co-workers found that scattering preferentially occurs close to the specular angle (but at slightly larger angles relative to the surface normal) and with fairly narrow angular distributions,^[16] matching well the narrow scattering in the experiments here.

The wider polar angle distributions at lower incoming kinetic energies can also be observed in Figure 3, which shows the correlation between the polar angle and the final speed of

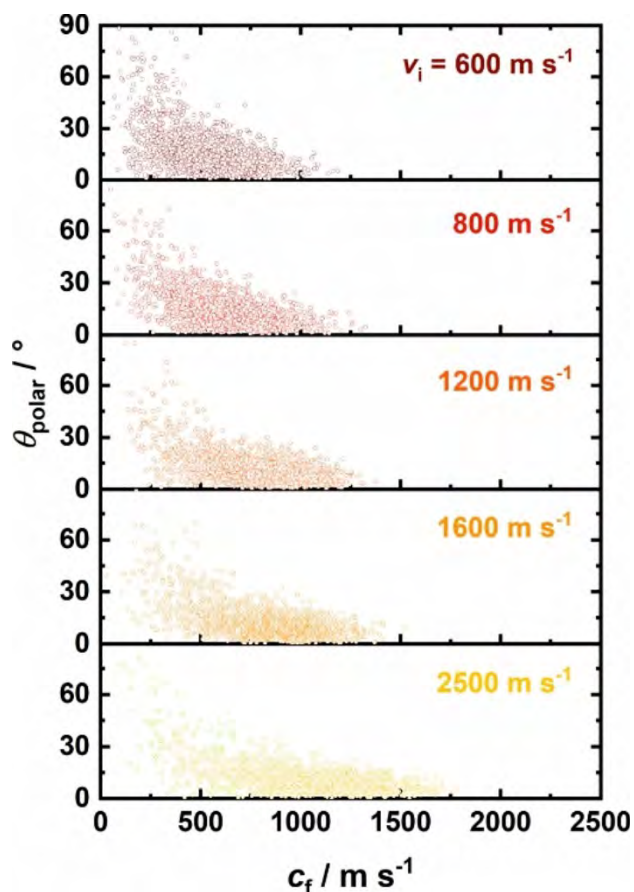


Figure 3. Polar angles θ_{polar} as a function of the final speed of the scattered NO molecules for the five different initial speeds as indicated.

the scattered NO molecules (but – ignoring the y-axis – also shows the speed distribution and its shift towards speeds higher than the incoming speed which has already been better illustrated in Figure 1). The downward trend (or slope) for all incoming speeds shows that scattering along the surface normal retains the most kinetic energy, while more energy is lost to rotations or the graphene lattice vibrations when the NO scatters away from the surface normal.

There are several distinct scattering mechanisms when the NO interacts with the graphene surface which largely depend on the incoming velocity, with some examples being shown in Figure 4. Previous studies have demonstrated that NO scatters off (a number of different) surfaces via two different mechanisms, namely an inelastic component which dominates at high incidence energies, and a trapping-desorption mechanism which dominates at low incidence energies and glancing angles.^[21,23,24] A typical result of the NO scattering with higher initial velocities is a single ‘bounce’ off the graphene surface with very little rotation of the NO molecule itself, resulting in the almost straight yellow line in Figure 4 for an initial velocity of 2500 m s^{-1} . At lower initial velocities, a higher likelihood of trapping on the graphene surface can be observed, either 1) trapping for a short time, during which the NO bounces several times on the surface before being released into the vacuum as

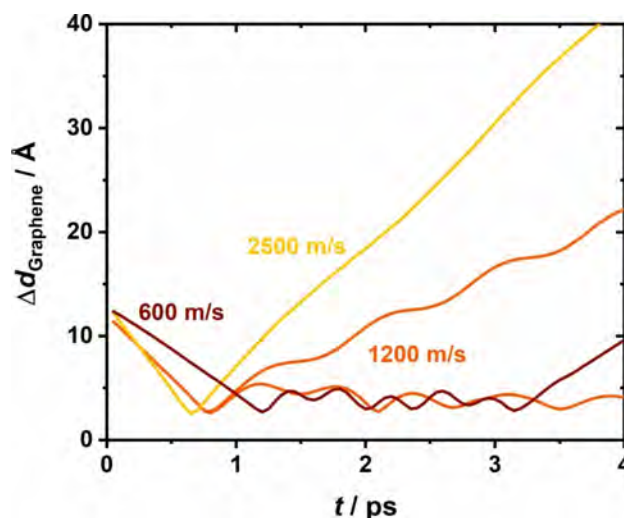


Figure 4. Four different but characteristic trajectories of NO molecules scattering off graphene. Shown is the distance between the N atom (and not the center-of-mass of NO, in order to highlight rotational effects) and the average height of the six closest C atoms in graphene (not necessarily a hexagon) as a function of time. The 2500 m s^{-1} trajectory undergoes direct scattering, while the 600 m s^{-1} trajectory shows trapping-desorption behaviour. The two 1200 m s^{-1} trajectories (with the same initial slope) undergo direct scattering (yielding a rotationally excited NO) or permanent trapping (within the simulation time of 4 ps).

is the case for the 600 m s^{-1} initial velocity trajectory, or 2) the NO can be trapped for the entire simulation duration (4 ps) as shown for the second 1200 m s^{-1} trajectory. Previous work also displayed these three scattering pathways although using longer simulation times of 10 ps and 25 ps.^[15–17] Evidence from experimental work suggests that the majority of those molecules which are ‘trapped’ at the end of a simulation run do eventually leave the surface (at adsorption energies a fraction of the thermal energy, residence times are likely to be short) and do not thermalize at the surface.^[15] Theoretical work involving O_2 scattering off graphite demonstrated that around 60% of the molecules scattered with just a single bounce and a further 20% underwent multiple bounces.^[17]

Permanent trapping of NO at the surface is more likely to occur at lower initial velocities where there is less chance of the NO having sufficient energy to overcome the attractive van der Waals (vdW) forces after rebound, as shown in Figure 5. As is expected, the higher the initial velocity, the lower the chance of trapping. Interestingly, we also observe that for the five highest initial velocities, the rotationally excited molecules seem to have higher trapping probabilities (despite the initial kinetic energy of the NO molecules with and without rotational excitation being the same). A possible reason for this is that the rotating molecules are more likely to approach the graphene surface in a ‘side-on’ configuration, which would lead to a greater likelihood for the vdW forces to ‘take a hold’ of the NO. Another reason for this increased trapping could be that the rotating molecules are likely to scatter under a wider polar angle and hence spend more time close to the surface compared to NO molecules that scatter closer to the surface

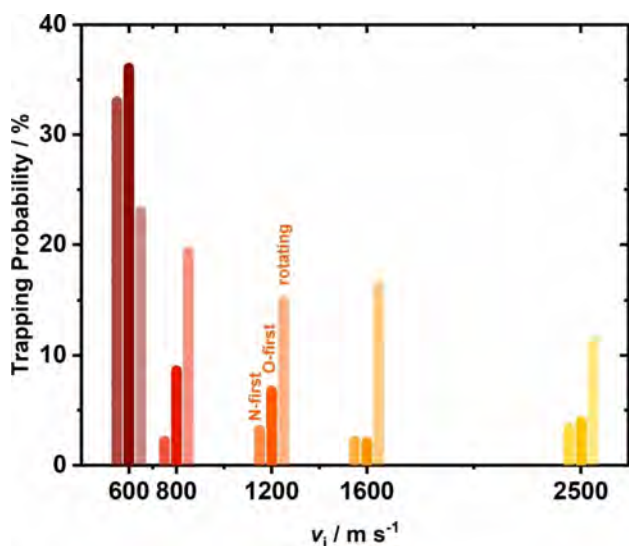


Figure 5. Trapping probabilities for collisions of NO molecules with graphene for the five indicated initial speeds, and separated for N-first and O-first orientation (without rotation), and NO molecules with a thermal rotational state distribution at 80 K.

normal, again increasing the likelihood of vdW interactions between the graphene surface and the NO to trap the nitric oxide. Previous work has shown that trapping increases in likelihood as the incidence angle increases,^[15] this suggests the increased trapping at lower velocities and in case of rotating molecules are indeed due to the vdW interactions as these effects would be felt more strongly at larger incidence angles. Research at even longer timescales (25 ps) also shows trapping probabilities increasing at lower velocities and higher incidence angles.^[16]

The final rotational state distributions after scattering off the graphene surface shown in Figure 6 reveal two findings. Firstly, the faster initial velocities result in higher rotational energy levels being populated, i.e. translational motion is coupled to rotational motion. Secondly, the initially rotationally excited molecules also have a higher rotational energy after collisions. Research by Hase and co-workers suggest that energy transfer is slightly dependent on incident velocity with a slightly higher proportion of energy going into rotations at lower velocities.^[16] If we focus on the 1600 m s^{-1} and 2500 m s^{-1} trajectories for the rotating NO molecules, there appears to be evidence for rotational rainbows, most interestingly in the case for the 2500 m s^{-1} which looks to display a 'double rainbow'. Rotational rainbows from NO scattering have been observed experimentally in both the gas phase^[27] and from solid surfaces.^[28] Theoretical studies have shown the presence of rotational rainbows off graphite, though only at high surface temperatures.^[18,19] Seminal studies on the scattering of NO off Ag(111) have also found evidence for rotational rainbows.^[29,30] Later studies involving NO on Ag(111) concluded that the orientation of the incoming molecule has an effect on the prominence of rotational rainbows, perhaps explaining why the rainbows are better seen in the simulations with rotating NO.^[31]

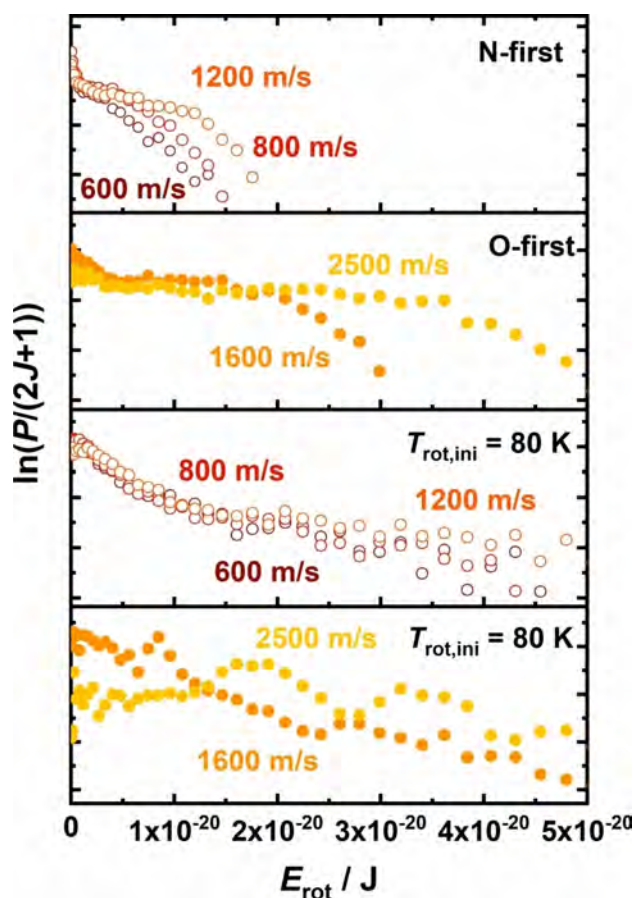


Figure 6. Selected rotational state distributions of NO radicals scattered off graphene. Top-two panels for N-first and O-first orientation without initial rotational excitation, bottom-two panels for initial thermal 80 K rotational distributions. Open symbols for 600, 800, and 1200 m s^{-1} , closed symbols for 1600 and 2500 m s^{-1} .

Studies of NO off graphite found that the NO is fully rotationally accommodated at surface temperatures below 170 K and scatters off with a rotational distribution that can be described by the surface temperature. Above 250 K, however, the NO is only partially accommodated and its rotational distribution can often not be described by a single temperature.^[22,23] It was also found that in the case of NO off Ag(111) at low rotational levels ($J < 20$), a Boltzmann-like distribution can be observed, followed by higher populations again at higher J levels similar to our results shown in Figure 6, thus making it impossible to assign one single rotational temperature to the scattered NO molecules.

Figure 7 shows the height of the N atom in NO above the average of the six closest C atoms at the turning point of the NO (i.e. at the closest approach) as a function of the final velocity of that NO molecule. A clear inverse correlation can be seen between the shortest distance and the final velocity. Despite the graphene surface not being perfectly flat with shallow peaks and troughs due to surface phonons (leading to slight variations in the shortest distance), it can be assumed that this inverse correlation is due to those NO radicals which

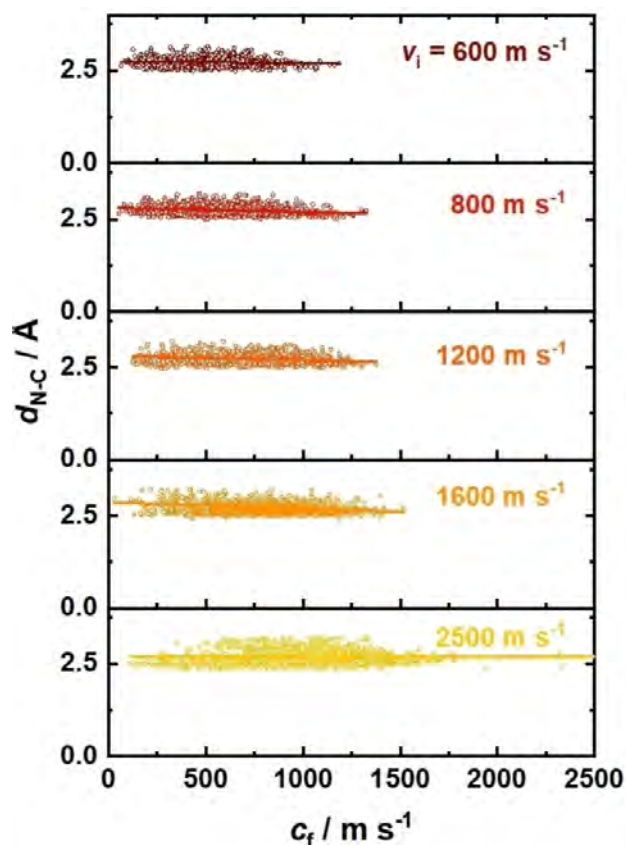


Figure 7. Shortest distance between the N atom of NO and the average of six closest C atoms in graphene at the turning point as a function of final speed, with the linear fit only as a guide to the eye. All data for N-first orientation, but data is very similar for O-first orientation.

happen to get closer to the graphene surface experiencing a greater repulsive force, resulting in a faster scattering velocity.

Conclusions

In summary, NO scattering off graphene using MD simulations qualitatively agrees with the previous experiments in that the more energy the NO has initially, the higher the energy lost as a ratio of the total initial energy, i.e. a larger fraction of energy is lost to graphene. Separate modes can be seen once the NO collides with the graphene in both direct scattering which is dominant at higher incoming velocities, and trapping/multiple bounces dominating at lower incidence velocities. In terms of trapping probabilities, the likelihood of trapping greatly increased at lower incidence velocities but also for the rotating NO at each initial velocity, with the exception of 600 m s^{-1} . Narrow polar angle distributions were observed, with these

distributions becoming narrower as the initial velocity of the NO increased; those narrow angular distributions confirmed that we did not miss in our experimental work, in which we are not able to detect the whole 2π hemisphere above the surface, any contributions to the overall distribution. We detected a range of turning points for each of the five monoenergetic initial velocities, and these turning points correlate with the final velocity such that the closer the approach, the faster the final velocity. Two features stand out in the rotational distributions, namely 1) the translational energy of the NO is converted to rotational energy as seen by the fact that the higher the initial velocity, the higher the rotational energy levels populated, and 2) some evidence at higher incidence velocities for rotational rainbows. These simulations trigger us to perform further laboratory experiments at different initial velocities, which will also allow us to extract residence times at the surface.

Methodology

The molecular dynamics simulations described here were performed within the DL_POLY Classic suite using a combination of force fields.^[32] A simulation box was selected with a 120° rhombus as a base in the x - y plane of length 17.3 \AA each and a z dimension perpendicular to the x - y plane of length 45 \AA . Periodic boundary conditions were applied along the x - y plane, but with no periodicity in the z dimension. The metal substrate was formed of a $6 \times 6 \times 6$ array of gold atoms (with only the bottom layer being frozen in position, i.e. those Au atoms furthest away from the surface) whose interactions were described by a Gupta potential with parameters shown in Table 2.^[33]

98 carbon atoms were positioned in a hexagonal 2D network in the x - y plane on top of the gold substrate. The bonds in the graphene sheet were described by a harmonic potential (rather than fixed bond lengths) to accurately reflect any compressions and stretches in the bonds as the NO collides with the graphene surface. A Morse bond potential as per equation 2 described the C–C bonds

$$V(r) = D[e^{-\alpha(r-r_0)} - 1]^2 \quad (2)$$

with parameters proposed by Kalosakas and co-workers,^[34] using the accepted carbon-carbon internuclear distance in graphene of 1.42 \AA , with $D = 5.7 \text{ eV}$ and $\alpha = 1.96 \text{ \AA}^{-1}$. This force field was selected as it has been derived from first principles, accurately describes the interactions in graphene and is suitable for atomistic simulations.

Angles and dihedrals were described by quartic and cosine functions, respectively, of the form (equations 3 and 4):

$$V_b(\theta) = \frac{k}{2} \left(\theta - \frac{2\pi}{3} \right)^2 - \frac{k'}{3} \left(\theta - \frac{2\pi}{3} \right)^3 \quad (3)$$

Table 2. Parameters used for the Gupta potential to describe interactions in gold.^[33]

λ	μ	$\alpha_\infty[\text{eV}]$	ζ	n_0	δ	$\beta_\infty[\text{eV}]$	γ	Δ	η	$R_\infty[\text{\AA}]$	ρ_0	ν	ξ
12.728	3.173	0.1730	6.5149	-1.234	1.593	2.7565	0.628	-2.041	1.952	2.927	0.144	6.247	3.330

$$V_r(\omega) = \frac{1}{2}V_2[1 - \cos(2\omega)] \quad (4)$$

where $k = 7.0 \text{ eV rad}^{-2}$ and $k' = 4.0 \text{ eV rad}^{-3}$, and $V_2 = 0.23 \text{ eV}$.^[35]

Non-bonding interactions were described by Lennard-Jones 12–6 potentials of the form

$$U(r) = 4\epsilon \left[\left(\frac{\sigma}{r} \right)^{12} - \left(\frac{\sigma}{r} \right)^6 \right] \quad (5)$$

with all parameters given by the universal force field set out by W. M. Skiff and co-workers,^[36] with the exception of the gold and graphene interaction being developed by E. E. Helgee and A. Isacson.^[37] Respective values are provided in Table 3. We stress here that we have *not* benchmarked these potentials against ab initio calculations which would have likely yielded a much better potential,^[16] and this possible discrepancy is one of the contributing factors for the only qualitative agreements between the simulations and experiments. Lorentz-Berthelot combining rules were applied for interactions between unlike atoms. The Lennard-Jones 12–6 potential was only applied to C–C interactions of carbon atoms at least four C–C bonds apart, i.e. not yet described by Morse bond potentials or angular or dihedral potentials.

The gold and graphene were relaxed and equilibrated by running simulations in an NVT ensemble regulated to 300 K by a Nosé-Hoover thermostat for 4 ns with a relaxation constant of 1 ps prior to the addition of a nitric oxide molecule. The equilibrated distance between the graphene and the top-layer of Au atoms is around 3 Å.

A single NO molecule was then positioned above the graphene surface, and its bond potential was also defined by a Morse potential with parameters $D_e = 6.61736 \text{ eV}$, $\beta = 2.636 \text{ \AA}^{-1}$ and $r_e = 1.151 \text{ \AA}$.^[38] Placing such a single NO molecule in a randomly selected position in the x - y plane $\sim 12 \text{ \AA}$ above the graphene is sufficient as interatomic forces were truncated after 7 Å. Both the N and O atom were then given a velocity of 600, 800, 1200, 1600, or 2500 m s^{-1} along the z axis towards the graphene (same geometry as in our experiments), i.e. no vibrational excitation was given to the NO molecule, just as no $\text{NO}(v=1)$ is expected in the cold molecular beam in our experiments. While these velocities do not match our experimental velocity exactly, they cover a range of velocities achievable in molecular beam experiments, and match our experimental kinetic energy to $< 0.1 \text{ eV}$.

Three cases in terms of orientation and rotational excitation of the nitric oxide were investigated: 1) no rotational excitation, NO aligned along the surface normal with the N-oriented towards the surface (see Figure 1); 2) same as (1), but with O facing the surface; 3) with a rotational distribution representative of a thermal 80 K sample (roughly equivalent to a molecular beam) *in addition* to the translational energy, and a random orientation in space. 2000 trajectories were run for each orientation/rotational excitation case, with the NO originating from a different position within the x - y

plane for every run in each of those cases, giving 6000 trajectories in total for each of the five velocities, making a total of 30,000 trajectories.

The molecular dynamics simulations were run with a timestep of 1 fs for 4 ps (8 ps for 600 m s^{-1} simulations, all starting after the 4 ns equilibration of the graphene and gold). After the NO has interacted with the graphene, it was registered once traversing a virtual plane 8 Å above the graphene, where there is no longer any interaction between the graphene and the NO. Properties such as the positions and velocity components of both the N and O atoms in all three dimensions separately were recorded. Molecular speeds were extracted from center-of-mass shifts per unit time and binned in 20 m s^{-1} wide intervals. The simulation parameters are schematically shown in Figure 8.

Acknowledgements

We thank the Royal Society for funding (IEC\R2\181028), Christopher Lester for help with the Molecular Dynamics simulations, and Emmanuel Nwokedi and Dafydd Marshman for performing some of the simulation runs.

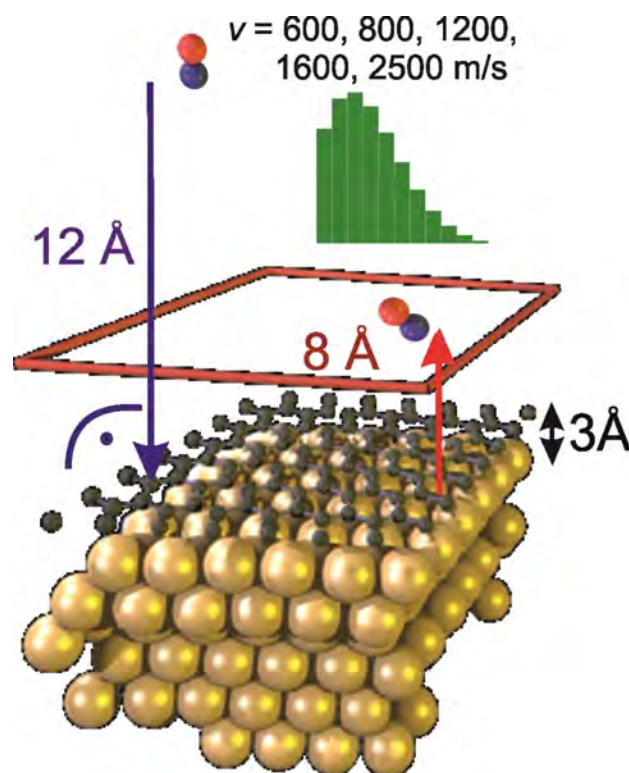


Figure 8. Schematic of input parameter of the molecular dynamics simulations. NO molecules are placed 12 Å above the graphene surface and given a certain velocity, and in some cases rotational excitation. They are directed along the surface normal towards a random position on the graphene, from where they scatter back before they are recorded when traversing a virtual plane 8 Å above the surface.

Table 3. Parameters for the van der Waals interactions.

Interaction	ϵ [eV]	σ [Å]
C–C	0.004553	3.431
C–O	0.003442	3.2745
C–N	0.003691	3.346
N–Au	0.00225	3.0972
C–Au	0.0341	3.003
O–Au	0.002098	3.0259

Conflict of Interest

The authors declare no conflict of interest.

Data Availability Statement

The data that support the findings of this study are available from the corresponding author upon reasonable request.

Keywords: graphene · scattering · molecular dynamics · surface scattering · nitric oxide

- [1] P. R. Arantes, A. Saha, G. Palermo, *ACS Cent. Sci.* **2020**, *6*, 1654.
- [2] D. J. Tildesley, M. P. Allen, *Computer Simulation of Liquids*, Clarendon Press, Oxford, **1987**.
- [3] C. Verma, H. Lgaz, D. K. Verma, E. E. Ebenso, I. Bahadur, M. A. Quraishi, *J. Mol. Liq.* **2018**, *260*, 99.
- [4] E.-H. Patel, M. A. Williams, S. P. K. Koehler, *J. Phys. Chem. B* **2017**, *121*, 233.
- [5] J. N. Murrell, S. D. Bosana, *Chem. Soc. Rev.* **1992**, *21*, 17.
- [6] A. Monari, J.-L. Rivail, X. Assfeld, *Acc. Chem. Res.* **2013**, *46*, 596.
- [7] T. V. Albu, J. C. Corchado, D. G. Truhlar, *J. Phys. Chem. A* **2001**, *105*, 8465.
- [8] T. D. Kühne, *Wiley Interdiscip. Rev. Comput. Mol. Sci.* **2014**, *4*, 391.
- [9] T. Greenwood, S. P. K. Koehler, *J. Phys. Chem. C* **2021**, *125*, 17853.
- [10] R. Nieman, A. J. A. Aquino, H. Lischka, *J. Phys. Chem. A* **2021**, *125*, 1152.
- [11] H. Y. Jiang, M. Kammler, F. Z. Ding, Y. Dorenkamp, F. R. Manby, A. M. Wodtke, T. F. Miller, A. Kandratenka, O. Bünermann, *Science* **2019**, *364*, 379.
- [12] H. Jiang, X. Tao, M. Kammler, F. Ding, A. M. Wodtke, A. Kandratenka, T. F. Miller III, O. Bünermann, *J. Phys. Chem. Lett.* **2021**, *12*, 1991.
- [13] R. Nieman, R. Spezia, B. Jayee, T. K. Minton, W. L. Hase, H. Guo, *J. Chem. Phys.* **2020**, *153*, 184702.
- [14] B. Jayee, R. Nieman, T. K. Minton, W. L. Hase, H. Guo, *J. Phys. Chem. C* **2021**, *125*, 9795.
- [15] N. A. Mehta, V. J. Murray, C. Xu, D. A. Levin, T. K. Minton, *J. Phys. Chem. C* **2018**, *122*, 9859.
- [16] M. Majumder, H. N. Bhandari, S. Pratihar, W. L. Hase, *J. Phys. Chem. C* **2018**, *122*, 612.
- [17] A. R. Santamaría, M. Alducin, R. D. Muiño, J. I. Juaristi, *J. Phys. Chem. C* **2019**, *123*, 31094.
- [18] J. B. C. Pettersson, G. Nyman, L. Holmlid, *J. Chem. Phys.* **1988**, *89*, 6963.
- [19] G. Nyman, L. Holmlid, J. B. C. Pettersson, *J. Chem. Phys.* **1990**, *93*, 845.
- [20] J. Oh, T. Kondo, K. Arakawa, Y. Saito, W. W. Hayes, J. R. Manson, J. Nakamura, *J. Phys. Chem. A* **2011**, *115*, 7089.
- [21] J. A. Barker, D. J. Auerbach, *Surf. Sci. Rep.* **1984**, *4*, 1.
- [22] M. C. Lin, G. Ertl, *Annu. Rev. Phys. Chem.* **1986**, *37*, 587.
- [23] J. Häger, M. Fink, H. Walther, *Surf. Sci.* **2004**, *550*, 35.
- [24] F. Frenkel, J. Häger, W. Krieger, H. Walther, G. Ertl, J. Segner, W. Vielhaber, *Chem. Phys. Lett.* **1982**, *90*, 225.
- [25] C. T. Rettner, E. K. Schweizer, C. B. Mullins, *J. Chem. Phys.* **1989**, *90*, 3800.
- [26] A. Rodríguez-Fernández, L. Bonnet, C. Crespos, P. Larrégaray, R. Díez Muiño, *J. Phys. Chem. Lett.* **2019**, *10*, 7629.
- [27] X. D. Wang, P. A. Robertson, F. J. J. Cascarini, M. S. Quinn, J. W. McManus, A. J. Orr-Ewing, *J. Phys. Chem. A* **2019**, *123*, 7758.
- [28] A. E. Wiskerke, C. A. Taatjes, A. W. Kleyn, R. J. W. E. Lahaye, S. Stolte, D. K. Bronnikov, B. E. Hayden, *Faraday Discuss.* **1993**, *96*, 297.
- [29] A. W. Kleyn, A. C. Luntz, D. J. Auerbach, *Surf. Sci.* **1982**, *117*, 33.
- [30] A. W. Kleyn, A. C. Luntz, D. J. Auerbach, *Phys. Rev. Lett.* **1981**, *47*, 1169.
- [31] A. W. Kleyn, *Surf. Rev. Lett.* **1994**, *1*, 157.
- [32] I. T. Todorov, W. Smith, K. Trachenko, M. T. Dove, *J. Mater. Chem.* **2006**, *16*, 1911.
- [33] J. T. Titantah, M. Karttunen, *Eur. Phys. J. B* **2013**, *86*, 1.
- [34] G. Kalosakas, N. N. Lathiotakis, C. Galiotis, K. Papagelis, *J. Appl. Phys.* **2013**, *113*, 134307.
- [35] Z. G. Fthenakis, G. Kalosakas, G. D. Chatzidakis, C. Galiotis, K. Papagelis, N. N. Lathiotakis, *Phys. Chem. Chem. Phys.* **2017**, *19*, 30925.
- [36] A. K. Rappe, C. J. Casewit, K. S. Colwell, W. A. Goddard, W. M. Skiff Uff, *J. Am. Chem. Soc.* **1992**, *114*, 10024.
- [37] E. E. Helgee, A. Isacsson, *AIP Adv.* **2016**, *6*, 015210.
- [38] S. Mishra, M. Meuwly, *Biophys. J.* **2009**, *96*, 2105.

Manuscript received: March 31, 2022
Revised manuscript received: July 25, 2022
Accepted manuscript online: July 27, 2022
Version of record online: September 1, 2022

Velocity-Selected Rotational State Distributions of Nitric Oxide Scattered off Graphene Revealed by Surface-Velocity Map Imaging

Published as part of *The Journal of Physical Chemistry virtual special issue "Paul L. Houston Festschrift"*.

Thomas Greenwood, Huda AlSalem, and Sven P. K. Koehler*



Cite This: *J. Phys. Chem. A* 2023, 127, 1124–1129



Read Online

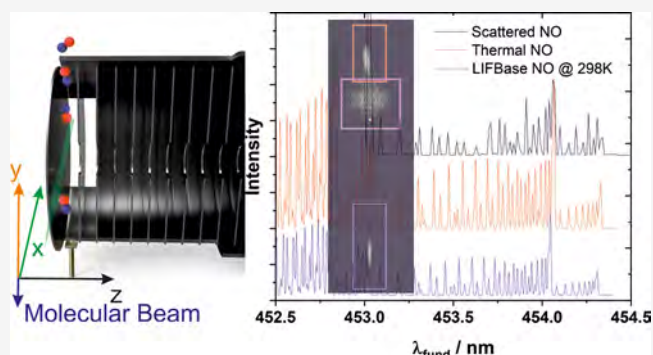
ACCESS |

Metrics & More

Article Recommendations

Supporting Information

ABSTRACT: We report velocity-dependent internal energy distributions of nitric oxide molecules, NO, scattered off graphene supported on gold to further explore the dynamics of the collision process between NO radicals and graphene. These experiments were performed by directing a molecular beam of NO onto graphene in a surface-velocity map imaging setup, which allowed us to record internal energy distributions of the NO radicals as a function of their velocity. We do not observe bond formation but (1) major contributions from direct inelastic scattering and (2) a smaller trapping–desorption component where some physisorbed NO molecules have residence times on the order of microseconds. This is in agreement with our classical molecular dynamics simulations which also observe a small proportion of two- and multi-bounce collisions events but likewise a small proportion of NO radicals trapped at the surface for the entire length of the molecular dynamics simulations (a few picoseconds). Despite a collision energy of 0.31 eV, which would be sufficient to populate NO($v = 1$), we do not detect vibrationally excited nitric oxide.



1. INTRODUCTION

Internal state distributions of radicals after reactions (where reactions include both chemical reactions and pure collision processes) allow us a glimpse of the detailed dynamics of such processes.^{1,2} This is because knowing the degrees of freedom into which some of the available energy is channeled enables us to learn about the flow of energy during the entire reaction and to draw conclusions from that information with regard to the actual dynamics of the process.³ Most famously, the Polanyi rules (broadly speaking) allow us to determine the position of the transition state of a chemical reaction along the reaction coordinate based on the vibrational state distribution of the products.⁴ Equally, the rotational state distributions can yield information about the geometry of a transition state,^{5,6} and phenomena such as rainbow scattering can provide insight into oscillatory behavior during reactions.^{7,8}

One of the collision processes that has garnered much attention in the past few years is between atoms or molecules and graphene, i.e., the scattering off a graphene surface. The modification of graphene by chemical reactions on its surface to form covalent bonds is technologically important as such functionalizations can introduce a tunable band gap (pristine graphene is a zero band gap material),^{9,10} and scattering studies of graphene can reveal the fundamentals of the collision process and the potential bond-formation process on the graphene surface. While much of the experimental and

computational work focused on translational energy and angular distributions of the scattered particles (the only possible degree of freedom for atomic collisions),^{11–16} Juaristi and co-workers,¹⁷ Rutigliano and Pirani,¹⁸ and Hase and co-workers¹⁹ also explored the rotational state distribution of O₂ and N₂ scattered off graphite. Hase and co-workers found that only a small fraction of the available energy is channeled into rotations but none into vibrations. Our group has previously investigated the translational energy distribution of NO after scattering off graphene supported on gold and detected a significant loss of ~80% of the molecules' kinetic energy and a surprisingly narrow angular distribution.²⁰ In addition to this, we can also learn from state-resolved scattering studies off graphite.^{8,21} Walther and co-workers found that cold surfaces could lead to a cooling of the rotational temperature of the NO radicals in a rotationally hot molecular beam after collision with the graphite;²² however, a cold molecular beam of NO tends to result in a hotter rotational temperature for those NO

Received: August 30, 2022

Revised: January 9, 2023

Published: January 26, 2023



radicals that are quasi-specularly scattered and an even hotter rotational distribution close to the surface temperature for the diffusely scattered NO molecules, i.e., the trapping–desorption component.²³ Higher surface temperatures lead to hotter rotational temperatures of the specularly scattered NO.²⁴ The same group found that at cryogenic graphite temperatures, the rotational temperature of the scattered NO is almost constant, and the group concluded that the formation of a short-lived collision complex which unimolecularly decomposes is responsible for this almost constant rotational distribution.²⁵ Nyman et al. also found a rotational temperature of the NO after collision with graphite colder than the surface temperature (rotational cooling) in their modeling studies and even rotational rainbows at higher surface temperatures.²⁶

We hence set out to record rotational state distributions of nitric oxide radicals after collisions with graphene in our surface-velocity map imaging (VMI) setup.^{27,28} VMI (typically applied to gas-phase dynamics) has recently been applied more and more to study surface dynamics,^{29–33} allowing one to derive speed and angular distributions of the scattered products. A resonance-enhanced multiphoton ionization (REMPI) scheme is frequently applied in VMI studies, guaranteeing state-selectivity. The beauty of combining VMI with REMPI in these surface scattering studies here is due to the fact that while REMPI spectra traditionally integrate over the entire ion yield, we can now define regions of interest (ROI) in the VM images (which record the velocity information) and only sum over the ion yield in those ROIs, corresponding in our case to NO radicals flying with a certain speed in a certain direction.³⁴ Since we measured the velocity distributions of NO after scattering off graphene already,²⁰ we now investigate the rotational state distributions of the various components that make up the scattered cloud (i.e., inelastically scattered and trapping-desorbed NO) in the same experiment to derive information about the collision dynamics of NO radicals with graphene.

2. METHODOLOGY

Our surface-VMI apparatus has been described previously,²⁰ but specifics to the measurement of velocity-selected rotational state distributions are briefly described here. The skimmed (Beam Dynamics, 0.5 mm) molecular beam of ~2% NO in He (a General Valve series 9 valve is used; the fwhm of the kinetic energy distribution is ~0.08 eV; see Figure S1) is expanded into the main chamber housing the graphene surface (at room temperature) at a base pressure of 5×10^{-9} Torr, increasing to 3×10^{-8} Torr when the beam is on. The NO molecules fly toward the graphene along the surface normal and are intersected by the REMPI laser at right angle in the center of the VMI chamber twice, both on the way toward the surface and after the scattering event. Nitric oxide molecules are ionized in a (1 + 1) REMPI scheme (via the $A^2\Sigma$ state) using the frequency-doubled output of a Radiant Dyes NarrowScan laser running on coumarin 450, yielding pulse energies of ~0.8 mJ at around 227 nm with a resolution of around 0.08 cm^{-1} . The doubled dye laser output is unfocused due to the ease with which NO can be ionized. The ionized NO particles are then accelerated toward the position-sensitive detector (in a direction normal to the plane spanned by the molecular beam and the laser; see Figure S3) where the images are recorded by a NET GmbH CMOS camera. The time at which the laser fires in relation to the opening of the molecular beam is adjusted via an SRS DG645 delay generator. This

adjustment of the timing is necessary to select for events in the scattering process which are separated in time such as (1) the molecular beam on the way down to the surface or (2) once it has scattered which is usually 100–300 μs later. Due to the opening time of the molecular beam (~300 μs), the signal on the detector can be a combination of molecular beam and scattered molecules, but crucially, NO molecules in the molecular beam (which are flying “downward” in the lab frame) appear in the lower half of the velocity-mapped image, i.e., below our zero velocity pixel, while scattered NO molecules with an upward velocity component in our laboratory frame appear in the upper half of the detector. We can thus differentiate the various components of the beam and the scattering event not only by varying the delay time between the molecular beam and the REMPI laser but in a much better way by observing certain ROIs on the detector. We hence extract rotational distributions of scattered NO molecules for (1) a fast and narrow spot presumably due to direct inelastic scattering and (2) a much weaker component likely due to trapping–desorption which appears as a broad and slower diffuse cloud in the images, and we thus integrate over the ion signals on the imaging detector for the various components separately by concentrating on the ROI relevant to each component.

The accompanying classical molecular dynamics simulations have been described previously.³⁵ The gold substrate was formed of a $6 \times 6 \times 6$ array of gold atoms, and 98 carbon atoms were positioned in a hexagonal 2D network in the x – y plane on top of the gold substrate. Periodic boundary conditions were applied along the x – y plane but with no periodicity in the z dimension. We stress that these are purely classical calculations which do not account for the quantum behavior of molecular motions.

3. RESULTS AND DISCUSSION

Before delving into the rotational spectra, we first briefly discuss the various NO species we investigated. As discussed in the Methodology section, the various rotational spectra were collected by integrating the ion signal only over certain ROI on the detector. These regions are shown in Figure 1, which itself is a composite image consisting of individual images recorded at different delay times between the molecular beam and the REMPI laser, purely for the benefit of highlighting the different components.

One can observe the signal from the molecular beam itself (within the blue rectangle in Figure 1), the directly scattered component (red), and a slow (but crucially upward in the lab frame, pink) component. This slower component, which we assign to a trapping desorbing mechanism, is much weaker than the scattered component, and we in fact failed to observe it in our previous work.²⁰ While it appears as if some components may overlap in the images, most notably the signal for the direct inelastic scattering and the slower trapping component, varying the delay time between the molecular beam and the REMPI laser allows us to separate the integrated signals. Relative to the molecular beam itself, which was recorded at its peak in the time-of-flight profile, the directly scattered NO signal was recorded 100 μs after the molecular beam in order to image the “same” NO molecules that were imaged in the beam initially, and the trapping–desorption component was recorded a further 300 μs after the directly scattered NO.

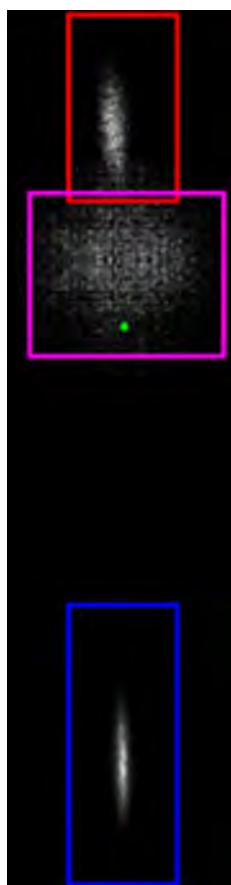


Figure 1. Images of the various NO components along with their respective regions of interest: blue for NO in the molecular beam at a relative time (t_{rel}) of 0 μs , red for scattered NO ($t_{\text{rel}} + 100 \mu\text{s}$), pink for the trapping-desorption component ($t_{\text{rel}} + 400 \mu\text{s}$), and the green dot indicating our center spot relating to zero overall velocity in the x and y dimensions.

The trapping-desorption component is rather wide such that not all ions detected follow true VMI conditions, and due to the long image acquisition time, noise and background ions are appearing.

Table 1 shows the average velocities of those events; not shown in the table is the thermal gas-phase background NO

Table 1. Various NO Species Detected in Our Experiment with Their Respective Speeds at Peak Delay Times^a

event	beam	scatter	trapping-desorption
$v, \text{m s}^{-1}$	1428 ± 114	638 ± 108	184 ± 161

^aThe beam is naturally traveling in opposite direction to the scatter and trapping-desorption components.

(see section 4 of the Supporting Information), which has been discussed previously,²⁰ but briefly, nitric oxide gas was admitted into the chamber through a leak valve at a temperature of 298 K. Imaging those thermal background molecules yields a two-dimensional Maxwell-Boltzmann distribution on the detector whose center is taken to be the zero-velocity center of our actual images, i.e., the green dot in Figure 1. A composite image of all components including the thermal background spot is shown in Figure S7 of the Supporting Information, highlighting the difference in position between the thermal background image and the trapping-

desorption components. The three components (molecular beam, direct scatter, trapping-desorption) were velocity-analyzed separately and with respect to the center spot of zero velocity using a conversion factor of 5.1 $\text{m s}^{-1}/\text{pixel}$, fitted to eq 1,

$$F(c) \, dc = A c^3 \exp \frac{-(c - c_0)}{\alpha^2} \, dc \quad (1)$$

where A is a scaling factor and α is related to the width of the distribution,³⁶ and errors are standard errors.

The average translational energy of the Maxwell-Boltzmann distribution of particles originating from a flat surface is $2kT$ (equivalent to $\sim 575 \text{ m s}^{-1}$ for nitric oxide desorbing from a 298 K surface); thus the directly scattered component is despite the large energy loss noticeable faster, while the trapping-desorption component is slower.

Rotationally resolved REMPI spectra were recorded by scanning the laser over the desired wavelength range (at the appropriate delay time) while using the MCP detector in imaging mode and by integrating the ion signal in each of the three ROIs separately for each wavelength. The resulting spectra are then converted to rotational state populations using a relative calibration scheme by means of comparison with a thermal background spectrum in LIFBase as a reference.³⁷ Only the O_{12} and P_{12} branches were recorded to avoid overlapping lines, as in particular the first 20 transitions of the O_{12} branch do not overlap with any other lines. A raw REMPI spectrum of scattered NO is shown in Figure 2, and a composite of a scattered, thermal background and LIFBase simulation spectra are shown in Figure S8 of the Supporting Information.

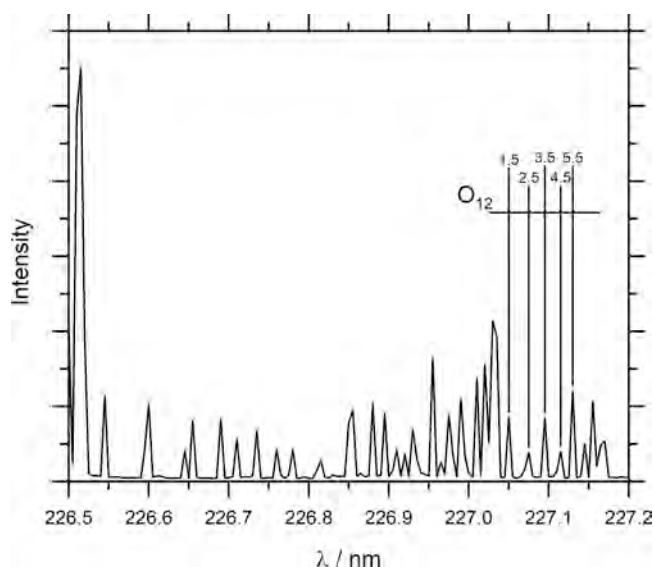


Figure 2. Rotational spectrum of the scattered NO with the relevant lines of the O_{12} branch highlighted.

Once the populations of the rotational energy levels were assigned, Boltzmann plots were created for each branch. Example plots from the O_{12} branch of the scattered NO and the P_{12} branch of the trapping-desorption component are shown in Figure 3.

Rotational temperatures for each component were derived from the gradients of these Boltzmann plots. While there is no reason for either rotational distribution here to follow a

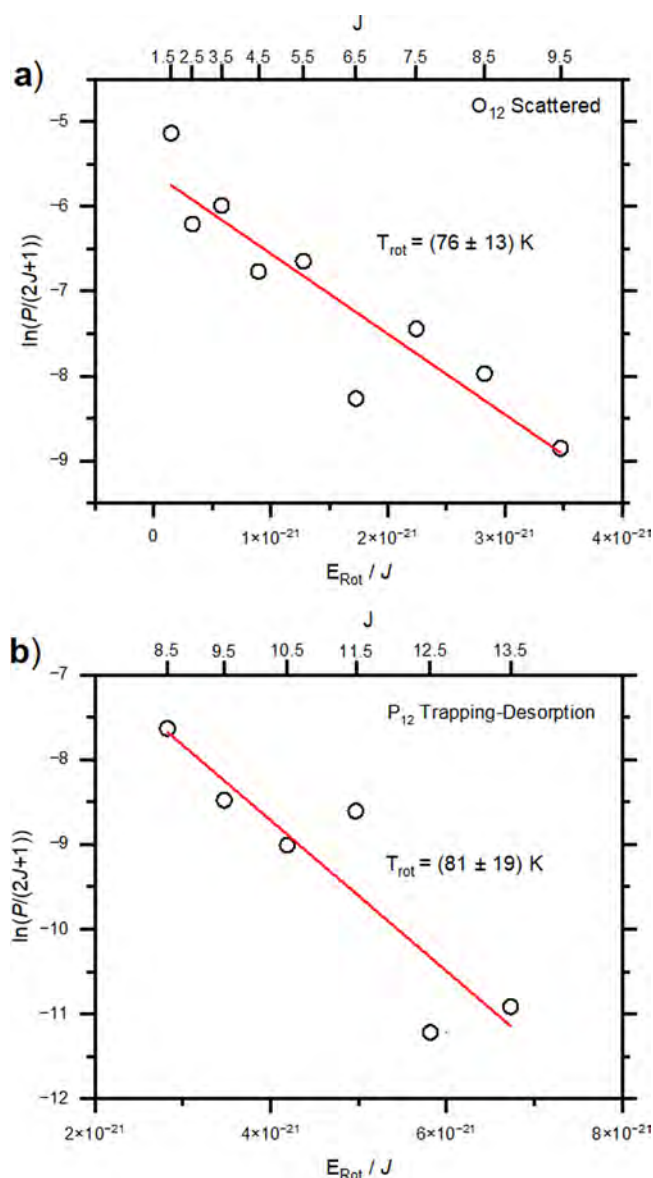


Figure 3. (a) Boltzmann plot of O_{12} branch of the scattered NO. (b) P_{12} branch of the trapping-desorption component.

Boltzmann distribution, the assignment of a single rotational temperature eases comparison between the components. The temperatures of the various NO components are shown in Table 2.

Table 2. Rotational Temperatures of the Various NO Events Derived from the Linear Fits to the Boltzmann Plots in Figure 3^a

event	beam	scatter	trapping-desorption
T_{rot} K	64 ± 11	76 ± 11	81 ± 19

^aErrors are standard errors.

As is clear from the velocities derived from the images and now the rotational temperatures, there are two channels from the scattering of NO, the directly scattered component and a trapping-desorption component. Both components gain some rotational energy, which is modest, but despite the errors discernible. The directly scattered component is likely only

undergoing a single collision with the surface and expectedly does not gain much rotational energy. However, even the trapping-desorption component (despite losing a significant amount of translational energy) does not gain much more rotational energy as compared to the directly scattered component. It appears as if the NO molecules transfer much of their translational energy to the graphene substrate in just a few collisions, but it is possible that only those with a cold(er) rotational temperature are scattered back, while those that are (partly) thermalizing may become trapped, leading to the relatively cold rotational state distribution of the trapping-desorption component. Our previous MD simulations for NO scattering off graphene can shed some light onto that,³⁵ though they do not compare quantitatively and do not reproduce the two well-separated scattered components observed here (directly scattered and trapping-desorption). In the simulations, the majority of NO scatters off graphene directly, undergoing only a single collision, but there is a small fraction of NO molecules that interact with the surface for only a couple of picoseconds before desorbing again (though these do not show up as a separate component in our time-of-flight profiles), presumably undergoing too few collisions to rotationally thermalize.

Directly scattered and diffuse spots for scattered NO have also been recorded after interactions with graphite.²³ A slower diffuse component was observed which was likely to be due to temporary, i.e., nonequilibrium, trapping, similar to our experimental results.

This behavior of incomplete thermalization of NO has also been identified before in the scattering off graphite,^{24,38} where NO only accommodates to the surface temperature up to 170 K, above which the surface temperature and the rotational temperature deviate. However, a direct comparison to our experiments is not entirely justified due to the different properties of graphene vs graphite, of course, but mainly due to the different incidence angles.

A further notable difference, however, is that the rotational temperatures of both components in our study here on graphene are rotationally cooler than previous studies of scattering of NO off graphite at around room temperature, and our values align better with those rotational temperatures measured at graphite temperatures of around 80 K as reported by Häger et al.²⁵ In the case of NO scattered off graphite at 80 K, the resulting rotational temperatures were 88 and 90 K for the directly scattered and trapped NO, respectively, similar to our results, though our experiments were performed at a surface temperature of 298 K; however, incidence angles are not the same in these two studies. It is worth highlighting, though, the fact that in the studies by Häger et al. as well as in our studies here, the rotational temperatures of the two components do not differ much.

While experimental studies of NO scattering off silver have led to rotational rainbows,³⁹ and we have found evidence for those in our MD simulations, no rotational rainbows were observed in this experimental study here or in other experimental studies of NO on graphite.²⁶

4. CONCLUSIONS

A molecular beam of nitric oxide molecules was scattered off graphene supported on gold, and the velocities and internal energy distributions of the scattered NO molecules were probed using a surface-velocity map imaging setup. No bond formation was observed at the graphene surface, and despite

sufficient collision energies of 0.31 eV, no vibrationally excited NO molecules were observed. Two components of scattered NO were observed, namely, (1) a directly scattered component and (2) a trapping–desorption component which had lost a significant proportion of its initial translational energy. This compares at least qualitatively with our previous MD simulations in which most NO molecules collide with the graphene surface only once, but a small fraction undergoes multiple collisions, though in our MD work, this latter component could not be separated clearly from the direct component based on time-of-flight profiles.

Both the direct and the trapping–desorption components gain some rotational energy but are remarkably similar in their rotational temperatures, with the trapping–desorption component only marginally hotter but far away from having reached thermal equilibrium with the surface.

This fairly unusual behavior appears typical for graphene with its perfectly flat structure, but since we were limited to incidence angles along the surface normal and room temperature surfaces in these studies, we intend to perform further studies to shed light onto this behavior in graphene scattering.

■ ASSOCIATED CONTENT

SI Supporting Information

The Supporting Information is available free of charge at <https://pubs.acs.org/doi/10.1021/acs.jpca.2c06196>.

Experimental setup, raw data, molecular beam characterization, calibration of VMI setup and beam positions, and the spectroscopy of nitric oxide (PDF)

■ AUTHOR INFORMATION

Corresponding Author

Sven P. K. Koehler – *Institut für Verfahrenstechnik, Energietechnik und Klimaschutz, Hochschule Hannover, 30459 Hannover, Germany*; orcid.org/0000-0002-6303-6524; Email: sven.koehler@hs-hannover.de

Authors

Thomas Greenwood – *Department of Natural Sciences, Manchester Metropolitan University, Manchester M1 5GD, U.K.*; orcid.org/0000-0002-7723-1259

Huda AlSalem – *Department of Chemistry, College of Science, Princess Nourah bint Abdulrahman University, Riyadh 11671, Saudi Arabia*; orcid.org/0000-0003-0110-7769

Complete contact information is available at: <https://pubs.acs.org/10.1021/acs.jpca.2c06196>

Notes

The authors declare no competing financial interest.

■ ACKNOWLEDGMENTS

We thank the Royal Society for funding (Grant IEC\R2\181028) and Princess Nourah bint Abdulrahman University Researchers Supporting Project (Grant PNURSP2023R185), Princess Nourah bint Abdulrahman University, Riyadh, Saudi Arabia. We also thank Prof Nick Lockyer and Prof Mark Dickinson at The University of Manchester for the loan of a frequency-tripling unit.

■ REFERENCES

- (1) Valentini, J. J. State-to-state chemical reaction dynamics in polyatomic systems: case studies. *Annu. Rev. Phys. Chem.* **2001**, *52*, 15–39.
- (2) Whitehead, J. C. Molecular beam studies of free-radical processes: photodissociation, inelastic and reactive collisions. *Rep. Prog. Phys.* **1996**, *59*, 993–1040.
- (3) Liu, K. Crossed-beam studies of neutral reactions: State-Specific Differential Cross Sections. *Annu. Rev. Phys. Chem.* **2001**, *52*, 139–164.
- (4) Polanyi, J. C. Concepts in Reaction Dynamics. *Acc. Chem. Res.* **1972**, *5*, 161–168.
- (5) Andresen, P.; Luntz, A. C. The chemical dynamics of the reactions of O(3P) with saturated hydrocarbons. I. Experiment. *J. Chem. Phys.* **1980**, *72*, 5842–5850.
- (6) Ausfelder, F.; McKendrick, K. G. The Dynamics of Reactions of O(²P) Atoms with Saturated Hydrocarbons and Related Compounds. *Prog. Reaction Kinet. Mech.* **2000**, *25*, 299–370.
- (7) Xiahou, C.; Connor, J. N. L. Glories, hidden rainbows and nearside-farside interference effects in the angular scattering of the state-to-state H + HD → H₂ + D reaction. *Phys. Chem. Chem. Phys.* **2021**, *23*, 13349–13369.
- (8) Barker, J. A.; Auerbach, D. J. Gas-surface interactions and dynamics; Thermal energy atomic and molecular beam studies. *Surf. Sci. Rep.* **1984**, *4*, 1–99.
- (9) AlSalem, H. S.; Holroyd, C.; Danial Iswan, M.; Horn, A. B.; Denecke, M. A.; Koehler, S. P. K. Characterisation, coverage, and orientation of functionalised graphene using sum-frequency generation spectroscopy. *Phys. Chem. Chem. Phys.* **2018**, *20*, 8962–8967.
- (10) AlSalem, H. S.; Just-Baringo, X.; Larrosa, I.; Monteverde, U.; Jiang, X.; Feng, Y.; Koehler, S. P. K. Evidence for Site-Specific Reversible Hydrogen Adsorption on Graphene by Sum-Frequency Generation Spectroscopy and Density Functional Theory. *J. Phys. Chem. C* **2019**, *123*, 25883–25889.
- (11) Mehta, N. A.; Murray, V. J.; Xu, C.; Levin, D. A.; Minton, T. K. Nonreactive Scattering of N₂ from Layered Graphene Using Molecular Beam Experiments and Molecular Dynamics. *J. Phys. Chem. C* **2018**, *122*, 9859–9874.
- (12) Nieman, R.; Spezia, R.; Jayee, B.; Minton, T. K.; Hase, W. L.; Guo, H. Exploring reactivity and product formation in N(⁴S) collisions with pristine and defected graphene with direct dynamics simulations. *J. Chem. Phys.* **2020**, *153*, 184702.
- (13) Jayee, B.; Nieman, R.; Minton, T. K.; Hase, W. L.; Guo, H. Direct Dynamics Simulations of Hyperthermal O(¹⁵P) Collisions with Pristine, Defected, Oxygenated, and Nitridated Graphene Surfaces. *J. Phys. Chem. C* **2021**, *125*, 9795–9808.
- (14) Nieman, R.; Aquino, A. J. A.; Lischka, H. Exploration of Graphene Defect Reactivity toward a Hydrogen Radical Utilizing a Preactivated Circumcoronene Model. *J. Phys. Chem. A* **2021**, *125*, 1152–1165.
- (15) Oh, J.; Kondo, T.; Arakawa, K.; Saito, Y.; Hayes, W. W.; Manson, J. R.; Nakamura, J. Angular intensity distribution of a molecular oxygen beam scattered from a graphite surface. *J. Phys. Chem. A* **2011**, *115*, 7089–7095.
- (16) Jiang, H. Y.; Kammler, M.; Ding, F. Z.; Dorenkamp, Y.; Manby, F. R.; Wodtke, A. M.; Miller, T. F.; Kandratsenka, A.; Bünermann, O. Imaging covalent bond formation by H atom scattering from graphene. *Science* **2019**, *364*, 379–382.
- (17) Santamaría, A. R.; Alducin, M.; Muñoz, R. D.; Juaristi, J. I. Ab Initio Molecular Dynamics Study of Alignment-Resolved O₂ Scattering from Highly Oriented Pyrolytic Graphite. *J. Phys. Chem. C* **2019**, *123*, 31094–31102.
- (18) Rutigliano, M.; Pirani, F. On the Influence of Rotational Motion of Oxygen Molecules on the Scattering from Graphite Surfaces. *J. Phys. Chem. C* **2019**, *123*, 11752–11762.
- (19) Majumder, M.; Bhandari, H. N.; Pratihari, S.; Hase, W. L. Chemical Dynamics Simulation of Low Energy N₂ Collisions with Graphite. *J. Phys. Chem. C* **2018**, *122*, 612–623.

(20) Greenwood, T.; Koehler, S. P. K. Nitric Oxide Scattering off Graphene using Surface-Velocity Map Imaging. *J. Phys. Chem. C* **2021**, *125*, 17853–17860.

(21) Lin, M. C.; Ertl, G. Laser Probing of Molecules Desorbing and Scattering from Solid Surfaces. *Annu. Rev. Phys. Chem.* **1986**, *37*, 587–615.

(22) Häger, J.; Roth, C.; Fink, M.; Walther, H. Scattering of rotationally excited NO molecules from a graphite surface. *Chem. Phys. Lett.* **1992**, *189*, 420–424.

(23) Häger, J.; Shen, Y. R.; Walther, H. State-selective velocity and angular distributions of NO molecules scattered from a graphite surface. *Phys. Rev. A* **1985**, *31*, 1962–1964.

(24) Frenkel, F.; Häger, J.; Krieger, W.; Walther, H.; Ertl, G.; Segner, J.; Vielhaber, W. Rotational state populations and angular distributions on surface scattered molecules: NO on graphite. *Chem. Phys. Lett.* **1982**, *90*, 225–229.

(25) Häger, J.; Fink, M.; Walther, H. Scattering of NO from a graphite surface at cryogenic temperatures. *Surf. Sci.* **2004**, *550*, 35–45.

(26) Nyman, G.; Holmlid, L.; Pettersson, J. B. C. Surface scattering of NO from graphite: A statistical description of energy distributions. *J. Chem. Phys.* **1990**, *93*, 845–853.

(27) Eppink, A. T. J. B.; Parker, D. H. Velocity map imaging of ions and electrons using electrostatic lenses: Application in photoelectron and photofragment ion imaging of molecular oxygen. *Rev. Sci. Instrum.* **1997**, *68*, 3477–3484.

(28) Abujarada, S.; AlSalem, H.; Chohan, U. K.; Draper, G. L.; Koehler, S. P. K. Photodesorption of NO from Au(100) using 3D surface-velocity map imaging. *J. Chem. Phys.* **2016**, *145*, 184201.

(29) Koehler, S. P. K.; Ji, Y.; Auerbach, D. J.; Wodtke, A. M. Three-dimensional velocity map imaging of KBr surface photochemistry. *Phys. Chem. Chem. Phys.* **2009**, *11*, 7540–7544.

(30) Sporleder, D.; Wilson, D. P.; White, M. G. Final State Distributions of O₂ Photodesorbed from TiO₂(110). *J. Phys. Chem. C* **2009**, *113*, 13180–13191.

(31) Roscioli, J. R.; Bell, D. J.; Nelson, D. J.; Nesbitt, D. J. State-resolved velocity map imaging of surface-scattered molecular flux. *Phys. Chem. Chem. Phys.* **2012**, *14*, 4070–4080.

(32) Hadden, D. J.; Messider, T. M.; Leng, J. G.; Greaves, S. J. Velocity map imaging the scattering plane of gas surface collisions. *Rev. Sci. Instrum.* **2016**, *87*, 106104.

(33) Abujarada, S.; Flathmann, C.; Koehler, S. P. K. Translational and Rotational Energy Distributions of NO Photodesorbed from Au(100). *J. Phys. Chem. C* **2017**, *121*, 19922–19929.

(34) Suits, A. G.; Bishwakarma, C. K.; Song, L.; Groenenboom, G. C.; van der Avoird, A.; Parker, D. H. Direct Extraction of Alignment Moments from Inelastic Scattering Images. *J. Phys. Chem. A* **2015**, *119*, 5925–5931.

(35) Greenwood, T.; Koehler, S. P. K. Molecular Dynamics Simulations of Nitric Oxide Scattering off Graphene. *ChemPhysChem* **2022**, *23*, No. e202200216.

(36) Rettner, C. T.; Schweizer, E. K.; Mullins, C. B. Desorption and trapping of argon at a 2H–W(100) surface and a test of the applicability of detailed balance to a nonequilibrium system. *J. Chem. Phys.* **1989**, *90*, 3800–3813.

(37) Luque, J.; Crosley, D. R. *LIFBASE: Database and Spectral Simulation Program*, version 1.5; SRI International Report MP 99-009; SRI International, 1999.

(38) Häger, J.; Walther, H. Laser investigation of the dynamics of molecule–surface interaction: Rotational and translational energy of scattered molecules. *J. Vac. Sci. Technol. B* **1985**, *3*, 1490–1497.

(39) Kleyn, A. W.; Luntz, A. C.; Auerbach, D. J. Rotational Energy Transfer in Direct Inelastic Surface Scattering: NO on Ag(111). *Phys. Rev. Lett.* **1981**, *47*, 1169–1172.

Recommended by ACS

Differential Cross Sections for Pair-Correlated Rotational Energy Transfer in NO(A²Σ⁺) + N₂, CO, and O₂: Signatures of Quenching Dynamics

Thomas F. M. Luxford, Matthew L. Costen, *et al.*

JULY 23, 2023

THE JOURNAL OF PHYSICAL CHEMISTRY A

READ 

Quantum and Semiclassical Dynamics of Nonadiabatic Electronic Excitation of C(³P) to C(¹D) by Hyperthermal Collisions with N₂

Dandan Lu and Hua Guo

MARCH 29, 2023

THE JOURNAL OF PHYSICAL CHEMISTRY A

READ 

Vector Correlations in the 225 nm Photodissociation of Co(CO)₃NO

Aaron C. Martinez, Jeffrey A. Bartz, *et al.*

JANUARY 03, 2023

THE JOURNAL OF PHYSICAL CHEMISTRY A

READ 

Cold Collisions of Ro-Vibrationally Excited D₂ Molecules

James F. E. Croft, N. Balakrishnan, *et al.*

FEBRUARY 14, 2023

THE JOURNAL OF PHYSICAL CHEMISTRY A

READ 

Get More Suggestions >